Borehole Effects on Downhole Seismic Measurements

by

Chengbin Peng

B.S., Beijing University (1985)
M.S., Graduate School of the Chinese Academy of Sciences (1988)

Submitted to the Department of Earth, Atmospheric, and Planetary Sciences
in partial fulfillment of the requirements for the degree of

Doctor of Philosophy

at the

MASSACHUSETTS INSTITUTE OF TECHNOLOGY

February 1994

Author .
Department of Earth, Atmospheric, and Planetary Sciences
November 10, 1993

Certified by. .
.....
M. Nafi Toksöz
Professor of Geophysics
Thesis Supervisor

Accepted by .
.....
Thomas H. Jordan
Chairman
Department of Earth, Atmospheric, and Planetary Sciences

Borehole Effects on Downhole Seismic Measurements

by

Chengbin Peng

Submitted to the Department of Earth, Atmospheric, and Planetary Sciences
on November 10, 1993, in partial fulfillment of the
requirements for the degree of
Doctor of Philosophy

Abstract

In this thesis, a complete and systematic investigation was carried out on borehole coupling theory, modeling techniques for VSP and crosswell surveys, and downhole hydrophone data processing. Our principal goal was to understand the borehole effects on downhole seismic measurements and consequently develop both modeling methods that take them into account and processing techniques that remove them from field data.

The first part of this thesis was concerned with the interaction of an incident elastic wave with open, cased, and noncircular boreholes. Exact formulations for borehole coupling were given. Explicit solutions for cased boreholes at low frequencies were also obtained. The borehole reception patterns for both the pressure in fluid (hydrophone measurement) and the solid displacement on the borehole wall (geophone measurement) were computed. The borehole effects on particle motion and the effect of geophone orientation were investigated in detail. We found that a significant fluid resonance exists when the formation is very soft and when the incident wave is of the SV-type. This resonance is associated with the excitation of a tube wave in the fluid. In an open borehole, it only prevails at low frequencies. However, in a cased borehole it is also prominent at very high frequencies, because the tube wave velocity is raised well above the formation shear wave speed by the steel pipe. In a cased borehole, for plane P-wave incidence at low frequencies, the pressure in the fluid vanishes at a particular angle of incidence if the casing thickness exceeds a critical value – the cased borehole screening effect. This behavior prevails in both hard and soft formations. In a borehole of irregular cross-section, the pressure in the fluid splits into two distinct branches depending on the azimuthal angle of the incident wave. The branch of larger amplitude is associated with incident waves propagating along the effective minor axis, and the one of smaller amplitude is associated with the incident waves along the effective major axis. Correction of the borehole effects on downhole geophone measurements should be made for frequencies above 500 Hz in the hard formation. In the soft formation, if the angle of incidence differs significantly from the resonance

angle for SV-wave incidence, no borehole correction is needed for frequencies below 300 Hz. For downhole experiments with frequency above 1000 Hz, boreholes can significantly alter the particle motion direction, thus data-based horizontal component rotation is unreliable.

The second part of this thesis was concerned with the modeling of hydrophone data in VSP and crosswell experiments. We first considered the case where the fluid-filled borehole was embedded in a stratified formation. A method was proposed for computing the pressure in the borehole fluid for a source in the formation, in which the borehole coupling theory was hybridly combined with the discrete wavenumber–global matrix algorithm. This method is accurate at low frequencies and is as fast as existing ones for modeling elastic wave propagation in a horizontally layered medium. We used this method to simulate the Kent Cliffs borehole experiment, where synthetic predictions of both the traveltime and the RMS amplitude were found to match the observed hydrophone data. We also considered the case where the formations adjacent to the borehole were neither homogeneous nor stratified. A method for calculating the pressure in the fluid-filled borehole was developed by cascading the 3-D elastic finite difference formulation with the borehole coupling theory. An optimal absorbing boundary condition was discovered and incorporated into the 3-D finite difference algorithm. Directly including the borehole in the finite difference model was found not to be feasible even for the currently available parallel computer. We circumvented this difficulty by dividing the whole problem into two parts: propagation from the source to the presumed borehole location by the finite difference method, and coupling into the fluid by applying the borehole coupling equations. This method was applied to simulate the Kent Cliffs hydrophone VSP data with a 3-D geological model including dipping formations. The synthetic P-wave amplitudes were found to match the observed ones better than the previous predictions with a stratified medium.

In the third part of this thesis, we developed a method for removing the borehole effects from downhole hydrophone data by applying inverse borehole coupling filters. In this method, the hydrophone VSP and crosswell data were transformed into the borehole squeeze pressures, whereby the tube waves were effectively eliminated and the P-wave and S-wave were partially compensated for the borehole effects on their amplitudes. A follow-up procedure was then employed to convert the borehole squeeze pressure to either the pressure or the displacement of an incident wave in the formation. This procedure was successfully applied to process the Kent Cliffs hydrophone VSP data. The processed data could be directly used as inputs to tomographic imaging and full-waveform inversion schemes in which the receiver borehole is not taken into account.

Thesis Supervisor: M. Nafi Toksöz
Title: Professor of Geophysics

Acknowledgment

I was told that I could not be admitted into MIT without the insistence of Prof. M. Nafi Toksöz and the recommendation of Prof. Ru-Shan Wu. For this, I would like first and foremost to thank both of them. Nafi, my thesis advisor, has taught me the skill of doing excellent research and of working with a diverse and stimulating group of students and staff. Arthur Cheng was an inspiration and a ready source of knowledge. I can not remember exactly how he convinced me to think seriously about the borehole coupling problem as a topic of thesis work. Anyway, I would like to thank him for his guidance during my thesis research and for his patience in answering my numerous questions. I am also grateful to Bill Rodi for this cooperation and knowledge on inverse problem. Bill and I have published a series of papers on Tikhonov regularization with a differential operator. I must apologize to him for not choosing this exciting field as my thesis topic (I had been diving in two disconnected pools of research: borehole acoustics and tomography. I made a decision to give up the latter in the middle of my third year at MIT, apparently realizing that Joe Matarese and Delaine Thompson have accomplished a lot on nonlinear tomography and there wouldn't be much free sky left for me to fly in). I am also thankful to Jung M. Lee for his help and effort in modeling and analyzing the Kent Cliffs hydrophone VSP data, and to Roger Turpening for his encouragement to look at real data.

Along the way, I received an enormous amount of help from people at ERL, present and past: Bob Cicerone, Ted Charrette, Anton Dainty, Rick Gibson, Joe Matarese, Jeff Meredith, Edmond Reiter, Craig Schultz, Delaine Thompson, Zhenya Zhu and others. Among them, I am especially thankful to Dr. Zhenya Zhu for helping me with laboratory experiments, and to Dr. Ted Charrette for his enduring help with the nCUBE parallel supercomputer, and to Dr. Joe Matarese for letting me share his expertise on all aspects of computer and computation knowledges (and for his thesis template with which all the figures in this thesis are incorporated into LaTex), and to Drs Rick Gibson, Jung M. Lee and Delaine Thompson for helping me reading parts of the thesis. No one else would appreciate the helps of Sara Brydges, Naida Buckingham, Liz Henderson and Sue Turbak more than I do. They must have borne their disappointments of my poor English writing many times when I requested for them to read my papers. I am very thankful to them.

I might be the only person who has stayed in room E34-370 during the entire stay at MIT. This room has its reputation for being too hot in both winter and summer. Nevertheless, I enjoyed being a member of consortium-370 comprised of myself, Matthias Imhof and Matthijs Haartsen (The people in room 370 developed a PostScript graphics library on workstations. More than 80% of the figures in this thesis are produced using this graphics library). I am thankful to both Matts.

My final two and a half study years were funded through an nCUBE fellowship. I wish to thank nCUBE Corporation for providing me with both financial and com-

putational support. I also wish to thank Shell Offshore Inc. and Shell development Company for providing me internships during the summers of 1991 and 1992, where my knowledge about exploration geophysics was broadened. Especially, I want to thank Dr. Won N. King, Shari Griswood, Fred Hoffman, Drs. V. K. Cung, T. Padhi and Archi Robison.

I would like to thank my Chinese fellow students in the department: Ningya Cheng, Danan Dong, Wenjie Dong, Huaimin Zhang, Jie Zhang and Xiaomin Zhao, who have shared with me the experiences and interests of being a foreign student from the People's Republic of China. I am also thankful to Drs. Yingpin Li, Xiaoming Tang and Zhenya Zhu for being both teachers and friends.

I will always cherish the love and sacrifice of my wife Cannie Liu. It is her patience, understanding and love that uphold me through the hardship of being a graduate student at MIT. I am most grateful to my family: my parents, my younger brother and three younger sisters. My wife and my family are responsible for keeping me sane during these past few years.

Contents

Chapter 1

Introduction

1.1 Overview

In this thesis, we study the interaction of an incident elastic wave with a fluid-filled borehole. The goal is to understand the borehole effects on downhole seismic measurements and consequently develop both modeling methods that take them into account and processing techniques that remove them from field data. The chief use of this study will be to help unravel, interpret, and process the field data in crosswell and vertical seismic profiling (VSP) experiments.

Using full-waveform seismic data to infer subsurface structures becomes an important pursuit in exploration geophysics as well as earthquake seismology. Full-waveform inversion (Mora, 1988; Cao et al., 1990; Crase et al., 1990), geophysical diffraction tomography (Devaney, 1984; Wu and Toksöz, 1987; Pratt and Worthington, 1988; Pratt and Goulty, 1991; Thompson, 1993), and true amplitude migration (Clayton and Stolt, 1981; Bleistein et al., 1987; Schleicher et al., 1993), as well as AVO (amplitude versus offset) analysis (Ostrander, 1984; Castagna, 1993; and others), have been subjects of intensive research in the past decade. These techniques

require true amplitude data at the locations where measurements are made.

Increasing interest is shown towards the crosshole and vertical seismic profiling surveys at frequencies up to 1 kHz or more in order to resolve the fine details of structures and lithology between wells (Harris 1988; Bregman et al., 1989; Albright et al., 1990; Rechtien, 1993; Matarese, 1993). However, at frequencies on the order of 1 kHz, the existence of a fluid-filled borehole exercises a strong influence on the downhole measurements. Depending on the frequency and angle of incidence, as well as on the formation properties, the measured displacement on the borehole wall or the pressure at the center of the fluid may significantly differ from that of the incident wave. Without proper attention to this effect, imaging and inversion techniques that utilize both the amplitude and phase information of the recorded energy may be erroneous because the borehole is not included as part of the formulations.

Developing a method for computing the hydrophone response in crosswell and VSP geometries has also practical implications, since a variety of borehole applications measure the pressure inside a fluid-filled borehole for a source on the surface or in another well (Huang and Hunter, 1981; Hardage 1981; Marzetta et al., 1988; Lee, 1990; Albright et al., 1990; Krohn, 1992; Toksöz et al., 1992). Although numerical simulations of elastic wave propagation in the crosswell and VSP configurations have been well studied in recent years (Wyatt, 1981; Temme and Mueller, 1982; Sullivan, 1984; McMechan, 1985; Schmidt et al., 1986; Aminzadeh, 1989; Bouchon, 1993), none of the studies included the receiver borehole. Thus, they were incapable of handling events associated with the borehole fluid and yielded erroneous amplitudes for the direct and reflected waves refracted at the fluid-solid interface.

With these aspects in mind, we devote this thesis to the following objectives:

- We study the borehole effects on downhole seismic measurements: specifically, the dependence of both the pressure in the fluid (hydrophone data) and the solid displacement on the borehole wall (geophone data) on the frequency, angle

of incidence, formation properties, and tool orientation, for open, cased and irregular boreholes.

- We propose methods for modelling downhole hydrophone measurements that include a fluid-filled borehole. The formation surrounding the borehole can be either stratified or heterogeneous. In the first case, our method employs the propagator matrices–discrete wavenumber technique and the borehole coupling theory. In the second case, our method vigorously combines the 3-D elastic finite difference formulation with the borehole coupling equation. These abilities to simulate downhole hydrophone data were not available previously.

- We develop inverse borehole coupling techniques for removing borehole effects from downhole seismic data. Unlike the conventional processing of VSP and crosswell hydrophone data, our techniques are based on the physics of the borehole coupling process and yield a quantity that directly resembles the incident wave field in the formation. The data resulting from our procedure can be used subsequently in full-waveform inversion, diffraction tomography, and true amplitude migration.

1.2 Background

White (1953) presented a picture of the borehole coupling at a zero frequency limit. As frequency goes to zero, the size of the borehole becomes much smaller than the wavelength such that the stress caused by an incident elastic plane wave is almost homogeneous in the vicinity (much larger than the borehole radius) around the presumed borehole location. The introduction of a borehole will disturb the local homogeneous stress field and the subsequent change of shape of the borehole can then be exactly computed. The volume change of the borehole sets up a disturbance inside the fluid in the same way as a piston source. The pressure at a given location is the summation of contributions from all the secondary sources along the borehole with appropriate

time delays.

Schoenberg (1986) developed a complete theory for the interaction of a plane elastic wave with a fluid-filled (open) borehole and gave an explicit formulation for the low-frequency limit. In his theory, both the elastic wave field in the solid and the acoustic wave field inside the fluid satisfy the corresponding wave equations, and the coupling between them is accomplished through the fluid-solid interface boundary conditions. It turns out that, as the frequency approaches zero, Schoenberg's (1986) formulation reduces to that of White (1953).

Lee (1987) also derived the low frequency formulation for borehole coupling by applying the reciprocity relationships with respect to the borehole radiation. White and Welsh (1988) gave expressions for pressure in a fluid-filled borehole due to the passage of plane elastic waves in a porous and permeable medium, using the same quasi-static analysis of White (1983). Lovell and Hornby (1990) presented a complete formulation for both low and high frequencies for the azimuthally symmetric component, so their formulation can only apply to the pressure measurement at the center of the borehole. The result given by Blair (1984) was a special case of that by Lovell and Hornby at a normal incidence.

In the closely related literature in acoustics journals, Gaunaurd et al. (1978) studied the elastic wave scatterings by spherical cavities filled with a fluid. Dickey et al. (1978) studied the scattering of acoustic wave by elastic cylinders. Flax et al. (1977) studied the acoustic wave scattering by concentrically layered elastic cylinders; Uginčius et al. (1968) studied the acoustic wave scattering by elastic cylindrical shells. To the best of our knowledge, no paper relevant to the present problem has been published.

Complementary to the theoretical works describing borehole coupling are theoretical investigations on borehole radiations. Heelan (1952, 1953) studied the far field radiation for a source in an empty borehole, where he noticed a significant shear

wave amplitude for an explosive source inside the borehole. Greenfield (1978) considered radiation from an empty borehole from a point force on the borehole wall, where a substantial numerical treatment of wave propagation was devised. Lee and Balch (1982) extended Heelan's work by considering a fluid in the borehole and used the stationary phase method in deriving a low frequency approximation. Meredith (1990) developed both numerical and analytical solutions to describe radiation from a downhole source in the near and far field for a variety of downhole sources, and identified the Mach wave radiation in a slow formation. The stationary phase formulation is also employed by Gibson (1993) in studying radiation from a source in a cased borehole, where the stationary phase wavenumber is determined analytically and the boundary condition equations are solved numerically.

Also complementary to this work is the substantial volume of papers on acoustic well logging (White and Zechman, 1968; Rosenbaum, 1974; Cheng and Toksöz, 1981; Schoenberg et al., 1981; Tubman et al., 1984; Kurkjian, 1985). Excellent reviews on this topic can be found in a review paper by Toksöz and Cheng (1984) and in the book by Paillet and Cheng (1991).

According to the elastic reciprocity theorem, the radiation problem is, in theory, reciprocal to the borehole reception problem. As a matter of fact, White (1960) applied the theorem to obtain a simple formula for open borehole radiation from a ring of radial force acting on the borehole wall, using results from his early work on borehole coupling (White, 1953). Conversely, Lee (1987) applied the theorem to study borehole coupling, using the earlier work of Lee and Balch (1982) on open borehole radiation. Gibson and Peng (1993) also applied the theorem to derive a simple formula for cased borehole radiation from a volume source, using results obtained by Peng et al. (1993b) (see Chapter 3 of this thesis) on cased borehole coupling.

However, the reciprocity theorem doesn't apply if the conditions pertaining to it are not satisfied. For a purely spatial reciprocity, the theorem states that the displacement in **n** direction at location **x** due to a unit impulse force in the **m** direction

acting at location **y** is equal to the displacement in **m** direction at location **y** due to a unit impulse force in the **n** direction acting at location **x** (Aki and Richard, 1980). A violation of this theorem could be, for instance, using the results of P-wave radiation from an axial source to compute the borehole fluid pressure due to an incident P-wave (see Fokkema et al., 1993, Chapter 6).

Even if the reciprocity theorem does apply, the reciprocal problem might be quite difficult to attack, as is the case of calculating an elastic wave field due to a force on the borehole wall and then applying the results to study a geophone response due to a P-wave incidence upon the borehole. In this particular example, the radiation problem is much harder to solve than the reception problem, and the results are difficult to interpret in terms of the coupling terminologies.

As far as the modeling techniques for the crosswell and VSP applications are concerned, numerous works have appeared in the literature. Methods for computing the displacement at a borehole location in a stratified medium include, to mention a few, those of Wyatt (1981) and Aminzadeh (1989) using the reflectivity method, Temme and Mueller (1982) and Suprajitno and Greenhalgh (1986) using the Kennett-type propagator matrix method, Schmidt et al. (1986) employing the global matrix method, and Dietrich and Bouchon (1985) using the discrete wavenumber representation. For a more general formation, Cormier and Mellen (1984) used the dynamical ray tracing method, Sullivan (1984) applied the finite element method, McMechan (1985) used the finite difference method, and Bouchon (1993) employed a boundary integral equation method. All of these methods are suitable to modeling downhole 3-component geophone data and implicitly assume that geophones are buried in the solid, as if the borehole has ceased to exist. The fluid-filled borehole is not included as a part of these formulations at all. It turns out that, for a low frequency experiment, these methods yield correct synthetic seismograms for 3-component geophone data (see Chapter 2). However, high frequencies are being used now to obtain good seismic resolution, and boreholes affect these measurements.

Pressure measurements using a vertical array of hydrophones permit rapid data acquisition for borehole seismic surveys. In addition, the overall cost, including tool design and field surveying, is also significantly less. The existing methods are incapable of handling events associated with the borehole and yield erroneous amplitudes of direct and reflected waves refracted at the fluid-solid interface. No efficient method for modelling hydrophone VSP and crosshole data is practically available as yet.

Numerous publications have also been devoted to hydrophone data processing, where the major goal is to reject the tube waves. Balch and Lee (1984) described a recipe for VSP data processing in which the multichannel velocity filtering is advocated. Tube waves, although providing useful information in sonic logging analysis, are generally considered noises in VSP and crosswell applications. These waves have a characteristic propagation speed and can be removed by applying 2-D fan filtering (DiSiena et al., 1984; Robinson, 1986; Marzetta et al., 1988; Lee, 1990). Other types of techniques have also appeared in the literature. For instances, Beydoun (1984) suggested a method for removing tube waves by applying a transfer function between the pressure data in fluid and the geophone data in formation. However, the processed hydrophone data still bear no direct resemblance to the wave fields in the formation. They are not directly useful for tomographic imaging and inversion schemes that make use of the amplitudes of both P-wave and, hopefully, S-wave, for the borehole is not included as a part of their formulations.

The fluid-filled borehole can be viewed as a reception antenna in receiving the incident elastic energy from the surrounding formation. It is linear, causal, and time invariant, suggesting that an inverse filter can be applied to remove the coupling effect. Using the inverse borehole coupling theory to reject the tube waves from hydrophone vertical seismic profiling data was recently proposed by Marzetta (1992). In his paper, apparently realizing the usefulness of an old but elegant analysis of White (1953, 1983), Marzetta showed that a physically meaningful quantity called the *borehole squeeze strain* could be obtained from an array of hydrophone data. The limitations of Marzetta's method are twofold: it applies to an open borehole only,

and the borehole squeeze strain is not a quantity commonly used by the scientific community.

1.3 Thesis Outline

Chapter 2 gives an exact formulation for borehole coupling that is valid for all frequencies and all azimuthally symmetric and nonsymmetric components. The borehole effects on downhole seismic measurements are studied in detail as functions of frequency, angle of incidence, and polarization of an incident wave, as well as geophone orientation. We find that correction for the borehole effect on downhole measurements should be made for frequencies above 500 Hz in a hard formation. In a soft formation, if the angle of incidence is well away from the resonance angle for SV-wave incidence, no borehole correction is needed for frequencies below 300 Hz. While for frequencies above 300 Hz, the borehole can cause severe problems on downhole measurements. The borehole can also significantly alter the particle motion direction, which implies that the horizontal component rotation from data is unreliable for experiments with frequencies above 1 kHz in the hard formation and around 500 Hz in the soft formation.

In Chapter 3, approximate and exact formulations are presented for the interaction of an incident wave with a cased borehole. In the approximate method, the borehole coupling theory is used to compute pressure in the fluid at a low frequency. The results are simple and explicit. They are useful in the study of cased borehole coupling and radiation as well. In the exact method, elastic potentials in each annulus are represented as a superposition of fundamental solutions to the Helmholtz equations. Continuity of displacements and stresses across layer boundaries are used to determine unknown coefficients. The global matrix method is employed to simultaneously compute these coefficients in individual layers. Our results show that, in a cased borehole, the borehole effects on downhole seismic measurements are more sig-

nificant than those in an open borehole, especially when the formation is soft and the casing is steel. For hard formations and frequencies below 1 kHz, the cased borehole influence on a downhole geophone measurement is minimal, while at high frequencies, large discrepancies occur, especially at grazing incidence. For soft formations, both the pressure in the fluid and the solid displacement on the borehole wall show strong dependence on frequency and angle of incidence, even at very low frequencies. Strong resonance occurs in the fluid for SV-wave incidence at an angle $\delta = cos^{-1}\beta/C_T$, where C_T is the tube wave velocity in a cased borehole. This resonance is prominent even at very high frequencies and at a large angle of incidence, because the tube wave velocity is raised well above the formation shear velocity by the steel pipe. This behavior is very different from that in an open borehole. At a particular angle of incidence of plane P-wave, the pressure in the fluid is near zero at low frequencies. This angle is dependent on the casing thickness and can be computed exactly. In general the casing behaves like a shield (or screen) in such a way that the amplitude of both pressure in the fluid and solid displacement on the borehole wall are reduced compared to those in an open borehole.

Boreholes with 10% ellipticity are not uncommon. In Chapter 4, we consider the coupling of elastic wave energy into a borehole of irregular cross-section, in order to quantify the effect of borehole irregularity on a downhole seismic measurement, and to investigate the cross-mode coupling phenomenon in sonic well logging in the presence of borehole irregularity. The latter might be mistakenly attributed to formation anisotropy. The mode-matching method is used. Different from its original formulation, we employ the Reichel et al. algorithm to obtain the discrete least square approximation by trigonometric polynomials, a technique closely related to the fast Fourier transform (FFT). Our method not only yields great accuracy but also gains computational speed. Our study shows that the pressure in the borehole fluid is sensitive to the irregularity of the borehole cross-section, it is larger if the incident wave is along the effective minor axis and smaller if the incident wave is along the effective major axis. In the frequency range of a typical borehole experiment, the

solid displacement in the formation is much less affected by the borehole irregularity. In an elliptical borehole, a monopole source excites dipole wave trains that are characteristic of the tube waves, and a centered dipole source excites monopole wave trains that are characteristic of the flexural waves.

In Chapter 5, we present a method to model hydrophone VSP data in a stratified formation. The method makes use of the borehole coupling theory and the global matrices formulation for computing synthetic seismograms in a stratified medium. Our approach greatly reduces the difficulties of the original problem: to compute the pressure in a fluid-filled borehole for a source in a stratified formation. Comparison with an exact solution for an open borehole in a homogeneous and unbounded formation shows that this method is accurate for a frequency below 2 kHz. It is used to simulate the Kent Cliffs hydrophone VSP data, where good agreements between the numerical simulations and the field measurements have been found, in both travel-time and amplitude of the direct P-wave. Examples given in this chapter show that this method is efficient and accurate, and can be applied to model hydrophone VSP and crosshole data.

The contributions in Chapter 6 are threefold. Firstly, an optimal absorbing boundary condition is designed to model acoustic and elastic wave propagation in 2-D and 3-D media using the finite difference method. In our method, extrapolation on the artificial boundaries of a finite difference domain is expressed as a linear combination of wave fields at previous time steps and/or interior grids. The acoustic and elastic reflection coefficients from the artificial boundaries are derived. They are found to be identical with the transfer functions of two cascaded systems: one is the inverse of a causal system and the other is an anticausal system. This method makes use of the zeros and poles of reflection coefficients in a complex plane. The optimal absorbing boundary condition designed in this paper yields about 10 dB smaller in magnitude of reflection coefficients than Higdon's absorbing boundary condition, and around 20 dB smaller than Reynolds' absorbing boundary condition.

Secondly, a 3-D elastic finite difference algorithm is developed in this chapter in which the optimal absorbing boundary condition is employed. This algorithm utilizes the stress-velocity formulation of Virieux (1986) and has a fourth-order accuracy in space and a second-order accuracy in time. It is parallelized on nCUBE-2[1]. Comparison with the classic discrete wavenumber–global matrix method shows that the finite difference algorithm is accurate.

Thirdly, a hybrid method for computing the pressure in a fluid-filled borehole embedded in a heterogeneous formation is proposed, where the 3-D elastic finite difference algorithm is combined with the borehole coupling equations. This method is very general and can be applied to a variety of heterogeneous models. We have applied this method to simulate the Kent Cliffs hydrophone data, using a revised model including dipping formations. The theoretical predictions of the P-wave arrivals match the field data better than the simulations with a stratified geological model.

Chapter 7 describes a new procedure for processing hydrophone VSP and crosswell data. This procedure consists of three steps using three techniques. In the first step we apply an inverse borehole coupling equation to convert hydrophone pressure data into borehole squeeze pressure data, by which the tube waves are significantly attenuated and the P-wave and S-wave are partially compensated for the borehole effects. In the second step, we make use of a partial differential equation that relates the borehole squeeze pressure to the pressure of the incident P-wave. In solving this equation, we are able to obtain the P-wave signal as if the hydrophone is measuring the incident wave in the formation, not in the borehole fluid. Several synthetic examples are used to demonstrate its accuracy. The Kent Cliffs hydrophone data is successfully processed using the above two steps, and the data quality is found to be significantly improved. In the third step, we show that one can also map the hydrophone pressure data into the geophone responses, provided that both the P-wave and S-wave velocity profiles along the borehole are known.

[1]nCUBE-2 is a massively parallelized supercomputer made by nCUBE corporation.

Conclusions are provided in Chapter 8 along with future directions of research. For ease of reading and coherence of this thesis, many of the mathematical details are placed in Appendices. Appendix A gives some basic equations in a cylindrical coordinate and lists the coefficients of the displacements and stresses in Chapter 2 and Chapter 4. Appendix B lists the coefficients of the displacements and stresses in Chapter 3. Appendix C presents expressions for the elements of coefficient matrices in Chapter 4. Appendix D presents a brief summary of the Reichel et al. algorithm for discrete least squares approximation by trigonometric polynomials. Appendix E outlines a method for determining the coefficients of the optimal absorbing boundary condition and is associated with Chapter 6.

Chapter 2

Open Borehole Effects on Downhole Seismic Measurements[1]

Borehole coupling signifies the manner in which an incident elastic wave is distorted by a fluid-filled borehole. White (1953) studied the coupling theory in an open borehole at a zero frequency limit by applying a quasi-static analysis. Schoenberg (1986) developed a complete theory for the interaction of a plane elastic wave with a fluid-filled (open) borehole and gave an explicit formulation for the low-frequency limit. He showed that, as the frequency approaches zero, his formulation reduces to that of White (1953). Also independently, Lee (1987) derived the low frequency formulation for borehole coupling by applying the reciprocity relationships with respect to the borehole radiation. Lovell and Hornby (1990) presented a complete formulation for both low and high frequencies for the azimuthally symmetric case. Their formulation applies only to the pressure measurement at the center of the borehole. The result given by Blair (1984) was a special case of that by Lovell and Hornby at a normal incidence.

In this chapter, we present an exact formulation for the coupling of elastic wave

[1]This chapter has been published in *Geophysical Prospecting*, volume 41, pp 883–912, 1993.

energy into a fluid-filled borehole, which is valid for all frequencies as well as both azimuthally symmetric and nonsymmetric components. The objective is to investigate, in great details, the effects of a borehole on downhole seismic measurements as functions of frequency, angle of incidence, polarization of incoming elastic waves (P-wave, SV-wave and SH-wave), and the geophone orientation.

This chapter is organized as follows. In the first section, we present a theoretical formulation for the interaction of elastic wave energy with an open borehole. Incident plane P-, SV- and SH-waves are considered. Formulae for computing the pressure response in fluid and the solid displacements in formation are given. In the second section, we study, for a plane compressional wave incidence, the borehole reception pattern, the borehole effect on particle motion, and the effects of geophone orientation. The case of shear wave incidence is given in the third section. Finally, in the forth section, we discuss the results and draw some conclusions.

2.1 Theoretical Formulation

Consider an elastic wave incident on an infinite borehole drilled into a homogeneous elastic medium with density ρ, compressional wave speed α and shear wave speed β (Figure 2-1). The borehole is filled with a fluid of density ρ_f and compressional wave speed α_f. The radius of the borehole is r_b. When the wave hits the borehole, a transmitted compressional wave (denoted by the displacement $\vec{u}^f$) is generated in the fluid and, at the same time, a scattered elastic wave (denoted by $\vec{u}^s$) is produced in the solid. If a three component geophone is placed in the fluid, as is the case of very poor clamping, $\vec{u}^f$ will be recorded. If it is clamped tightly against the formation, $\vec{u}^i + \vec{u}^s$ will be measured, where $\vec{u}^i$ denotes the incident wave.

The fluid displacement $\vec{u}^f$ can be expressed in terms of a potential ϕ_f which

satisfies the fluid wave equation given by

$$\nabla^2\phi_f + \frac{\omega^2}{\alpha_f^2}\phi_f = 0, \tag{2.1}$$

where $\vec{u}^f = \nabla\phi_f$. The displacement of the scattered wave in the elastic solid can be represented by three elastic potentials ϕ (P-wave potential), ξ (SV-wave potential) and ψ (SH-wave potential), and is given by (Morse and Feshbach, 1953)

$$\vec{u}^s = \nabla\phi + \nabla\times(\nabla\times(\xi\hat{e}_z)) + \nabla\times(\psi\hat{e}_z), \tag{2.2}$$

where

$$\nabla^2\phi + \frac{\omega^2}{\alpha^2}\phi = 0,$$

$$\nabla^2\xi + \frac{\omega^2}{\beta^2}\xi = 0,$$

$$\nabla^2\psi + \frac{\omega^2}{\beta^2}\psi = 0.$$

The general solution of these potentials in the cylindrical coordinate is given by Schoenberg (1986)[2] as

$$\phi_f = -\frac{\alpha_f V(\omega)}{\omega^2}\left[A_0 J_0(k_f r) + 2\sum_{n=1}^{\infty} i^n (A_n \cos n\theta + A_n' \sin n\theta) J_n(k_f r)\right], \tag{2.3a}$$

$$\phi = -\frac{\alpha V(\omega)}{\omega^2}\left[B_0 H_0^{(1)}(k_p r) + 2\sum_{n=1}^{\infty} i^n (B_n \cos n\theta + B_n' \sin n\theta) H_n^{(1)}(k_p r)\right], \tag{2.3b}$$

$$\xi = -\frac{i\beta^2 V(\omega)}{\omega^3}\left[C_0 H_0^{(1)}(k_s r) + 2\sum_{n=1}^{\infty} i^n (C_n \cos n\theta + C_n' \sin n\theta) H_n^{(1)}(k_s r)\right], \tag{2.3c}$$

$$\psi = -\frac{\beta V(\omega)}{\omega^2}\left[-D_0' H_0^{(1)}(k_s r) + 2\sum_{n=1}^{\infty} i^n (D_n \sin n\theta - D_n' \cos n\theta) H_n^{(1)}(k_s r)\right], \tag{2.3d}$$

where time and depth dependence $e^{i(k_z z - \omega t)}$ is assumed, and $k_f = \sqrt{\omega^2/\alpha_f^2 - k_z^2}$, $k_p = \sqrt{\omega^2/\alpha^2 - k_z^2}$ and $k_s = \sqrt{\omega^2/\beta^2 - k_z^2}$. The signs of k_f, k_p, k_z are chosen such that $\mathbf{Im}(k_p, k_s, k_f) \geq 0$. $V(\omega)$ denotes the source function at a given frequency ω. Without loss of generality, $V(\omega) = -\omega^2$ is assumed.

[2]Certainly not the original reference. Schoenberg is credited here for his contributions to the borehole coupling theory, where he shows that the exact formulation reproduces White's results at low frequencies.

Given the potentials in equations (2.3a)–(2.3d), the components of displacement and stress involved in the boundary conditions can be written as

$$u_r^f = \mathcal{U}_0^{(f)}(r)A_0 + 2\sum_{n=1}^{\infty} i^n \mathcal{U}_n^{(f)}(r)\ (A_n \cos n\theta + A_n' \sin n\theta), \tag{2.4a}$$

$$u_r^\phi = \mathcal{U}_0^{(\phi)}(r)B_0 + 2\sum_{n=1}^{\infty} i^n \mathcal{U}_n^{(\phi)}(r)\ (B_n \cos n\theta + B_n' \sin n\theta), \tag{2.4b}$$

$$u_r^\xi = \mathcal{U}_0^{(\xi)}(r)C_0 + 2\sum_{n=1}^{\infty} i^n \mathcal{U}_n^{(\xi)}(r)\ (C_n \cos n\theta + C_n' \sin n\theta), \tag{2.4c}$$

$$u_r^\psi = \mathcal{U}_0^{(\psi)}(r)D_0 + 2\sum_{n=1}^{\infty} i^n \mathcal{U}_n^{(\psi)}(r)\ (D_n \cos n\theta + D_n' \sin n\theta), \tag{2.4d}$$

and

$$-p^f = \sigma_{rr}^f = \mathcal{R}_0^{(f)}(r)A_0 + 2\sum_{n=1}^{\infty} i^n \mathcal{R}_n^{(f)}(r)\ (A_n \cos n\theta + A_n' \sin n\theta), \tag{2.5a}$$

$$\sigma_{rr}^\phi = \mathcal{R}_0^{(\phi)}(r)B_0 + 2\sum_{n=1}^{\infty} i^n \mathcal{R}_n^{(\phi)}(r)\ (B_n \cos n\theta + B_n' \sin n\theta), \tag{2.5b}$$

$$\sigma_{rr}^\xi = \mathcal{R}_0^{(\xi)}(r)C_0 + 2\sum_{n=1}^{\infty} i^n \mathcal{R}_n^{(\xi)}(r)\ (C_n \cos n\theta + C_n' \sin n\theta), \tag{2.5c}$$

$$\sigma_{rr}^\psi = \mathcal{R}_0^{(\psi)}(r)D_0 + 2\sum_{n=1}^{\infty} i^n \mathcal{R}_n^{(\psi)}(r)\ (D_n \cos n\theta + D_n' \sin n\theta), \tag{2.5d}$$

and

$$\sigma_{r\theta}^\phi = \mathcal{T}_0^{(\phi)}(r)B_0' + 2\sum_{n=1}^{\infty} i^n \mathcal{T}_n^{(\phi)}(r)\ (-B_n \sin n\theta + B_n' \cos n\theta), \tag{2.6a}$$

$$\sigma_{r\theta}^\xi = \mathcal{T}_0^{(\xi)}(r)C_0' + 2\sum_{n=1}^{\infty} i^n \mathcal{T}_n^{(\xi)}(r)\ (-C_n \sin n\theta + C_n' \cos n\theta), \tag{2.6b}$$

$$\sigma_{r\theta}^\psi = \mathcal{T}_0^{(\psi)}(r)D_0' + 2\sum_{n=1}^{\infty} i^n \mathcal{T}_n^{(\psi)}(r)\ (-D_n \sin n\theta + D_n' \cos n\theta), \tag{2.6c}$$

and

$$\sigma_{rz}^\phi = \mathcal{Z}_0^{(\phi)}(r)B_0 + 2\sum_{n=1}^{\infty} i^n \mathcal{Z}_n^{(\phi)}(r)\ (B_n \cos n\theta + B_n' \sin n\theta), \tag{2.7a}$$

$$\sigma_{rz}^\xi = \mathcal{Z}_0^{(\xi)}(r)C_0 + 2\sum_{n=1}^{\infty} i^n \mathcal{Z}_n^{(\xi)}(r)\ (C_n \cos n\theta + C_n' \sin n\theta), \tag{2.7b}$$

$$\sigma_{rz}^{\psi} = \mathcal{Z}_0^{(\psi)}(r)D_0 + 2\sum_{n=1}^{\infty} i^n \mathcal{Z}_n^{(\psi)}(r)\ (D_n \cos n\theta + D_n' \sin n\theta), \tag{2.7c}$$

where the superscripts f, ϕ, ξ and ψ in the parentheses denote the displacement or stress due to the corresponding potentials. The details of the derivation and the coefficients are given in Appendix A.

The coefficients $A_n, A_n', B_n, B_n', C_n, C_n', D_n, D_n'$ are determined by applying the continuity of radial displacement and normal stress at the borehole wall

$$u_r^s(r_b^+) + u_r^i(r_b^+) = u_r^f(r_b^-), \tag{2.8}$$

$$\sigma_{rr}^s(r_b^+) + \sigma_{rr}^i(r_b^+) = -p^f(r_b^-), \tag{2.9}$$

and vanishing tangential stresses

$$\sigma_{r\theta}^s(r_b^+) + \sigma_{r\theta}^i(r_b^+) = 0, \tag{2.10}$$

$$\sigma_{rz}^s(r_b^+) + \sigma_{rz}^i(r_b^+) = 0, \tag{2.11}$$

where the superscript i denotes the displacement and stress of the incident wave, s denotes those of the scattered wave and f those in the fluid.

The displacement and stress of incident elastic plane waves (P-wave, SV-wave or SH-wave) are also expressible in terms of mode summation. For P-wave incidence, we have

$$u_r^P = \mathcal{U}_0^{(P)}(r) + 2\sum_{n=1}^{\infty} i^n \mathcal{U}_n^{(P)}(r)\ (\cos n\nu \cos n\theta + \sin n\nu \sin n\theta), \tag{2.12a}$$

$$\sigma_{rr}^P = \mathcal{R}_0^{(P)}(r) + 2\sum_{n=1}^{\infty} i^n \mathcal{R}_n^{(P)}(r)\ (\cos n\nu \cos n\theta + \sin n\nu \sin n\theta), \tag{2.12b}$$

$$\sigma_{r\theta}^P = \mathcal{T}_0^{(P)}(r) + 2\sum_{n=1}^{\infty} i^n \mathcal{T}_n^{(P)}(r)\ (-\cos n\nu \sin n\theta + \sin n\nu \cos n\theta), \tag{2.12c}$$

$$\sigma_{rz}^P = \mathcal{Z}_0^{(P)}(r) + 2\sum_{n=1}^{\infty} i^n \mathcal{Z}_n^{(P)}(r)\ (\cos n\nu \cos n\theta + \sin n\nu \sin n\theta). \tag{2.12d}$$

For SV-wave incidence, we have

$$u_r^{SV} = \mathcal{U}_0^{(SV)}(r) + 2\sum_{n=1}^{\infty} i^n \mathcal{U}_n^{(SV)}(r)\ (\cos n\nu \cos n\theta + \sin n\nu \sin n\theta), \tag{2.13a}$$

$$\sigma_{rr}^{SV} = \mathcal{R}_0^{(SV)}(r) + 2\sum_{n=1}^{\infty} i^n \mathcal{R}_n^{(SV)}(r)\ (\cos n\nu \cos n\theta + \sin n\nu \sin n\theta), \tag{2.13b}$$

$$\sigma_{r\theta}^{SV} = \mathcal{T}_0^{(SV)}(r) + 2\sum_{n=1}^{\infty} i^n \mathcal{T}_n^{(SV)}(r)\ (-\cos n\nu \sin n\theta + \sin n\nu \cos n\theta), \tag{2.13c}$$

$$\sigma_{rz}^{SV} = \mathcal{Z}_0^{(SV)}(r) + 2\sum_{n=1}^{\infty} i^n \mathcal{Z}_n^{(SV)}(r)\ (\cos n\nu \cos n\theta + \sin n\nu \sin n\theta). \tag{2.13d}$$

And for SH-wave incidence, we have

$$u_r^{SH} = \mathcal{U}_0^{(SH)}(r) + 2\sum_{n=1}^{\infty} i^n \mathcal{U}_n^{(SH)}(r)\ (-\cos n\nu \sin n\theta + \sin n\nu \cos n\theta), \tag{2.14a}$$

$$\sigma_{rr}^{SH} = \mathcal{R}_0^{(SH)}(r) + 2\sum_{n=1}^{\infty} i^n \mathcal{R}_n^{(SH)}(r)\ (-\cos n\nu \sin n\theta + \sin n\nu \cos n\theta), \tag{2.14b}$$

$$\sigma_{r\theta}^{SH} = \mathcal{T}_0^{(SH)}(r) + 2\sum_{n=1}^{\infty} i^n \mathcal{T}_n^{(SH)}(r)\ (\cos n\nu \cos n\theta + \sin n\nu \sin n\theta), \tag{2.14c}$$

$$\sigma_{rz}^{S} = \mathcal{Z}_0^{(SH)}(r) + 2\sum_{n=1}^{\infty} i^n \mathcal{Z}_n^{(SH)}(r)\ (-\cos n\nu \sin n\theta + \sin n\nu \cos n\theta). \tag{2.14d}$$

In all these equations, ν is the azimuth of the incident wave. The details are given in Appendix A-4.

Applying the boundary conditions will lead to the following equations for the unknown coefficients

$$\mathrm{D}\begin{bmatrix} A_n \\ B_n \\ C_n \\ D_n \end{bmatrix} = \left[\begin{array}{c|c|c} \mathcal{U}_n^{(P)}\cos n\nu & \mathcal{U}_n^{(SV)}\cos n\nu & \mathcal{U}_n^{(SH)}\sin n\nu \\ \mathcal{R}_n^{(P)}\cos n\nu & \mathcal{R}_n^{(SV)}\cos n\nu & \mathcal{R}_n^{(SH)}\sin n\nu \\ \mathcal{Z}_n^{(P)}\cos n\nu & \mathcal{Z}_n^{(SV)}\cos n\nu & \mathcal{Z}_n^{(SH)}\sin n\nu \\ \mathcal{T}_n^{(P)}\cos n\nu & \mathcal{T}_n^{(SV)}\cos n\nu & -\mathcal{T}_n^{(SH)}\sin n\nu \end{array}\right], \tag{2.15}$$

and

$$\mathrm{D}\begin{bmatrix} A_n' \\ B_n' \\ C_n' \\ D_n' \end{bmatrix} = \left[\begin{array}{c|c|c} \mathcal{U}_n^{(P)}\sin n\nu & \mathcal{U}_n^{(SV)}\sin n\nu & -\mathcal{U}_n^{(SH)}\cos n\nu \\ \mathcal{R}_n^{(P)}\sin n\nu & \mathcal{R}_n^{(SV)}\sin n\nu & -\mathcal{R}_n^{(SH)}\cos n\nu \\ \mathcal{Z}_n^{(P)}\sin n\nu & \mathcal{Z}_n^{(SV)}\sin n\nu & -\mathcal{Z}_n^{(SH)}\cos n\nu \\ \mathcal{T}_n^{(P)}\sin n\nu & \mathcal{T}_n^{(SV)}\sin n\nu & \mathcal{T}_n^{(SH)}\cos n\nu \end{array}\right], \tag{2.16}$$

where

$$\mathrm{D} = \begin{bmatrix} \mathcal{U}_n^{(f)}(r_b) & -\mathcal{U}_n^{(\phi)}(r_b) & -\mathcal{U}_n^{(\xi)}(r_b) & -\mathcal{U}_n^{(\psi)}(r_b) \\ \mathcal{R}_n^{(f)}(r_b) & -\mathcal{R}_n^{(\phi)}(r_b) & -\mathcal{R}_n^{(\xi)}(r_b) & -\mathcal{R}_n^{(\psi)}(r_b) \\ 0 & -\mathcal{Z}_n^{(\phi)}(r_b) & -\mathcal{Z}_n^{(\xi)}(r_b) & -\mathcal{Z}_n^{(\psi)}(r_b) \\ 0 & -\mathcal{T}_n^{(\phi)}(r_b) & -\mathcal{T}_n^{(\xi)}(r_b) & -\mathcal{T}_n^{(\psi)}(r_b) \end{bmatrix}.$$

The vertical lines in equations (2.15) and (2.16) separate the cases where the incident wave is either a plane P-wave (first column), a SV-wave (second column) or a SH-wave (third column).

Once the coefficients $A_n, A_n', B_n, B_n', C_n, C_n', D_n, D_n'$ are determined, the displacements in both fluid and solid, as well as the pressure inside the fluid, can be computed easily. Numerical calculations require computing rapidly and accurately the Bessel and Hankel functions of integer order with a complex argument. The computation of the zeroth and first order Bessel and Hankel functions can be found in Abramowitz and Stegun (1965) and other known software packages (IMSL, MATLAB). However, the computation of high order Bessel and Hankel functions with a complex argument proves to be nontrivial. du Toit (1990, 1993) published a series of papers in IEEE journals on this topic. His method is elegant and yields accurate function values for an unlimited range of orders and arguments. We have carefully coded his method, and checked results against those in the series of tables of the Bessel functions published by the Computation Laboratory, National Bureau of Standards (Columbia University Press, New York).

Our calculations are performed in the frequency range of 0 to 2 kHz and an angle of incidence of 0^o to 90^o for two types of formation: fast (Berea sandstone) and slow (Pierre shale). Their properties, together with those of the borehole fluid, are given in Table 2.1. The borehole radius is $r_b = 0.1016$ m. Unless otherwise indicated in the text, $\nu = 0^o$ (azimuth of the incidence wave) and $\theta = 0^o$ (azimuth of the geophone) are assumed. The infinite series in the summation is truncated around 10 term. The truncation error is found to be negligible in all the cases examined. Contributions from higher order modes decrease very rapidly as the mode number increases, such

that a few terms are enough to yield very accurate results.

2.2 Compressional Plane Wave Incidence

The borehole distorts not only the amplitude of the incident elastic wave but also the direction of particle motion, depending on the frequency, the angle of incidence, and the formation properties. In the worst case, the surface wave is excited such that the nature of particle motion is changed (from linear motion to elliptic motion). Furthermore, because the problem is nonsymmetric, measurements are also dependent on the position of the geophone at which the experiment is conducted. This section is devoted to the case of a plane P-wave incidence. We examine the frequency and angle of incidence dependence of the displacement and pressure in the fluid as well as the displacements of waves scattered into the solid. We show how different the measurements (distorted by the borehole effect) are from the true incoming waves, both in amplitude and in particle motion, and how the measurement may vary as the position of the geophone changes around the borehole.

2.2.1 Dependence on Frequency and Angle of Incidence

For an incident P-wave and for a receiver at $(r = r_b, \theta = 0^o)$, Figure 2-2 shows the radial and vertical components of the wave scattered by the borehole, scaled by the total displacement of the incident wave, i.e., $||u_r^s(r_b)||/||\vec{u}^i(r_b)||$ and $||u_z^s(r_b)||/||\vec{u}^i(r_b)||$, at the solid side of the borehole wall. For both hard and soft formations, the borehole scattered energy is negligible compared to the incident wave for frequencies below several hundred Hertz (500 Hz for the hard formation and 250 Hz for the soft formation). For a frequency above 1 kHz, the scattered energy is a significant fraction of geophone output. For a frequency of 2 kHz, the amplitude of the radial component of the borehole scattered wave can reach almost 60% of the incident total displacement

at 90° incidence for both formations. The vertical component can reach 30% at 45° incidence for the hard formation. For the soft formation the corresponding values are about 40% at 45° incidence and over 60% at grazing incidence. The radial component of the borehole scattered wave increases with frequency and angle of incidence. The vertical component increases with frequency and angle of incidence up to 45°. Later it decreases with the increase of angle of incidence. An exception occurs at grazing incidence for the soft formation, where the vertical and radial components of the borehole scattered wave increase with the decrease of angle of incidence. This is because, for the very soft formation, some surface mode (complex) is excited at grazing incidence, especially at high frequencies (see the plot of rectilinearity in Figure 2-5).

2.2.2 Borehole Reception Pattern

At a given frequency, the pressure inside the fluid or the individual components of displacement in the solid depend on the angle of incidence. The graphical representation of the magnitude of this dependence is known as the **borehole reception pattern**. Examples are: $||p^f||/||p_0||$ for the pressure measurement, $||\vec{u}_r^i + \vec{u}_r^s||/||\vec{u}^i||$ and $||\vec{u}_z^i + \vec{u}_z^s||/||\vec{u}^i||$ for the radial and vertical components of the solid displacement which are the recordings of a downhole geophone, where $p_0 = -\rho\alpha\omega^2 J_0(k_p r)$ is a normalization factor (Lovell and Hornby, 1990).

Figure 2-3 shows the borehole reception pattern for the pressure at the center of the fluid at frequencies 100 Hz, 500 Hz, 1000 Hz and 2000 Hz. For the hard formation, the reception pattern shows a main lobe at 90° incidence (and is almost independent of frequency) below 1 kHz. For the soft formation, dependence on angle of incidence is very weak compared to the previous case. This is because the impedance contrast between the formation and the borehole fluid is much smaller compared to the hard formation. At 2 kHz, the curve deflects toward grazing incidence rather than normal incidence, indicating the excitation of a surface mode along the fluid-solid interface.

Figure 2-4 shows the borehole reception pattern for the radial and vertical components of the sound displacement at the borehole wall. The radial component has a main lobe at normal incidence. The vertical component has a main lobe at grazing incidence. For the hard formation, the reception pattern is almost independent of frequency. For the soft formation, the frequency dependence is insignificant for frequencies below 500 Hz, while for frequencies above 1 kHz, the amplitude at 90° incidence decreases (recall that the geophone is at the shadow zone in the forward direction, i.e., $\theta = 0°$) and the amplitude at grazing incidence increases.

2.2.3 Borehole Effect on Particle Motion

Since the displacement is a vector, the borehole distorts not only its amplitude but also its direction, i.e., the particle motion. The estimation of the particle motion is very important for data rotation of downhole 3-component measurements. It is beneficial to understand how and how much the borehole can change the polarization of an incident elastic wave.

We define **inclination deviation** as the difference between the inclination (angle of the displacement vector with the borehole axis) of the measured displacement and that of the incident wave; and **azimuth deviation** as the difference between the azimuth angle of the measured displacement and that of the incident wave. Another important concept is **rectilinearity** which is a measure for the nature of polarization: for a perfect linear polarization the rectilinearity is 1, for a perfect circular polarization it is zero. The rectilinearity is defined in terms of the eigenvalues of a data covariance matrix (see Esmersoy, 1984).

Figure 2-5 shows the rectilinearity of the displacement at the solid side of the borehole wall as a function of angle of incidence at frequencies 100 Hz, 500 Hz, 1000 Hz and 2000 Hz. For the hard formation, the rectilinearity is very close to 1, indicating that the solid motion is linear. Near grazing incidence some surface mode is excited at

2 kHz. For the soft formation the dependence on the frequency and angle of incidence is more obvious, although the particle motion is predominantly linear except at 2 kHz.

Figure 2-6 shows the inclination deviation for the displacement at the solid side of the borehole wall. For the hard formation, the inclination deviation is less than 1^o for frequencies below 1 kHz and 3^o at 2 kHz. It peaks at 45^o incidence at 2 kHz. For the soft formation, the inclination deviation tends to be larger than that for the hard formation and can reach 6^o at grazing incidence at 2 kHz.

2.2.4 Effect of Geophone Orientation

Because the problem of borehole coupling is nonsymmetric, the displacement in the solid and the pressure in the fluid will be dependent on the azimuthal orientation of a geophone with respect to the incident wave. Figure 2-7 shows a polar plot of the calculation for a plane P-wave incidence with angle of incidence $\delta = 45^o$. The amplitude of the total solid displacement, scaled by that of the incident wave, is plotted as a function of the azimuthal angle θ (0^o– 180^o) of the geophone. For the hard formation, the pattern is independent of the geophone orientation for frequencies below 1 kHz, while for frequencies above 1 kHz it has a large lobe at 180^o azimuthal angle (i.e, the geophone faces the incident wave and picks up the strong backscattered wave). For the soft formation the pattern appears similar to that for the hard formation for frequencies below 500 Hz. However, for frequencies above 500 Hz, the reception pattern is significantly less than unity in the forward scattering direction (0^o) and is significantly larger than unity in the backward scattering direction (180^o).

2.3 Shear Plane Wave Incidence

The interaction of a shear wave (SV-type) with a fluid-filled borehole is more complicated than that of a P-wave. When the incident wave is a shear wave, a critical

reflection of the P-wave in the solid occurs at an angle of incidence $\delta = \cos^{-1}\beta/\alpha$. A critical P-wave refraction in the fluid occurs at $\delta = \cos^{-1}\beta/\alpha_f$ when the formation is soft ($\beta < \alpha_f$). In some cases, a significant fluid resonance exists at $\delta = \cos^{-1}\beta/C_T(\omega)$ if the formation is soft enough such that $\beta < C_T(\omega)$, where C_T is the tube wave phase velocity which is frequency dependent. These mode conversions and possible excitations of surface waves (e.g., tube wave) occur at the interface and their amplitudes increase with frequency, which makes the effect of the borehole coupling even more significant for shear-wave incidence.

2.3.1 Dependence on Frequency and Angle of Incidence

Figure 2-8 shows the radial and vertical components of the borehole scattered wave, scaled by the total displacement of the incident wave, i.e., $||u_r^s(r_b)||/||\vec{u}^i(r_b)||$ and $||u_z^s(r_b)||/||\vec{u}^i(r_b)||$, at the solid side of the borehole wall with geophone orientation $\theta = 0°$. The incident wave is a plane SV-wave. For the hard formation, the borehole scattered energy is negligible at low frequencies, while at high frequencies the scattered wave can be a significant portion of the total measurement. At 2 kHz, the radial component of the borehole scattered wave can reach nearly 110% of the incident total displacement at grazing incidence and the vertical component can reach 70% at 0° incidence and 50% at normal incidence. The radial component of the borehole scattered wave increases with frequency and decreases with angle of incidence. The vertical component of the scattered wave shows a minimum at 45° incidence and has two peaks at both grazing incidence and normal incidence. An explanation for the minimum at 45° in the vertical component of the scattered wave is as follows: for SV-wave incidence, the S-wave reflection peaks at normal incidence (polarized vertically) and vanishes at grazing incidence, while the P-wave reflection peaks at grazing incidence (also polarized vertically) and vanishes at normal incidence. The summation of the P-wave reflection and the S-wave reflection yields a minimum exactly at 45° incidence.

For the soft formation, strong resonances in the fluid occur at low frequencies and at an angle of incidence for which the vertical wavenumber ($\omega/\beta\cos\delta$) is equal to the tube wave wavenumber (ω/C_T). The tube wave is excited in the fluid-filled borehole. At that particular frequency and angle of incidence, the scattered wave can be several times larger than the incident wave. Away from the resonance region, the dependence on frequency and angle of incidence is similar to that for the hard formation.

The angle of incidence at which resonance occurs can be predicted theoretically for a given frequency. From the tube wave dispersion equation we derive an analytical approximation for the tube wave phase velocity at a low frequency. Up to the order $\omega^2 \ln\omega$, the tube wave phase velocity can be written as

$$C_T = \frac{\alpha_f}{\sqrt{1+\frac{\rho_f\alpha_f^2}{\rho\beta^2}}}\left[1-\frac{1}{4}\frac{\rho_f\alpha_f^2}{\rho\beta^2+\rho_f\alpha_f^2}(1-\frac{2\beta^2}{\alpha_f^2}-\frac{2\rho_f}{\rho})(1-\frac{2\beta^2}{\alpha^2})\frac{\omega^2 r_b{}^2}{\beta^2}\ln\frac{\omega r_b}{2\alpha}\right] \qquad (2.17)$$

which agrees with the result of Biot (1952) and White (1983) as $\omega \to 0$. For a soft formation such as Pierre shale, equation (2.17) predicts that $C_T > \beta$ for frequencies below 1.2 kHz and $C_T < \beta$ for frequencies above 1.2 kHz. The actual cut-off frequency from a numerical solution to the dispersion equation is around 900 Hz. It should be pointed out that, if the tube wave phase velocity is larger than the formation shear wave velocity, C_T contains an imaginary part of the order ω^2 that has been neglected in the above low frequency approximation.

The resonance occurs at $\frac{\omega}{\beta}\cos\delta = \frac{\omega}{C_T}$, so we have

$$\delta = \cos^{-1}\frac{\beta}{C_T}. \qquad (2.18)$$

This equation has a solution only for $C_T > \beta$, implying that the borehole resonance is a low frequency phenomenon. A comparison of the resonance angle predicted by equation (2.18) under the low frequency approximation with the exact solution shows an excellent agreement, especially for frequencies below 400 Hz.

2.3.2 Borehole Reception Pattern

Figure 2-9 shows the borehole reception pattern for pressure, i.e., $||p^f||/||p_0||$, at the center of fluid at frequencies 100 Hz, 500 Hz, 1000 Hz and 2000 Hz for plane SV-wave incidence. For the hard formation, the reception pattern shows a lobe at 45^o incidence and is almost independent of frequency for frequency below 1 kHz. The pressure at the center of the fluid is zero at normal incidence and very small at grazing incidence. For the soft formation, significant fluid resonance occurs at 25^o at 100 Hz and 20^0 at 500 Hz. For frequencies above 1 kHz, the fluid resonance disappears. In this case, the pressure in the fluid decreases with the increase of frequency, contrary to the P-wave incidence shown in Figure 2-3. The reception pattern shows a strong and complicated dependence on frequency and angle of incidence.

Figure 2-10 shows the borehole reception pattern for the radial and vertical components of the solid displacement, i.e., $(||\vec{u}_r^s + \vec{u}_r^i||)/||\vec{u}^i||$ and $(||\vec{u}_z^s + \vec{u}_z^i||)/||\vec{u}^i||$, at the borehole wall for a plane SV-wave incidence. The radial component has a main lobe at grazing incidence and the vertical component at normal incidence. For the hard formation, the reception pattern shows little frequency dependence except at 2 kHz. For the soft formation, the resonance in the fluid at low frequencies and at small angles of incidence also affects the solid displacement. The sharp peaks in the figure at 25^o at 100 Hz and at 20^o at 500 Hz are due to the excitation of the tube wave in the fluid. Away from the resonance angles, the reception pattern has similarities to that for the hard formation, although, for the soft formation, the dependence on frequency and angle of incidence is strong.

For plane SH-wave incidence, the wave fields inside and outside the borehole prove to be much simpler because the SH-motion is not coupled to the P- and SV-motions. Figure 2-11 shows the borehole reception pattern for the solid displacement at the borehole wall for plane SH-wave incidence. For the hard formation, the reception pattern is nearly a circle of unit amplitude except at 2 kHz. For the soft formation, at frequencies below 1 kHz, the reception pattern is also nearly a unit circle. At

frequencies above 1 kHz, two lobes at 20^o and 90^o can be seen.

2.3.3 Borehole Effect on Particle Motion

Figure 2-12 shows the rectilinearity of displacement at the solid side of the borehole wall as a function of angle of incidence at frequencies 100 Hz, 500 Hz, 1000 Hz and 2000 Hz for a plane SV-wave incidence. For the hard formation, the rectilinearity is very close to 1 except at 2 kHz near grazing incidence. For the soft formation the dependence on frequency and angle of incidence is more pronounced, although the particle motion is predominantly linear, except where the tube wave is excited at low frequencies, or where some critically refracted and reflected (or leaking) modes appear at high frequencies as indicated in the figures.

Figure 2-13 shows the inclination deviation for the displacement at the solid side of the borehole wall for plane SV-wave incidence. For the hard formation, the inclination deviation is less than 1^o for frequencies below 1 kHz and 3^o at 2 kHz. For the soft formation, the inclination deviation can be as large as 20^o at low frequencies and near the fluid resonance angle. For frequencies above 1 kHz, a significant deviation of particle motion occurs in the soft formation for a geophone at $\theta = 0^o$, which is in the shadow zone (i.e., the scattered wave is out of phase with the incident wave at high frequencies, where the wavelength is of the same order as the borehole diameter). The deviation of the particle motion is found to be less significant if the geophone is facing the incident wave (i.e., $\theta = 180^o$ at which the backscattered energy is in phase with the incident wave).

2.3.4 Effect of Geophone Orientation

Figure 2-14 shows a polar plot of the solid displacement on the borehole wall for plane SV-wave incidence with an angle of incidence $\delta = 45^o$. The amplitude of the total solid displacement, scaled by that of the incident wave, is plotted as a function

of geophone orientation angle θ (0°- 180°). For the hard formation, the reception pattern is independent of the geophone orientation for frequencies below 1 kHz, while for frequencies above 1 kHz, it has a large lobe at 180° azimuthal angle (i.e, the geophone is facing the incident wave). For the soft formation the pattern looks similar to that for the hard formation for frequencies below 100 Hz. For frequencies between 100 - 500 Hz, the reception pattern is less than unity in the forward scattering direction (0°) and is almost equal to a unity in the backward direction. For frequencies above 500 Hz, the pattern is significantly less than unity in the forward direction and significantly larger than unity in the backward scattering direction (180°).

Figure 2-15 shows the same polar plot as that in Figure 2-14 but for SH-wave incidence. For the hard formation, the reception pattern for the SH-wave incidence is nearly a unit circle for frequencies below 1 kHz. For frequencies above 1 kHz, it also has a large lobe at 180° azimuth angle. For the soft formation the pattern is similar to that for the hard formation for frequencies below 500 Hz. For frequencies around 1 kHz, the reception pattern has a large lobe at 180° azimuthal direction. However, for frequencies around 2 kHz, the main lobe occurs at 110° azimuth.

2.4 Discussions and Conclusions

In this chapter, we have presented an exact formulation for borehole coupling based on Schoenberg's theory, which is valid for all frequency and all azimuthally symmetric and nonsymmetric components. We have studied the borehole effects on downhole seismic measurements (both amplitude and particle motion) as functions of frequency, angle of incidence, and polarization of the incident wave as well as the geophone orientation. We found the following results:

- For the hard formation and frequencies below 500 Hz, the borehole scattered wave in the solid is less than 10 % in amplitude of the incident wave. The

downhole geophone measurement is practically unaffected by the fluid-filled borehole. Although frequency plays a less significant role in this case, the pressure measured at the center of the fluid depends strongly on the direction of the incidence wave, e.g., for P-wave incidence the pressure reception pattern has a big lobe around normal incidence, for SV-wave incidence it has a lobe at 45° incidence.

- For the hard formation and frequencies above 500 Hz (especially on the order of 1 kHz), the borehole scattered energy is a significant part of the total measurement of the downhole geophone for all types of incident waves. The particle motion direction can differ from that of the incoming wave by several degrees depending on the angle of incidence and frequency. The solid displacement measured with a geophone facing the incoming wave will be noticeably larger than that with the geophone opposite. The pressure at the center of the fluid shows dependence on frequency as well as on angle of incidence.

- For the soft formation and frequencies below 300 - 500 Hz, the borehole scattered energy in the solid is also negligible for P-wave incidence. In this case the pressure at the center of the fluid becomes significantly less dependent on angle of incidence than in the hard formation. For SV-wave incidence, a significant fluid resonance occurs at certain angles of incidence for frequencies below 1 kHz due to the excitation of a tube wave. At these particular frequencies and angles of incidence, the solid displacement measured by a downhole geophone as well as the pressure measured by a downhole hydrophone will be several times larger than those of the incident wave. The particle motion measured by the geophone differs from that of the incident wave by as much as 20°.

- For the soft formation and frequencies above 1 kHz, the fluid resonance disappears for the SV-wave incidence. In this case, the solid displacement and the fluid pressure are strongly dependent on both frequency and angle of incidence in a complicated manner. For P-wave incidence, the displacement in the solid is smaller than that of the incidence wave at normal incidence and is significantly

larger at grazing incidence. Also the measured solid displacement is much larger than the incident wave when the geophone is facing the incident wave and is smaller when the geophone faces to the opposite direction.

We conclude that correction of the borehole effect on downhole measurements should be made for frequencies above 500 Hz in hard formations. In soft formations, if the angle of incidence differs significantly from the resonance angle for SV-wave incidence, no borehole correction is needed for frequencies below 300 Hz. For frequencies above 300 Hz, the borehole can affect downhole measurements significantly and should be taken into account. Since the borehole can significantly alter the particle motion direction, the horizontal component rotation from data is unreliable for experiments with frequencies above 1 kHz. Data rotations should be done from downhole gyro readings instead.

Physical Properties Table

Lithology	V_p	V_s	ρ	C_T(open)	C_T(cased)
Solenhofen limestone	5970	2880	2656	1430	1457
Pierre shale	2074	869	2000	950	1425
Berea sandstone	4206	2664	2140	1399	1450
soil	1670	170	1290	191	1421
steel (casing)	6100	3350	7500		
water (borehole fluid)	1500		1000		

Table 2.1: Physical properties of lithologies and materials used in this thesis. Physical properties include P-wave (V_p) and S-wave (V_s) velocities, densities (ρ), and zero-frequency tube wave velocities for open and cased boreholes (C_T). The velocities are in meters per second, densities in kilograms per cubic meters. References, not the original, are Thomsen (1986) and Meredith (1990). The physical properties for soil are taken from our own laboratory experiments. The borehole radius is 0.1016 m, the casing thickness is 0.0203 m.

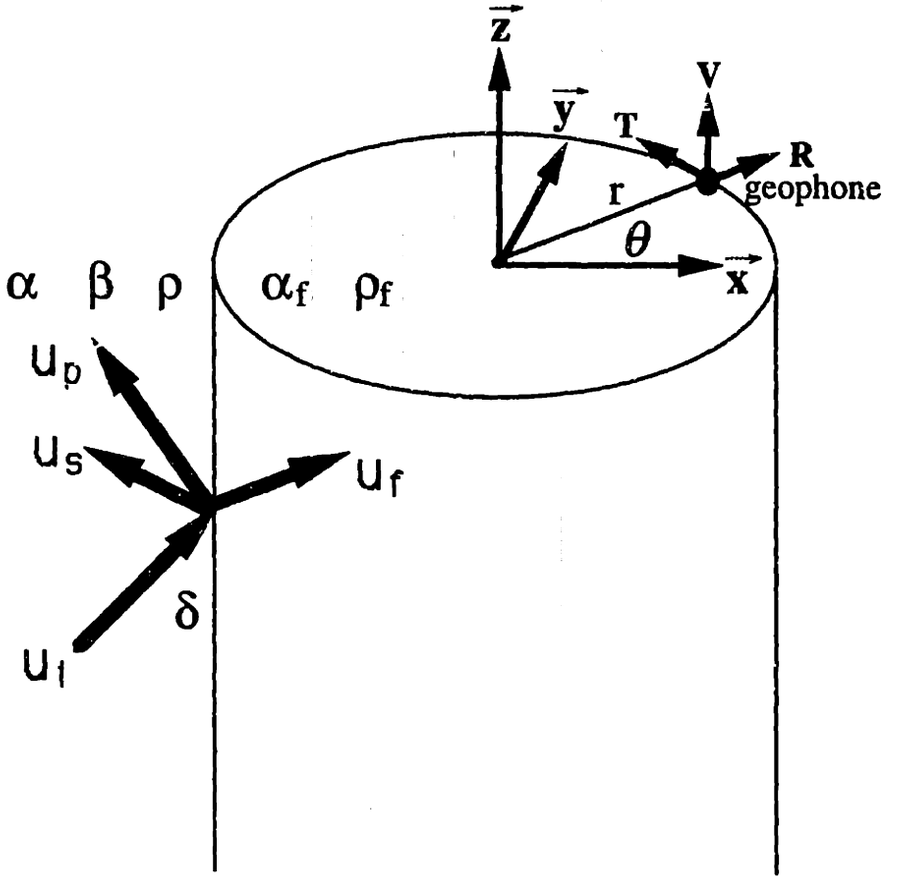

Figure 2-1: A fluid-filled borehole (α_f, ρ_f) in a solid formation (α, β, ρ). An elastic wave $\vec{u}^i$ incident on the borehole causes scattered wave $\vec{u}^s$ in the formation and fluid motion $\vec{u}^f$ in the borehole. The borehole radius is r_b. The angle of incidence is δ and azimuth is $\nu = 0$. In the calculation we will assume that a hydrophone measures the pressure at $r = 0$ and a geophone measures the three component displacement at $(r = r_b, \theta)$, where r_b is the borehole radius. The orientation with $-90^o \leq \theta < 90^o$ is referred to as the forward direction and $90^o \leq \theta < 270^o$ as the backward direction.

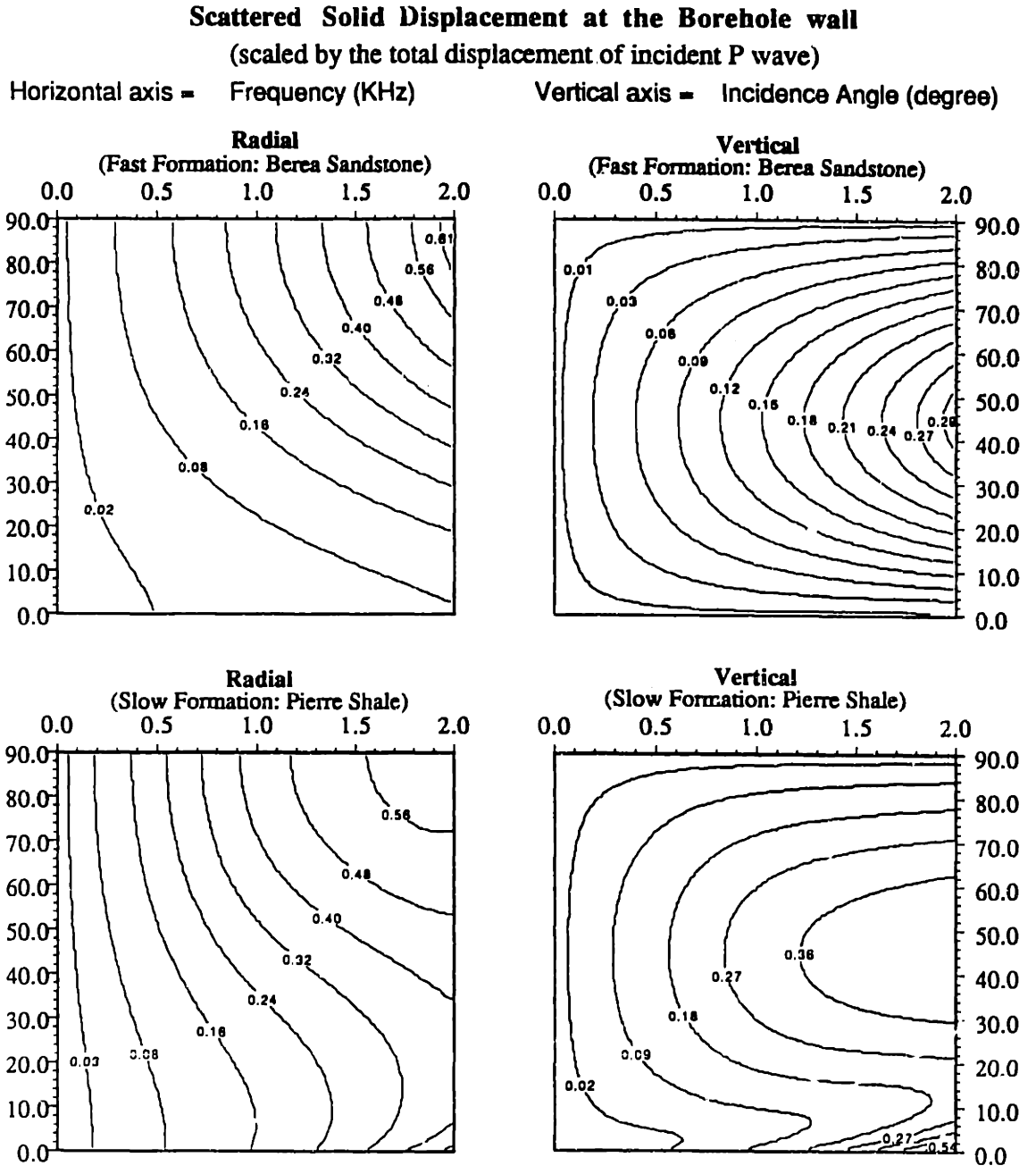

Figure 2-2: The radial and vertical components of the borehole scattered wave in the hard (top) and soft (bottom) formations. They are scaled by the total displacement of the incident wave. The incident wave is a plane P-wave. The geophone is at $(r = r_b, \theta = 0^o)$.

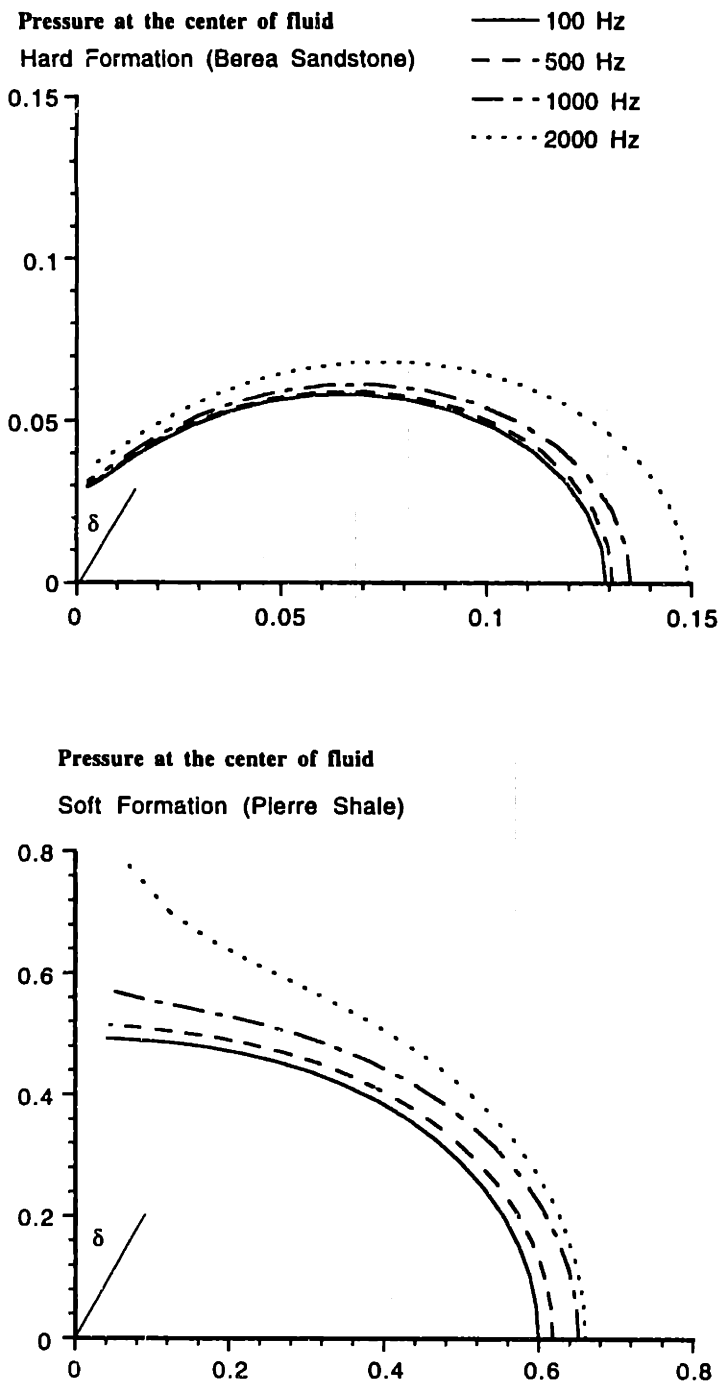

Figure 2-3: Borehole reception pattern for the pressure at the center of the fluid at frequencies 100 Hz, 500 Hz, 1000 Hz and 2000 Hz for the hard (top) and soft (bottom) formations. The incident wave is a plane P-wave. δ is the angle of incidence.

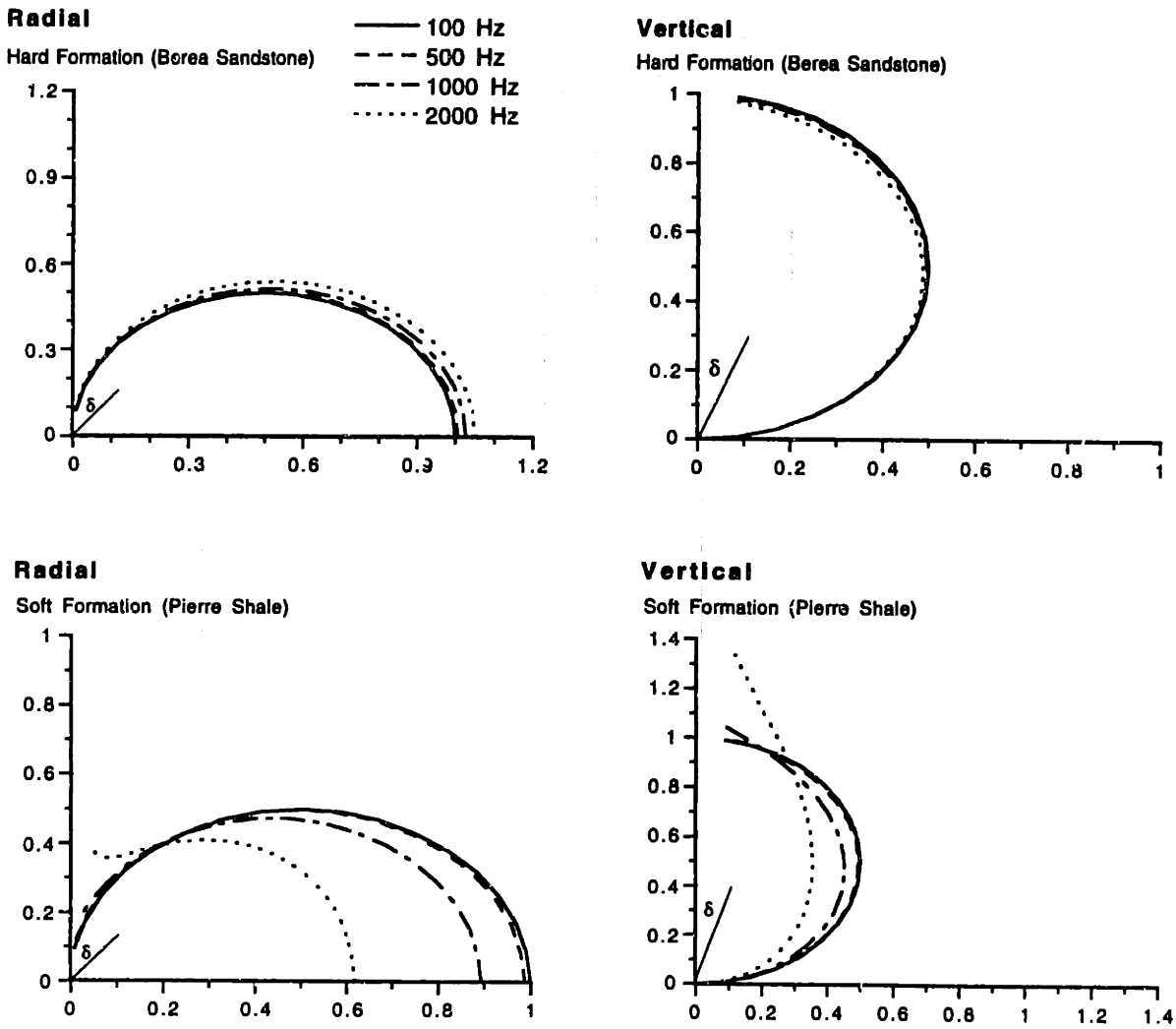

Figure 2-4: Borehole reception pattern for the radial and vertical components of the solid displacement at frequencies 100 Hz, 500 Hz, 1000 Hz and 2000 Hz for the hard (top) and soft (bottom) formations. The incident wave is a plane P-wave. The geophone is at $(r = r_b^+, \theta = 0^o)$.

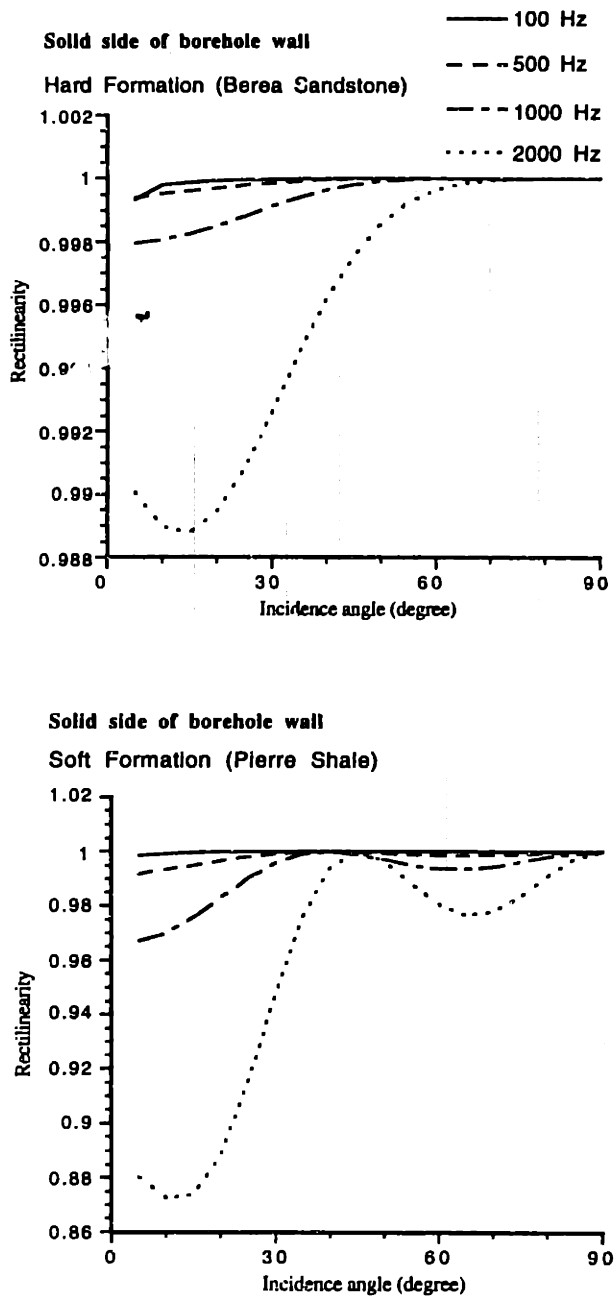

Figure 2-5: Rectilinearity of the solid displacement at frequencies 100 Hz, 500 Hz, 1000 Hz and 2000 Hz for the hard (top) and soft (bottom) formations. The incident wave is a plane P-wave. The geophone is at $(r = r_b^+, \theta = 0^o)$.

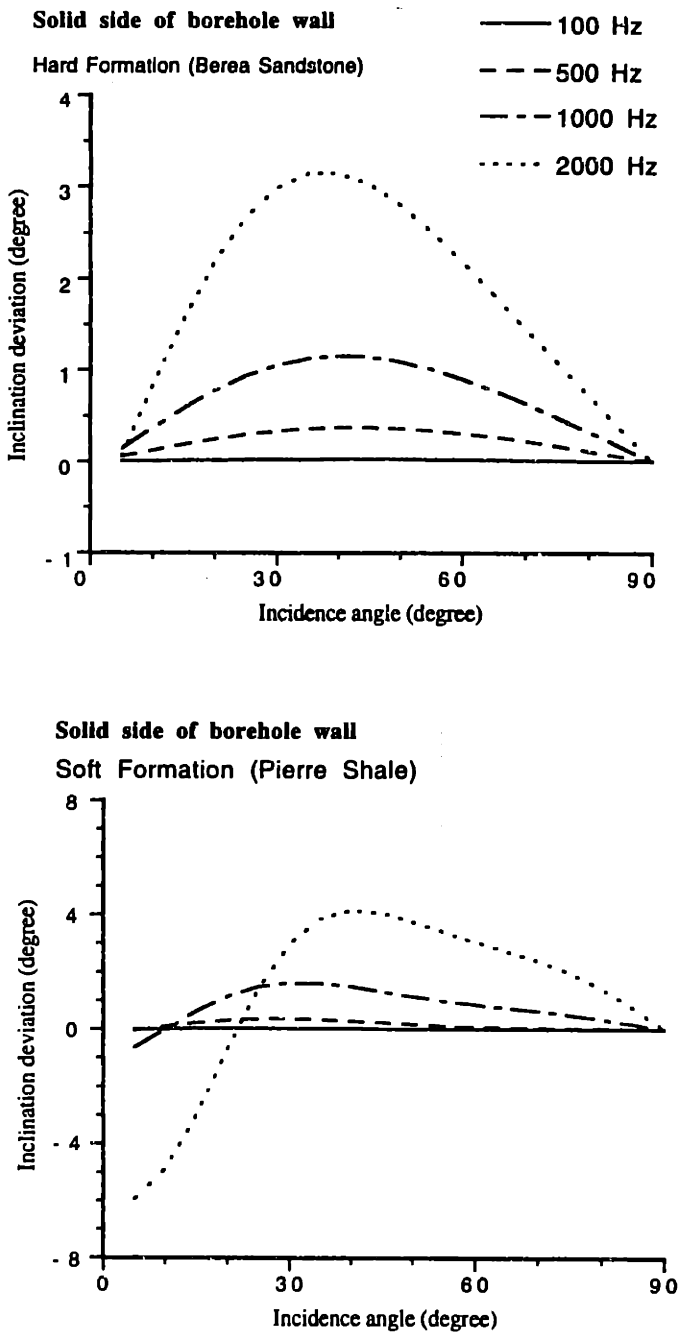

Figure 2-6: Inclination deviation from the incident wave at frequencies 100 Hz, 500 Hz, 1000 Hz and 2000 Hz for the hard (top) and soft (bottom) formations. The incident wave is a plane P-wave. The geophone is at $(r = r_b^+, \theta = 0^o)$.

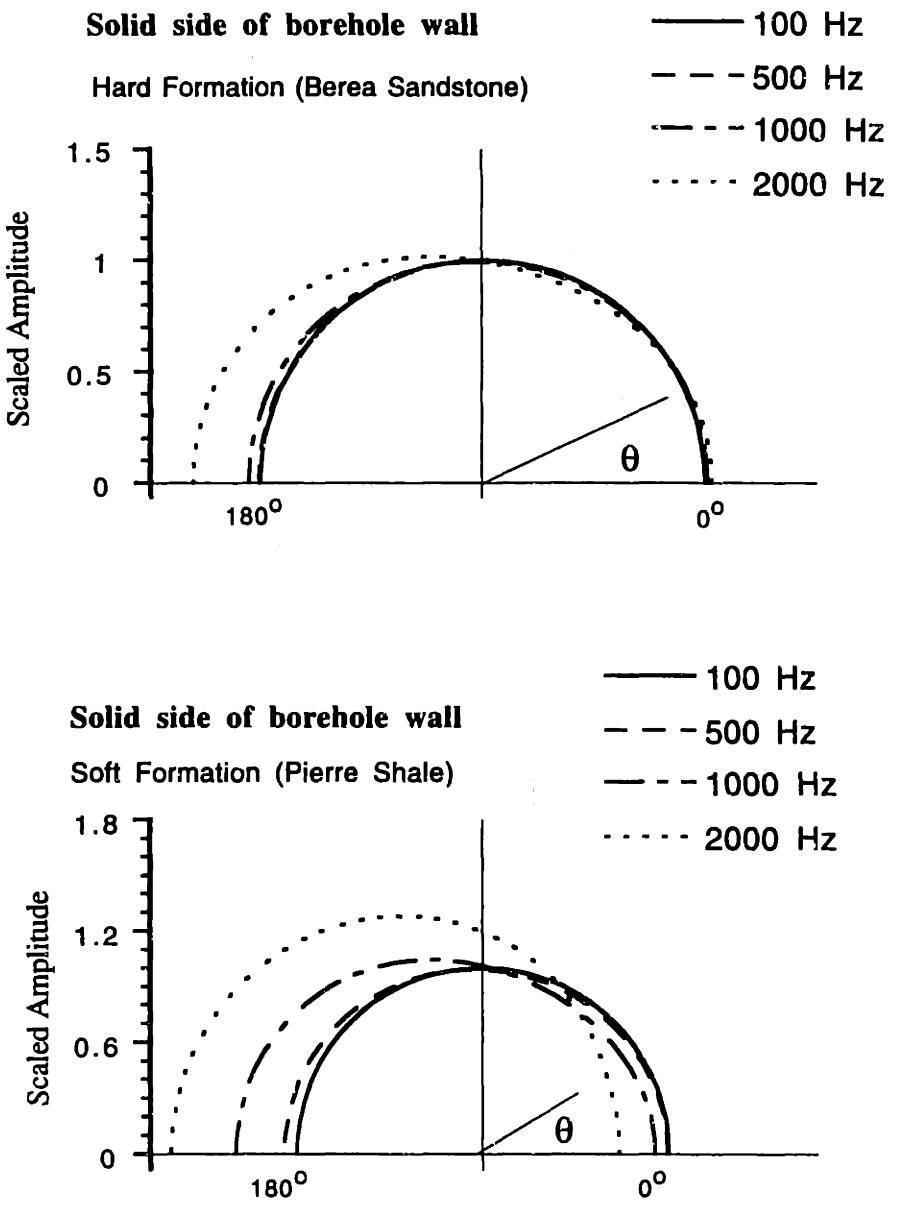

Figure 2-7: Effect of geophone orientation on the borehole reception pattern at frequencies 100 Hz, 500 Hz, 1000 Hz and 2000 Hz for hard (top) and soft (bottom) formations. The incident wave is a plane P-wave with $\delta = 45^o$. The geophone is at $r = r_b^+$. The geophone orientation θ varies from $0^o - 180^o$.

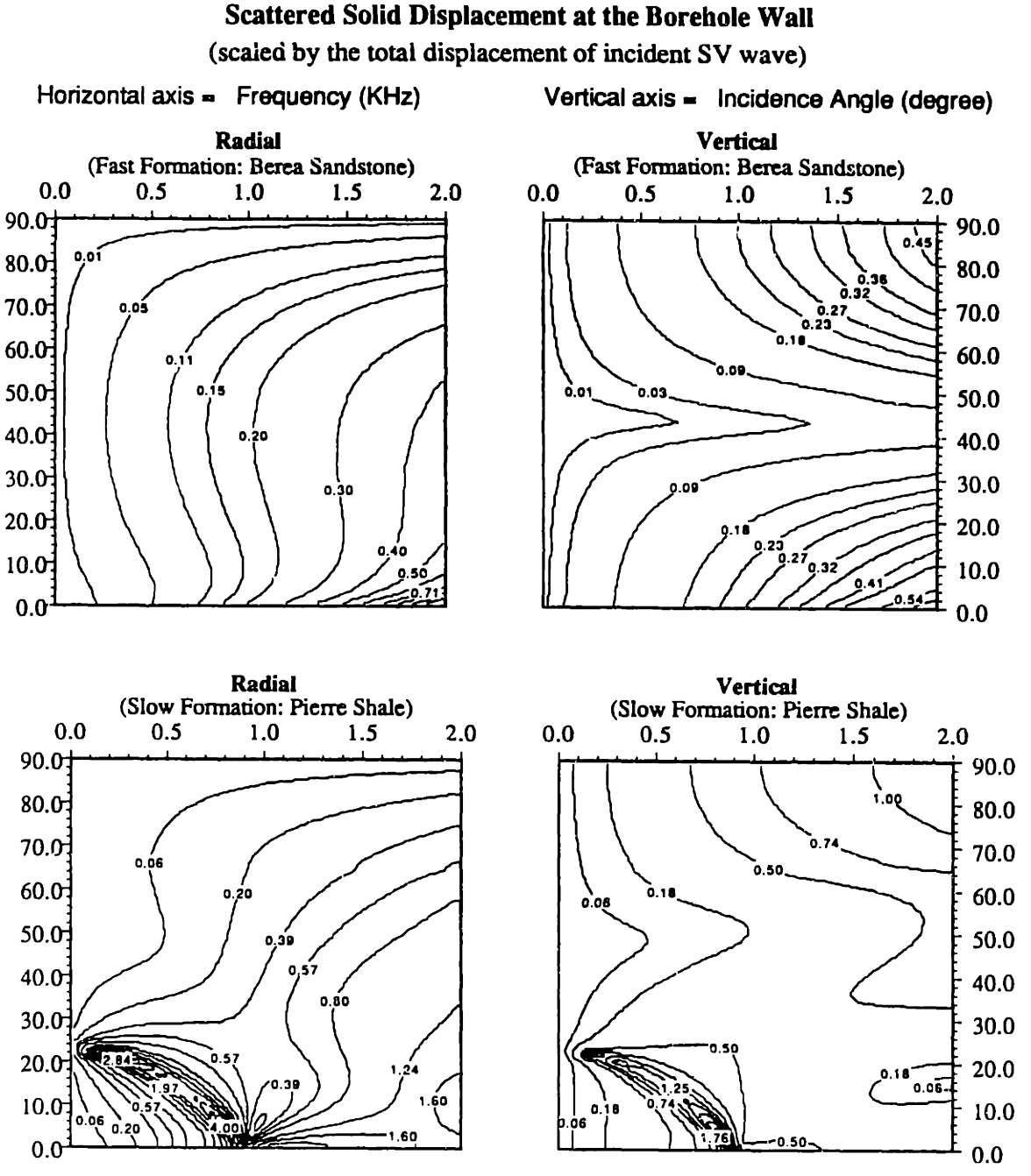

Figure 2-8: The radial and vertical components of the borehole scattered wave in the hard (top) and soft (bottom) formations. They are scaled by the total displacement of the incident wave. The incident wave is a plane SV-wave. The geophone is at $(r = r_b, \theta = 0^o)$.

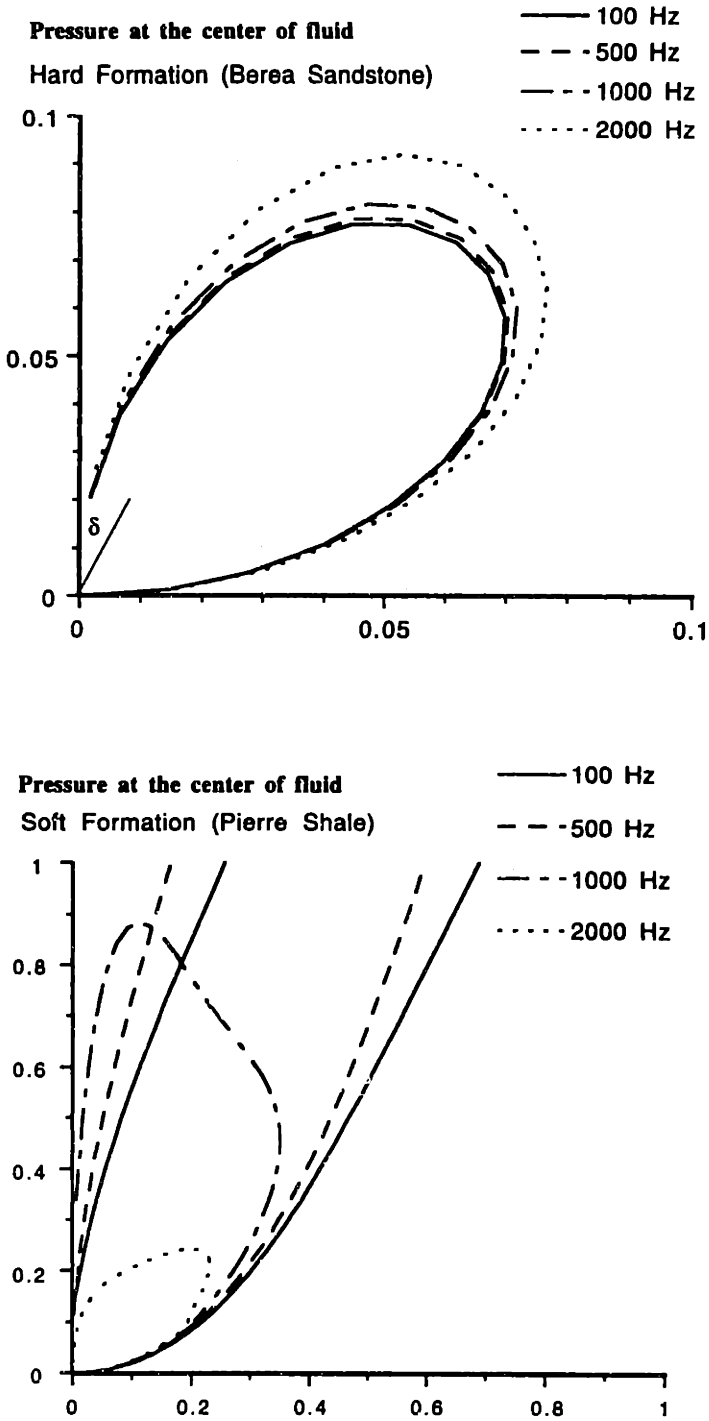

Figure 2-9: The borehole reception pattern for the pressure at the center of the fluid at frequencies 100 Hz, 500 Hz, 1000 Hz and 2000 Hz for the hard (top) and soft (bottom) formations. The incident wave is a plane SV-wave.

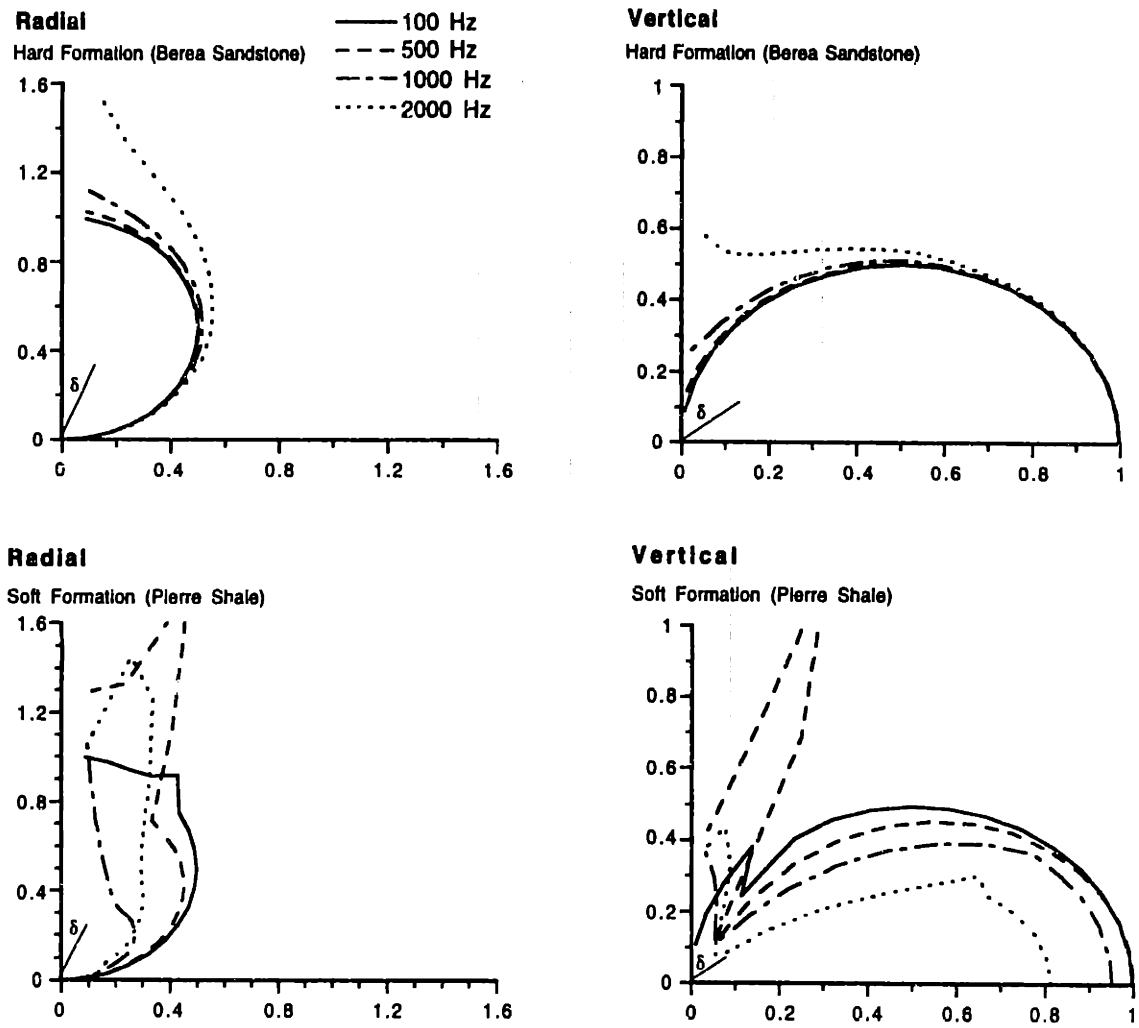

Figure 2-10: The borehole reception pattern for the radial and vertical components of the solid displacement at frequencies 100 Hz, 500 Hz, 1000 Hz and 2000 Hz for the hard (top) and soft (bottom) formations. The incident wave is a plane SV-wave. The geophone is at $(r = r_b^+, \theta = 0^o)$.

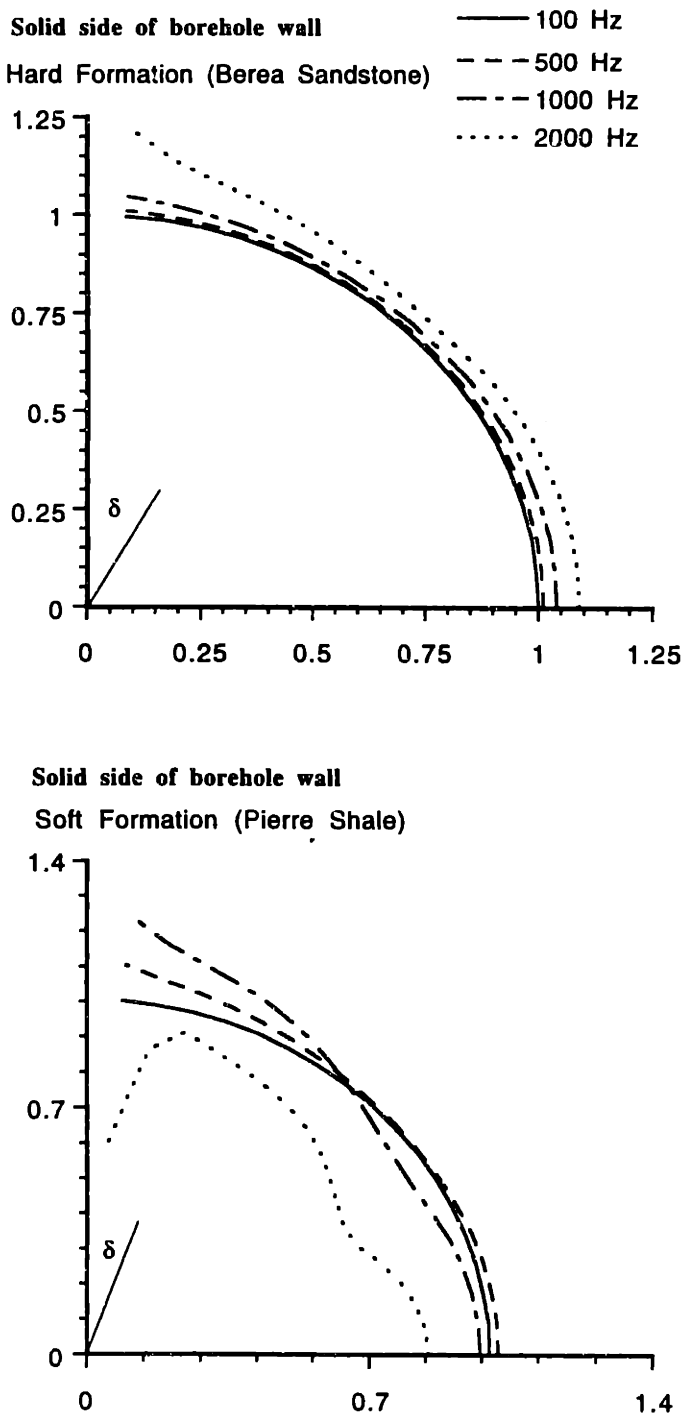

Figure 2-11: The borehole reception pattern for the solid displacement at frequencies 100 Hz, 500 Hz, 1000 Hz and 2000 Hz for the hard (top) and soft (bottom) formations. The incident wave is a plane SH-wave. The geophone is at $(r = r_b^+, \theta = 0^o)$.

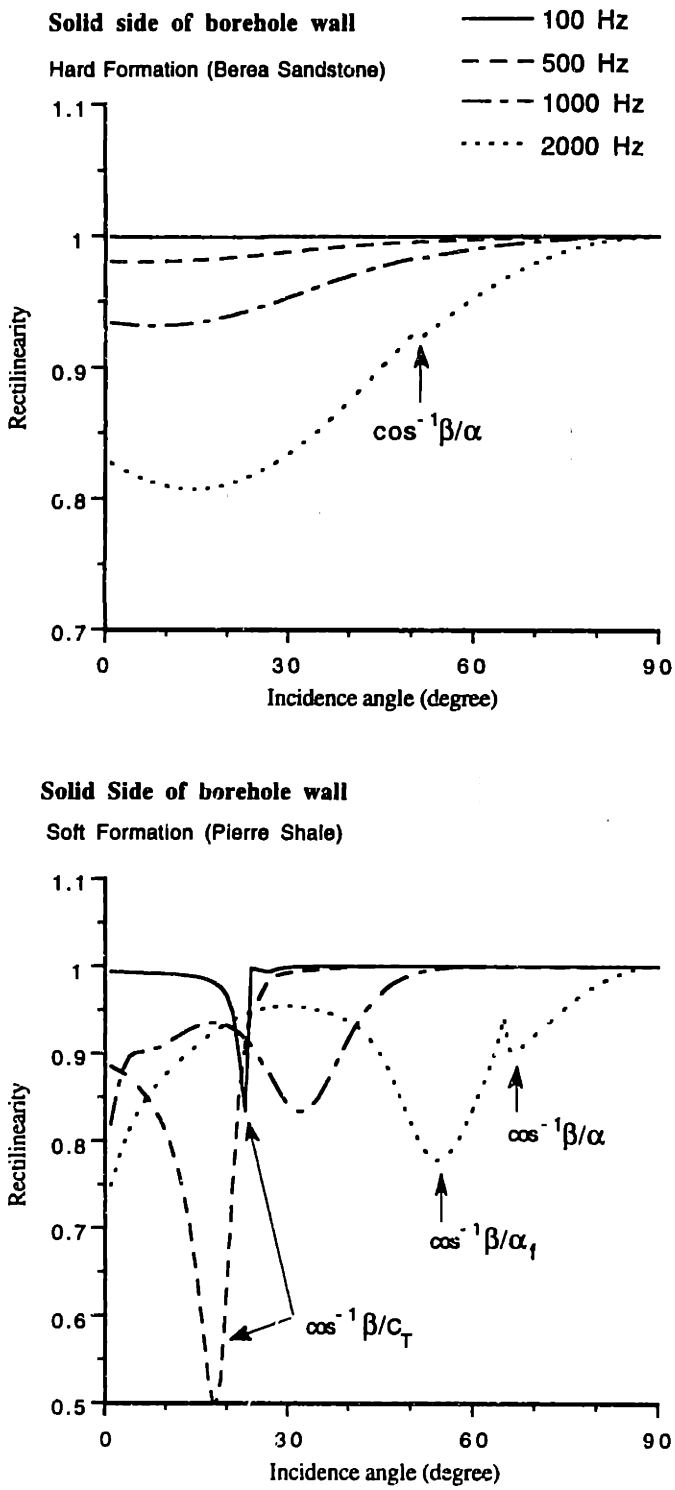

Figure 2-12: Rectilinearity of the solid displacement at frequencies 100 Hz, 500 Hz, 1000 Hz and 2000 Hz for the hard (top) and soft (bottom) formations. The incident wave is a plane SV-wave. The geophone is at $(r = r_b^+, \theta = 0^o)$.

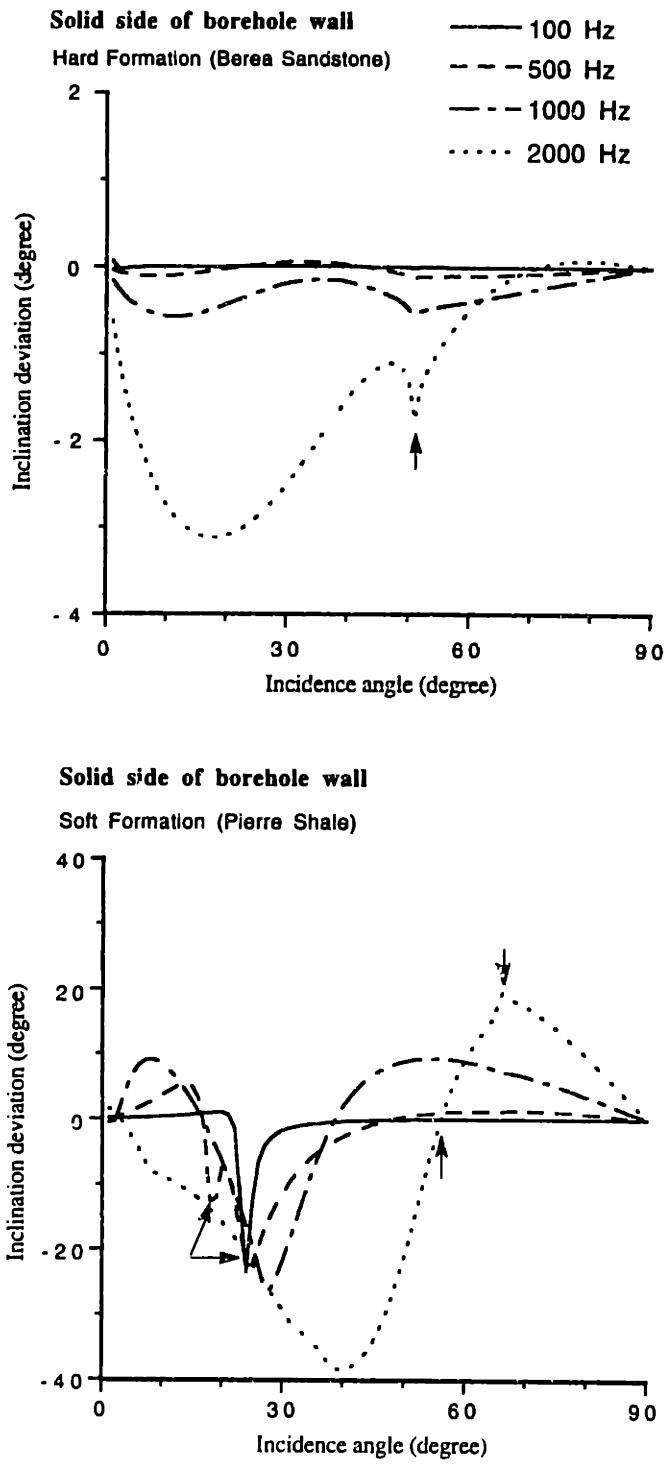

Figure 2-13: Inclination deviation from the incident wave at frequencies 100 Hz, 500 Hz, 1000 Hz and 2000 Hz for the hard (top) and soft (bottom) formations. The incident wave is a plane SV-wave. The geophone is at $(r = r_b^+, \theta = 0^o)$.

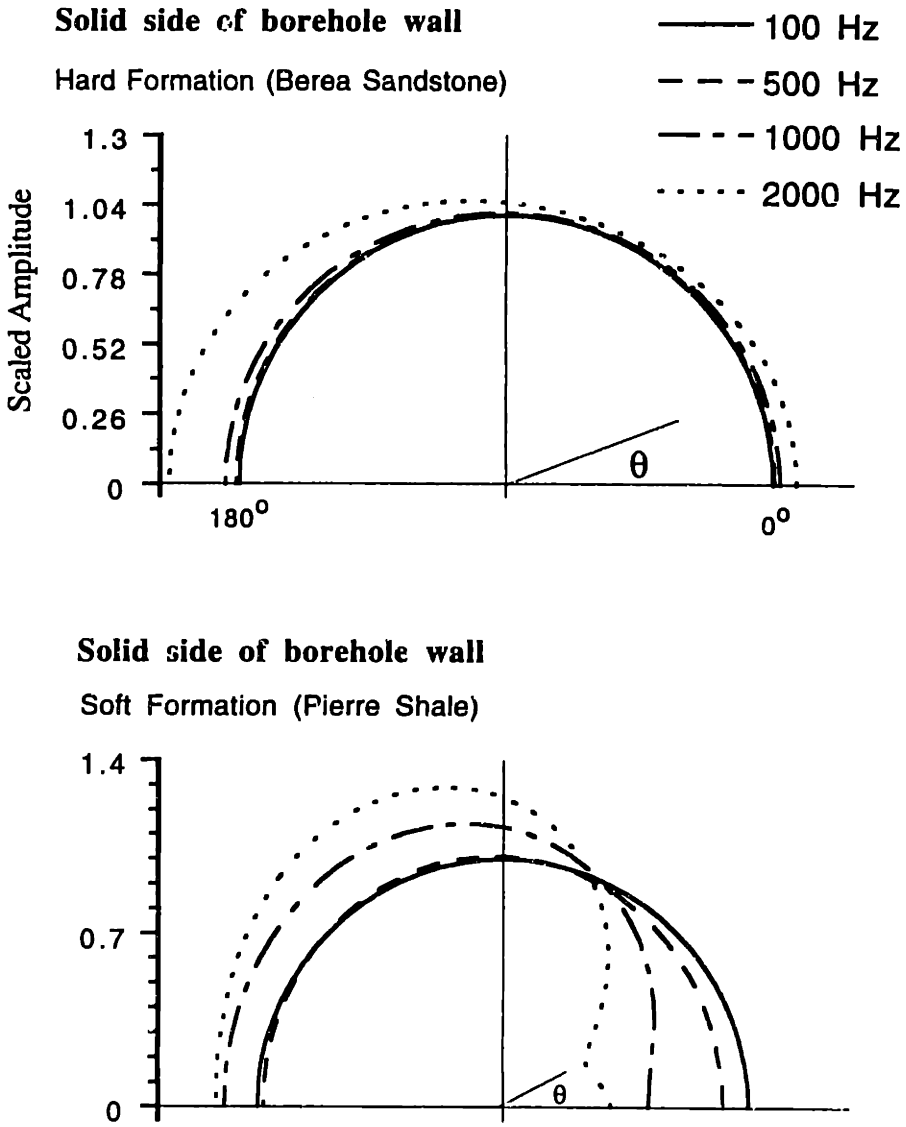

Figure 2-14: The effect of geophone orientation on the borehole reception pattern at frequencies 100 Hz, 500 Hz, 1000 Hz and 2000 Hz for the hard (top) and soft (bottom) formations. The incident wave is a plane SV-wave with $\delta = 45^o$. The geophone is at $r = r_b^+$. The geophone orientation θ varies from $0^o - 180^o$.

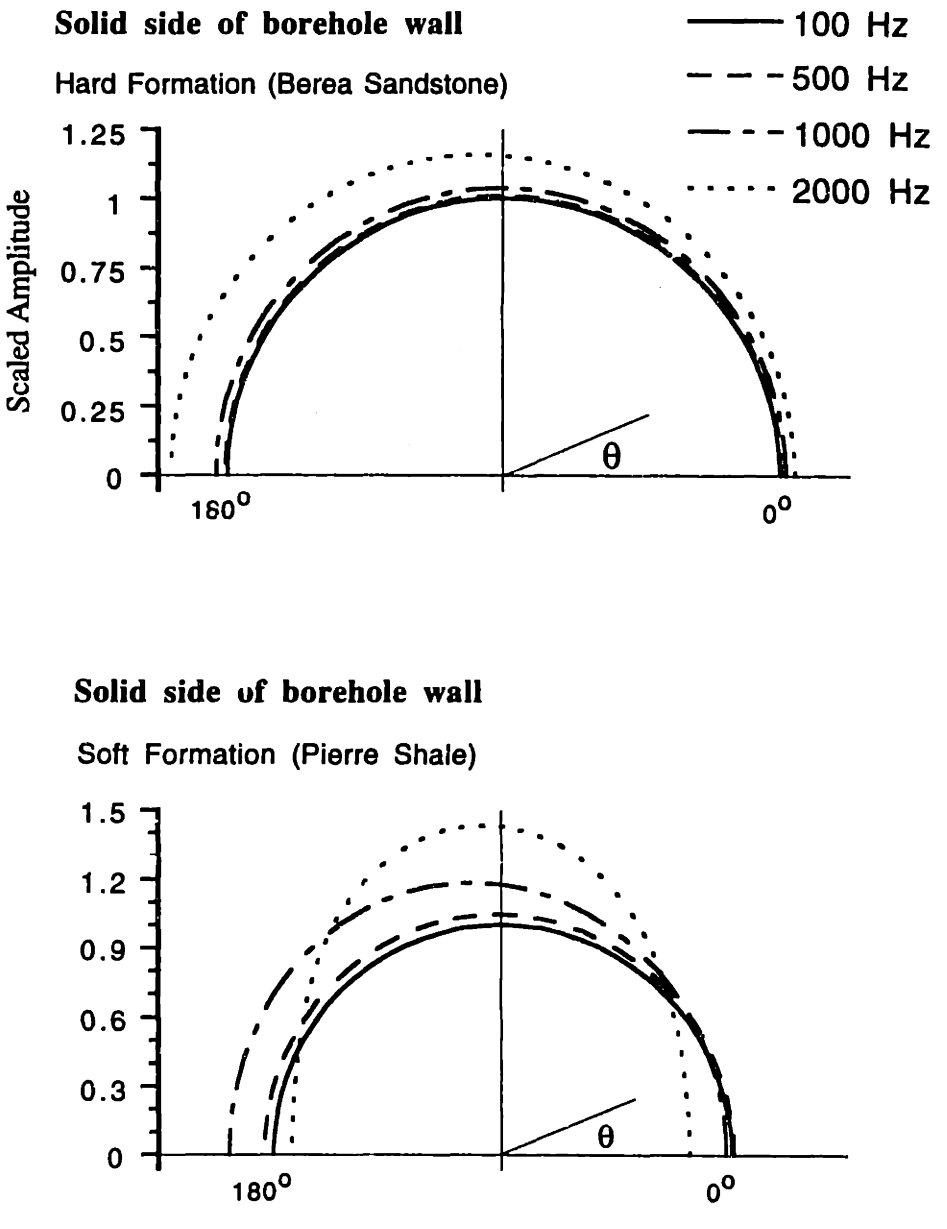

Figure 2-15: The effect of geophone orientation on the borehole reception pattern at frequencies 100 Hz, 500 Hz, 1000 Hz and 2000 Hz for the hard (top) and soft (bottom) formations. The incident wave is a plane SH-wave with $\delta = 45^o$. The geophone is at $r = r_b^+$. The geophone orientation θ varies from $0^o - 180^o$.

Chapter 3

Cased Borehole Effect on Downhole Seismic Measurements

The interaction of seismic waves with an open borehole has been extensively studied in the literature and in the previous chapter, especially at the low frequency limits. However, most downhole measurements are made in cased and cemented boreholes. The borehole coupling in such a complicated environment and the distortion of the incident wave by radially layered casing and cement around a fluid-filled borehole are not known. This chapter is devoted to understanding the cased borehole effects on downhole seismic measurements by approximately and exactly solving the problem of an elastic wave impinging on a radially layered fluid-filled borehole. We present first a general solution to the problem in terms of a superposition of fundamental modes in cylindrical coordinates. Using a low frequency approximation, we also develop a quasi-static approach to the borehole coupling, where simple, explicit and accurate expressions are obtained. We then solve, without an approximation, the general formulation developed in the first section by a global matrix algorithm. With the exact method, the high frequency behaviors of the pressure in the fluid (hydrophone data) and the solid displacement on the borehole wall (geophone data) are studied in detail. In the last section, we present some discussions and summary of the contributions.

3.1 Theoretical Formulation

3.1.1 Problem Statement

Consider the case of an elastic plane wave incident on a radially layered borehole as shown in Figure 3-1. Each radial layer is a homogeneous elastic medium with density ρ_m, compressional wave speed α_m and shear wave speed β_m, where m denotes the layer number with $1 \leq m \leq M+1$. M is the total number of annuli between the borehole fluid and formation. The borehole is filled with a fluid that has density ρ_f and compressional wave speed α_f. The inner radius of the borehole is r_b. The primary goal is to investigate the pressure in the fluid (hydrophone data) and the solid motion on the borehole wall (geophone data) due to an incident elastic plane wave from the formation.

The fluid displacement $\vec{u}_f$ inside the borehole and the solid displacement $\vec{u}_m$ in the m-th layer satisfy the acoustic and elastic wave equations, respectively. In terms of the corresponding potentials (Tubman, 1984; Schoenberg et al., 1981), the wave equations are:

$$\nabla^2\phi_f + \frac{\omega^2}{\alpha_f^2}\phi_f = 0, \tag{3.1}$$

and

$$\nabla^2\phi_m + \frac{\omega^2}{\alpha^2}\phi_m = 0, \tag{3.2a}$$

$$\nabla^2\xi_m + \frac{\omega^2}{\beta^2}\xi_m = 0, \tag{3.2b}$$

$$\nabla^2\psi_m + \frac{\omega^2}{\beta^2}\psi_m = 0. \tag{3.2c}$$

The displacements are related to these potentials by

$$\vec{u}_f = \nabla\phi_f, \tag{3.3a}$$

$$\vec{u}_m = \nabla\phi_m + \nabla \times (\nabla \times (\xi_m \hat{e}_z)) + \nabla \times (\psi_m \hat{e}_z). \tag{3.3b}$$

Expressions for the stresses can be found in Appendix A-1.

3.1.2 General Solutions

When an incident wave hits the outermost radial interface from the formation, some energy is reflected back and some is transmitted through the cement and casing. The general solution to the problem, in a cylindrical coordinate system (r, θ, z) with θ the angle with respect to the azimuth of the incident wave, is given by

$$\phi_f = -\frac{\alpha_f V(\omega)}{\omega^2} \sum_{n=0}^{\infty} \varepsilon_n i^n A_n J_n(k_f r) \cos n\theta, \tag{3.4a}$$

$$\phi_m = -\frac{\alpha V(\omega)}{\omega^2} \sum_{n=0}^{\infty} \varepsilon_n i^n \left[E_n^{(m)} H_n^{(1)}(k_p^{(m)} r) + P_n^{(m)} H_n^{(2)}(k_p^{(m)} r) \right] \cos n\theta, \tag{3.4b}$$

$$\xi_m = -\frac{i\beta^2 V(\omega)}{\omega^3} \sum_{n=0}^{\infty} \varepsilon_n i^n \left[F_n^{(m)} H_n^{(1)}(k_s^{(m)} r) + Q_n^{(m)} H_n^{(2)}(k_s^{(m)} r) \right] \cos n\theta, \tag{3.4c}$$

$$\psi_m = -\frac{\beta V(\omega)}{\omega^2} \sum_{n=0}^{\infty} \varepsilon_n i^n \left[G_n^{(m)} H_n^{(1)}(k_s^{(m)} r) + R_n^{(m)} H_n^{(2)}(k_s^{(m)} r) \right] \sin n\theta, \tag{3.4d}$$

where $\varepsilon_n = \begin{cases} 1 & \text{if } n = 0 \\ 2 & \text{if } n \geq 1 \end{cases}$. The z and time dependence $e^{i(k_z z - \omega t)}$ is assumed. In these expressions, $k_f = \sqrt{\omega^2/\alpha_f^2 - k_z^2}$, $k_p^{(m)} = \sqrt{\omega^2/\alpha_m^2 - k_z^2}$ and $k_s^{(m)} = \sqrt{\omega^2/\beta_m^2 - k_z^2}$. The signs of $k_f, k_p^{(m)}, k_s^{(m)}$ are chosen such that $\mathbf{Im}(k_p^{(m)}, k_s^{(m)}, k_f) \geq 0$. $V(\omega)$ denotes the source function at a given frequency ω (without loss of generality, $V(\omega) \equiv -\omega^2$ is assumed subsequently). $H_n^{(1)}(x)$ is the Hankel function of the first kind, representing energy traveling outward. $H_n^{(2)}(x)$ is the Hankel function of the second kind, representing energy traveling inward. $E_n^{(m)}, P_n^{(m)}, F_n^{(m)}, Q_n^{(m)}, G_n^{(m)}$ and $R_n^{(m)}$ are dimensionless, unknown constants in the m-th layer, and A_n is the coefficient in the fluid. They are determined by satisfying appropriate boundary conditions.

The above expansions apply to the case where the incident wave is either a plane P-wave or a plane SV-wave. For the SH case, however, the $\underline{\cos n\theta}$ factors should be replaced by $\underline{\sin n\theta}$ and the $\underline{\sin n\theta}$ factors by $\underline{-\cos n\theta}$. With such a convention, the formulation is valid for an incident wave of all the types (P-wave, SV-wave and SH-wave).

Let $u_{rn}^{(m)}$, for example, denote the n-th harmonic component (mode n) of the radial displacement in layer m (the borehole fluid column corresponds to m=0). The radial, tangential and vertical displacements $u_{rn}^{(m)}$, $u_{\theta n}^{(m)}$ and $u_{zn}^{(m)}$ are given by

$$\begin{aligned} u_{rn}^{(m)} = & \quad [\, \mathcal{U}_n^{\phi(1)}(r)\, E_n^{(m)} + \mathcal{U}_n^{\phi(2)}(r)\, P_n^{(m)} \,] \cos n\theta \\ & + [\, \mathcal{U}_n^{\xi(1)}(r)\, F_n^{(m)} + \mathcal{U}_n^{\xi(2)}(r)\, Q_n^{(m)} \,] \cos n\theta \\ & + [\, \mathcal{U}_n^{\psi(1)}(r)\, G_n^{(m)} + \mathcal{U}_n^{\psi(2)}(r)\, R_n^{(m)} \,] \cos n\theta \ , \end{aligned} \tag{3.5a}$$

$$\begin{aligned} u_{\theta n}^{(m)} = & \quad [\, \mathcal{V}_n^{\phi(1)}(r)\, E_n^{(m)} + \mathcal{V}_n^{\phi(2)}(r)\, P_n^{(m)} \,] (-\sin n\theta) \\ & + [\, \mathcal{V}_n^{\xi(1)}(r)\, F_n^{(m)} + \mathcal{V}_n^{\xi(2)}(r)\, Q_n^{(m)} \,] (-\sin n\theta) \\ & + [\, \mathcal{V}_n^{\psi(1)}(r)\, G_n^{(m)} + \mathcal{V}_n^{\psi(2)}(r)\, R_n^{(m)} \,] (-\sin n\theta) \ , \end{aligned} \tag{3.5b}$$

$$\begin{aligned} u_{zn}^{(m)} = & \quad [\, \mathcal{W}_n^{\phi(1)}(r)\, E_n^{(m)} + \mathcal{W}_n^{\phi(2)}(r)\, P_n^{(m)} \,] \cos n\theta \\ & + [\, \mathcal{W}_n^{\xi(1)}(r)\, F_n^{(m)} + \mathcal{W}_n^{\xi(2)}(r)\, Q_n^{(m)} \,] \cos n\theta \ . \end{aligned} \tag{3.5c}$$

And the stresses on the surface where r = constant are given by

$$\begin{aligned} \sigma_{rrn}^{(m)} = & \quad [\, \mathcal{R}_n^{\phi(1)}(r)\, E_n^{(m)} + \mathcal{R}_n^{\phi(2)}(r)\, P_n^{(m)} \,] \cos n\theta \\ & + [\, \mathcal{R}_n^{\xi(1)}(r)\, F_n^{(m)} + \mathcal{R}_n^{\xi(2)}(r)\, Q_n^{(m)} \,] \cos n\theta \\ & + [\, \mathcal{R}_n^{\psi(1)}(r)\, G_n^{(m)} + \mathcal{R}_n^{\psi(2)}(r)\, R_n^{(m)} \,] \cos n\theta \ , \end{aligned} \tag{3.6a}$$

$$\begin{aligned} \sigma_{r\theta n}^{(m)} = & \quad [\, \mathcal{T}_n^{\phi(1)}(r)\, E_n^{(m)} + \mathcal{T}_n^{\phi(2)}(r)\, P_n^{(m)} \,] (-\sin n\theta) \\ & + [\, \mathcal{T}_n^{\xi(1)}(r)\, F_n^{(m)} + \mathcal{T}_n^{\xi(2)}(r)\, Q_n^{(m)} \,] (-\sin n\theta) \\ & + [\, \mathcal{T}_n^{\psi(1)}(r)\, G_n^{(m)} + \mathcal{T}_n^{\psi(2)}(r)\, R_n^{(m)} \,] (-\sin n\theta) \ , \end{aligned} \tag{3.6b}$$

$$\begin{aligned} \sigma_{rzn}^{(m)} = & \quad [\, \mathcal{Z}_n^{\phi(1)}(r)\, E_n^{(m)} + \mathcal{Z}_n^{\phi(2)}(r)\, P_n^{(m)} \,] \cos n\theta \\ & + [\, \mathcal{Z}_n^{\xi(1)}(r)\, F_n^{(m)} + \mathcal{Z}_n^{\xi(2)}(r)\, Q_n^{(m)} \,] \cos n\theta \\ & + [\, \mathcal{Z}_n^{\psi(1)}(r)\, G_n^{(m)} + \mathcal{Z}_n^{\psi(2)}(r)\, R_n^{(m)} \,] \cos n\theta \ . \end{aligned} \tag{3.6c}$$

The coefficients are given in Appendix B-1.

The boundary conditions for determining $A_n, E_n^{(m)}, P_n^{(m)}, F_n^{(m)}, Q_n^{(m)}, G_n^{(m)}$ and $R_n^{(m)}$ are the continuities of radial displacement and normal stress, vanishing of tangential stresses at the fluid-solid interface, and the continuities of displacements and tractions at the solid-solid interfaces. In the outermost layer M + 1, i.e., the formation, $P_n^{(M+1)}, Q_n^{(M+1)}$ and $R_n^{(M+1)}$ are zero because of the radiation boundary condition at infinity. After the coefficients $A_n, E_n^{(m)}, P_n^{(m)}, F_n^{(m)}, Q_n^{(m)}, G_n^{(m)}$ and $R_n^{(m)}$ are known, the displacement on the borehole wall and the pressure in the fluid can be computed.

3.2 A Quasi-Static Approach

In this section, we give a quasi-static approach to the theory of borehole coupling in a cased borehole. Results for an open borehole have been obtained by White (1953, 1983). The quasi-static approach gives a profound physical insight into the interaction of an incident elastic wave with a fluid-filled borehole. In addition, it yields a simple and explicit formula for the pressure in the cased borehole at low frequencies. The results given in this section can also be applied to study the radiation of a volume injection source, such as an air gun or a piezoelectric source, in a cased borehole using the reciprocity relationships (Aki and Richards, 1980; Gibson and Peng, 1993).

3.2.1 Pressure in the Fluid

At a low frequency limit, the mathematically involved expressions in the previous section can be greatly simplified. The pressure in the fluid is homogeneous across the borehole section and is related to the axial motion v in the fluid and the radial motion u_r in the solid by the equations of conservation of vertical momentum and the constitutive law (White, 1983)

$$\frac{\partial P}{\partial z} = \rho_f \omega^2 v, \tag{3.7}$$

and

$$P = -K_f(\frac{\partial v}{\partial z} + \frac{2u_r(r_b, z)}{r_b}), \tag{3.8}$$

where $K_f = \rho_f \alpha_f^2$ is the fluid bulk modulus and r_b the borehole radius.

Eliminating v in equation (3.7) and equation (3.8) results in the following time-domain equation:

$$\frac{\partial^2 P}{\partial t^2} - \alpha_f^2 \frac{\partial^2 P}{\partial z^2} = 2\rho_f \alpha_f^2 \frac{\partial^2 \epsilon_r(r_b, z)}{\partial t^2}, \tag{3.9}$$

where $\epsilon_r(r_b, z) = u_r(r_b, z)/r_b$ is the change of borehole radius, which acts as a source of pressure in the fluid-filled borehole.

3.2.2 Borehole Coupling Equation

The function $\epsilon_r(r_b, z)$ in equation (3.9) can be decomposed into two parts:

$$\epsilon_r(r_b, z) = (\frac{\bar{u}_r(r_b, z)}{r_b})^{(inc)} - \frac{P}{2M}, \tag{3.10}$$

where the first term on the right-hand side is the deformation of an empty borehole due to an incident elastic wave from the formation, the second term is the fluid resistance against this borehole deformation (White, 1983). The $\bar{u}_r$ in the equation is the azimuthally averaged radial displacement on the borehole wall, representing the net change of the cross-section of an empty borehole. M is the effective modulus of a cased borehole against internal expansion, and is given by

$$M = \mu_c \frac{\mu + (\mu_c - \mu)(1 - \gamma_c)(1 - \frac{r_b^2}{r_c^2})}{\mu_c - (\mu_c - \mu)\gamma_c(1 - \frac{r_b^2}{r_c^2})}, \tag{3.11}$$

where $\gamma_c = \beta_c^2/\alpha_c^2$, μ and μ_c are the shear moduli of the formation and the casing, respectively. This expression is identical with those of Marzetta and Shoenberg (1985) and Norris (1990) and is independently derived in Peng et al. (1993d).

An alternative expression for the pressure in the fluid, obtained by substituting equation (3.10) into equation (3.9), is

$$\frac{1}{C_T^2} \frac{\partial^2 P}{\partial t^2} - \frac{\partial^2 P}{\partial z^2} = 2\rho_f \frac{\partial^2 \epsilon_r^{(inc)}(z)}{\partial t^2} \tag{3.12}$$

where $\epsilon_r^{(inc)}(z) = (\bar{u}_r(r_b, z)/r_b)^{(inc)}$ is called the borehole squeeze strain. The definition is different from that of Marzetta (1992) by a factor of two. Equation (3.12) is also referred to as the *borehole coupling equation.* In this equation, C_T is the tube wave speed in a cased borehole, and is given by

$$C_T = \frac{\alpha_f}{\sqrt{1 + \rho_f \alpha_f^2 / M}}. \tag{3.13}$$

It should be pointed out that the borehole squeeze strain is different from the radial strain $\partial u_r/\partial r$ on the borehole wall. The former is the average change of the cross section when an incident elastic wave impinges on an *empty* borehole. If $\epsilon_r^{(inc)}$ is known, the pressure in the fluid can be determined by

$$P(z,\omega) = -\rho_f \omega^2 \int_{-\infty}^{\infty} \epsilon_r^{(inc)}(z') \frac{i}{k_T} e^{-ik_T|z-z'|} dz', \tag{3.14}$$

where $k_T = \omega/C_T$ is the wavenumber of the tube wave. For an incident plane wave, the z dependence can be assumed to be $e^{ik_z z}$ where k_z is the vertical wavenumber. Then the above equation, neglecting terms associated with energies arriving from infinite distances (out of any observational time window), yields

$$P(z,\omega) = 2\rho_f \omega^2 \frac{\epsilon_r^{(inc)}(z)}{{k_z}^2 - k_T^2}. \tag{3.15}$$

3.2.3 Borehole Squeeze Strain

By definition, the borehole squeeze strain is the azimuthally averaged radial displacement on the wall divided by the radius, i.e.,

$$\epsilon_r^{(inc)} = \frac{1}{2\pi} \int_0^{2\pi} u_r(r_b, \theta, z) d\theta \; / \; r_b \; .$$

It depends only on the net change of the borehole cross section, not on details of deformation. In the case where the borehole deformation is equivoluminal, i.e., $\epsilon_r^{(inc)} = 0$, equation (3.15) implies that no pressure will be set up in a fluid-filled borehole, a phenomenon that will be referred to as the cased borehole screening effect.

To determine the borehole squeeze strain, we need to compute the average change of borehole radius when an empty borehole is subjected to a given stress. A quasi-static approach will be adopted here, which follows the technique used by White (1983) for an open borehole.

As the frequency $\omega \rightarrow 0$, the wavelength becomes much larger than the diameter of the borehole. In a region around the borehole that is much larger than the borehole radius and, at the same time, much smaller than the wavelength, the stresses are nearly homogeneous and equal to those of the incident wave. Introduction of a cased borehole only disturbs locally the stress field at the expense of borehole deformation. The volume change of the borehole sets up a pressure inside the fluid in the same way as a piston source does. In an open borehole, the change of the borehole radius due to an incident wave is easily calculated from known results (Timoshenko and Goodier, 1951). In a cased borehole, extra work is needed to derive the effective moduli. In Appendix B-3, we give a derivation of the borehole squeeze strain by using the Airy function method in the static elasticity theory (Love, 1944), and the result is

$$\epsilon_r^{(inc)} = \frac{\sigma_{xx} + \sigma_{yy}}{E_{\parallel}} - \frac{\nu \sigma_{zz}}{E_{\perp}}, \tag{3.16}$$

where σ_{xx}, σ_{yy} and σ_{zz} are the principal stresses of an incident wave. $E_{\parallel}$ is the effective modulus of the cased borehole against horizontal deformation, and is given by

$$E_{\parallel} = \frac{E}{1+\zeta\nu} \left[1 + (\frac{\mu_c}{\mu} - 1)(1-\gamma_c)(1-\frac{r_b^2}{r_c^2}) \right],$$

and $E_{\perp}$ is the effective modulus of the cased borehole against vertical deformation, and is given by

$$E_{\perp} = \frac{E}{1+\zeta\nu^{-1}} \left[1 + (\frac{\mu_c}{\mu} - 1)(1-\gamma_c)(1-\frac{r_b^2}{r_c^2}) \right],$$

where

$$\zeta = (\frac{\mu_c}{\mu} - 1)\,(\frac{1}{2} - \gamma_c)\,(1 - \frac{r_b^2}{r_c^2})\,.$$

In these equations, E and ν are the Young's modulus and the Poisson ratio of the formation. μ_c and μ are the shear moduli of the casing and formation, respectively.

As a reminder, $\gamma_c = \beta_c^2/\alpha_c^2$, r_b is the inner radius of the casing and r_c is the outer radius of the casing. In the case where $r_b = r_c$ or $E_c = E$ and $\nu_c = \nu$, $E_{\|}$ and $E_{\perp}$ both reduce to E, the Young's modulus of the formation. In this case, equation (3.16) is identical with that given by White (1953, 1983).

Figure 3-2 and Figure 3-3 show the effective moduli of a cased borehole as a function of the casing thickness $(r_c - r_b)/r_b$ for the hard and soft formations, respectively. Evidently, $E_{\perp} \leq E_{\|}$ when the casing is harder than the formation. This implies that the cased borehole is stronger horizontally than vertically. $E_{\|}$ increases rapidly with the increase of casing thickness, while $E_{\perp}$ decreases slowly in the hard formation and increases slowly in the soft formation.

3.2.4 Plane P-Wave Incidence: Cased Borehole Screening Phenomenon

From equation (3.15) and equation (3.16), using the principal stresses σ_{xx}, σ_{yy} and σ_{zz} of an incident plane P-wave, we obtain

$$\frac{P}{P_0} = \frac{\rho_f C_T^2}{\rho\beta^2} \; \frac{E}{(1-\nu^2)E_{\perp}} \; \frac{\eta[\,1-(1-2\nu)\cos^2\delta\,] - \nu[\,\nu+(1-2\nu)\cos^2\delta\,]}{1 - C_T^2/\alpha^2\cos^2\delta}, \qquad (3.17)$$

where P is the pressure in a cased borehole. $P_0 = -\rho\alpha\omega^2$ is a normalization factor. δ is the angle of incidence with respect to the borehole axis. $\eta = E_{\perp}/E_{\|}$ is the ratio of the vertical and horizontal effective moduli. α and β are the compressional and shear velocities of the formation. When the thickness of the casing vanishes or its physical properties are the same as the formation, this equation reduces exactly to

$$\frac{P}{P_0} = \frac{\rho_f C_T^2}{\rho\beta^2} \; \frac{1 - 2\beta^2/\alpha^2\cos^2\delta}{1 - C_T^2/\alpha^2\cos^2\delta}, \qquad (3.18)$$

the pressure in an open borehole induced by an incident plane P-wave (White, 1953, 1983; Lovell and Hornby, 1990).

A particular angle of incidence exists where the pressure in the fluid vanishes if

$$\eta < \frac{1-\nu}{2},$$

and this angle δ_0 is given by

$$\delta_0 = \cos^{-1} \sqrt{\frac{\eta - \nu^2}{(\eta + \nu)(1 - 2\nu)}}, \tag{3.19}$$

at which there is no net change of the borehole cross-section due to the passage of an incident P-wave. In this case, the casing acts like a screen such that a hydrophone can not see the incident compressional wave. For the hard formation (Berea sandstone) with steel casing, this angle occurs at $\delta_0 = 8.64^o$; for the soft formation (Pierre shale), it is at $\delta_0 = 35.67^o$, where $r_b = 0.1016\ m$ (borehole radius) and $r_c = 0.1219\ m$ (casing radius) are used. These estimates are verified by the exact solutions given later in this section.

The critical thickness $h_c = r_c - r_b$ is given by

$$\frac{h_c}{r_c} = 1 - \sqrt{1 - \frac{2\nu(1 - \nu_c)}{\nu_c(1 - 2\nu)} \frac{\mu}{\mu_c - \mu}}, \tag{3.20}$$

below which the screening effect disappears. If $h \ll r_b$, the above equation reduces to

$$h_c/r_b = \frac{\nu(1 - \nu_c)}{\nu_c(1 - 2\nu)} \frac{\mu}{\mu_c - \mu}\ . \tag{3.21}$$

For example, taking the formation to be Berea sandstone and the casing to be steel, the above analysis yields a critical casing thickness $h_c = 0.1731\ r_b$. Beyond this thickness there is an angle of incidence δ_0 given by equation (3.19) where, for an incident P-wave, the pressure in the fluid vanishes. When the formation is Pierre shale, the critical thickness is $h_c = 0.0978\ r_b$. These estimates have been confirmed by solving the exact equations given in the next section. It is interesting to note that the critical thickness is smaller in the soft formation than in the hard formation, implying that the screening effect occurs more often in a cased borehole with a soft formation.

The following two examples are to show that equation (3.17) agrees with the exact solution at all angles of incidence at low frequencies. Figure 3-4a shows the pressure in the fluid calculated by two methods. The formation is Berea sandstone. The

incident wave is a plane P-wave. The left figure is computed by the exact method at 1 Hz, the right figure is computed by equation (3.17). These two calculations are indistinguishable. They both show a zero for the pressure in the fluid at 8.6^o. Figure 3-4b is the same as Figure 3-4a but for Pierre shale. Again, one can not tell the difference between the exact solution and the quasi-static approximation. In this case, both calculations show a zero at $\delta = 35.7^o$.

3.2.5 Plane S-Wave Incidence: Fluid Resonance Phenomenon

Following the same derivations as in the previous subsection, for an incident plane SV-wave we obtain:

$$\frac{P}{P_0} = \frac{\rho_f C_T^2}{\rho\beta^2} \frac{(\eta+\nu)E}{(1+\nu)E_\perp} \frac{\sin 2\delta}{1 - C_T^2/\beta^2 \cos^2\delta}, \tag{3.22}$$

where P is the pressure in the cased borehole. When the casing thickness vanishes or its properties are the same as the formation, equation (3.22) reduces to

$$\frac{P}{P_0} = \frac{\rho_f C_T^2}{\rho\beta^2} \frac{\sin 2\delta}{1 - C_T^2/\beta^2 \cos^2\delta}, \tag{3.23}$$

the pressure in an open borehole induced by an incident plane SV-wave, a result first obtained by White (1953).

Figure 3-5a and Figure 3-5b show the pressures in the fluid-filled borehole for both the hard and the soft formations. The incident wave is a plane SV-wave. The plots on the left are calculated by the exact method at 1 Hz. The plots on the right are computed by equation (3.22). As expected, no discrepancies between the two methods can be identified. For the hard formation, the pressure has a lobe around $\delta = 45^o$. For the soft formation, a strong fluid resonance occurs at $\delta = \cos^{-1}\beta/C_T = 54^o$ for SV-wave incidence, where the denominator in equation (3.22) vanishes.

3.3 Matrix Formulation for the Exact Solution

3.3.1 Displacement-Stress Vector

For a fixed harmonic component or mode n in equations (3.4a)-(3.4d), the displacement-stress vector $\vec{\mathrm{b}}_n^{(m)}(r)$ in layer m and at position r is related to the unknown coefficient vector $\vec{\mathrm{c}}_n^{(m)}$ by (Greenfield, 1977; for the symmetric mode n=0, also see Tubman, 1984 and Meredith, 1990)

$$\vec{\mathrm{b}}_n^{(m)}(r) = \mathrm{D}_n^{(m)}(r)\ \vec{\mathrm{c}}_n^{(m)}, \tag{3.24}$$

where

$$\vec{\mathrm{b}}_n^{(m)}(r) = \begin{pmatrix} u_{rn}^{(m)} \\ u_{\theta n}^{(m)} \\ u_{zn}^{(m)} \\ \sigma_{rrn}^{(m)} \\ \sigma_{r\theta n}^{(m)} \\ \sigma_{rzn}^{(m)} \end{pmatrix}(r),$$

and

$$\vec{\mathrm{c}}_n^{(m)} = \begin{pmatrix} E_n^{(m)} \\ P_n^{(m)} \\ F_n^{(m)} \\ Q_n^{(m)} \\ G_n^{(m)} \\ R_n^{(m)} \end{pmatrix}.$$

The coefficient matrix $\mathrm{D}_n^{(m)}(r)$ is given in Appendix B-1. In the above expressions, the superscript (m) is the layer index and the subscript n is the harmonic mode number.

3.3.2 Boundary Conditions

The boundary conditions at the interface between radial layer i and $i+1$ require that the displacements and stresses be continuous, i.e.,

$$\vec{\mathrm{b}}_n^{(i)}(r_{i+1}) = \vec{\mathrm{b}}_n^{(i+1)}(r_{i+1}), \tag{3.25}$$

when both sides are solids, or the normal stresses and displacements are continuous and the tangential stresses vanish when either side is a fluid, e.g., at $r = r_b$,

$$\mathrm{S}\ \vec{\mathrm{b}}_n^{(1)}(r_b) = \begin{bmatrix} u_{r_n}^f(r_b) \\ -p_n^f(r_b) \\ 0 \\ 0 \end{bmatrix} = \vec{\mathrm{f}}\, A_n, \tag{3.26}$$

where $u_{r_n}^f$ and p_n^f are the radial displacement and the pressure inside the fluid, respectively. S is an index matrix defined as

$$\mathrm{S} = \begin{bmatrix} 1 & 0 & 0 & 0 & 0 & 0 \\ 0 & 0 & 0 & 1 & 0 & 0 \\ 0 & 0 & 0 & 0 & 1 & 0 \\ 0 & 0 & 0 & 0 & 0 & 1 \end{bmatrix}_{4\times 6}$$

and $\vec{\mathrm{f}} = (\alpha_f k_f J_n'(k_f r_b), -\rho_f \alpha_f \omega^2 J_n(k_f r_b), 0, 0)^T$ (see Appendix A-3). In equation (3.26), A_n is the unknown coefficient in the fluid displacement potential.

At the outermost layer $i = M + 1$, radiation conditions must be satisfied for a source free problem, i.e.,

$$P_n^{(M+1)} = Q_n^{(M+1)} = R_n^{(M+1)} = 0,$$

such that no secondary reflected energy arrives from infinity.

3.3.3 Propagator Matrices

Let

$$\vec{\mathrm{w}}_n(r) = \begin{bmatrix} u_{rn}^{(inc)} \\ u_{\theta n}^{(inc)} \\ u_{zn}^{(inc)} \\ \sigma_{rrn}^{(inc)} \\ \sigma_{r\theta n}^{(inc)} \\ \sigma_{rzn}^{(inc)} \end{bmatrix} (r),$$

be the displacement-stress vector of an incident plane wave from the formation (i.e., where $r \geq r_{M+1}$). For a plane wave of either P-, SV-, or SH-type, this vector is explicitly given in Appendix B-2.

The boundary condition at the outermost interface $r = r_{M+1}$ can be written as

$$\mathrm{D}_n^{(M+1)}(r_{M+1})\, \vec{\mathrm{c}}_n^{(M+1)} + \vec{\mathrm{w}}_n(r_{M+1}) = \mathrm{D}_n^{(M)}(r_{M+1})\, \vec{\mathrm{c}}_n^{(M)}, \tag{3.27}$$

while at an interior interface $r = r_i$, assuming the casing layers are well-bonded to each other, we have

$$\mathrm{D}_n^{(i)}(r_i)\, \vec{\mathrm{c}}_n^{(i)} = \mathrm{D}_n^{(i-1)}(r_i)\, \vec{\mathrm{c}}_n^{(i-1)} \tag{3.28}$$

for $2 \leq i \leq M$.

By recursively applying equations (3.27) and (3.28), we obtain

$$\mathrm{D}_n^{(1)}(r_b)\, \vec{\mathrm{c}}_n^{(1)} = \mathrm{G}_n [\, \mathrm{D}_n^{(M+1)}(r_{M+1})\, \vec{\mathrm{c}}_n^{(M+1)} + \vec{\mathrm{w}}_n(r_{M+1})\,], \tag{3.29}$$

which relates the wave fields at the borehole wall ($r = r_b$) to those in the formation $r = r_{M+1}$, where

$$\mathrm{G}_n = \prod_{i=1}^{M} \mathrm{D}_n^{(i)}(r_i)[\, \mathrm{D}_n^{(i)}(r_{i+1})]^{-1}$$

is a matrix that propagates energy across boundaries.

The coupling of energy into the borehole fluid is accomplished by substituting equation (3.29) into the fluid-solid boundary condition in equation (3.26) at $r = r_b$,

yielding

$$\mathrm{S}\ \mathrm{G}_n\left[\ \mathrm{D}_n^{(\mathrm{M+1})}(r_{\mathrm{M+1}})\ \vec{\mathrm{c}}_n^{(\mathrm{M+1})} + \vec{\mathrm{w}}_n(r_{\mathrm{M+1}})\ \right] = \vec{\mathrm{f}}\, A_n,$$

from which, in addition to the radiation condition in the outermost layer, the coefficients A_n, $E_n^{(\mathrm{M+1})}$, $F_n^{(\mathrm{M+1})}$ and $G_n^{(\mathrm{M+1})}$ can be solved. This equation can be further simplified as

$$\vec{\mathrm{f}}_E\, E_n^{(\mathrm{M+1})} + \vec{\mathrm{f}}_F\, F_n^{(\mathrm{M+1})} + \vec{\mathrm{f}}_G\, G_n^{(\mathrm{M+1})} + \vec{\mathrm{f}}_w = \vec{\mathrm{f}}\, A_n, \tag{3.30}$$

where

$$\vec{\mathrm{f}}_w = \begin{bmatrix} (\mathrm{G}_n)_{1i}\,(\vec{\mathrm{w}}_n)_i \\ (\mathrm{G}_n)_{4i}\,(\vec{\mathrm{w}}_n)_i \\ (\mathrm{G}_n)_{5i}\,(\vec{\mathrm{w}}_n)_i \\ (\mathrm{G}_n)_{6i}\,(\vec{\mathrm{w}}_n)_i \end{bmatrix} (r_{\mathrm{M+1}}),$$

$$\vec{\mathrm{f}}_E = \begin{bmatrix} (\mathrm{G}_n)_{1i}\,(\mathrm{D}_n^{(\mathrm{M+1})})_{i1} \\ (\mathrm{G}_n)_{4i}\,(\mathrm{D}_n^{(\mathrm{M+1})})_{i1} \\ (\mathrm{G}_n)_{5i}\,(\mathrm{D}_n^{(\mathrm{M+1})})_{i1} \\ (\mathrm{G}_n)_{6i}\,(\mathrm{D}_n^{(\mathrm{M+1})})_{i1} \end{bmatrix} (r_{\mathrm{M+1}}),$$

$$\vec{\mathrm{f}}_F = \begin{bmatrix} (\mathrm{G}_n)_{1i}\,(\mathrm{D}_n^{(\mathrm{M+1})})_{i3} \\ (\mathrm{G}_n)_{4i}\,(\mathrm{D}_n^{(\mathrm{M+1})})_{i3} \\ (\mathrm{G}_n)_{5i}\,(\mathrm{D}_n^{(\mathrm{M+1})})_{i3} \\ (\mathrm{G}_n)_{6i}\,(\mathrm{D}_n^{(\mathrm{M+1})})_{i3} \end{bmatrix} (r_{\mathrm{M+1}}),$$

and

$$\vec{\mathrm{f}}_G = \begin{bmatrix} (\mathrm{G}_n)_{1i}\,(\mathrm{D}_n^{(\mathrm{M+1})})_{i5} \\ (\mathrm{G}_n)_{4i}\,(\mathrm{D}_n^{(\mathrm{M+1})})_{i5} \\ (\mathrm{G}_n)_{5i}\,(\mathrm{D}_n^{(\mathrm{M+1})})_{i5} \\ (\mathrm{G}_n)_{6i}\,(\mathrm{D}_n^{(\mathrm{M+1})})_{i5} \end{bmatrix} (r_{\mathrm{M+1}})\ .$$

A 4×4 matrix inversion is required to solve A_n, $E_n^{(\mathrm{M+1})}$, $F_n^{(\mathrm{M+1})}$ and $G_n^{(\mathrm{M+1})}$, the coefficients in the borehole fluid and in the outermost formation. In intermediate layers,

the solution can be obtained by recursively applying equations (3.27) and (3.28) in a backward matching fashion, starting from the layer adjacent to the formation.

As in any integral transform method applied to solve the elastic wave equation in a layered medium, instability and loss of accuracy are problematic when the vertical number k_z exceeds the medium wavenumbers such that the radial wavenumbers become imaginary. In this case, the wave field is evanescent. The matrix equation involves both negative and positive exponentials. Theoretically, terms having positive exponentials cancel each other exactly, but numerically this never happens (Dunkin, 1965). The Thomson-Haskell type propagator matrix method described here has a block bidiagonal structure and is essentially a two-point shooting algorithm (Chin et al., 1984). Numerical instability, if handled improperly, might become troublesome. On the other hand, the global matrix method proposed by Chin et al. (1984) is well suited to this problem.

3.3.4 Global Matrix Method

We adopt a special type of the global matrix method to solve A_n, $E_n^{(1)}$, $P_n^{(1)}$, $F_n^{(1)}$, $Q_n^{(1)}$, $G_n^{(1)}$ and $R_n^{(1)}$. These are coefficients needed in computing the pressure in fluid and the solid displacement in casing.

The starting equations for this method are

$$\mathrm{B}_0\,\mathrm{D}_n^{(1)}(r_b)\,\vec{\mathrm{c}}_n^{(1)} = \mathrm{B}_0\,\mathrm{G}_n\,\mathrm{B}_0^{-1}\,[\,\mathrm{B}_0\,\mathrm{D}_n^{(M+1)}(r_{M+1})\,\vec{\mathrm{c}}_n^{(M+1)} + \mathrm{B}_0\,\vec{\mathrm{w}}_n(r_{M+1})\,], \tag{3.31}$$

and

$$\mathrm{b}_0\,\mathrm{S}\,\mathrm{D}_n^{(1)}(r_b)\,\vec{\mathrm{c}}_n^{(1)} = \mathrm{b}_0\,\vec{\mathrm{f}}\,A_n, \tag{3.32}$$

where equation (3.26) and equation (3.29) have been used, and where

$$b_0 = \begin{pmatrix} (B_0)_{11} & & & \\ & (B_0)_{44} & & \\ & & (B_0)_{55} & \\ & & & (B_0)_{66} \end{pmatrix}_{4\times 4}$$

and

$$B_0 = \begin{pmatrix} \frac{1}{\lambda_1} & & & & & \\ & \frac{1}{\lambda_2} & & & & \\ & & \frac{1}{\lambda_3} & & & \\ & & & \frac{1}{\lambda_4} & & \\ & & & & \frac{1}{\lambda_5} & \\ & & & & & \frac{1}{\lambda_6} \end{pmatrix}_{6\times 6}$$

with $\lambda_i = \max_{j\in[1,6]} |(D_n^{(1)})_{ij}|$ being the absolute maximum in the i-th row. The matrices B_0 and b_0 are introduced to precondition the propagator matrix equations.

Let us define a coefficient vector of ten elements as

$$\vec{x}_n = (A_n, E_n^{(1)}, P_n^{(1)}, F_n^{(1)}, Q_n^{(1)}, G_n^{(1)}, R_n^{(1)}, E_n^{(M+1)}, F_n^{(M+1)}, G_n^{(M+1)})^T,$$

where the first entry is the coefficient of the potential in the fluid, the next six entries are those in the first casing layer, and the last three are those in the formation. Using equation (3.31) and equation (3.32), we can solve this vector by the following set of linear equations

$$L_n \ \vec{x}_n = \begin{bmatrix} \vec{0} \\ \vec{w}_n^* \end{bmatrix}, \tag{3.33}$$

where

$$L_n = \begin{bmatrix} \vec{f}_0 & -\widetilde{K} & \\ & \widetilde{D}_1 & -\widetilde{D}_2 \end{bmatrix}_{10\times 10}$$

is a 10×10 square matrix, and where

$$\widetilde{G}_n = B_0 \ G_n \ B_0^{-1},$$

$$\widetilde{\mathrm{D}}_1 = \mathrm{B}_0 \; \mathrm{D}_n^{(1)}(r_1),$$

$$\widetilde{\mathrm{D}}_2 = \widetilde{\mathrm{G}}_n \, \mathrm{B}_0 \; \mathrm{D}_n^{(M+1)}(r_{M+1}),$$

$$\widetilde{\mathrm{K}} = \mathrm{b}_0 \; \mathrm{S} \; \mathrm{B}_0^{-1} \; \widetilde{\mathrm{D}}_1,$$

$$\vec{\mathrm{f}}_0 = \mathrm{b}_0 \; \vec{\mathrm{f}},$$

$$\vec{\mathrm{w}}_n^* = \widetilde{\mathrm{G}}_n \; \mathrm{B}_0 \; \vec{\mathrm{w}}_n(r_{M+1}).$$

The advantage of this global matrix formulation is that, after $\vec{c}_n^{(1)}$ and $\vec{c}_n^{(M+1)}$ are known, the $\vec{c}_n^{(i)}$ in the i-th annulus can be determined by either a backward matching from the outermost layer, or a forward matching from the innermost layer. In terms of matrix structures, as shown in Chin et al. (1984), L_n has a block tridiagonal form and its inversion can be adequately computed by the Gaussian elimination method with partial pivoting (Schmidt and Tango, 1986). This method tends to yield great accuracy compared to those that employ the Thompson-Haskell propagator matrix algorithm directly.

3.3.5 Dispersion Equation

The dispersion equation in a cased borehole is given by

$$\det \mathrm{L}_n = 0, \tag{3.34}$$

i.e., the determinant of the 10×10 matrix L_n is zero.

Suppose $\mathrm{L}_n = \mathrm{L} \cdot \mathrm{U}$ is the LU decomposition of the matrix L_n by Crout's algorithm (Press et al., 1989), and let γ_{ii} be the diagonal elements of the upper triangle matrix U, then equation (3.34) is equivalent to

$$F(k_z) = \prod_{i=1}^{10} \gamma_{ii} = 0 \, .$$

We are concerned with possible excitations of surface and trapped modes generated by the casing. Instead of solving the above nonlinear equation for its roots, we contour

the amplitude of $F(k_z)$ on a logarithmic scale in the complex k_z plane for a frequency up to 2 kHz. The purpose of this analysis is to identify all singularities along the path of $k_z = \omega/\alpha \cos\delta$, for example, as δ varies from 0° to 90°.

Detailed analyses show that (Peng et al. 1993d) for a frequency up to 2 kHz, no mode other than the tube wave has potential impact on the fluid-solid motion in a cased borehole for both the hard and soft formations. Since there is a pole k_T (the tube wave wavenumber) between the compressional branch cut k_α and the shear wavenumber branch cut k_β in a soft formation, a significant fluid resonance occurs for an SV-wave incidence at

$$\delta = \cos^{-1} \beta/C_T(\omega), \tag{3.35}$$

at which the tube wave wavelength is equal to the vertical wavelength of the incident shear wave. Unlike the fluid resonance in an open borehole (see Chapter 2), in a cased borehole it is prominent at all frequencies and at a large angle of incidence, implying that it is easily observable.

3.4 Cased Borehole Effect on Downhole Hydrophone Measurements

At low frequencies, the pressure in a cased borehole due to a source in the formation has been studied using the quasi-static approach, where explicit and closed form expressions have been derived. However, at high frequencies, no such expressions can be easily obtained. Numerical investigations by the global matrix method are needed to study how the cased borehole can influence a downhole hydrophone measurement. In this and the following sections, calculations are made with the benchmark formations Berea sandstone (fast) and Pierre shale (slow). The casing is steel with a thickness of 2.03 cm. The inner radius of the borehole is 10.16 cm.

3.4.1 Plane P-Wave Incidence

Figure 3-6 shows the pressure at the center of the fluid as a function of angle of incidence at frequencies 100 Hz, 500 Hz, 1000 Hz and 2000 Hz. The incident wave is a plane P-wave. The casing is steel, and the formation is Berea sandstone. The physical parameters are listed on the top of the figure. The pressure is scaled by $P_0 = -\rho\alpha\omega^2$, the normalization factor. Evidently, the pressure in the fluid has a main lobe at the normal incidence $\delta = 90^o$. At low frequencies ($< 500\ Hz$), there exists an angle of incidence where the pressure in the cased borehole is nearly zero. This angle can be well predicted by equation (3.19).

For the soft formation (Pierre shale), as shown in Figure 3-7, the pressure in the fluid shows strong dependence on both frequency and angle of incidence. At low frequencies, it has two lobes at normal incidence and grazing incidence. A minimum occurs at 35°, which is in fair agreement with the angle predicted by equation (3.19). This minimum disappears as frequency increases. It is interesting to note that near normal incidence, the pressure for the soft formation is similar to that for the hard formation. Away from normal incidence, it is strongly dependent on both frequency and angle of incidence.

3.4.2 Plane S-Wave Incidence

Figure 3-8 shows the pressure at the center of the fluid as a function of angle of incidence at frequencies 100 Hz, 500 Hz, 1000 Hz and 2000 Hz for a plane SV-wave incidence. The casing is steel and the formation is Berea sandstone. In this case, the pressure in the fluid shows a main lobe at $\delta \approx 40^o$ and is almost independent of frequency.

For the soft formation and for a plane SV-wave incidence, a significant fluid resonance occurs at $\delta = \cos^{-1}\beta/C_T(\omega) \approx 52.4^o$ (Figure 3-9). Unlike the case with an

open borehole (see Chapter 2), in the steel cased borehole the resonance is at a large angle of incidence and is prominent at very high frequencies. This is because the tube wave velocity is raised well above the formation shear velocity by the steel pipe. The kink at $\delta = 65^o$ and at 2 kHz is associated with the critical reflection of the P-wave at the formation-casing interface.

3.5 Cased Borehole Effect on Downhole Geophone Measurements

This section is devoted to the study of the effect of a cased borehole on downhole geophone measurements. Three aspects are of interest: the borehole reception pattern which illustrates the influence of a fluid-filled borehole on the solid displacement as a function of angle of incidence, the borehole effect on the direction of particle motion which is important for horizontal component rotation from data, and the effect of geophone orientation since, generally, the exact location of a geophone on the borehole wall is unknown in the experiment.

3.5.1 Borehole Reception Pattern

The *borehole reception pattern*, as is defined in Chapter 2, is the dependence of pressure in the fluid and solid displacement in the formation on angle of incidence. Calculations in the following examples are made with a geophone at the forward direction ($r = r_b, \theta = 0^o$).

A Plane P-Wave Incidence

Figure 3-10a shows the borehole reception pattern for the radial component of solid displacement at the borehole wall. The incident wave is a plane P-wave. The for-

mation is Berea sandstone (hard). As expected, the radial component is zero at grazing incidence and maximum at normal incidence. It increases with the increase of frequency, especially at normal incidence.

Figure 3-10b shows the borehole reception pattern for the vertical component of solid displacement at the borehole wall. Obviously, the vertical component is zero at normal incidence and posseses a lobe at grazing incidence. Unexpectedly, it decreases with the increase of frequency, especially at grazing incidence.

Figure 3-11a shows the borehole reception pattern for the radial component of solid displacement at the borehole wall when the formation is Pierre shale. Unlike Figure 3-10a, in this example the radial component increases with the increase of frequency up to 1 kHz. Beyond 1 kHz, it decreases, especially at normal incidence.

Figure 3-11b shows the borehole reception pattern for the vertical component of solid displacement at the borehole wall in the same formation Pierre shale. Obviously, the low frequency behavior is the same as that shown in Figure 3-10b. However, at high frequencies, the vertical component of solid displacement becomes significantly smaller than the incident wave, decreasing with the increase of frequency. The transition zone in terms of angle of incidence is in between the critical P-S refraction and P-P refraction at the casing-formation interface.

A Plane S-Wave Incidence

For a hard formation and a plane SV-wave incidence, at low frequencies the reception pattern for the radial component of solid displacement has a lobe at grazing incidence (Figure 3-12a), while the reception pattern for the vertical component of solid displacement exhibits a lobe at normal incidence (Figure 3-12b). Increase of frequency will increase the radial component of solid displacement, especially at grazing incidence. The vertical component shows little dependence on frequency.

For a soft formation and a plane SV-wave incidence, the solid displacement on the borehole wall is also strongly affected by the excitation of the tube wave in the fluid. Away from the resonance angle, at low frequencies, the borehole reception patterns are similar to those for the hard formation. Figures 3-13a and 3-13b show the radial and vertical components of solid displacement at the borehole wall in Pierre shale. The arrows mark the place where the fluid resonance occurs. Evidently, the impact of the tube wave is strong on the vertical component at low frequencies. However, at high frequencies, its influence on the radial component becomes significant. At high frequencies and away from the fluid resonance regime, the radial and vertical components of solid displacement both decrease rapidly with the increase of frequency. The solid displacement on the borehole wall is significantly less than the incident wave.

3.5.2 Borehole Effect on Particle Motion

The borehole distorts not only the amplitude of solid displacement on the borehole wall but also its polarization, including the direction of particle motion and the rectilinearity (Esmersoy, 1984; Peng et al., 1990). We are interested in the deviation of particle motion direction of the geophone measurement from that of the incident wave. The following examples show, in polar coordinates, the solid displacement vector on the borehole wall for plane P-wave and SV-wave incidences. Calculations are made at location ($r = r_b, \theta = 0°$), i.e., in the forward scattering direction.

A Plane P-Wave Incidence

Figure 3-14 shows the solid displacement on the borehole wall for an incident plane P-wave. The formation is Berea sandstone (hard) and the casing is steel. Shown in the figure is the displacement vector as a function of angle of incidence for frequencies of 100 Hz, 500 Hz, 1000 Hz and 2000 Hz. The dashed lines radiating from the origin are the directions of the incident plane P-waves. The angle of incidence is labeled

along the circle. Since the P-wave is polarized along the direction of propagation, the dashed lines also represent the polarization directions of the incident energies. The displacement vector on the borehole wall, which is the output of a downhole geophone, is represented by a solid arrow. Its length is the amplitude of the displacement vector, and its direction is the particle motion direction. The deviation of the arrow from the corresponding dashed line is the inclination deviation of a 3-component geophone measurement from that of the incident wave in the presence of a cased borehole. Apparently, the borehole effect on particle motion is minimal for a frequency below 1 kHz for the hard formation. At 2 kHz, noticeable inclination deviation can be found around 40° incidence. Also, in this case, the amplitude of solid displacement is smaller than unity at grazing incidence, while at normal incidence measurement is less affected by the cased borehole.

For the soft formation (Pierre shale), as shown in Figure 3-15, the effect of the cased borehole on downhole geophone measurement is more prominent except at very low frequencies ($\sim$ 100 Hz). For a frequency above 500 Hz, significant deviations in both the amplitude and the particle motion direction are obvious. The inclination deviation can reach 25° around $\delta = 45°$ at 2 kHz. The solid displacement, in amplitude, is significantly smaller than the incident wave, especially at grazing incidence and at 2 kHz. Since the geophone is at $\theta = 0°$, i.e., the forward scattering direction where the borehole scattered energy is out of phase with the incident wave, the behavior shown in this figure is not unexpected at all.

A Plane S-Wave Incidence

Unlike a plane P-wave, an S-wave is polarized perpendicular to the incidence direction in an isotropic medium. For graphic presentation, we rotate the polarization direction by 90° so that it is in line with the direction of incidence. Figure 3-16 shows the solid displacement on the borehole wall for a plane SV-wave incidence at 100 Hz, 500 Hz, 1000 Hz and 2000 Hz. The formation is Berea sandstone (hard). In this figure,

the dashed lines are the ray direction of the incident plane SV-wave; the arrows are the displacement vectors at the solid side of the borehole wall after a 90° rotation. It is obvious that the deviation of the arrow from the corresponding dashed line also represents the inclination deviation of measured particle motion direction from that of the incident wave. As evident from the figure, in the hard formation the borehole effect on particle motion is small for frequencies below 1 kHz. At 2 kHz, a large inclination deviation by as much as 12° can be found around the 40° incidence. Unlike the case of the P-wave, at high frequencies the amplitude tends to be larger than unity at grazing incidence and smaller than unity at normal incidence.

Figure 3-17 shows the solid displacement on the borehole wall for the soft formation (Pierre shale) and for a plane SV-wave incidence. In this case, the solid displacement is significantly smaller than the incident wave, even at low frequencies. This is because the geophone is in the shadow zone of the fluid-filled borehole. Calculations show that, if the geophone is at the backward scattering direction, i.e., $\theta = 180°$, the amplitude of solid displacement is much larger than that with $\theta = 0°$. The deviation of particle motion direction is significant, reaching 70° for frequencies above 1 kHz except at normal and grazing incidences.

3.5.3 Effect of Geophone Orientation

Borehole coupling is nonsymmetric. Measurements are dependent on the position of a geophone on the borehole wall, but this position is generally unknown in field surveys. The following examples study the variations of the solid displacement as the geophone moves azimuthally around the borehole wall.

A Plane P-Wave Incidence

Figure 3-18 shows the solid displacement on the borehole wall as a function of the azimuthal orientation of the geophone. The formation is hard (Berea sandstone).

The incident wave is a plane P-wave at a fixed angle of incidence $\delta = 45^o$. The frequency of the incident wave is 1 kHz. Five plots are shown here: the middle one is a 3-D presentation of the borehole deformation when a plane P-wave impinges on the cased borehole; the one in the upper-left corner shows the magnitude of the solid displacement as a function of geophone orientation; the upper-right one shows the polarization characteristics – rectilinearity – as a function of the geophone orientation (see Chapter 2, also Esmersoy, 1984); the lower-left and lower-right ones show the azimuthal and inclination deviations between the solid displacement and the incident wave, respectively. For the hard formation at 1 kHz, the geophone measurement is almost identical with the incident wave, and the azimuthal deviation is negligible. The inclination deviation is less than 2^o. The solid motion is predominantly linear.

When it comes to the soft formation, the story is quite different. Figure 3-19 shows the solid displacement on the borehole wall as a function of the geophone orientation for the soft formation Pierre shale. Again, the incident wave is a plane P-wave at a fixed angle of incidence $\delta = 45^o$. In this case, obviously, the solid displacement vector deflects horizontally. The deviation in inclination reaches 26^o to 30^o depending on the exact location of the geophone. The polarization in the forward scattering direction becomes elliptic with rectilinearity 0.65 at $\theta = 0^o$, while in the backward scattering direction, the particle motion is linear. It is interesting to note that, while the inclination deviation is significant, the azimuthal deviation is small.

A Plane S-Wave Incidence

Figure 3-20 shows the solid displacement on the borehole wall as a function of the azimuthal orientation of the geophone for the hard formation at 1 kHz. The incident wave is a plane SV-wave at a fixed angle of incidence $\delta = 45^o$. In this case, the solid motion is linear and perpendicular to the direction of incidence. The maximum inclination deviation is about 4^o in the forward scattering direction. The borehole distortion of the geophone measurement is minimal.

Figure 3-21 shows the solid displacement on the borehole wall for a plane SV-incidence at 1 kHz. The formation is Pierre shale (soft). Like the case of P-wave incidence, the solid motion is predominantly horizontal. The inclination deviation reaches more than 32^o. Unlike the previous examples, the azimuthal deviation is also significant in this case. It is about 21^o at $\theta = 90^o$ where the solid motion is no longer linear (see the drop in rectilinearity in the upper-right plot). The amplitude of solid displacement is much smaller in the forward scattering direction than in the backward scattering direction.

3.6 Discussions and Conclusions

In this paper, approximate and exact formulations have been given for borehole coupling in a cased well. The approximate solutions are simple, explicit, and accurate at low frequencies, and are applicable to both cased and open boreholes. They tend to yield more physical insights into the coupling of an incident elastic wave into the borehole fluid than the numerical results. The approximate solutions can be applied to study cased borehole radiation as well, using the reciprocity principle. More precisely, the amplitude of P-wave radiation at a large distance due to a unit amplitude pressure source in the fluid, for example, is equal to the pressure in the fluid due to a unit amplitude plane P-wave incidence upon the cased borehole. This statement is justified by a comparison with the generalized stationary phase approximation for a volume source in the cased borehole (Gibson, 1993). Winbow (1991) gave an explicit low frequency formulation for the cased borehole radiation problem, and his formulation was accurate in the direction normal to the borehole axis (Gibson and Peng, 1993).

On the other hand, the exact solution is valid for all frequency and azimuthally symmetric and nonsymmetric components. It can handle many radial layers such as casing and cements. It is useful to study numerically the dependence of downhole

seismic measurements on frequency, angle of incidence, polarization of incident wave, and geophone orientation.

In summary, we come to the following conclusions:

- For the hard formation and plane P-wave incidence, the effect of the cased borehole on downhole geophone measurements is minimal for frequencies below 1 kHz. Above 1 kHz, the radial component is larger in amplitude than that of the incident wave, and the vertical component is smaller. The deviation of particle motion direction can reach several degrees at 2 kHz.

- For the hard formation and plane SV-wave incidence, downhole geophone measurements are not affected by the presence of a fluid-filled borehole for frequencies below 1 kHz. Above 1 kHz, the radial component increases with the increase of frequency, while the vertical component is less dependent on frequency. The particle motion direction may differ from that of the incident wave by as much as 12^o at 2 kHz.

- For the soft formation and plane P-wave incidence, the cased borehole effect on downhole geophone measurements is significant for frequencies above several hundred hertz ($>$ 500 Hz). The radial and vertical components are much smaller than those of the incident wave at high frequencies. The inclination deviation can reach 25^o at $\delta = 45^o$ at 2 kHz. The solid displacement vector deflects horizontally. The measurements also show strong dependence on geophone orientation. The polarization becomes elliptic in the forward scattering direction and remains linear in the backward scattering direction.

- For the soft formation and plane SV-wave incidence, the fluid resonance inside the borehole at $\delta = \cos^{-1} \beta/C_T$ exerts strong influence on the solid displacement at the borehole wall, even at very low frequencies. Away from the resonance angle, the radial and vertical components of solid displacement decrease rapidly with the increase of frequency. The deviation of particle motion direction from

that of the incident wave is large. It reaches 70° at 2 kHz. The solid motion becomes predominantly horizontal at high frequencies. The azimuthal deviation is also significant, reaching 21° at $\theta = 90°$ at 1 kHz.

- The pressure in the fluid shows two interesting phenomena, depending on the type of the incident wave. For plane SV-wave incidence in the soft formation, a significant fluid resonance occurs in the borehole where the pressure can be large. This phenomenon is prominent at all frequencies and is associated with the excitation of the tube wave in the fluid. For plane P-wave incidence at low frequencies, the pressure in the fluid vanishes at a particular angle of incidence if the casing thickness exceeds a critical value, a phenomenon referred to as the cased borehole screening effect. This behavior prevails in both the hard and the soft formations. The critical angles for both the fluid resonance and the screening effect can be well predicted by the simple and explicit relations in equation (3.19) and equation (3.35).

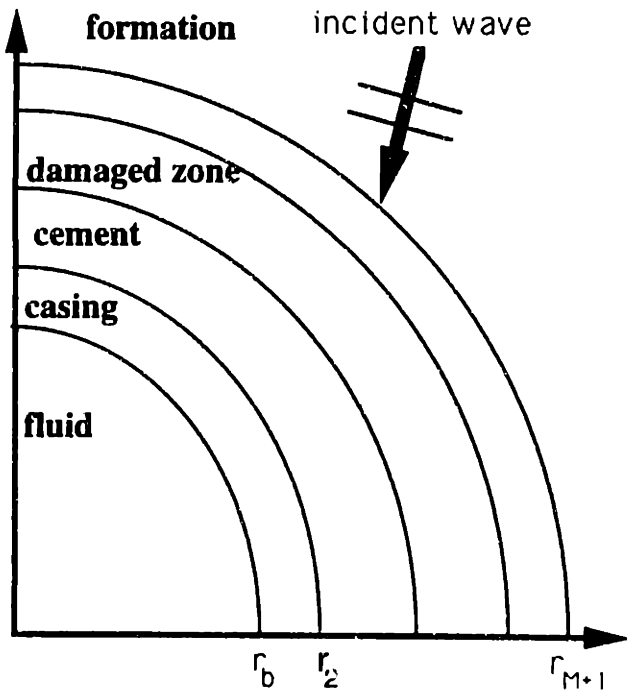

Figure 3-1: A fluid-filled borehole in a radially layered formation. An elastic wave impinges on the cased and cemented borehole with an angle of incidence δ (with respect to the borehole axis which is perpendicular to the plane). A hydrophone measures pressure at the center of the borehole. A geophone measures the three component displacement at $(r = r_b, \theta)$, where r_b is the borehole radius and θ is the azimuthal angle with respect to the incident wave. The direction with $-90^o \leq \theta < 90^o$ is referred to as the forward scattering direction and $90^o \leq \theta < 270^o$ as the backward scattering direction.

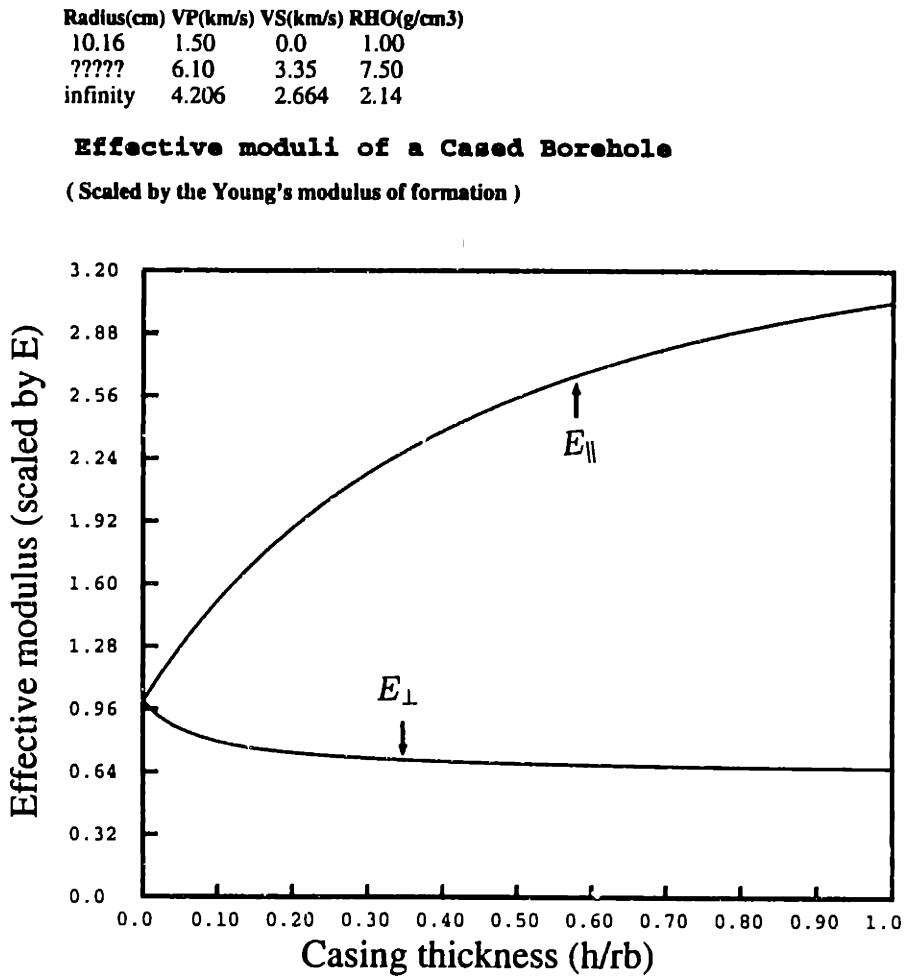

Figure 3-2: Effective moduli (scaled by E, the Young's modulus of formation) of a cased borehole as a function of casing thickness. The formation is Berea sandstone (hard). The casing is steel. The upward arrow points to $E_{\|}$, the effective modulus against horizontal deformation. The downward arrow points to $E_{\perp}$, the effective modulus against vertical deformation.

Radius(cm)	VP(km/s)	VS(km/s)	RHO(g/cm3)
10.16	1.50	0.0	1.00
?????	6.10	3.35	7.50
infinity	2.074	0.869	2.00

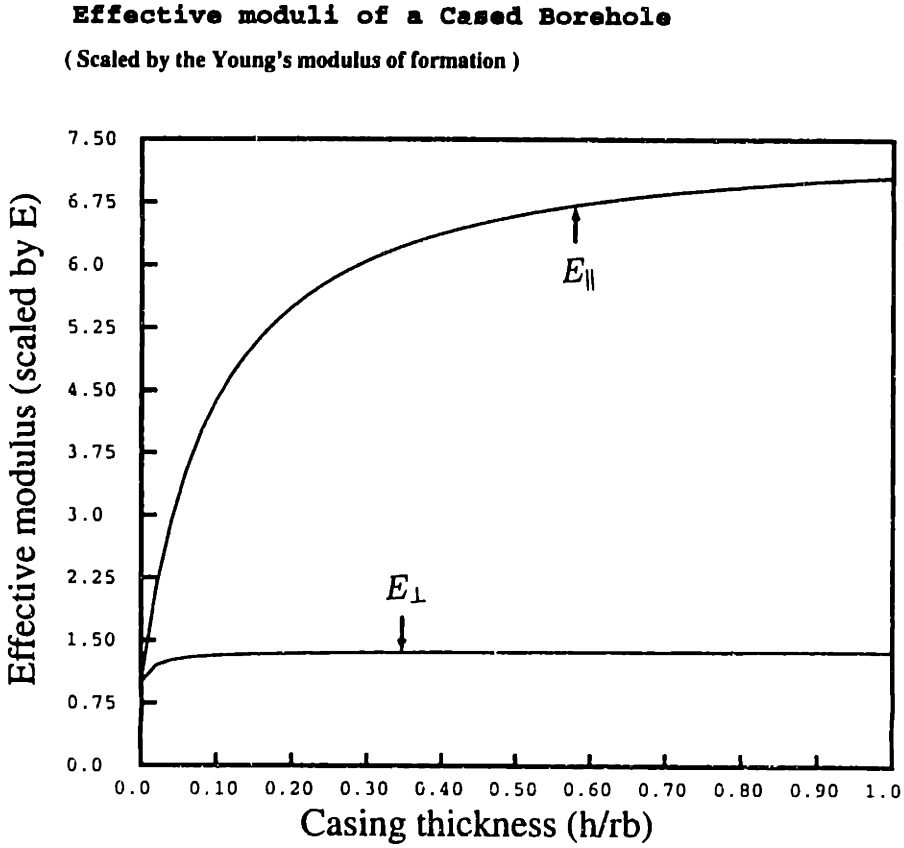

Figure 3-3: Effective moduli (scaled by E, the Young's modulus of formation) of a cased borehole as a function of casing thickness. The formation is Pierre shale (soft). The casing is steel. The upward arrow points to $E_{\|}$, the effective modulus against horizontal deformation. The downward arrow points to $E_{\perp}$, the effective modulus against vertical deformation.

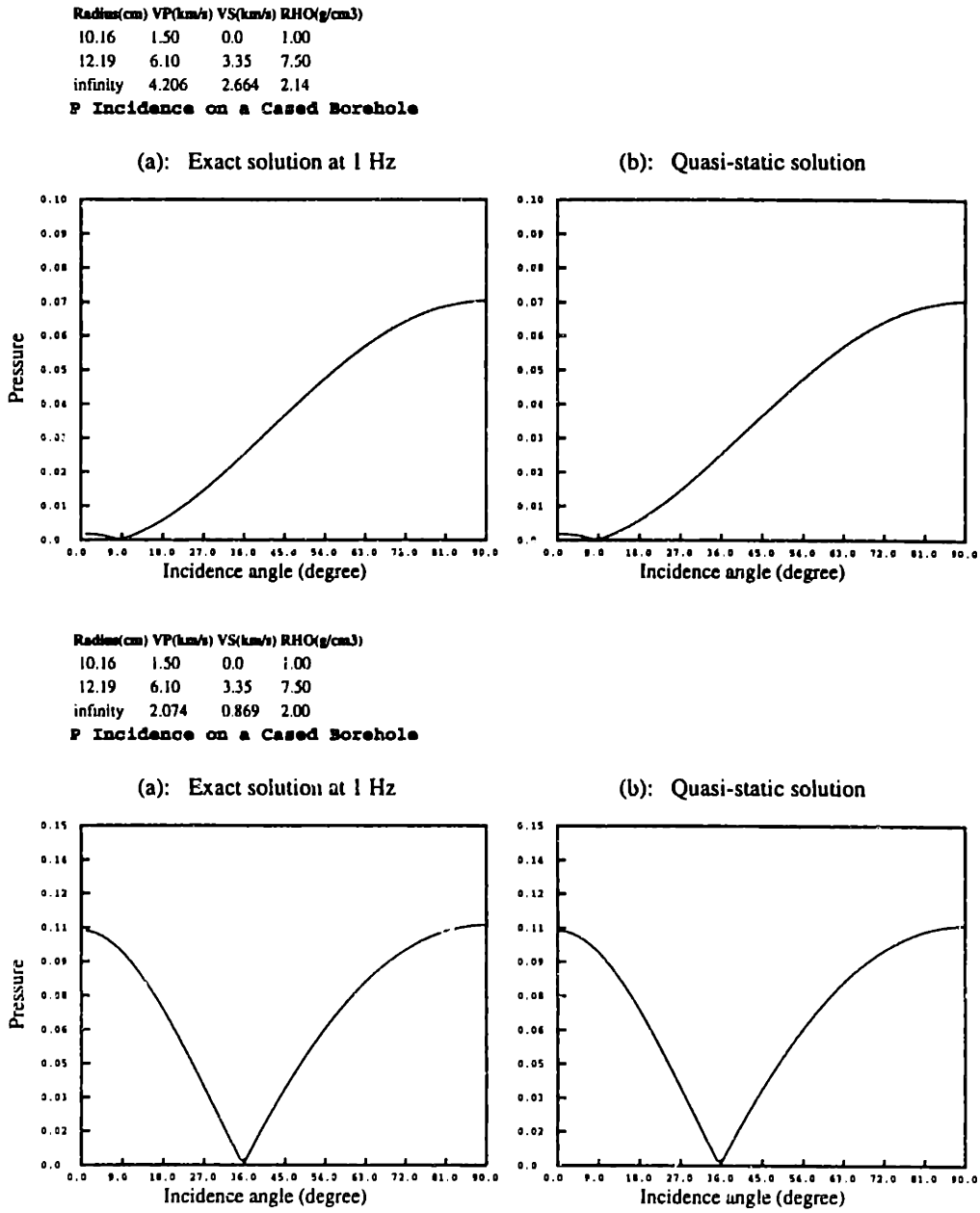

Figure 3-4: Comparison between the exact solution (left panel) and the quasi-static approximation (right panel). The formation is Berea sandstone (top) or Pierre shale (bottom). The incident wave is a plane P-wave. The exact solution is computed by the global matrix method at 1 Hz.

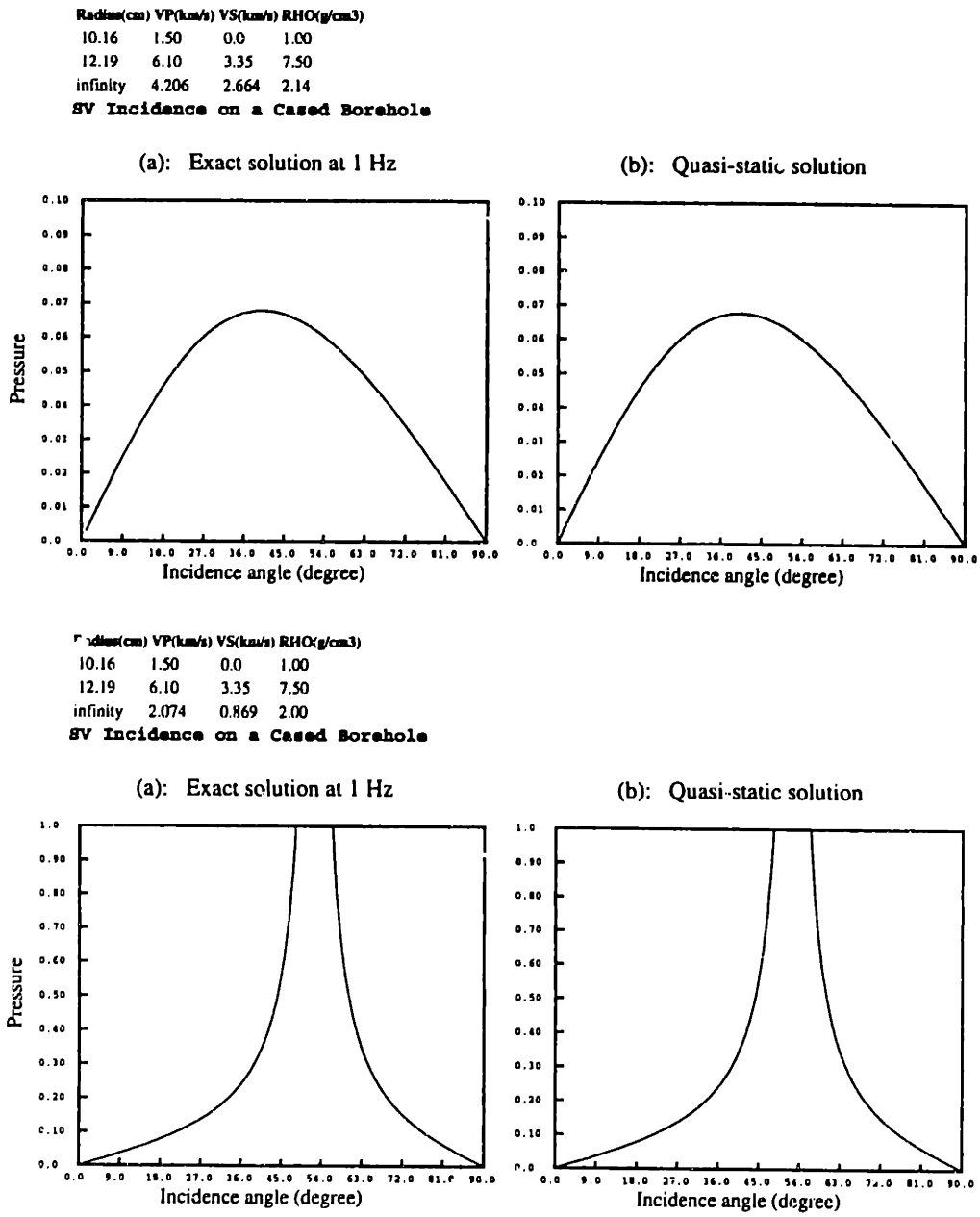

Figure 3-5: Comparison between the exact solution (left panel) and the quasi-static approximation (right panel). The formation is Berea sandstone (top) or Pierre shale (bottom). The incident wave is a plane SV-wave. The exact solution is computed by the global matrix method at 1 Hz.

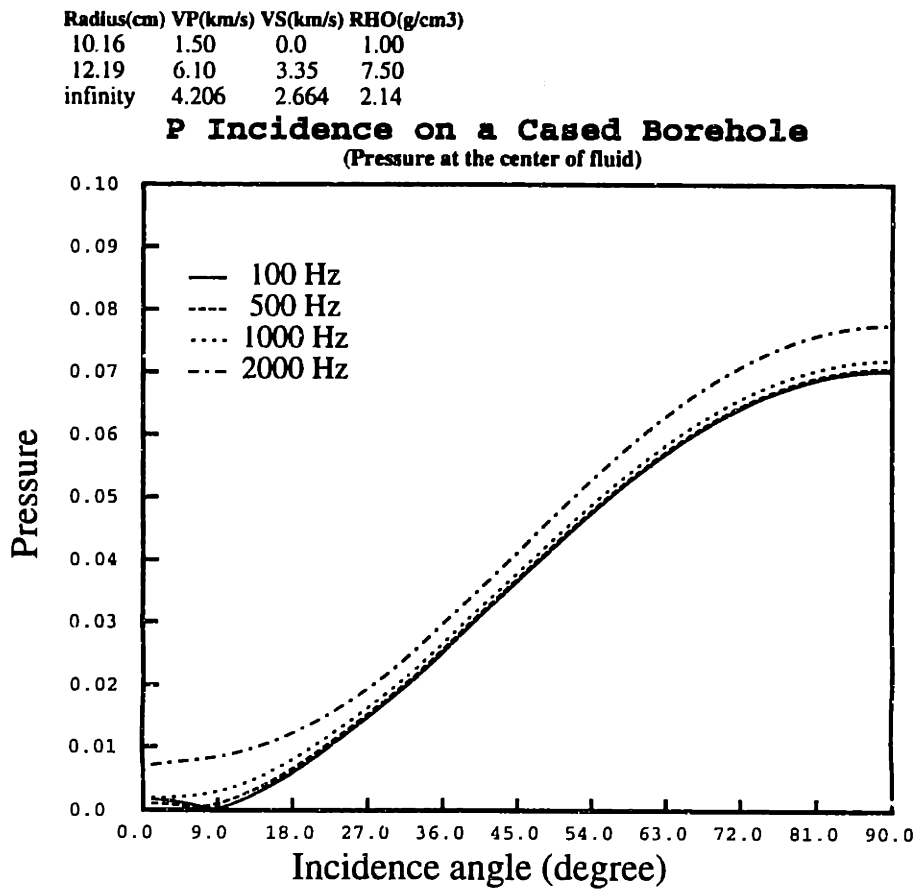

Figure 3-6: Pressure in a cased borehole as a function of angle of incidence. The formation is Berea sandstone (hard). The incident wave is a plane P-wave. Calculations are made at frequencies 100 Hz, 500 Hz, 1000 Hz, and 2000 Hz.

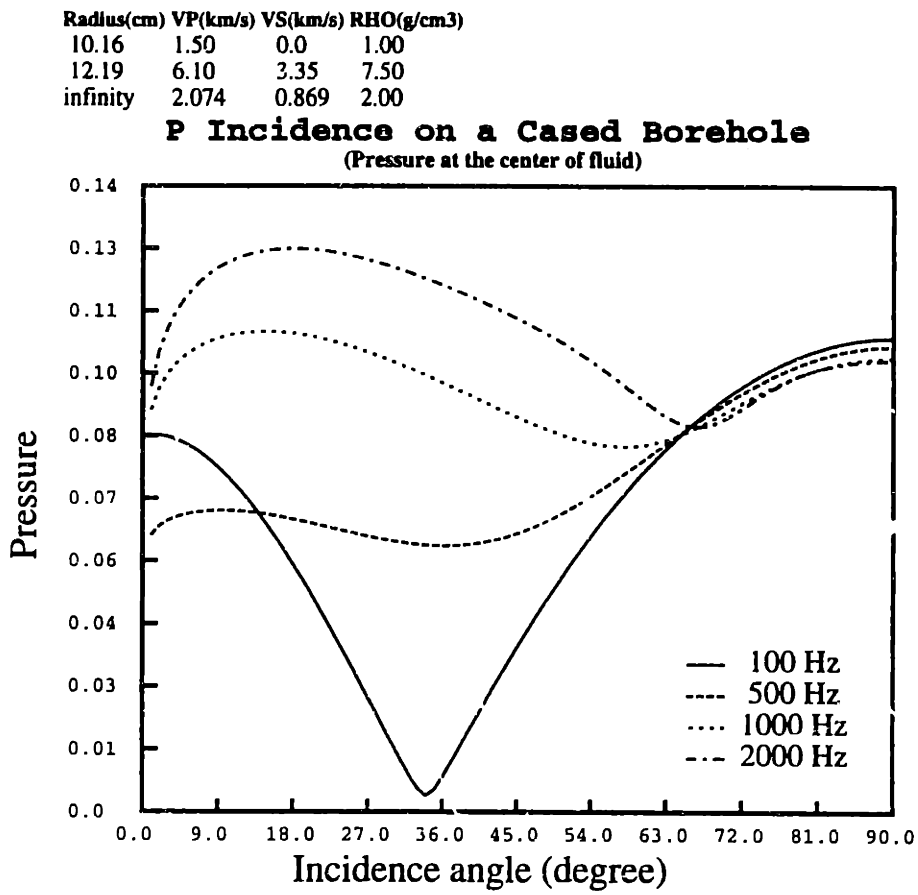

Figure 3-7: Pressure in a cased borehole as a function of angle of incidence. The formation is Pierre shale (soft). The incident wave is a plane P-wave. Calculations are made at frequencies 100 Hz, 500 Hz, 1000 Hz, and 2000 Hz.

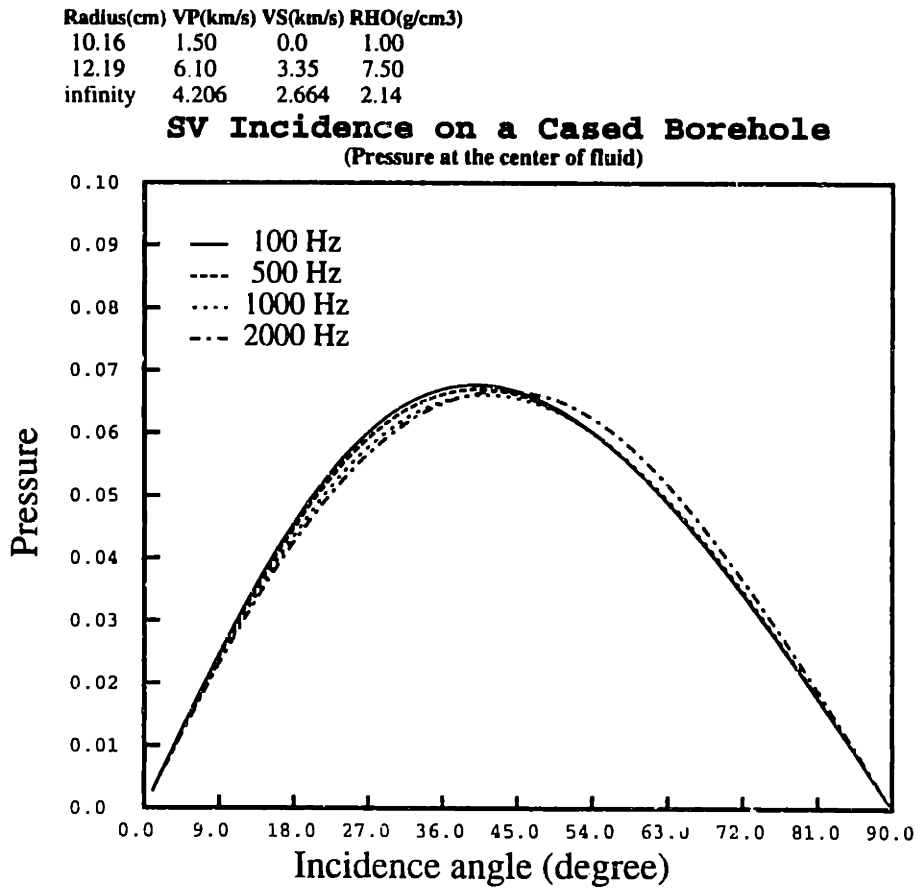

Figure 3-8: Pressure in a cased borehole as a function of angle of incidence. The formation is Berea sandstone (hard). The incident wave is a plane SV-wave. Calculations are made at frequencies 100 Hz, 500 Hz, 1000 Hz, and 2000 Hz.

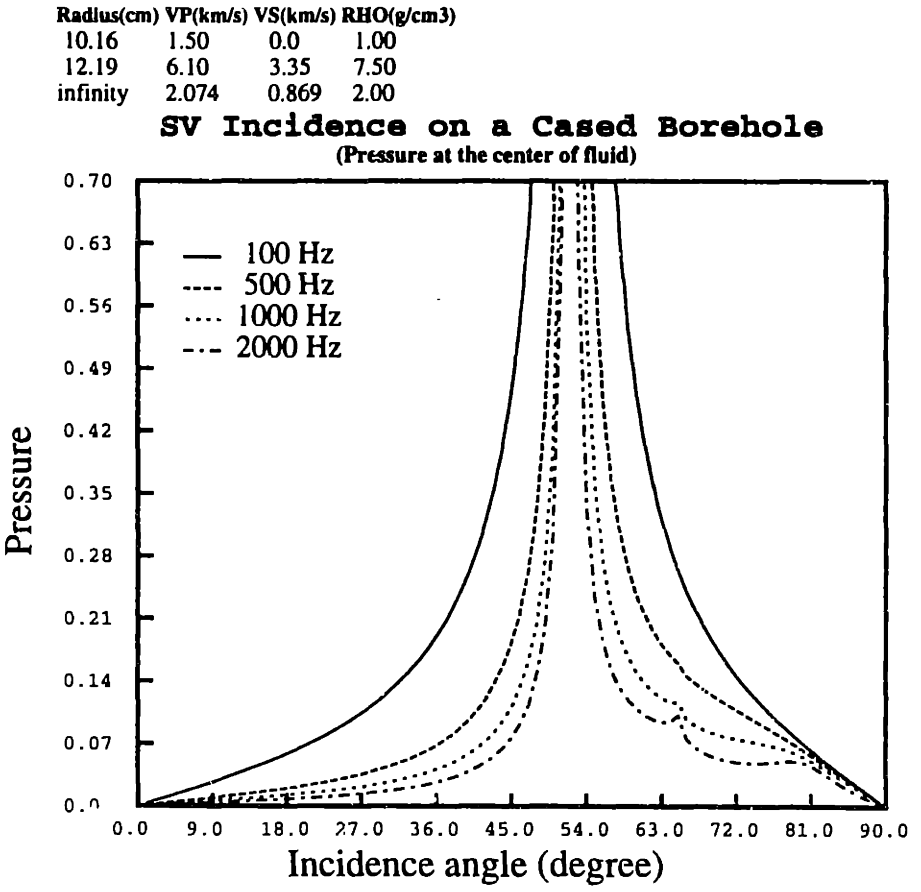

Figure 3-9: Pressure in a cased borehole as a function of angle of incidence. The formation is Pierre shale (soft). The incident wave is a plane SV-wave. Calculations are made at frequencies 100 Hz, 500 Hz, 1000 Hz, and 2000 Hz.

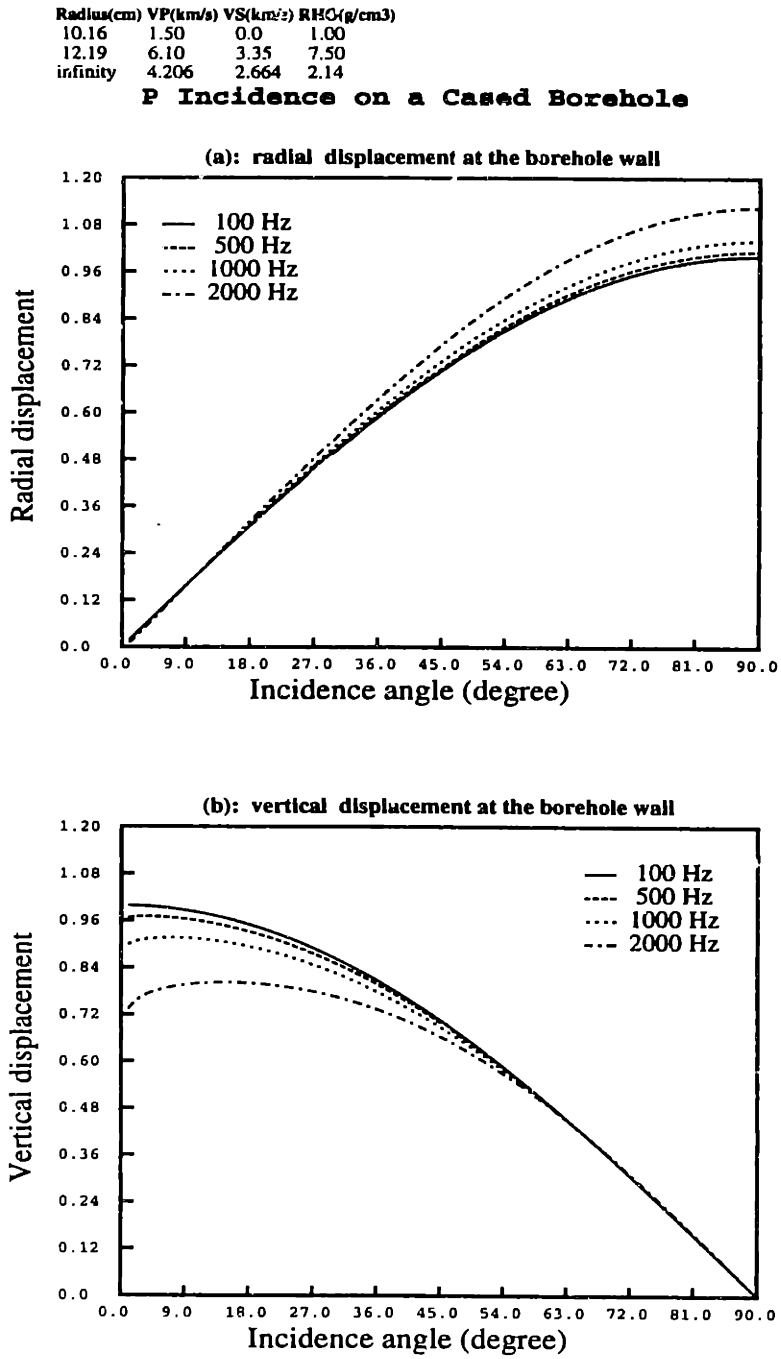

Figure 3-10: (a) Radial component of solid displacement on the borehole wall, and (b) Vertical component of solid displacement on the borehole wall. The incident wave is a plane P-wave. The formation is Berea sandstone (hard). Calculations are made at frequencies 100 Hz, 500 Hz, 1000 Hz, and 2000 Hz.

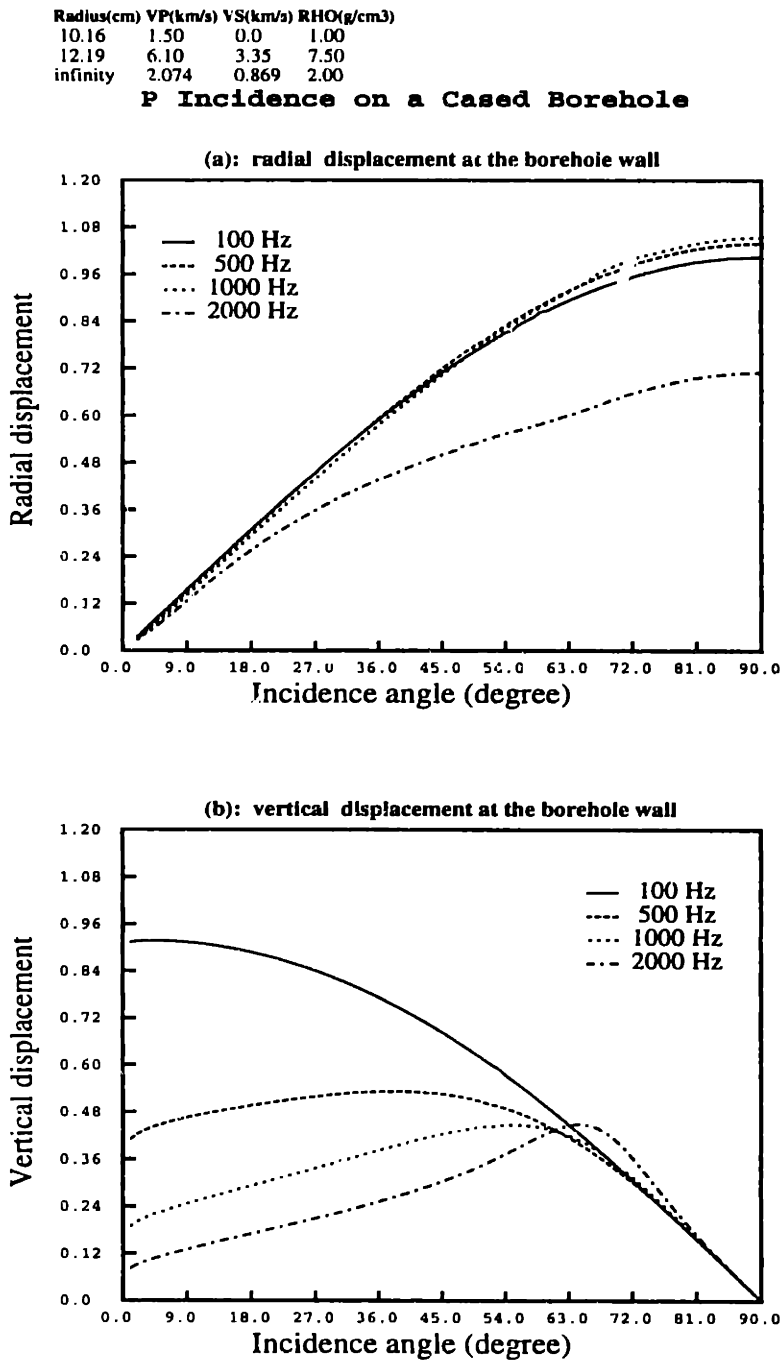

Figure 3-11: (a) Radial component of solid displacement on the borehole wall, and (b) Vertical component of solid displacement on the borehole wall. The incident wave is a plane P-wave. The formation is Pierre shale (soft). Calculations are made at frequencies 100 Hz, 500 Hz, 1000 Hz, and 2000 Hz.

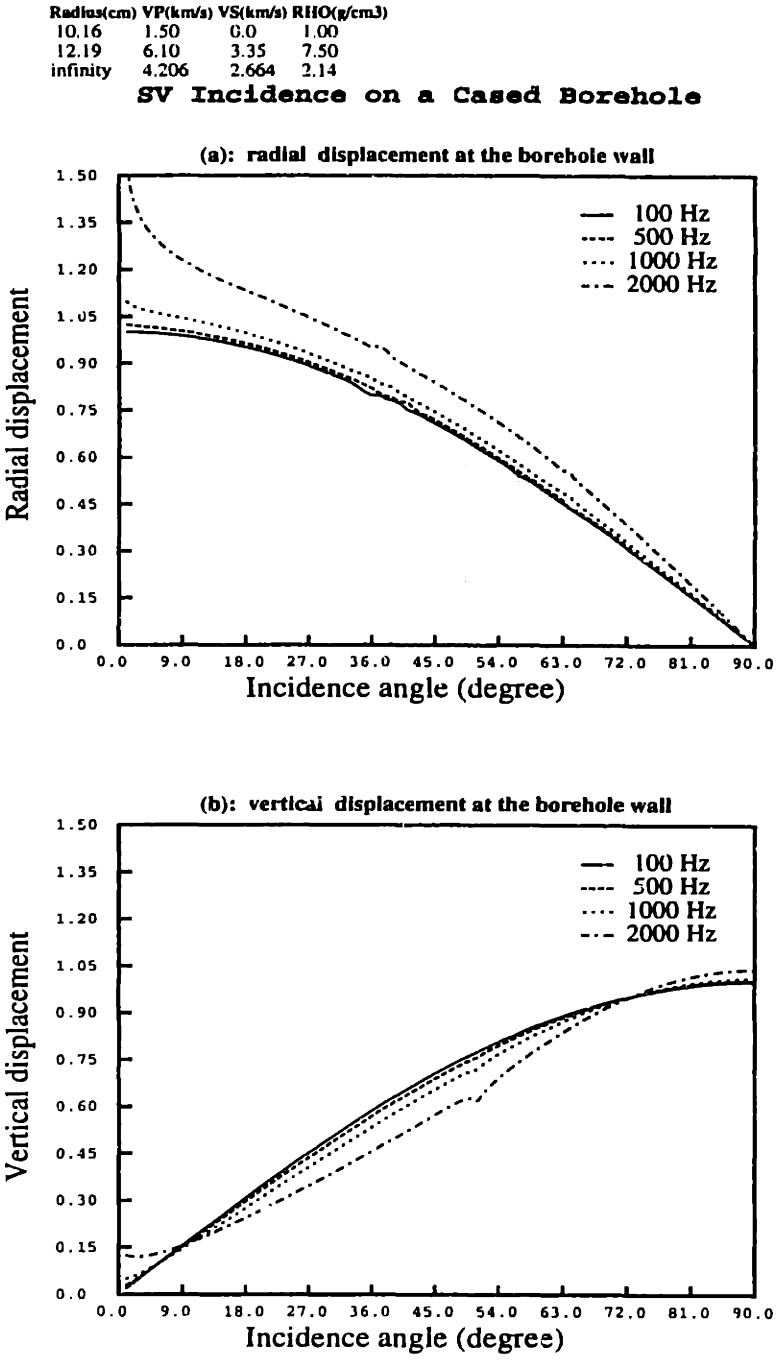

Figure 3-12: (a) Radial component of solid displacement on the borehole wall, and (b) Vertical component of solid displacement on the borehole wall. The incident wave is a plane SV-wave. The formation is Berea sandstone (hard). Calculations are made at frequencies 100 Hz, 500 Hz, 1000 Hz, and 2000 Hz.

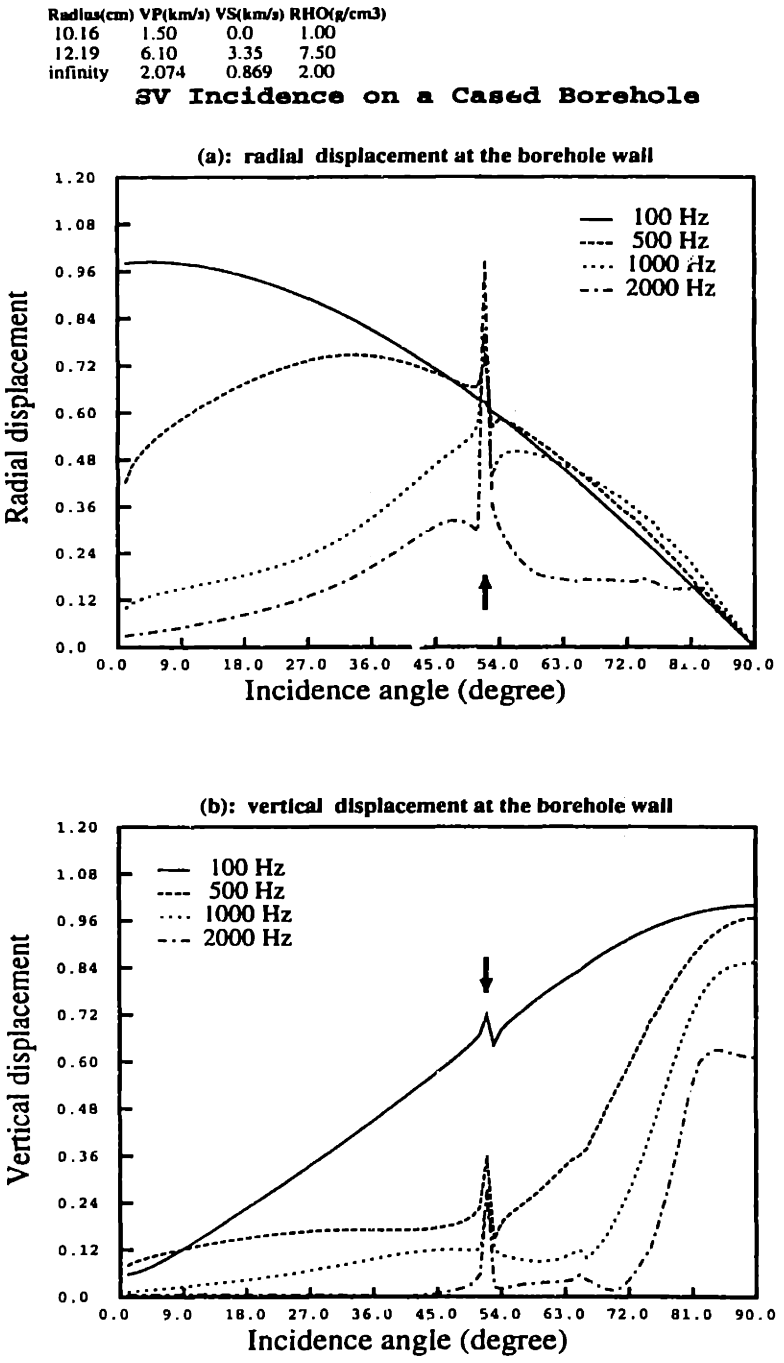

Figure 3-13: (a) Radial component of solid displacement on the borehole wall, and (b) Vertical component of solid displacement on the borehole wall. The incident wave is a plane SV-wave. The formation is Pierre shale (soft). Calculations are made at frequencies 100 Hz, 500 Hz, 1000 Hz, and 2000 Hz.

Radius(cm)	VP(km/s)	VS(km/s)	RHO(g/cm3)
10.16	1.50	0.0	1.00
12.19	6.10	3.35	7.50
infinity	4.206	2.664	2.14

P Incidence on a Cased Borehole

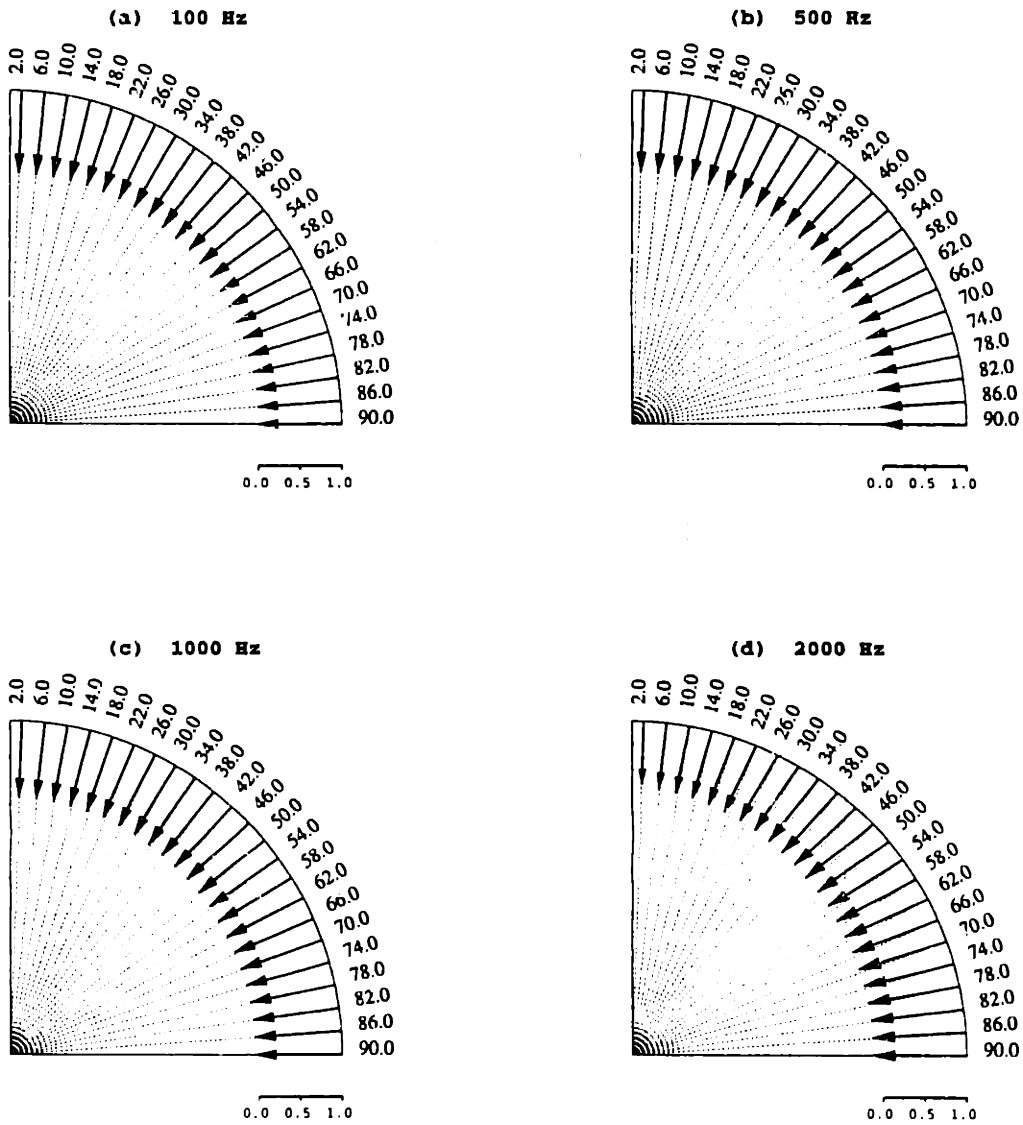

Figure 3-14: Particle motion on the borehole wall as a function of angle of incidence. The incident wave is a plane P-wave. The formation is Berea sandstone (hard). Calculations are made at frequencies 100 Hz, 500 Hz, 1000 Hz, and 2000 Hz. The dashed lines are directions of incidence whose incident angles are labeled along the circle. The solid arrow represents the particle motion vector.

Radius(cm)	VP(km/s)	VS(km/s)	RHO(g/cm3)
10.16	1.50	0.0	1.00
12.19	6.10	3.35	7.50
infinity	2.074	0.869	2.00

P Incidence on a Cased Borehole

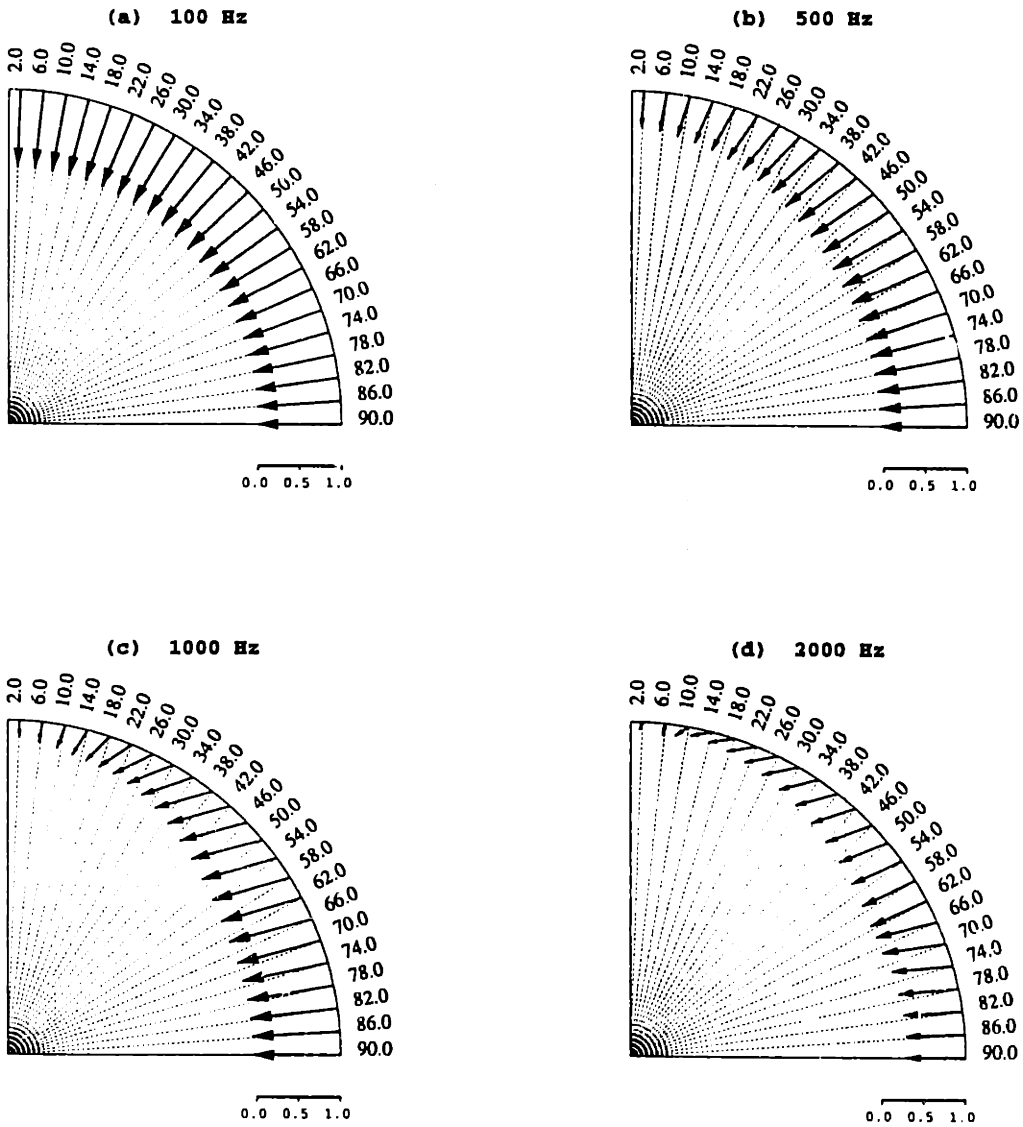

Figure 3-15: Particle motion on the borehole wall as a function of angle of incidence. The incident wave is a plane P-wave. The formation is Pierre shale (soft). Calculations are made at frequencies 100 Hz, 500 Hz, 1000 Hz, and 2000 Hz. The dashed lines are directions of incidence whose incident angles are labeled along the circle. The solid arrow represents the particle motion vector.

Radius(cm)	VP(km/s)	VS(km/s)	RHO(g/cm3)
10.16	1.50	0.0	1.00
12.19	6.10	3.35	7.50
infinity	4.206	2.664	2.14

SV Incidence on a Cased Borehole

(90 degree rotation applied)

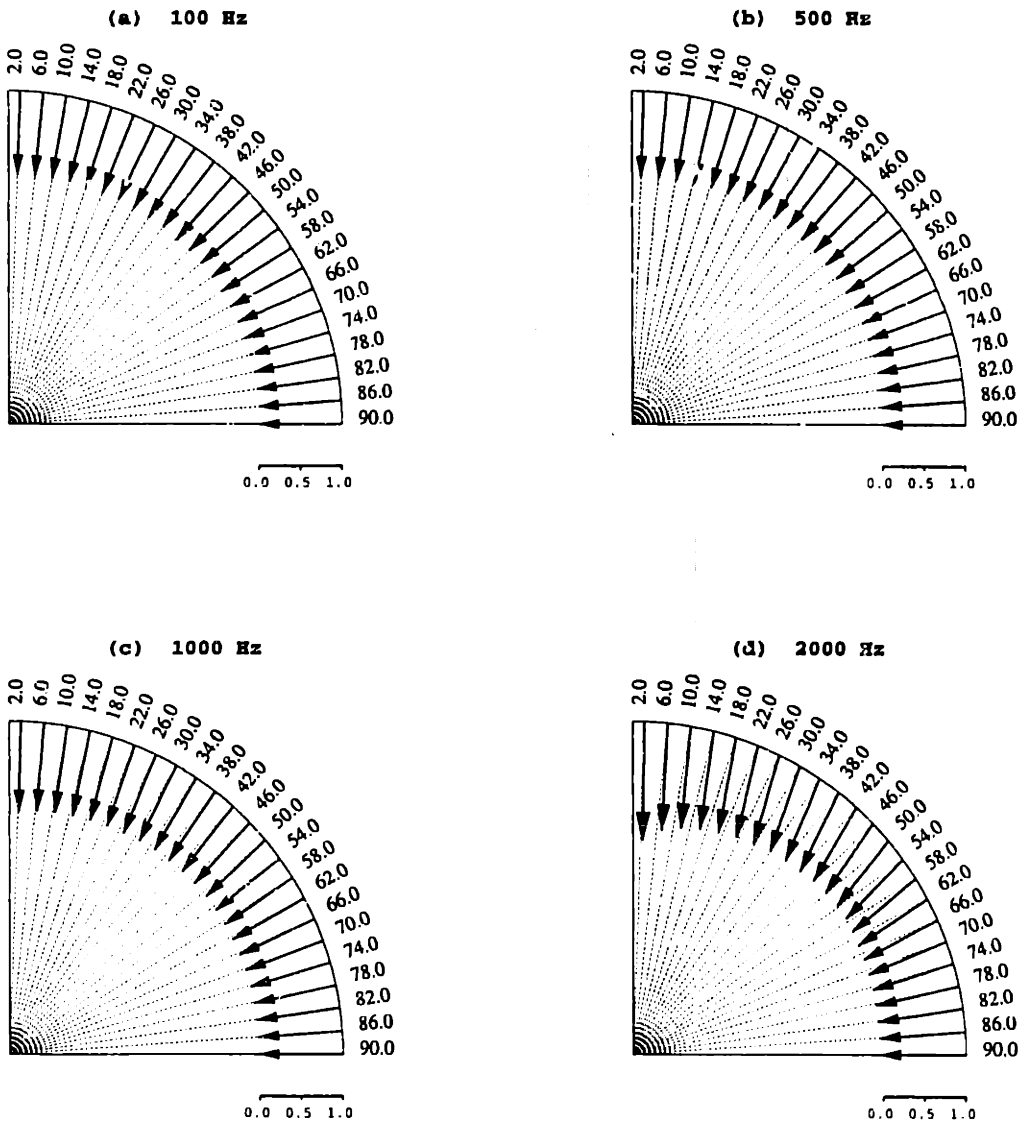

Figure 3-16: Particle motion on the borehole wall as a function of angle of incidence. The incident wave is a plane SV-wave. The formation is Berea sandstone (hard). Calculations are made at frequencies 100 Hz, 500 Hz, 1000 Hz, and 2000 Hz. The dashed lines are directions of incidence whose incident angles are labeled along the circle. The solid arrow represents the particle motion vector after a 90° rotation.

Radius(cm)	VP(km/s)	VS(km/s)	RHO(g/cm3)
10.16	1.50	0.0	1.00
12.19	6.10	3.35	7.50
infinity	2.074	0.869	2.00

SV Incidence on a Cased Borehole

(90 degree rotation applied)

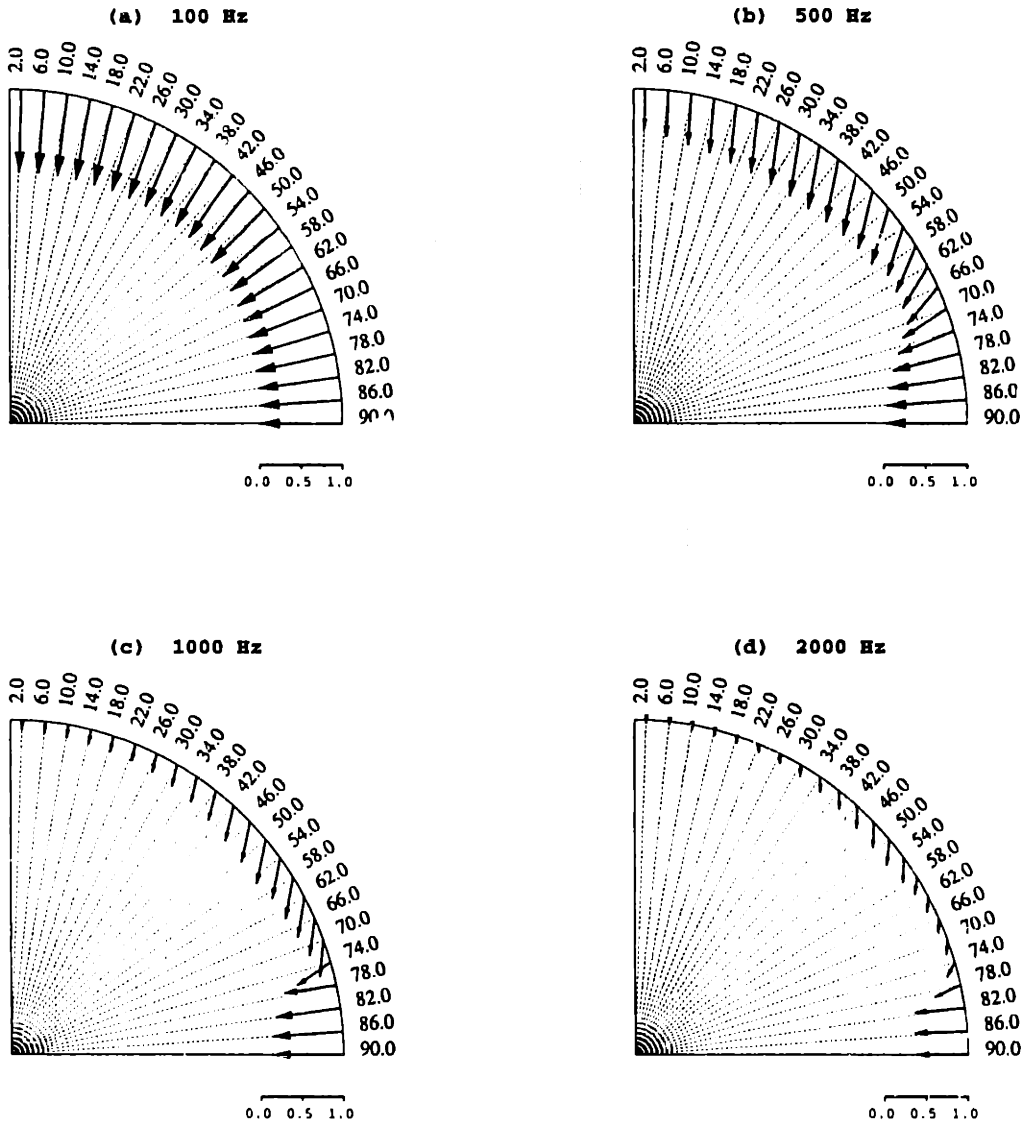

Figure 3-17: Particle motion on the borehole wall as a function of angle of incidence. The incident wave is a plane SV-wave. The formation is Pierre shale (soft). Calculations are made at frequencies 100 Hz, 500 Hz, 1000 Hz, and 2000 Hz. The dashed lines are directions of incidence whose incident angles are labeled along the circle. The solid arrow represents the particle motion vector after a 90° rotation.

Radius(cm)	VP(km/s)	VS(km/s)	RHO(g/cm3)
10.16	1.50	0.0	1.00
12.19	6.10	3.35	7.50
infinity	4.206	2.664	2.14

Frequency: 1000 Hz, P incidence at: 45 degree

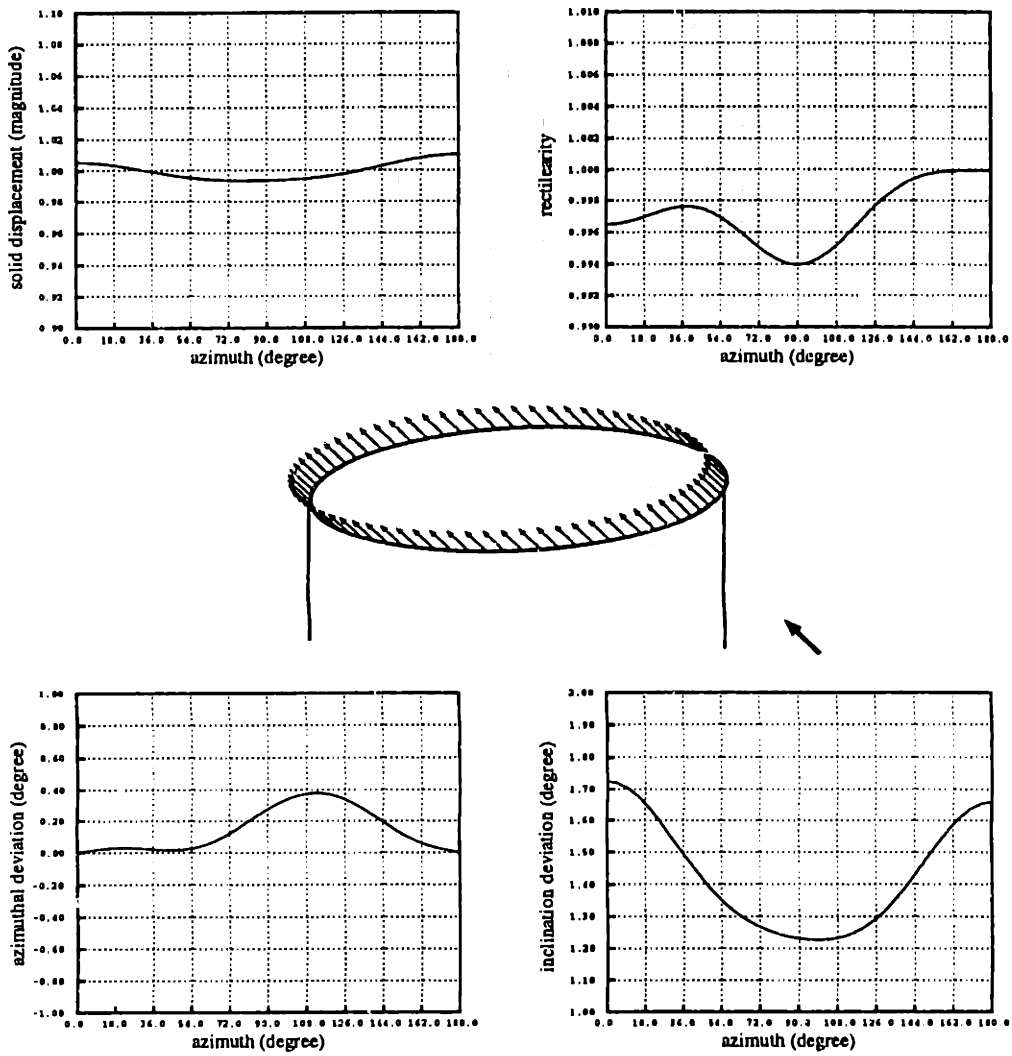

Figure 3-18: Solid displacement on the borehole wall as a function of azimuthal orientation of the geophone. The incident wave is a P-wave. The formation is Berea sandstone (hard). The calculation is made with $\delta = 45°$ and frequency 1000 Hz. The upper-left panel shows the magnitude of the solid displacement vector. The upper-right panel is rectilinearity. The lower-left and lower-right panels are the deviations in azimuth and inclination between the solid displacement on the borehole wall and the incident wave, respectively.

Radius(cm)	VP(km/s)	VS(km/s)	RHO(g/cm3)
10.16	1.50	0.0	1.00
12.19	6.10	3.35	7.50
infinity	2.074	0.869	2.00

Frequency: 1000 Hz, P incidence at: 45 degree

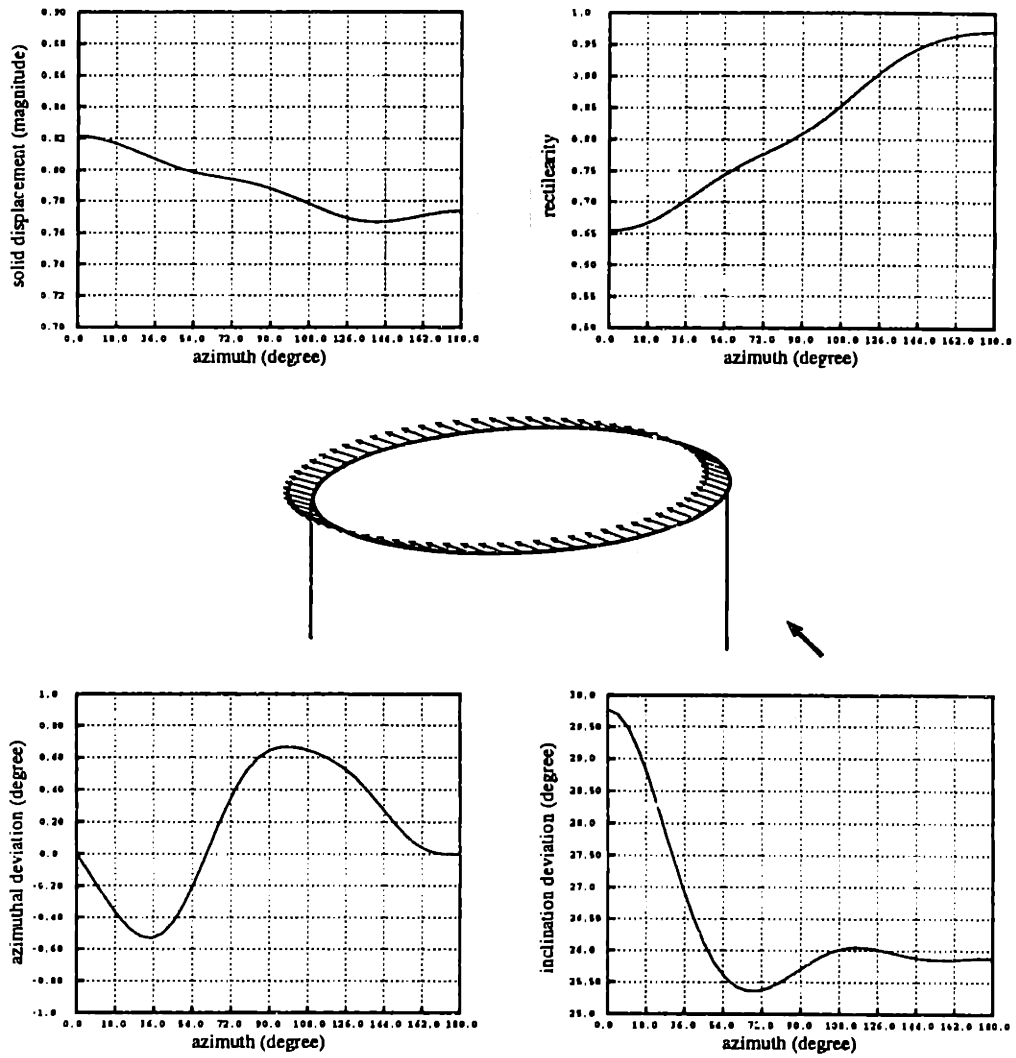

Figure 3-19: Solid displacement on the borehole wall as a function of azimuthal orientation of the geophone. The incident wave is a P-wave. The formation is Pierre shale (soft). The calculation is made with $\delta = 45^o$ and frequency 1000 Hz. The upper-left panel shows the magnitude of the solid displacement vector. The upper-right panel is rectilinearity. The lower-left and lower-right panels are the deviations in azimuth and inclination between the solid displacement on the borehole wall and the incident wave, respectively.

Radius(cm)	VP(km/s)	VS(km/s)	RHO(g/cm3)
10.16	1.50	0.0	1.00
12.19	6.10	3.35	7.50
infinity	4.206	2.664	2.14

Frequency: 1000 Hz, SV incidence at: 45 degree

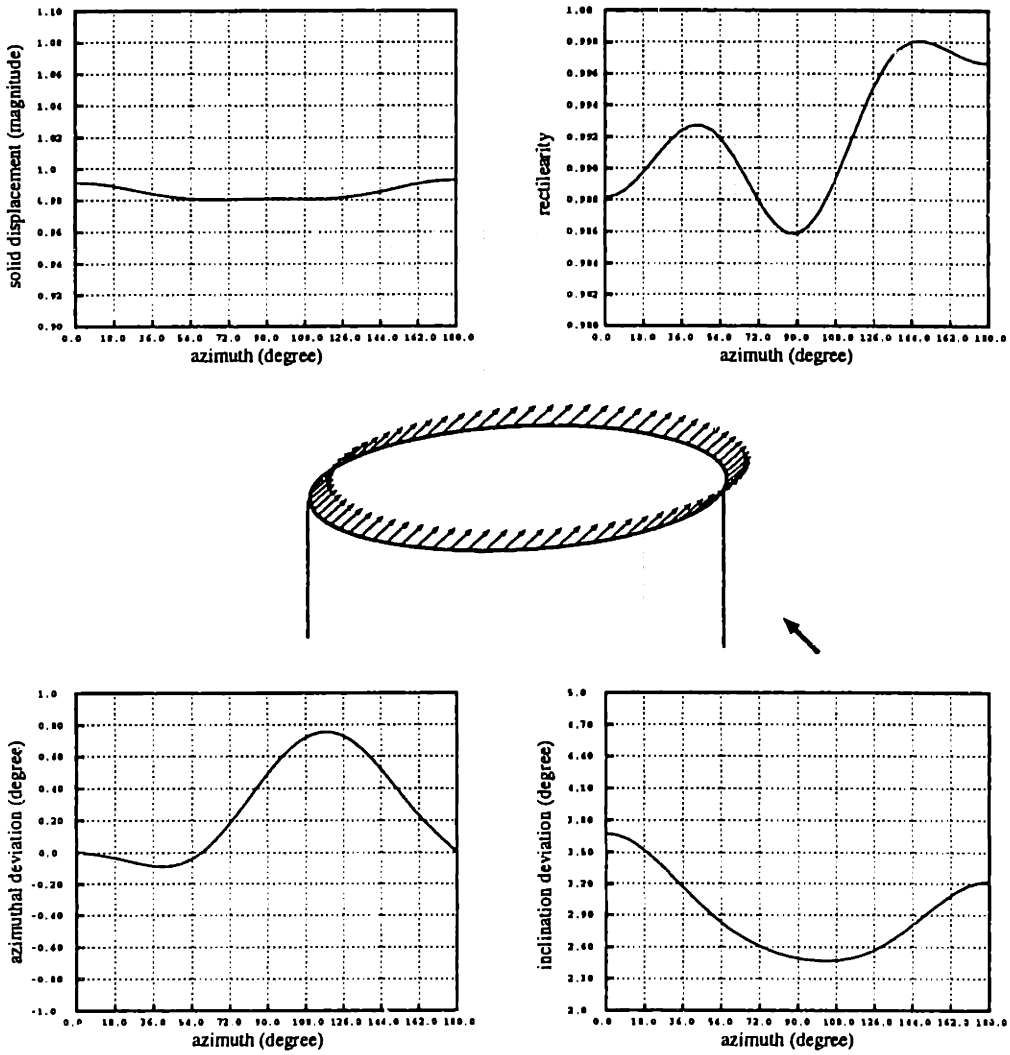

Figure 3-20: Solid displacement on the borehole wall as a function of azimuthal orientation of the geophone. The incident wave is a SV-wave. The formation is Berea sandstone (hard). The calculation is made with $\delta = 45^o$ and frequency 1000 Hz. The upper-left panel shows the magnitude of the solid displacement vector. The upper-right panel is rectilinearity. The lower-left and lower-right panels are the deviations in azimuth and inclination between the solid displacement on the borehole wall and the incident wave, respectively.

Radius(cm)	VP(km/s)	VS(km/s)	RHO(g/cm3)
10.16	1.50	0.0	1.00
12.19	6.10	3.35	7.50
infinity	2.074	0.869	2.00

Frequency: 1000 Hz, SV incidence at: 45 degree

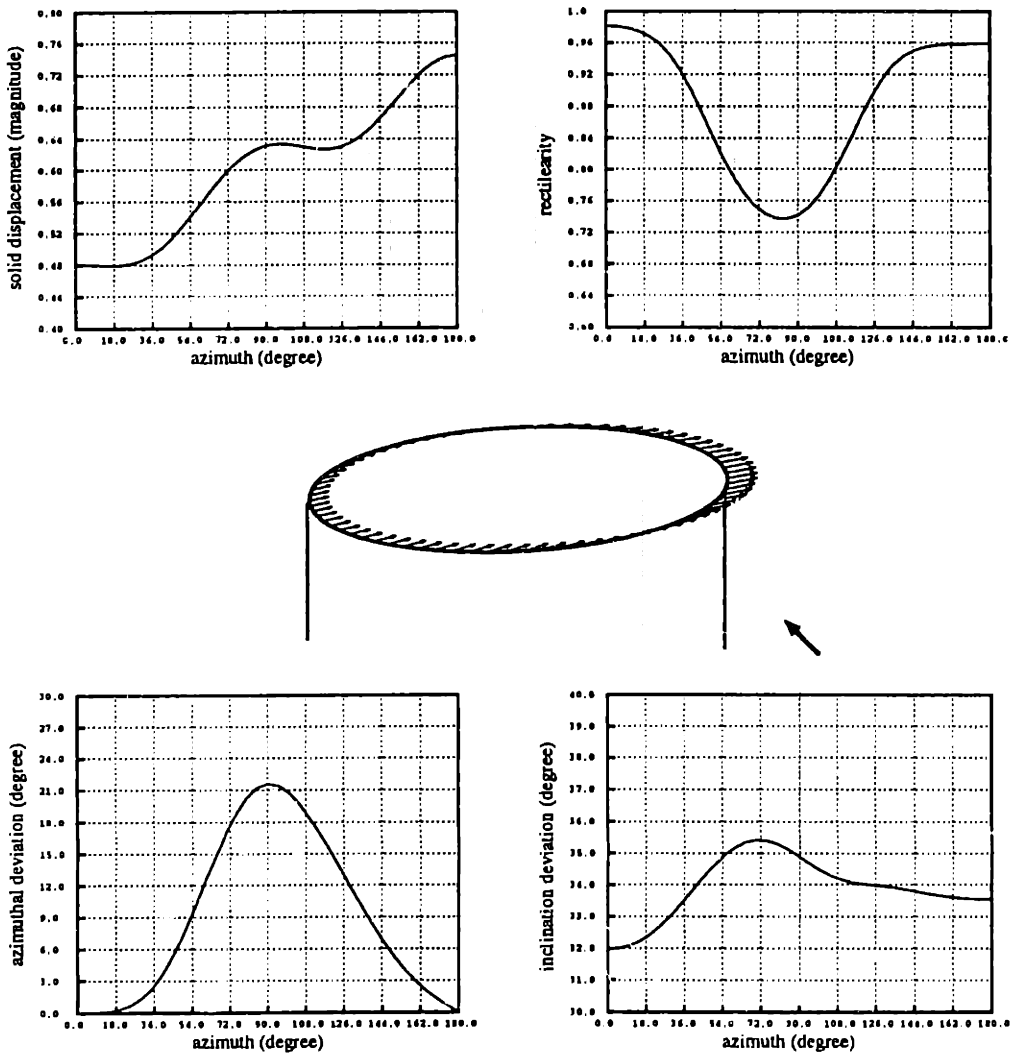

Figure 3-21: Solid displacement on the borehole wall as a function of azimuthal orientation of the geophone. The incident wave is a SV-wave. The formation is Pierre shale (soft). The calculation is made with $\delta = 45^o$ and frequency 1000 Hz. The upper-left panel shows the magnitude of the solid displacement vector. The upper-right panel is rectilinearity. The lower-left and lower-right panels are the deviations in azimuth and inclination between the solid displacement on the borehole wall and the incident wave, respectively.

Chapter 4

Borehole Coupling in an Irregular Borehole

It has been observed that the boreholes drilled into the earth are noncircular and often of irregular shape (Hilchie et al., 1968; Dart et al., 1989; among others). Elastic wave propagation in a noncircular borehole attracted some attention in recent years. For the low frequency limit, Zimmerman (1986) and Norris (1990) proposed a method to calculate the tube wave velocity in a borehole of arbitrary cross-section. They found that the tube wave speed is reduced compared to the one in a circular borehole. Ellefsen (1990) applied a perturbation method to study higher order mode dispersion in an elliptical borehole. He noticed that the percent change in phase velocity at any frequency was small in a slightly irregular borehole. Randall (1991a) calculated the dispersion curves for modes in a noncircular fluid-filled borehole in elastic formations by using the boundary integral formulation. He found that the flexural and screw modes split into two distinct branches delineated by their orientations. Using the same method, Randall (1991b) and Liu and Randall (1991) computed the dipole sonic logs in an elliptical borehole.

The goal of this chapter is to study the coupling between an incident elastic wave

and a fluid-filled borehole of irregular cross-section, in order to understand the effects of the borehole irregularity on downhole seismic measurements. We will apply a mode-matching method. Deviating from the original formulation (Okuno et al., 1982, 1987; Okuno, 1990), we will employ an algorithm by Reichel et al. (1991) (hereinafter referred to as the Reichel et al. algorithm in the text). This algorithm solves a discrete least squares approximation by trigonometric polynomials, a technique closely related to the fast Fourier transform. Compared to the boundary integral formulation (Randall, 1991a, 1991b), our method is faster because the number of unknowns to be determined is decreased by an order of magnitude. The method proposed in this chapter will also be applied to compute synthetic sonic logs in a borehole of irregular cross-section. In the latter application, multiple sources and arrays of multipole receivers will be used. The synthetic logging seismograms will be computed to study the cross-mode coupling phenomenon in the presence of irregular cross-section of the borehole, which may be mistakenly attributed to formation anisotropy (Hatchell and Cowles, 1992).

This chapter includes four sections. In the first section, we will give a theoretical formulation for elastic wave scattering in a fluid-filled borehole, using the mode-matching method as well as the Reichel et al. algorithm. We will also address issues concerning its implementation on a computer. In the next two sections, we will present some numerical examples of elastic wave coupling and synthetic sonic logging seismograms in a noncircular borehole, respectively. In the last section, we will give a brief discussion and draw some conclusions.

4.1 Theoretical Formulations for Elastic Wave Propagation in Irregular Boreholes

Consider an elastic plane wave incident upon an infinite fluid-filled borehole, as shown in Figure 4-1. The cross-section of the borehole is irregular. The formation is ho-

mogeneous and elastic with compressional wave speed α, shear wave speed β, and density ρ. The borehole is filled with a fluid of density ρ_f and compressional wave speed α_f. The radius of the borehole is parameterized by the following trigonometric series:

$$r(\theta) = r_0 + \sum_{l=1}^{L} (r_a(l) \cos l\theta + r_b(l) \sin l\theta). \tag{4.1}$$

The objective is to compute the pressure in the fluid and the solid displacements on the borehole wall for a source in the formation. And conversely, as applications to sonic well logging, we also compute the full acoustic waveforms for a multiple source in the borehole.

4.1.1 Modal Solutions

As presented in section 2.1, the general solutions to the displacement potentials in both fluid (ϕ_f) and solid (ϕ, ξ and ψ) can be expressed in a cylindrical coordinate system as (Schoenberg, 1986) [1]

$$\phi_f = -\frac{\alpha_f V(\omega)}{\omega^2} \left[A_0 \, J_0(k_f r) + 2 \sum_{n=1}^{\infty} i^n (A_n \cos n\theta + A_n' \sin n\theta) \, J_n(k_f r) \right], \tag{4.2a}$$

$$\phi = -\frac{\alpha V(\omega)}{\omega^2} \left[B_0 \, H_0^{(1)}(k_p r) + 2 \sum_{n=1}^{\infty} i^n (B_n \cos n\theta + B_n' \sin n\theta) \, H_n^{(1)}(k_p r) \right], \tag{4.2b}$$

$$\xi = -\frac{i\beta^2 V(\omega)}{\omega^3} \left[C_0 \, H_0^{(1)}(k_s r) + 2 \sum_{n=1}^{\infty} i^n (C_n \cos n\theta + C_n' \sin n\theta) \, H_n^{(1)}(k_s r) \right], \tag{4.2c}$$

$$\psi = -\frac{\beta V(\omega)}{\omega^2} \left[-D_0' \, H_0^{(1)}(k_s r) + 2 \sum_{n=1}^{\infty} i^n (D_n \sin n\theta - D_n' \cos n\theta) \, H_n^{(1)}(k_s r) \right], \tag{4.2d}$$

where z dependence and time dependence $e^{i(k_z z - \omega t)}$ is assumed. In these equations, $k_f = \sqrt{\omega^2/\alpha_f^2 - k_z^2}$, $k_p = \sqrt{\omega^2/\alpha^2 - k_z^2}$ and $k_s = \sqrt{\omega^2/\beta^2 - k_z^2}$ are the radial wavenumbers in the fluid and solid, respectively. The signs of k_f, k_p, k_z are chosen such that the imaginary part $\mathbf{Im}(k_p, k_s, k_f) \geq 0$. $V(\omega)$ ($\equiv -\omega^2$, without loss of generality) denotes the source function at a given frequency ω.

[1] No energy from ∞ is included in the solution. This may not be true if the borehole cross-section is highly irregular such that multiply scattered energies travel inward.

For this problem, the boundary conditions are the continuities of normal displacement $u_n(r^{\pm},\theta)$ and normal stress $\sigma_{nn}(r^{\pm},\theta)$, and vanishing of tangential stresses $\sigma_{nb}(r^{\pm},\theta)$ and $\sigma_{nz}(r^{\pm},\theta)$ at the borehole wall $r = r^{\pm}(\theta)$, that is,

$$u_n^{(f)}(r^-,\theta) = u_n^{(s)}(r^+,\theta) + u_n^{(i)}(r^+,\theta), \tag{4.3a}$$

$$-p^{(f)}(r^-,\theta) = \sigma_{nn}^{(s)}(r^+,\theta) + \sigma_{nn}^{(i)}(r^+,\theta), \tag{4.3b}$$

$$\sigma_{nb}^{(s)}(r^+,\theta) + \sigma_{nb}^{(i)}(r^+,\theta) = 0, \tag{4.3c}$$

$$\sigma_{nz}^{(s)}(r^+,\theta) + \sigma_{nz}^{(i)}(r^+,\theta) = 0. \tag{4.3d}$$

In the above expressions, the superscript (i) denotes the quantities associated with the incident wave, (s) denotes those of the scattered wave in the solid and (f) those in the fluid. The pressure in the fluid is denoted by p. A local coordinate frame is used here $\vec{n}$ is normal to the borehole boundary, $\vec{b}$ is tangential to the boundary, and $\vec{z}$ is in the axial direction (see Figure 4-1).

The transformation from the cylindrical coordinates ($\vec{r}$, $\vec{\theta}$, $\vec{z}$) to the local orthogonal coordinates ($\vec{n}$, $\vec{b}$, $\vec{z}$) on the boundary is accomplished through an angular rotation $\varphi = <\vec{n}, \vec{r}>$, which is given by

$$\varphi = \tan^{-1} \frac{\sum_{l=1}^{L} l\,(\,-r_a(l)\sin l\theta + r_b(l)\cos l\theta\,)}{r_0 + \sum_{l=1}^{L}(\,r_a(l)\cos l\theta + r_b(l)\sin l\theta\,)}. \tag{4.4}$$

We transform the displacements and stresses from the cylindrical coordinates ($\vec{r}$, $\vec{\theta}$, $\vec{z}$) to the local orthogonal coordinates ($\vec{n}$, $\vec{b}$, $\vec{z}$) using the following relations:

$$\begin{bmatrix} u_n \\ u_b \\ u_z \end{bmatrix} = \begin{bmatrix} \cos\varphi & \sin\varphi & 0 \\ -\sin\varphi & \cos\varphi & 0 \\ 0 & 0 & 1 \end{bmatrix} \begin{bmatrix} u_r \\ u_\theta \\ u_z \end{bmatrix},$$

and

$$\begin{bmatrix} \sigma_{nn} & \sigma_{nb} & \sigma_{nz} \\ \sigma_{bn} & \sigma_{bb} & \sigma_{bz} \\ \sigma_{zn} & \sigma_{zb} & \sigma_{zz} \end{bmatrix} = \begin{bmatrix} \cos\varphi & \sin\varphi & 0 \\ -\sin\varphi & \cos\varphi & 0 \\ 0 & 0 & 1 \end{bmatrix} \begin{bmatrix} \sigma_{rr} & \sigma_{r\theta} & \sigma_{rz} \\ \sigma_{\theta r} & \sigma_{\theta\theta} & \sigma_{\theta z} \\ \sigma_{zr} & \sigma_{z\theta} & \sigma_{zz} \end{bmatrix} \begin{bmatrix} \cos\varphi & -\sin\varphi & 0 \\ \sin\varphi & \cos\varphi & 0 \\ 0 & 0 & 1 \end{bmatrix}.$$

Upon these rotations, expressions for the normal displacement and tractions on the boundary are obtained. In terms of harmonic expansions, they are given by:

$$\begin{aligned} u_n^{(f)}(r,\theta) &= \sum_{n=0}^{\infty} i^n \varepsilon_n \mathcal{U}_n^{(f)}(r) [\, A_n \cos n\theta + A'_n \sin n\theta \,] \cos\phi \\ &+ \sum_{n=0}^{\infty} i^n \varepsilon_n \mathcal{V}_n^{(f)}(r) [\, -A_n \sin n\theta + A'_n \cos n\theta \,] \sin\phi, \end{aligned} \tag{4.5a}$$

$$\begin{aligned} u_n^{(s)}(r,\theta) &= \sum_{n=0}^{\infty} i^n \varepsilon_n \mathcal{U}_n^{(\phi)}(r) [\, B_n \cos n\theta + B'_n \sin n\theta \,] \cos\phi \\ &+ \sum_{n=0}^{\infty} i^n \varepsilon_n \mathcal{V}_n^{(\phi)}(r) [\, -B_n \sin n\theta + B'_n \cos n\theta \,] \sin\phi \\ &+ \sum_{n=0}^{\infty} i^n \varepsilon_n \mathcal{U}_n^{(\xi)}(r) [\, C_n \cos n\theta + C'_n \sin n\theta \,] \cos\phi \\ &+ \sum_{n=0}^{\infty} i^n \varepsilon_n \mathcal{V}_n^{(\xi)}(r) [\, -C_n \sin n\theta + C'_n \cos n\theta \,] \sin\phi \\ &+ \sum_{n=0}^{\infty} i^n \varepsilon_n \mathcal{U}_n^{(\psi)}(r) [\, D_n \cos n\theta + D'_n \sin n\theta \,] \cos\phi \\ &+ \sum_{n=0}^{\infty} i^n \varepsilon_n \mathcal{V}_n^{(\psi)}(r) [\, -D_n \sin n\theta + D'_n \cos n\theta \,] \sin\phi, \end{aligned} \tag{4.5b}$$

$$-p^{(f)}(r,\theta) = \sigma_{nn}^{(f)}(r,\theta) = \sum_{n=0}^{\infty} i^n \varepsilon_n \mathcal{R}_n^{(f)}(r) [\, A_n \cos n\theta + A'_n \sin n\theta \,], \tag{4.5c}$$

$$\begin{aligned} \sigma_{nn}^{(s)}(r,\theta) &= \sum_{n=0}^{\infty} i^n \varepsilon_n \mathcal{R}_n^{(\phi)}(r) [\, B_n \cos n\theta + B'_n \sin n\theta \,] \cos^2\phi \\ &+ \sum_{n=0}^{\infty} i^n \varepsilon_n \mathcal{T}_n^{(\phi)}(r) [\, -B_n \sin n\theta + B'_n \cos n\theta \,] \sin 2\phi \\ &+ \sum_{n=0}^{\infty} i^n \varepsilon_n \mathcal{M}_n^{(\phi)}(r) [\, B_n \cos n\theta + B'_n \sin n\theta \,] \sin^2\phi \\ &+ \sum_{n=0}^{\infty} i^n \varepsilon_n \mathcal{R}_n^{(\xi)}(r) [\, C_n \cos n\theta + C'_n \sin n\theta \,] \cos^2\phi \\ &+ \sum_{n=0}^{\infty} i^n \varepsilon_n \mathcal{T}_n^{(\xi)}(r) [\, -C_n \sin n\theta + C'_n \cos n\theta \,] \sin 2\phi \\ &+ \sum_{n=0}^{\infty} i^n \varepsilon_n \mathcal{M}_n^{(\xi)}(r) [\, C_n \cos n\theta + C'_n \sin n\theta \,] \sin^2\phi \\ &+ \sum_{n=0}^{\infty} i^n \varepsilon_n \mathcal{R}_n^{(\psi)}(r) [\, D_n \cos n\theta + D'_n \sin n\theta \,] \cos^2\phi \\ &+ \sum_{n=0}^{\infty} i^n \varepsilon_n \mathcal{T}_n^{(\psi)}(r) [\, -D_n \sin n\theta + D'_n \cos n\theta \,] \sin 2\phi \end{aligned}$$

$$+ \sum_{n=0}^{\infty} i^n \, \varepsilon_n \, \mathcal{M}_n^{(\psi)}(r) \, [\, D_n \, \cos n\theta + D'_n \, \sin n\theta \,] \, \sin^2 \phi, \qquad (4.5d)$$

$$\begin{aligned}
\sigma_{nb}^{(s)}(r,\theta) \;=\; & \sum_{n=0}^{\infty} i^n \, \varepsilon_n \, \frac{[\, \mathcal{M}_n^{(\phi)}(r) - \mathcal{R}_n^{(\phi)}(r) \,]}{2} \, [\, B_n \, \cos n\theta + B'_n \, \sin n\theta \,] \, \sin 2\phi \\
& + \sum_{n=0}^{\infty} i^n \, \varepsilon_n \, \mathcal{T}_n^{(\phi)}(r) \, [\, -B_n \, \sin n\theta + B'_n \, \cos n\theta \,] \, \cos 2\phi \\
& + \sum_{n=0}^{\infty} i^n \, \varepsilon_n \, \frac{[\, \mathcal{M}_n^{(\xi)}(r) - \mathcal{R}_n^{(\xi)}(r) \,]}{2} \, [\, C_n \, \cos n\theta + C'_n \, \sin n\theta \,] \, \sin 2\phi \\
& + \sum_{n=0}^{\infty} i^n \, \varepsilon_n \, \mathcal{T}_n^{(\xi)}(r) \, [\, -C_n \, \sin n\theta + C'_n \, \cos n\theta \,] \, \cos 2\phi \\
& + \sum_{n=0}^{\infty} i^n \, \varepsilon_n \, \frac{[\, \mathcal{M}_n^{(\psi)}(r) - \mathcal{R}_n^{(\psi)}(r) \,]}{2} \, [\, D_n \, \cos n\theta + D'_n \, \sin n\theta \,] \, \sin 2\phi \\
& + \sum_{n=0}^{\infty} i^n \, \varepsilon_n \, \mathcal{T}_n^{(\psi)}(r) \, [\, -D_n \, \sin n\theta + D'_n \, \cos n\theta \,] \, \cos 2\phi, \qquad (4.5e)
\end{aligned}$$

$$\begin{aligned}
\sigma_{nz}^{(s)}(r,\theta) \;=\; & \sum_{n=0}^{\infty} i^n \, \varepsilon_n \, \mathcal{Z}_n^{(\phi)}(r) \, [\, B_n \, \cos n\theta + B'_n \, \sin n\theta \,] \, \cos \phi \\
& + \sum_{n=0}^{\infty} i^n \, \varepsilon_n \, \mathcal{N}_n^{(\phi)}(r) \, [\, -B_n \, \sin n\theta + B'_n \, \cos n\theta \,] \, \sin \phi \\
& + \sum_{n=0}^{\infty} i^n \, \varepsilon_n \, \mathcal{Z}_n^{(\xi)}(r) \, [\, C_n \, \cos n\theta + C'_n \, \sin n\theta \,] \, \cos \phi \\
& + \sum_{n=0}^{\infty} i^n \, \varepsilon_n \, \mathcal{N}_n^{(\xi)}(r) \, [\, -C_n \, \sin n\theta + C'_n \, \cos n\theta \,] \, \sin \phi \\
& + \sum_{n=0}^{\infty} i^n \, \varepsilon_n \, \mathcal{Z}_n^{(\psi)}(r) \, [\, D_n \, \cos n\theta + D'_n \, \sin n\theta \,] \, \cos \phi \\
& + \sum_{n=0}^{\infty} i^n \, \varepsilon_n \, \mathcal{N}_n^{(\psi)}(r) \, [\, -D_n \, \sin n\theta + D'_n \, \cos n\theta \,] \, \sin \phi, \qquad (4.5f)
\end{aligned}$$

where $\varepsilon_n = \begin{cases} 1 & \text{if } n = 0 \\ 2 & \text{if } n \geq 1 \end{cases}$ is the Newmann factor. The radial dependences $\mathcal{U}_n^{(J)}(r), \mathcal{U}_n^{(\phi)}(r), ..., \mathcal{Z}_n^{(\psi)}(r), \mathcal{N}_n^{(\psi)}(r)$ have been given in the Appendix A-3.

Unlike the case of a circular borehole where the boundary conditions are satisfied by each individual mode in the harmonic expansions (4.2a)-(4.2d), in a noncircular borehole it is the total field that satisfies the boundary conditions. A least square formalism is used to determine the unknown coefficients $\{A_n, A'_n, B_n, B'_n, C_n, C'_n,$

$D_n, D_n'\}$ such that the errors in satisfying the boundary conditions are as small as possible.

4.1.2 Fourier Series Expansion

We expand the normal displacements and the normal as well as tangential stresses on the boundary $r^+ = r^- = r(\theta)$ in terms of Fourier series. The results for the normal displacements are:

$$u_n^{(f)}(r^-, \theta) = a_0 + \sum_{l=1}^{\infty} (a_l \cos l\theta + a_l' \sin l\theta), \tag{4.6a}$$

$$\begin{aligned} u_n^{(s)}(r^+, \theta) &= b_0 + \sum_{l=1}^{\infty} (b_l \cos l\theta + b_l' \sin l\theta) \\ &+ c_0 + \sum_{l=1}^{\infty} (c_l \cos l\theta + c_l' \sin l\theta) \\ &+ d_0 + \sum_{l=1}^{\infty} (d_l \cos l\theta + d_l' \sin l\theta), \end{aligned} \tag{4.6b}$$

where

$$\begin{aligned} a_l &= (a_{11})_{ln}\ A_n + (a_{12})_{ln}\ A_n'; & a_l' &= (a_{21})_{ln}\ A_n + (a_{22})_{ln}\ A_n'; \\ b_l &= \left(b_{11}\right)_{ln}\ B_n + \left(b_{12}\right)_{ln}\ B_n'; & b_l' &= \left(b_{21}\right)_{ln}\ B_n + \left(b_{22}\right)_{ln}\ B_n'; \\ c_l &= (c_{11})_{ln}\ C_n + (c_{12})_{ln}\ C_n'; & c_l' &= (c_{21})_{ln}\ C_n + (c_{22})_{ln}\ C_n'; \\ d_l &= \left(d_{11}\right)_{ln}\ D_n + \left(d_{12}\right)_{ln}\ D_n'; & d_l' &= \left(d_{21}\right)_{ln}\ D_n + \left(d_{22}\right)_{ln}\ D_n'. \end{aligned}$$

The elements of matrices $a_{11}, a_{12}, ..., d_{22}$ are the integrals of the corresponding modal functions for the displacements along the borehole boundary, and are given in Appendix C.

Similarly, the pressure on the fluid side of the borehole wall and the normal as well as tangential stresses on the solid side of the borehole wall can be written as

$$-p^{(f)}(r^-, \theta) = \sigma_{nn}^{(f)}(r^-, \theta) = e_0 + \sum_{l=1}^{\infty} (e_l \cos l\theta + e_l' \sin l\theta), \tag{4.7a}$$

$$\sigma_{nn}^{(s)}(r^+,\theta) = f_0 + \sum_{l=1}^{\infty} (f_l \cos l\theta + f_l' \sin l\theta)$$
$$+ g_0 + \sum_{l=1}^{\infty} (g_l \cos l\theta + g_l' \sin l\theta)$$
$$+ h_0 + \sum_{l=1}^{\infty} (h_l \cos l\theta + h_l' \sin l\theta), \qquad (4.7b)$$

$$\sigma_{nb}^{(s)}(r^+,\theta) = o_0 + \sum_{l=1}^{\infty} (o_l \cos l\theta + o_l' \sin l\theta)$$
$$+ p_0 + \sum_{l=1}^{\infty} (p_l \cos l\theta + p_l' \sin l\theta)$$
$$+ q_0 + \sum_{l=1}^{\infty} (q_l \cos l\theta + q_l' \sin l\theta), \qquad (4.8a)$$

and

$$\sigma_{nz}^{(s)}(r^+,\theta) = r_0 + \sum_{l=1}^{\infty} (r_l \cos l\theta + r_l' \sin l\theta)$$
$$+ s_0 + \sum_{l=1}^{\infty} (s_l \cos l\theta + s_l' \sin l\theta)$$
$$+ t_0 + \sum_{l=1}^{\infty} (t_l \cos l\theta + t_l' \sin l\theta), \qquad (4.8b)$$

where

$$e_l = (e_{11})_{ln}\ A_n + (e_{12})_{ln}\ A_n'; \qquad e_l' = (e_{21})_{ln}\ A_n + (e_{22})_{ln}\ A_n';$$

$$f_l = \left(f_{11}\right)_{ln}\ B_n + \left(f_{12}\right)_{ln}\ B_n'; \qquad f_l' = \left(f_{21}\right)_{ln}\ B_n + \left(f_{22}\right)_{ln}\ B_n';$$

$$g_l = (g_{11})_{ln}\ C_n + (g_{12})_{ln}\ C_n'; \qquad g_l' = (g_{21})_{ln}\ C_n + (g_{22})_{ln}\ C_n';$$

$$h_l = \left(h_{11}\right)_{ln}\ D_n + \left(h_{12}\right)_{ln}\ D_n'; \qquad h_l' = \left(h_{21}\right)_{ln}\ D_n + \left(h_{22}\right)_{ln}\ D_n';$$

$$o_l = (o_{11})_{ln}\ B_n + (o_{12})_{ln}\ B_n'; \qquad o_l' = (o_{21})_{ln}\ B_n + (o_{22})_{ln}\ B_n';$$

$$p_l = (p_{11})_{ln}\ C_n + (p_{12})_{ln}\ C_n'; \qquad p_l' = (p_{21})_{ln}\ C_n + (p_{22})_{ln}\ C_n';$$

$$q_l = (q_{11})_{ln}\ D_n + (q_{12})_{ln}\ D_n'; \qquad q_l' = (q_{21})_{ln}\ D_n + (q_{22})_{ln}\ D_n';$$

$$r_l = (r_{11})_{ln}\ B_n + (r_{12})_{ln}\ B_n'; \qquad r_l' = (r_{21})_{ln}\ B_n + (r_{22})_{ln}\ B_n';$$

$$s_l = (s_{11})_{ln}\ C_n + (s_{12})_{ln}\ C_n'; \qquad s_l' = (s_{21})_{ln}\ C_n + (s_{22})_{ln}\ C_n';$$

$$t_l = (t_{11})_{ln}\ D_n + (t_{12})_{ln}\ D'_n; \qquad t'_l = (t_{21})_{ln}\ D_n + (t_{22})_{ln}\ D'_n.$$

The elements of the matrices $e_{11}, e_{12}, ..., t_{22}$ are the integrals of the corresponding modal functions for stresses along the borehole boundary, and again, are given in Appendix C.

4.1.3 Least Squares Solution by Reichel et al. Algorithm

In the mode-matching method, a least square formulism is used to match the boundary conditions between solution regimes, whereby the coefficients in the expansion in terms of modal solutions are uniquely determined. To this end, we define the mean square errors on the boundary as

$$\mathcal{E}(u_n) = ||u_n^{(f)}(r^-,\theta) - u_n^{(s)}(r^+,\theta) - u_n^{(i)}(r^+,\theta)||^2, \tag{4.9a}$$

$$\mathcal{E}(\sigma_{nn}) = ||-p^{(f)}(r^-,\theta) - \sigma_{nn}^{(s)}(r^+,\theta) - \sigma_{nn}^{(i)}(r^+,\theta)||^2, \tag{4.9b}$$

$$\mathcal{E}(\sigma_{nb}) = ||-\sigma_{nb}^{(s)}(r^+,\theta) - \sigma_{nb}^{(i)}(r^+,\theta)||^2, \tag{4.9c}$$

$$\mathcal{E}(\sigma_{nz}) = ||-\sigma_{nz}^{(s)}(r^+,\theta) - \sigma_{nz}^{(i)}(r^+,\theta)||^2, \tag{4.9d}$$

where

$$||f||^2 = \oint_\Gamma \overline{f(s)}\ f(s)\ ds = \int_0^{2\pi} \overline{f(r(\theta))}\ f(r(\theta))\ r(\theta)\ d\theta$$

defines the norm of a square integrable function $f(\cdot)$ on the boundary. Notice that, in the above definition, the borehole radius is included as a positive weighting function. $\mathcal{E}(u_n)$ is the misfit of the normal displacement on the boundary, $\mathcal{E}(\sigma_{nn})$ is that of the normal stress, and $\mathcal{E}(\sigma_{nb})$ and $\mathcal{E}(\sigma_{nz})$ are those of the two tangential stresses. The objective is to find appropriate coefficients to minimize all these errors simultaneously[2].

We substitute the expressions in equations (4.6) through (4.8) into equations (4.9a)–(4.9d). For example, we calculate the mean square error of the normal displacement in equation (4.9a) and compare it with the minimization problem discussed

[2]In the case of a circular borehole, i.e., $r(\theta) \equiv r_0$, these errors are minimal if and only if all the individual modes satisfy the boundary conditions themselves. This is due to the orthogonality of the modal functions. In this case, the mode-matching method reduces to the method we have developed in the previous chapters.

in Appendix D. We found that the Reichel et al. algorithm (for least square approximations by trigonometric polynomials) can be employed to compute rapidly and accurately the coefficients $\{a_l, a_l', b_l, b_l', ...t_l, t_l'\}_{l=0}^{L}$, where L is the order of truncation. We have assumed that the displacement and stresses of the incident wave fields are known on the boundary at a set of distinct sample points. The weights in the Reichel et al. algorithm is chosen as $w_k = r_k$, corresponding to the radius of the irregular borehole at $\theta = \theta_k$.

Given that $\{a_l, a_l', b_l, b_l', ...t_l, t_l'\}_{l=0}^{L}$ are known, the coefficients $\{A_n, A_n',\ B_n, B_n',\ C_n, C_n',\ D_n, D_n'\}_{n=0}^{N}$ can then be determined uniquely by solving a (8N + 4)×(8N + 4) matrix equation[3] derived from the relationships given in section 4.1.2, where $N = L$ are the orders of truncation.

The truncation order is chosen such that the errors in equations (4.9a)–(4.9d) are much smaller than the norms of the incident wave field (relative error $< 10^{-4}$). This guarantees at least four digits of accuracy in the solution. The relative error is dependent on the shape of the borehole, i.e., the spectrum of the borehole cross-section in equation (4.1). Using double precision computations, we found that the relative error was less than 10^{-14} for a circular borehole and less than 10^{-9} for an elliptical borehole, where $L = N = 10$ was used.

Given the error bounds on the boundary, we can show that the error at any point away from the boundary is also bounded with

$$| \vec{u}_N(\vec{r}) - \vec{u}(\vec{r})|^2 \leq M(\Omega)\, \mathcal{E}(u_n), \tag{4.10}$$

where $M(\Omega)$ is a positive constant independent of both N (the order of truncation) and position $\vec{r} \in \Omega$. Here $\vec{u}_N$ is the calculated displacement by the mode-matching method, and $\vec{u}$ is the exact solution. The proof is straight forward by taking account of the decaying nature of the Hankel functions at large distances.

[3]The total number of unknown coefficients is 8 ×N +4, where the 4 is due to the property that $A_0' = B_0' = C_0' = D_0 \equiv 0$

4.1.4 Implementation

Several issues are of concern in the implementation of this technique. The most important one is the control of accuracy. The sources of inaccuracy may come from the singularity of the coefficient matrix, causing energy to leak between modes, or from the loss of significant digits in the evaluation of the Bessel functions $J_n(z) \to 0$ and the Hankel functions $H_n^{(1)}(z) \to \infty$ as $|z| \to 0$ and n large, or from the fact that the borehole cross-section may be so rough that more terms in the summations would be needed. In our experience, proper scaling and preconditioning can greatly improve the condition of the matrix equation. The method we have used to compute the Bessel and Hankel functions (adapted from du Toit, 1990) is accurate enough for any order and any complex argument.

Discretization along the borehole boundary also has some effects on accuracy. A denser discretization is needed at sharp corners, while in flat regions only sparse sampling is necessary. The automatic discretization scheme we use is based on the local curvature along the boundary. It is combined with the requirement that the size of the largest element be less than 1/25 of the shortest wavelength. The local curvature in polar coordinates is given by

$$\kappa = \frac{r^2 + 2\,(dr/d\theta)^2 - r\;d^2r/d\theta^2}{(r^2 + (dr/d\theta)^2)^{3/2}}. \tag{4.11}$$

In our calculations, the number of samples along the borehole boundary is 180, roughly in two degree intervals between two successive sampling points.

For a fixed discretization of the boundary, say, 180 elements or grid points, we compare the boundary integral method against the mode-matching method. The boundary integral method used in Randall (1991a, 1991b) has $J = 4{\times}180 = 720$ unknowns to be determined. This requires arithmetic operations on the order of $O(J^2)$ to solve the matrix equation alone, not including calculations for forming the coefficient matrices. The mode matching method developed here only needs arithmetic operations on the order of $O(J/4{\times}(8N + 4)) = O(J)$, where $N = 10$ is

the order of truncation. This makes the mode-matching method a practical tool of computing synthetical seismograms in an irregular borehole, where the calculation is repeated for many samples in both frequency and vertical wavenumber.

4.2 Application I: Borehole Coupling Problems

4.2.1 Case of an Elliptical Borehole

Boreholes with 10% ellipticity are not uncommon. Figure 4-2 shows a borehole cross section whose shape was determined with a borehole televiewer (Ellefsen, 1991). The major axis of the borehole is 19.1 cm in diameter; the minor one is 16.9 cm in diameter. The borehole is discretized with 180 elements where the boundary conditions are satisfied in the least square sense. In the following examples, the frequency of the incident wave is 1000 Hz. The formation is Berea sandstone. The fluid is ideal water. The order of truncation is $N = L = 10$.

Figure 4-3 shows the relative error in satisfying the boundary condition as a function of angle of incidence. The error is computed according to

$$E = \frac{||\sigma_{nn}^{(f)}(r^-, \theta) - \sigma_{nn}^{(s)}(r^+, \theta) - \sigma_{nn}^{(i)}(r^+, \theta)||}{||\sigma_{nn}^{(i)}(r^+, \theta)||}, \tag{4.12}$$

where the norm was defined in section 4.1.3. For a computation with double precision, this error is on the order of 10^{-9} for this particular example. This result implies that at least 8 significant digits are obtained in the solution. Surprisingly, the relative error increases with the increase of the angle of incidence (from 10^{-12} at grazing incidence to 6×10^{-9} at normal incidence). This behavior originates from approximating plane waves by superposition of finite sets of cylindrical waves.

Another way to demonstrate the accuracy of the mode-matching method is to examine the decay of the coefficients in the expansions (4.2a)-(4.2d), or in other words,

to evaluate the contributions of higher order modes to the summations. Figure 4-4 is a bar-plot of magnitudes of coefficients $\{A_n, B_n, C_n, D_n\}_{n=0}^{n=N}$ as a function of harmonic order n. Shown here are the first 12 modes. The vertical axis (magnitude) is in a logarithmic scale. It is evident that the decay of $\{B_n, C_n, D_n\}$ is faster than exponential, implying that very few terms are actually contributing to the summation, the higher order terms are negligible. The coefficient $\{A_n\}$ fluctuates at the beginning and decays later as the order increases. Recall that $\{A_n\}$ is always associated with $J_n(z)$, while the others are associated with $H_n^{(1)}(z)$, where $z = O(0.1)$. Taking this into account, we have found that only the first 7 modes are significant.

Figure 4-5 shows the pressure at the center of the fluid as a function of angle of incidence. The incident wave is a plane compressional wave. The pressure is scaled by $P_0 = -\rho\alpha\omega^2$ (see section 2.2.2 for notation). Three calculations are shown in this figure. The solid line is the result for an equivalent circular borehole, the long dash line shows the case where the P-wave incidents along the minor axis, and the short dash line shows the case where the P-wave travels along the major axis. The pressure in the fluid is greater than that in an equivalent circular borehole when the incident P-wave is parallel to the minor axis; it is smaller when the incident P-wave is parallel to the major axis. The difference is about 10% at normal incidence, which is of the same order as the borehole ellipticity. At grazing incidence, these three curves converge, showing that a P-wave propagating in the vertical direction can not 'see' the geometry of the fluid-filled borehole at all.

Figure 4-6 shows the pressure at the center of the fluid for a plane SV-wave incidence. The notations are the same as those in Figure 4-5. Again, the pressure in the fluid is larger when the incident SV-wave is parallel to the minor axis, and smaller when the incident SV-wave is parallel to the major axis. The difference is on the same order as the borehole ellipticity.

An explanation for these observations is that the elliptical borehole is stiffer against deformation along the minor axis than along the major axis. This has been

shown in Randall's analysis (Randall, 1991b). He found that the phase velocity of the odd dipole (polarized in the direction of the minor axis) is larger than that of the even dipole (polarized in the direction of the major axis).

The solid motion in the formation, however, is affected less by the irregularity of the fluid-solid boundary. Figure 4-7 shows both the horizontal and vertical components of the solid displacement on the borehole wall at an azimuthal angle $\theta = 0^o$ (measured from the major axis). The displacements are scaled by the total displacement of the incident P-wave. Obviously, the dependence of the solid motion on the direction of the incident wave is insignificant compared to the effect on the pressure in the fluid. This observation is also true for a plane SV-wave incidence.

4.2.2 Other Borehole Cross-sections

Figure 4-8 shows a borehole cross-section without a symmetry axis. The dashed line is its equivalent circular borehole (in the sense of equal surface area). We compute only the pressure at the center of the fluid (as marked by the solid dot in this figure) for waves coming from various directions, since the effect of irregularities on the solid displacement is insignificant in the frequency range we are interested in.

Figure 4-9 shows the pressure at the center of the fluid as a function of angle of incidence. The incident wave is a plane P-wave and the formation is Berea sandstone. A total of 8 curves are shown for the azimuth of the incident wave ranging from 0^o to 360^o at 45^o intervals. The pressure is scaled by P_0. As expected, the pressure in the fluid increases with the increase of the angle of incidence. However, the curves split into two branches depending on the azimuthal angle of the incident wave. A closer analysis shows that the curves labeled as $45^o, 90^o$ and 225^o belong to a cluster with smaller amplitudes, while the rest are in another cluster with larger amplitudes. The explanation is as follows. Independent of the irregularity of the borehole, the dipole motion tends to split into two and only two branches with the faster one polarized

along the effective minor axis and the slower one along the effective major axis. The predominant contribution to the pressure in the fluid comes from the monopole and dipole components of the incident wave, and the reminder are negligible.

Figure 4-10 shows the same calculation as Figure 4-9 but for a plane SV-wave incidence. The pressure shows a lobe around 45^o incidence. Again, the pressure in the fluid splits into two branches depending on the azimuthal angle of the incident wave. The one closer to the effective minor axis of the irregular borehole tends to generate larger pressure in the fluid; the one closer to the effective major axis tends to induce smaller pressure.

4.3 Application II: Acoustical Logging Problems

The mode-matching method developed in this chapter can also be applied to sonic logging problems where one is interested in the effects of borehole irregularity on multipole (especially dipole) logging seismograms. Among the possible effects is the mode splitting (or cross-mode coupling) in an irregular borehole, a phenomenon that could also be attributed to formation anisotropy (Hatchell and Cowles, 1992).

4.3.1 A Circular Borehole

Sonic logging in a circular borehole is a subject of intensive studies (among others, Cheng and Toksöz, 1981; Toksöz and Cheng, 1984). We compute synthetic dipole seismograms for a dipole source in a circular borehole using both the mode-matching and the discrete wavenumber methods (see Schmitt et al., 1988 for the latter method). Our objective is to compare the results of the two methods. This serves as an accuracy test for the application of the mode-matching method to sonic well logging problems. We use a model where the borehole is circular in cross-section, the radius is 0.1016 m, and the well is filled with fresh water. The formation is homogeneous with compres-

sional velocity 3464 m/s, shear velocity 2000 m/s, and density 2.0 g/cm^3. A dipole source is at the borehole center. The dipole receivers are evenly distributed at offsets between 1.0 m and 4.3 m from the source. Both the source and the receivers are polarized in the same direction. The source time history is a Ricker wavelet with the central frequency of 2500 Hz. Figure 4-11 shows the resulting synthetic seismograms. The solid lines in this figure are the dipole seismograms computed by the mode-matching method; the dashed lines are those by the discrete wavenumber method. The agreement between these two methods is remarkable, although the amplitudes at far offsets differ slightly.

4.3.2 An Elliptical Borehole

In the following examples, we use the elliptical borehole shown in Figure 4-2. The array of receivers is located at offsets between 1.0 m and 3.2 m from the source. The source time function is a Ricker wavelet. The central frequency is 4000 Hz. The formation is Berea sandstone.

In the first two examples, we use a monopole source and an array of dipole receivers whose orientation is in the direction of either the major axis (Figure 4-12) or the minor axis (Figure 4-13). In both figures, a low frequency event of large amplitude is clearly visible in the dipole waveform. Surprisingly, it travels with the phase velocity of the tube wave, suggesting that it is generated by the cross-mode coupling between the propagating tube wave and the dipole motion in the presence of borehole ellipticity. The dispersive wave trains surrounding this tube-wave-like event have the characteristics of the dipole waveform, and are generated by the tube wave continuously along its path of propagation. At low frequencies, the dipole motion has the phase speed of the formation shear velocity. At high frequencies, it travels much slower than the formation shear speed. Close comparisons also reveal that the phase velocity of the dipole wave in Figure 4-13 (polarized along the minor axis) is larger than that in Figure 4-12 (polarized along the major axis). This result is in

agreement with the theoretical prediction by Randall (1991a). The amplitude of the seismogram in Figure 4-13 is about 18% larger than that in Figure 4-12. Recall that the borehole ellipticity in these examples is about 10%. This observation seems to suggest that, for an elliptical borehole, differences in the excitation of the two perpendicularly polarized dipole modes by a monopole source are of the same order as the borehole ellipticity.

In the next two examples we use a dipole source and an array of monopole receivers. The source polarization is in the direction of either the major axis (Figure 4-14) or the minor axis (Figure 4-15). Instead of observing tube waves in the monopole seismograms, one sees a dispersive wave train with characteristics of a dipole motion. It is generated by a cross-mode coupling between the traveling dipole energy and the monopole motion at the receiver location. As expected, the phase velocity at high frequencies is larger in Figure 4-15 (polarized along the minor axis) than in Figure 4-14 (polarized along the major axis).

In summary, the synthetic examples in this section show that in an elliptical borehole the cross-mode coupling phenomena are evident in sonic logging seismograms using both monopole and multipole tools. Depending on the orientation of the dipole source or dipole receivers, the difference in the phase velocities of the dipole flexural waves at high frequencies and the excitations of the cross-modes are of the same order as the borehole ellipticity.

4.4 Discussions and Conclusions

In this chapter, we have presented a mode-matching method to compute the pressure in the fluid and the solid displacement in the formation for an elastic wave impinging upon an irregular borehole. In this method, the wave fields in both the fluid and the formation are expressed as a finite summation of mode solutions. The unknown

coefficients are determined by satisfying the boundary conditions at the fluid-solid interface in a least square sense. The Reichel et al. (1991) algorithm is incorporated into the formulation, achieving both accuracy and computational speed. This technique requires arithmetic operations on the order of $O(J)$ as compared to the boundary integral equation method which needs $O(J^2)$ arithmetic operations (J is the number of discrete samples on the boundary). For a circular borehole, this method reduces exactly to the one given in Chapter 2. For a borehole of any other cross-section, the relative errors in satisfying the boundary conditions are found to be negligible (of course, it is dependent on the order of truncation).

The method has also been applied to compute the synthetic sonic logs in a borehole of elliptical cross-section. Several examples have been given to demonstrate the cross-mode coupling phenomena. A monopole source excites dipole motions whose propagational properties are similar to tube waves, and a dipole source excites monopole motions whose propagational properties are similar to flexural waves.

In summary, we draw the following conclusions:

- The pressure in the fluid is sensitive to the irregularity of the borehole cross-section, while the solid displacement in the formation is less affected.
- For both P-wave and S-wave incidences, the pressure in an elliptical borehole is larger than the pressure in an equivalent circular borehole if the incident wave is along the minor axis. It is smaller than that in an equivalent circular borehole if the incident wave is along the major axis. The relative difference in the amplitudes of the pressures is on the same order as the borehole ellipticity.
- In a borehole of arbitrary cross-section, the pressure in the fluid splits into two distinct branches depending on the azimuthal angles of the incident P- and S-waves. The larger branch is associated with incident waves close to the minor axis, while the smaller branch is associated with those near the major axis.
- In an elliptical borehole, a centered monopole source excites dipole motions in

the borehole fluid whose characteristics are similar to tube waves. A centered dipole source excites monopole motions whose characteristics are similar to flexural waves.

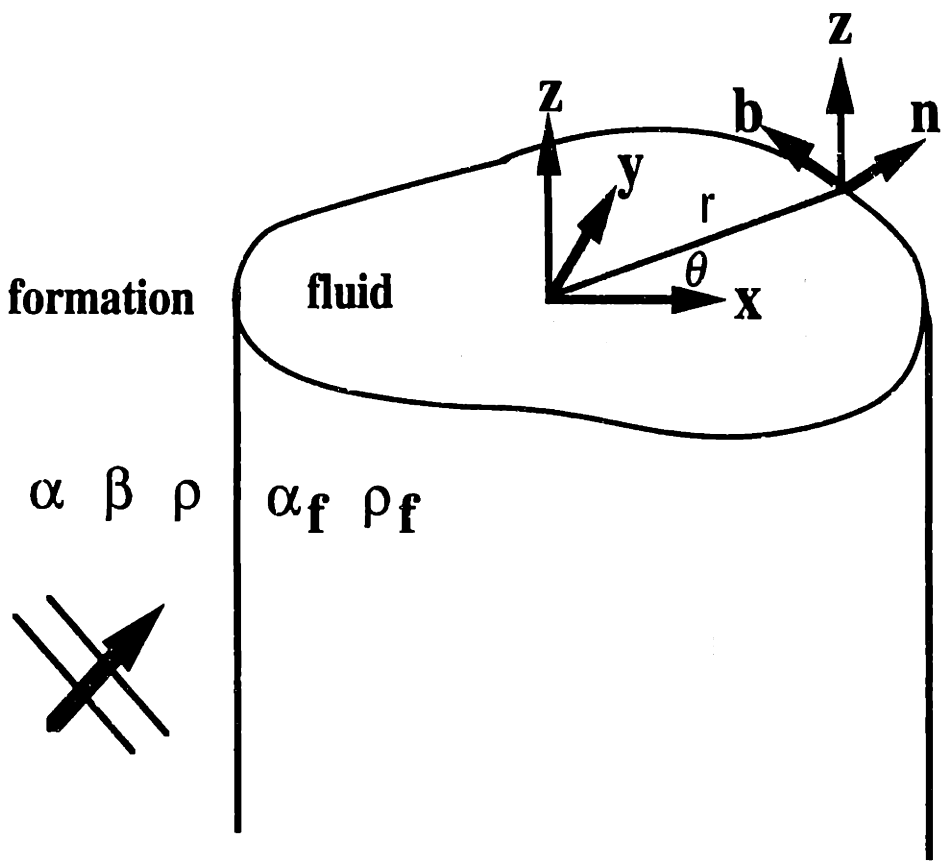

Figure 4-1: An irregular and fluid-filled borehole in a homogeneous and elastic formation. The fluid has a compressional velocity α_f and a density ρ_f. The formation has a compressional velocity α, a shear velocity β, and a density ρ. In this figure, $(\mathbf{r},\theta,\mathbf{z})$ is a cylindrical coordinate system; $(\mathbf{n},\mathbf{b},\mathbf{z})$ is a local orthogonal coordinate frame in which the boundary conditions between the fluid-solid interface are satisfied.

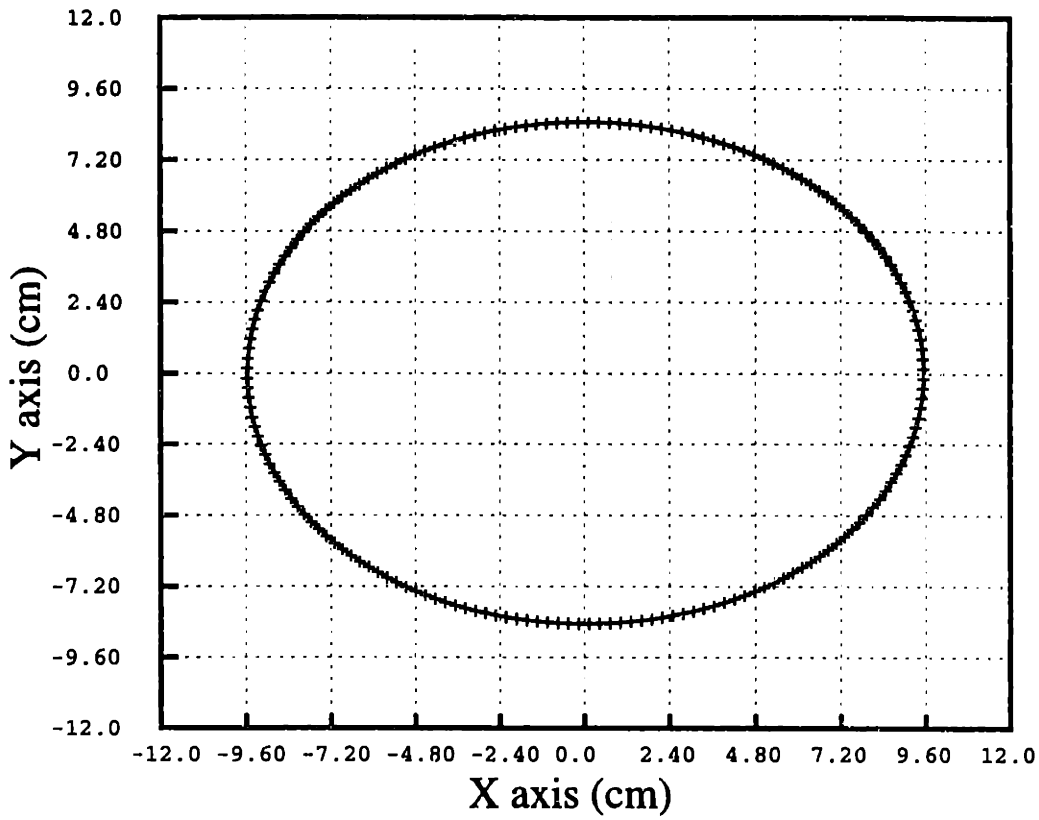

Figure 4-2: An elliptical borehole whose cross-section was determined with a downhole televiewer (adapted from Ellefsen, 1991). The major axis is 19.10 *cm*; the minor axis is 16.9 *cm*. The circumference of the borehole is divided into 180 elements.

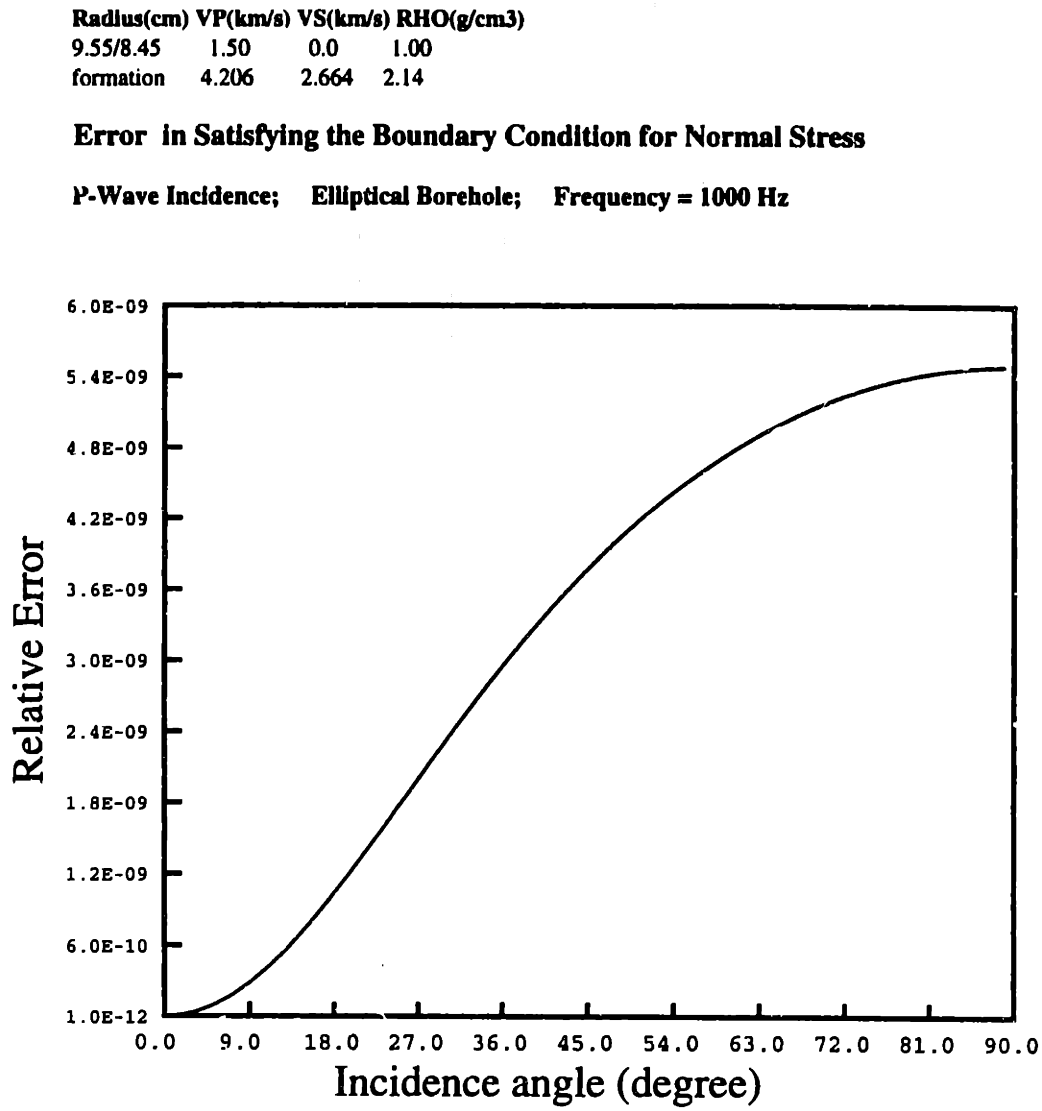

Figure 4-3: The relative error in satisfying the boundary condition as a function of angle of incidence. Shown is an example for the normal stress in the local coordinates (**n**,**b**,**z**) at the boundary. The borehole is shown in Figure 4-2. The horizontal axis is the angle of incidence. The vertical axis is the relative error in a logarithmic scale.

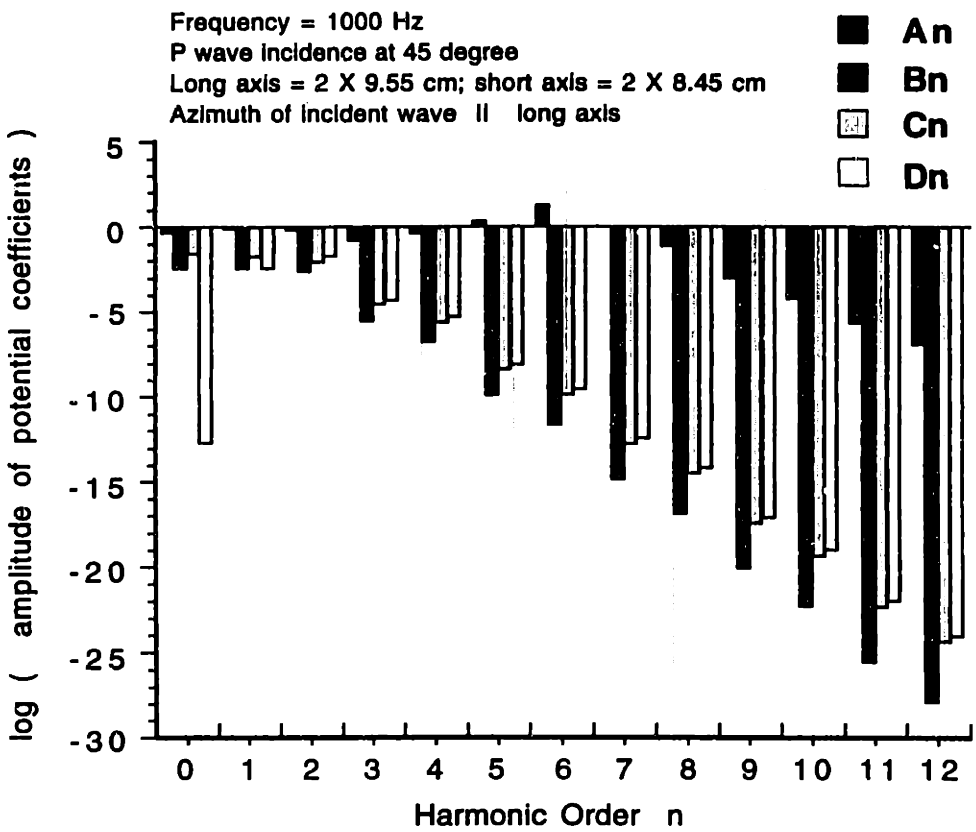

Figure 4-4: Magnitude of the coefficients $[A_n, B_n, C_n, D_n]_{n=0}^{n=N}$ in equations (4.2a)–(4.2d) at different harmonic orders n. The vertical axis is in a logarithmic scale. The calculation is done at a frequency of 1000 Hz and for a plane P-wave incidence at $\delta = 45^o$ with respect to the borehole axis. The borehole is shown in Figure 4-2.

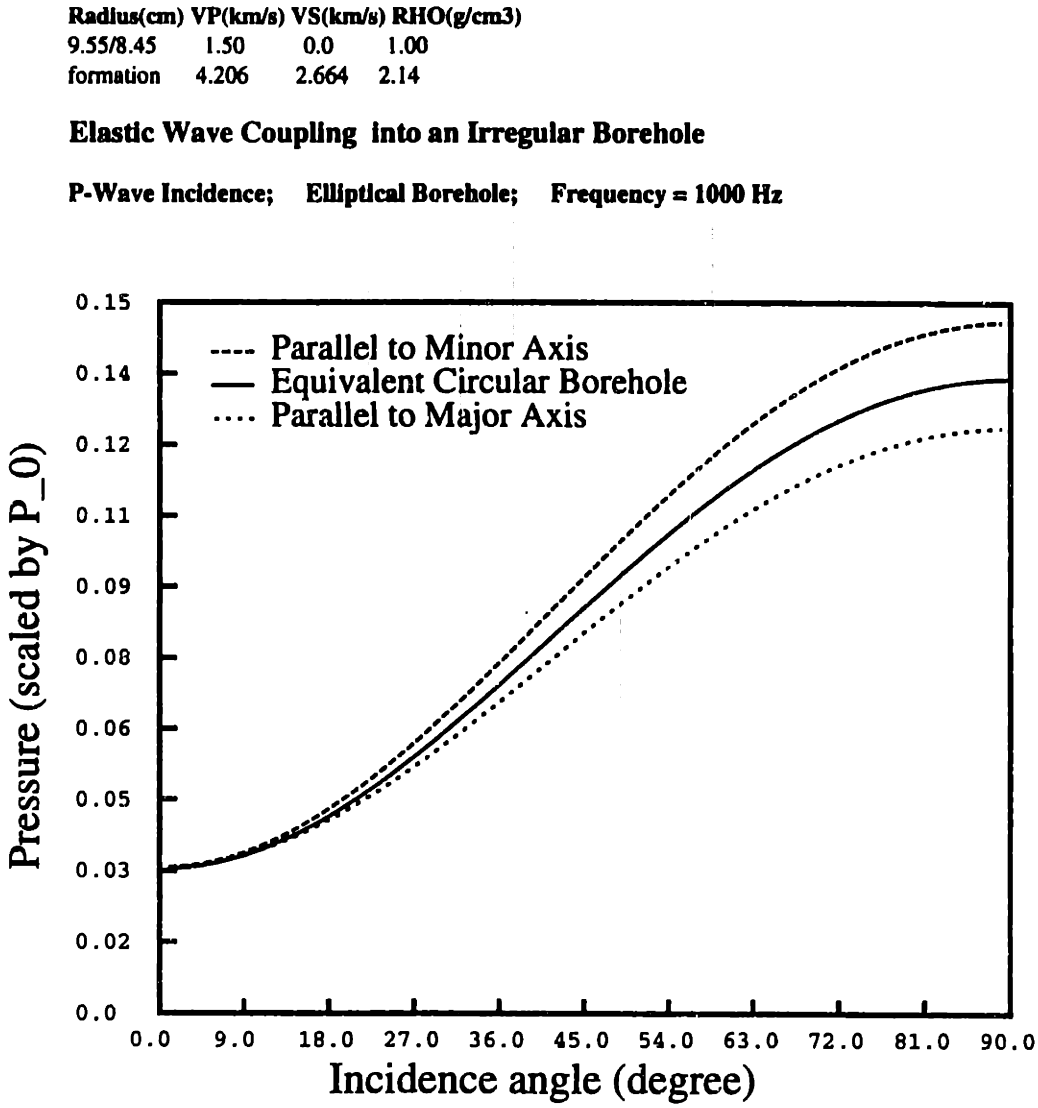

Figure 4-5: Pressure at the center of the fluid as a function of angle of incidence. The incident wave is a plane P-wave whose frequency is 1000 Hz. The formation is Berea sandstone. The pressure is scaled by the pressure of the incident P-wave. The solid line in this figure is the pressure in the fluid computed for an equivalent circular borehole. The line in long dashes is the pressure in the fluid for an incident P-wave propagating parallel to the minor axis. The line in short dashes is that for an incident P-wave propagating parallel to the major axis.

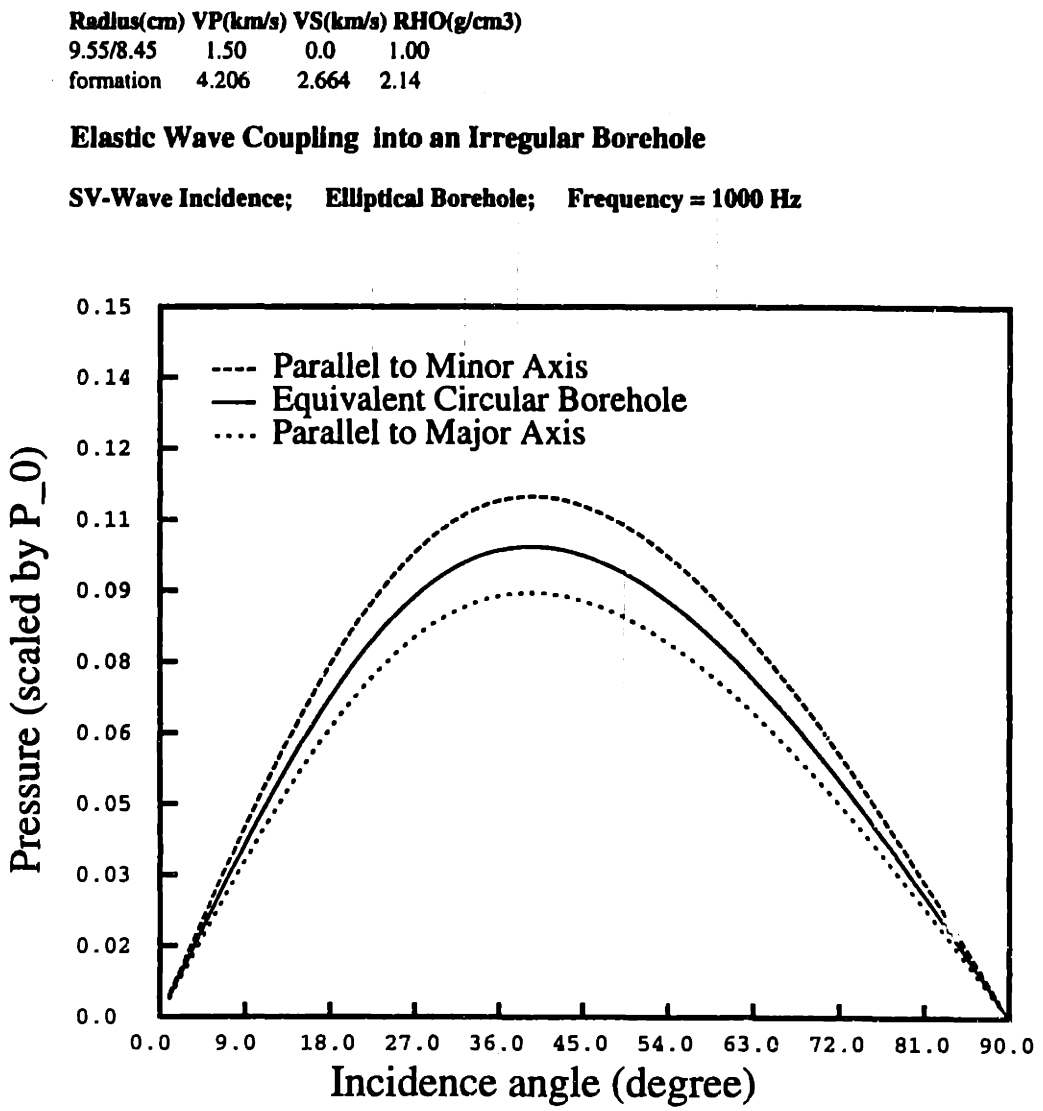

Figure 4-6: Pressure at the center of the fluid as a function of angle of incidence. The incident wave is a plane SV-wave whose frequency is 1000 Hz. The formation is Berea sandstone. The solid line in this figure is the pressure in the fluid computed for an equivalent circular borehole. The line in long dashes is the pressure in the fluid for an incident SV-wave propagating parallel to the minor axis. The line in short dashes is that for an incident SV-wave propagating parallel to the major axis.

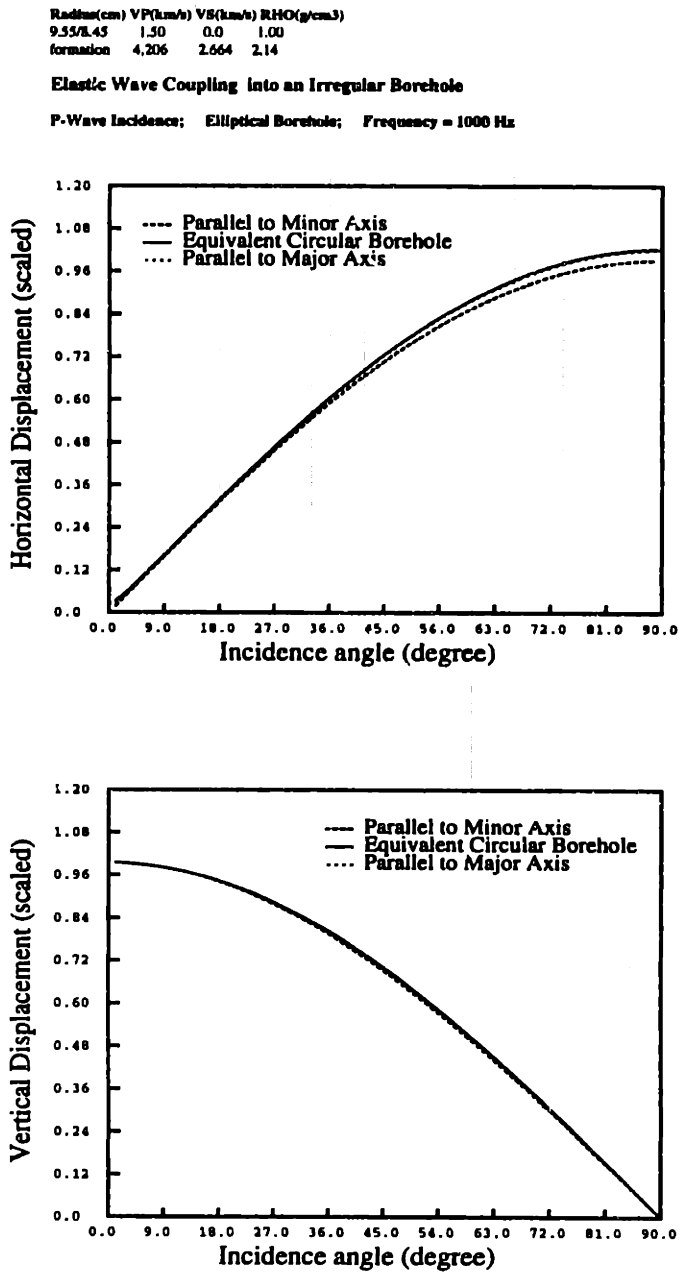

Figure 4-7: Horizontal (a) and vertical (b) components of the solid displacement at the borehole wall as a function of angle of incidence. The incident wave is a plane P-wave whose frequency is 1000 Hz. The formation is Berea sandstone. The borehole is elliptical. The displacements are scaled by the total displacement of the incident wave. The solid lines in these figures are the displacements in the formation computed for an equivalent circular borehole. The lines in long dashes are those for an incident P-wave propagating parallel to the minor axis. The lines in short dashes are those for an incident P-wave propagating parallel to the major axis.

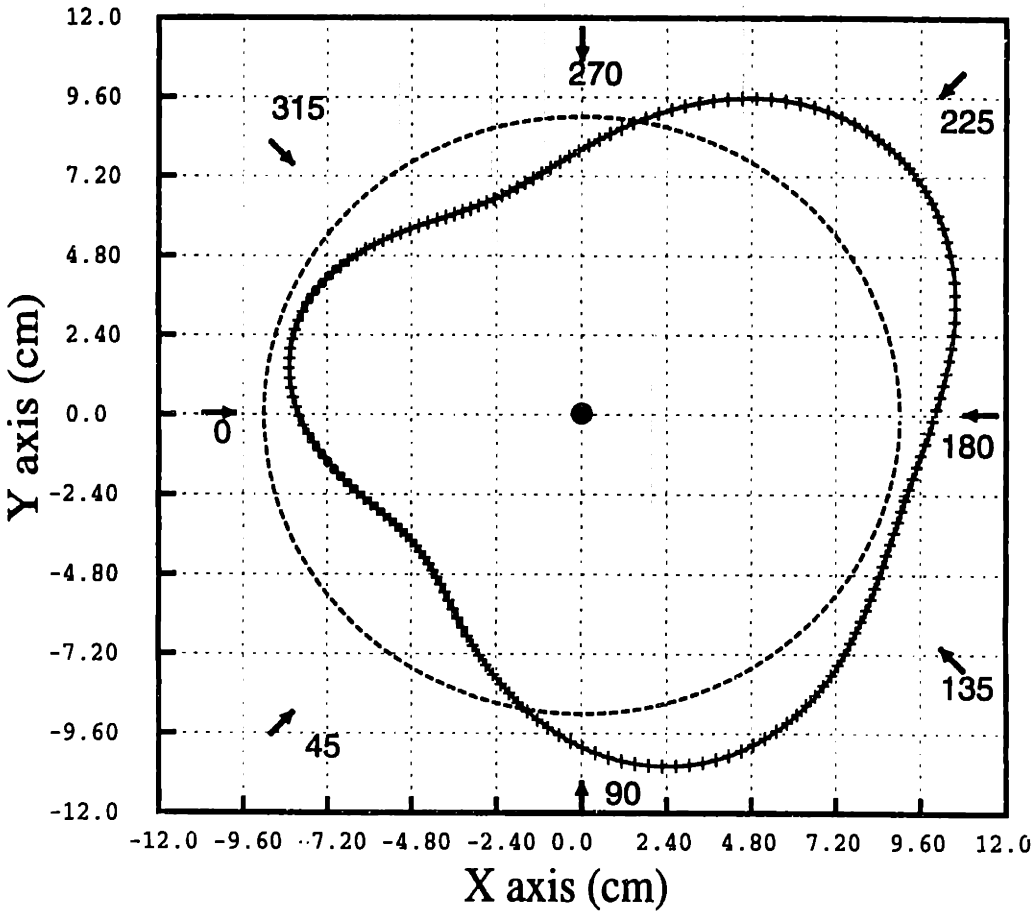

Figure 4-8: A borehole whose cross-section lacks any symmetry axis. The dashed circle in this figure is the equivalent circular borehole. The arrows are the azimuthal directions of the incident elastic wave in the formation. The dot at the center of the figure corresponds to the center of the borehole where the pressure in the fluid is computed. Also shown are 180 elements discretizing the circumference.

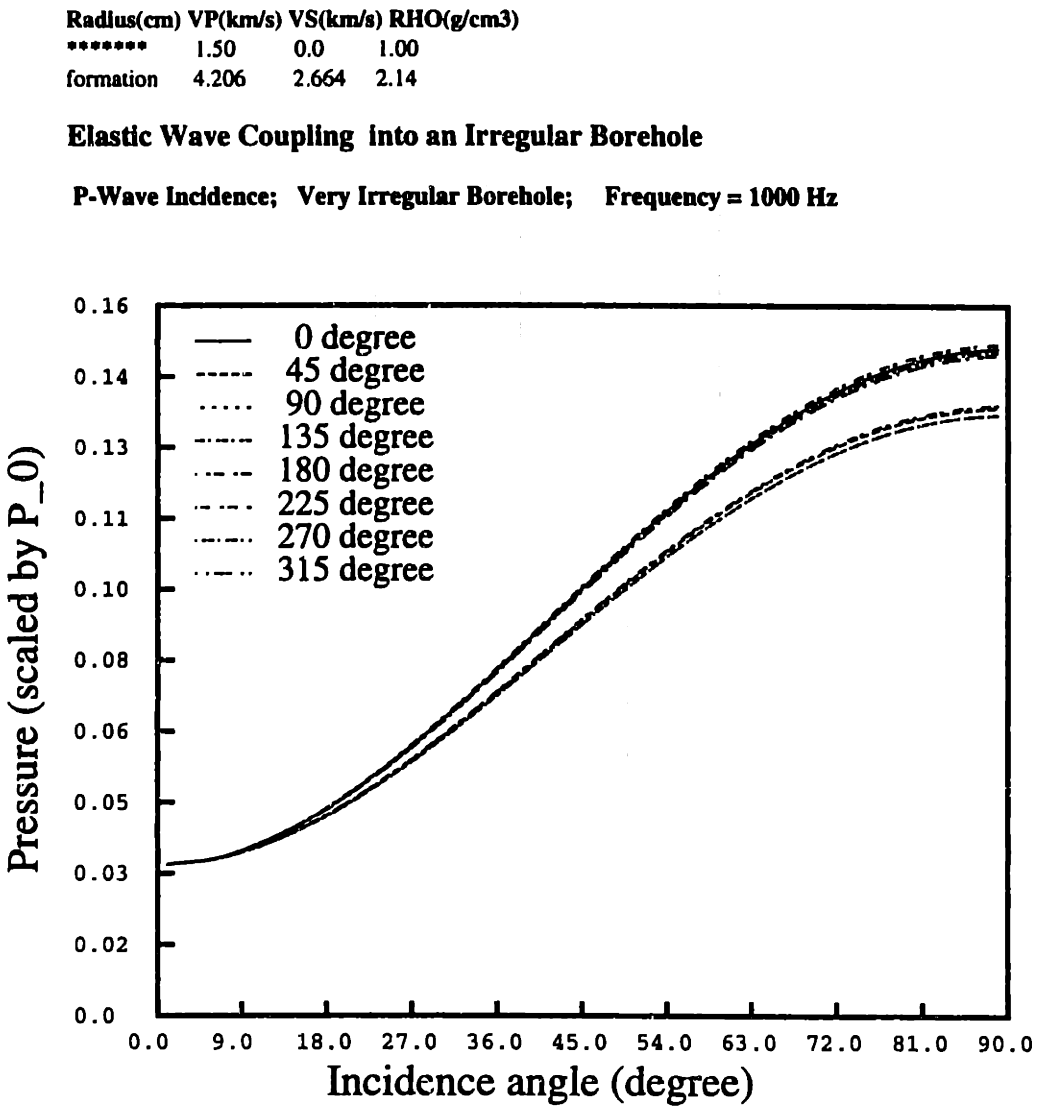

Figure 4-9: Pressure at the center of the fluid as a function of angle of incidence. The incident wave is a plane P-wave whose frequency is 1000 Hz. The formation is Berea sandstone. The borehole is shown in Figure 4-8. The pressure is scaled by the pressure of the incident P-wave. Shown in this figure are 8 curves with the azimuthal angle of the incident wave ranging from 0^o to 360^o in intervals of 45^o. The pressure in the irregular borehole splits into two distinct branches, depending on the azimuthal direction of the incident P-wave with respect to the effective major or minor axis of the borehole.

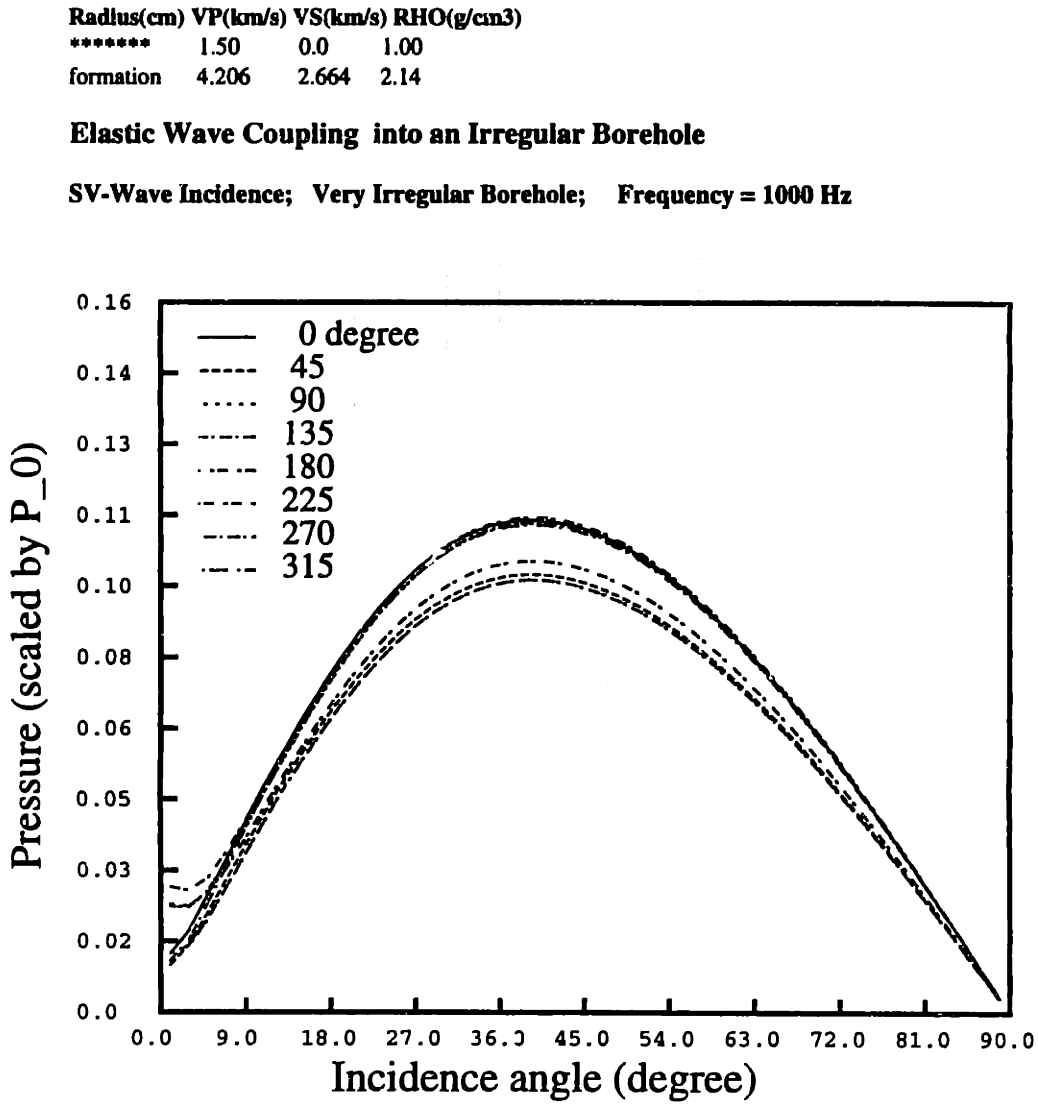

Figure 4-10: Pressure at the center of the fluid as a function of angle of incidence. The incident wave is a plane SV-wave whose frequency is 1000 Hz. The formation is Berea sandstone. The borehole is shown in Figure 4-8. A total of 8 curves are shown in this figure with the azimuthal angle of the incident wave ranging from 0^o to 360^o in intervals of 45^o. The pressure in the irregular borehole splits into two distinct branches, depending on the azimuthal direction of the incident SV-wave with respect to the effective major or minor axis of the borehole.

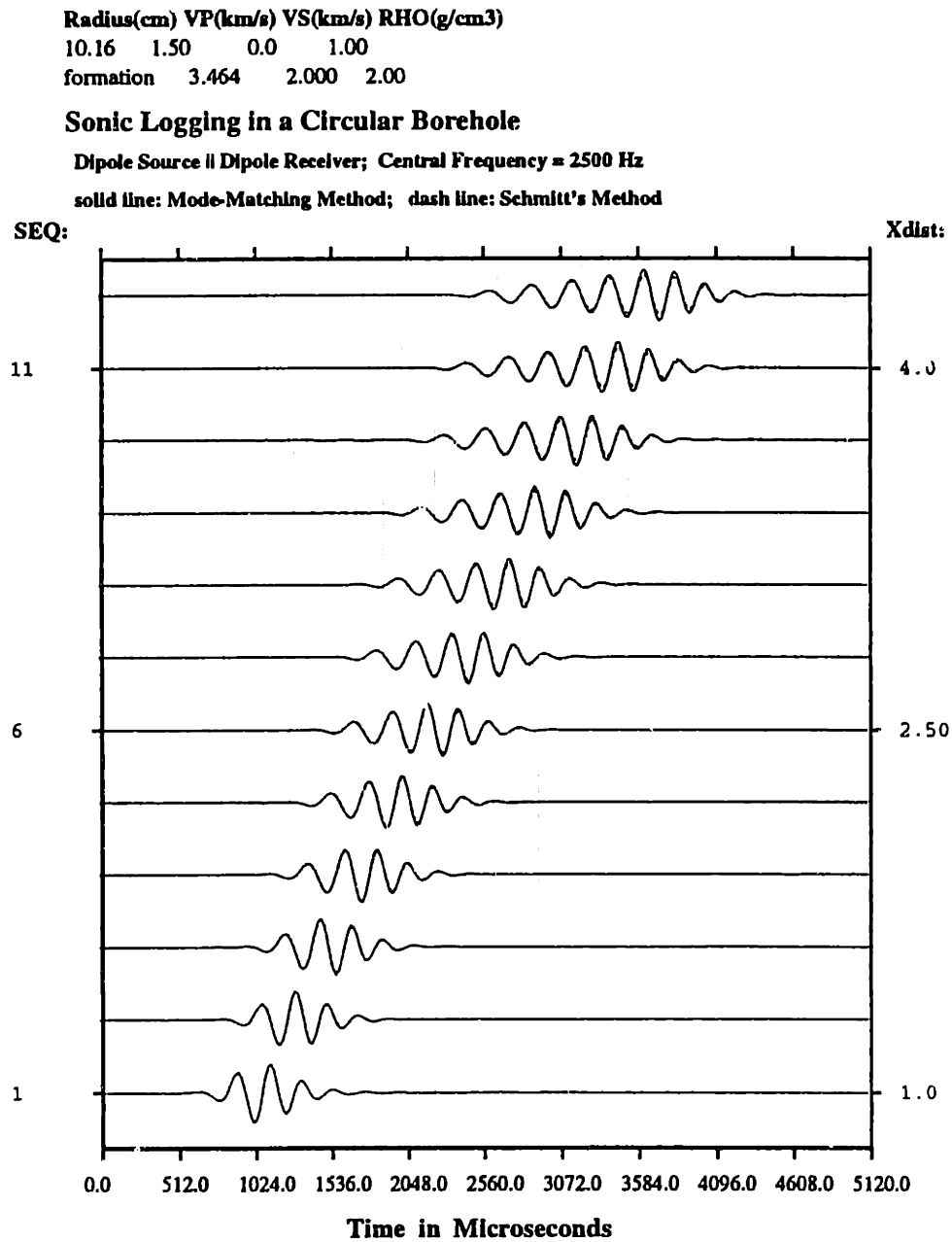

Figure 4-11: Comparison between the synthetic seismograms computed by the mode-matching method and by the classical discrete wavenumber method. The borehole is circular with a radius of 0.1016 m. The elastic parameters of the formation are: $\alpha = 3464\ m/s$, $\beta = 2000\ m/s$, and $\rho = 2.0\ g/cm^3$. A dipole source and an array of dipole receivers are used. Twelve (12) receivers are evenly distributed at offsets between 1.0 m and 4.3 m from the source. The source central frequency is 2500 Hz. The solid lines in this figure show the seismograms computed by the mode-matching method. The dashed lines are the ones computed by the discrete wavenumber method. The program for the discrete wavenumber method was written by D. P. Schmitt (1988).

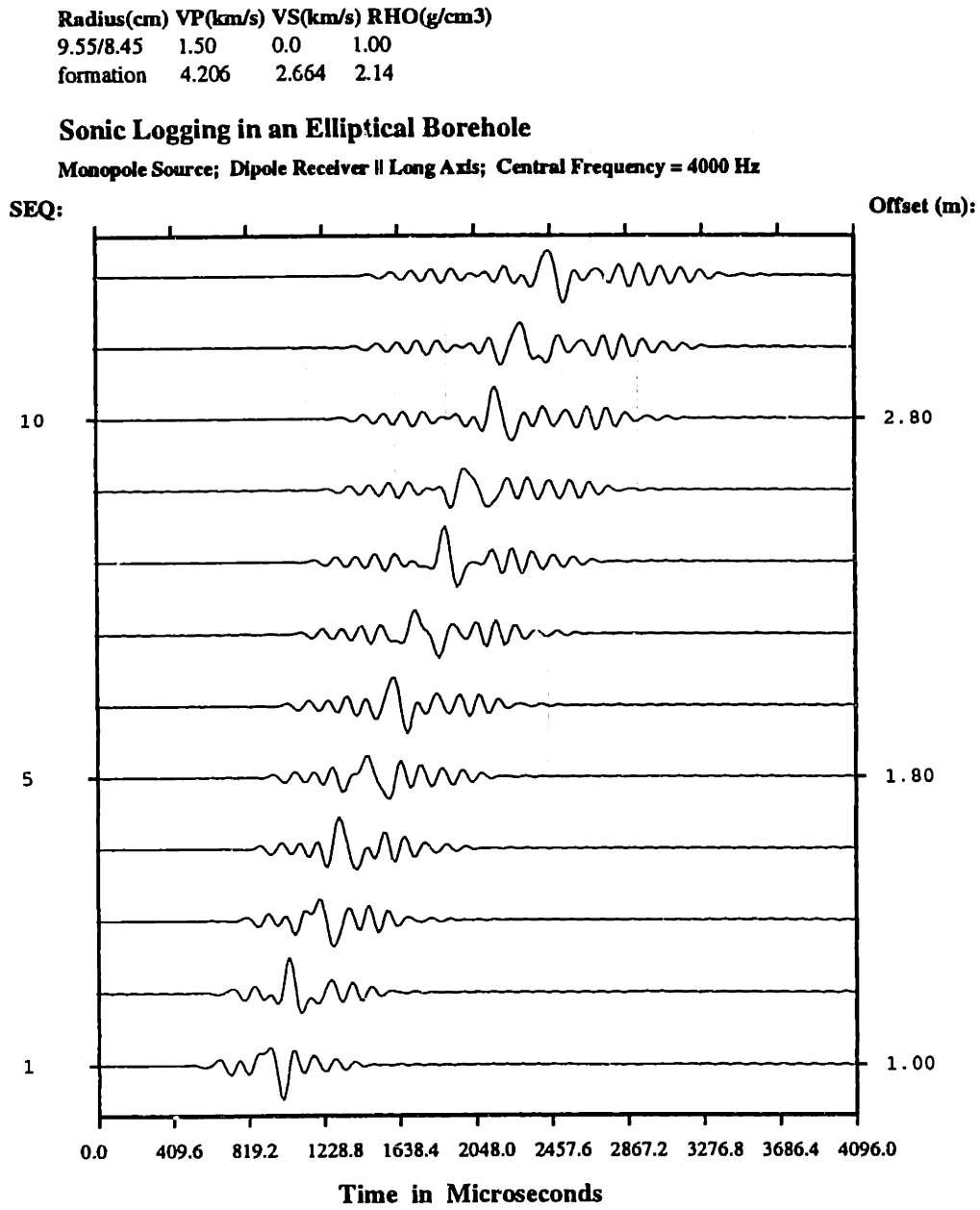

Figure 4-12: Synthetic seismograms in an elliptical borehole for a monopole source and an array of dipole receivers. The dipole receivers are polarized along the major axis of the borehole shown in Figure 4-2. The formation is Berea sandstone. The central frequency of the source is 4000 Hz. Twelve (12) receivers are evenly distributed at source-receiver offsets between 1.0 m and 3.2 m. The maximum amplitude is 0.833E+02.

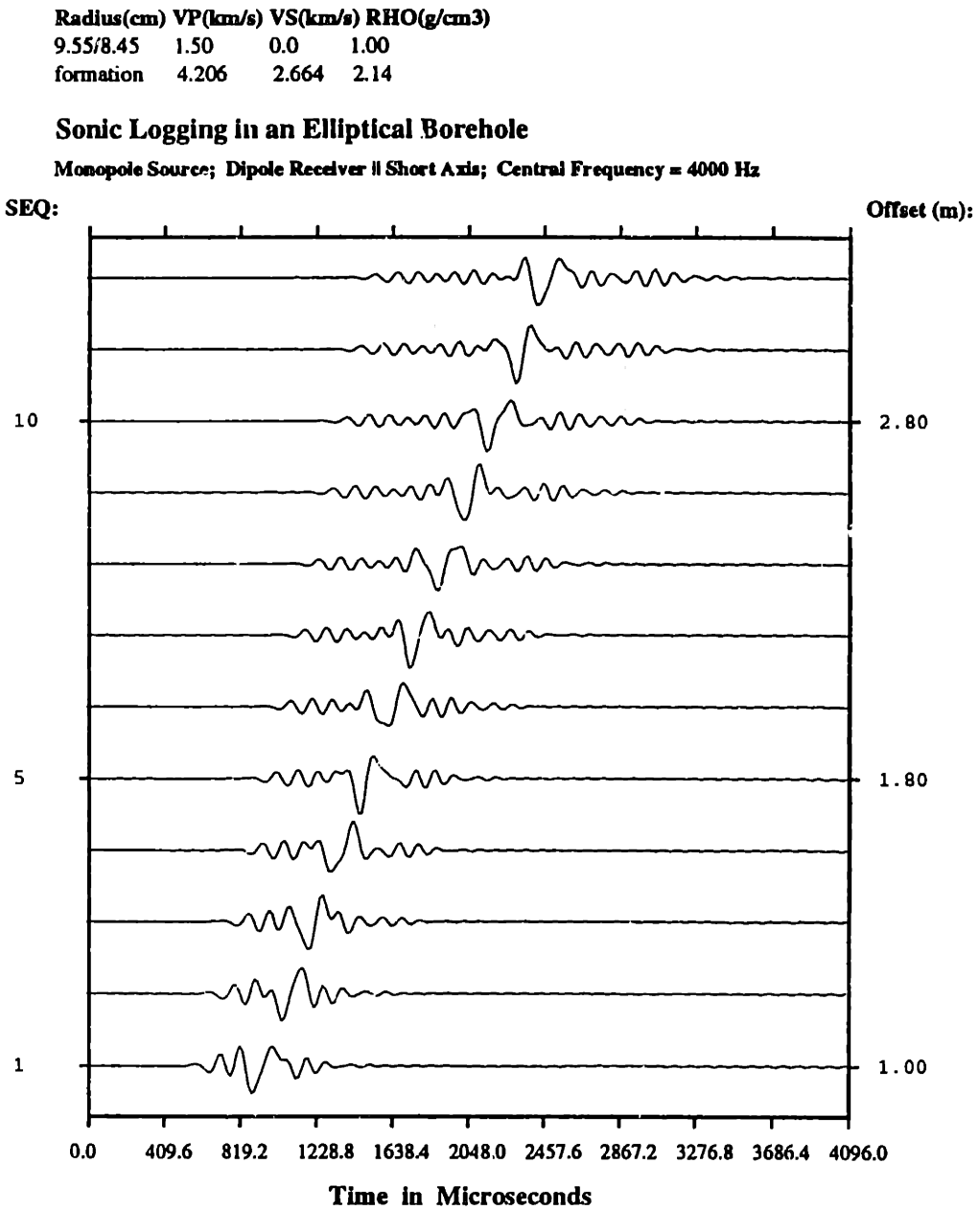

Figure 4-13: Synthetic seismograms in an elliptical borehole for a monopole source and an array of dipole receivers. The dipole receivers are polarized along the minor axis of the borehole shown in Figure 4-2. The formation is Berea sandstone. The central frequency of the source is 4000 Hz. Twelve (12) receivers are evenly distributed at source-receiver offsets between 1.0 m and 3.2 m. The maximum amplitude is 0.983E+02.

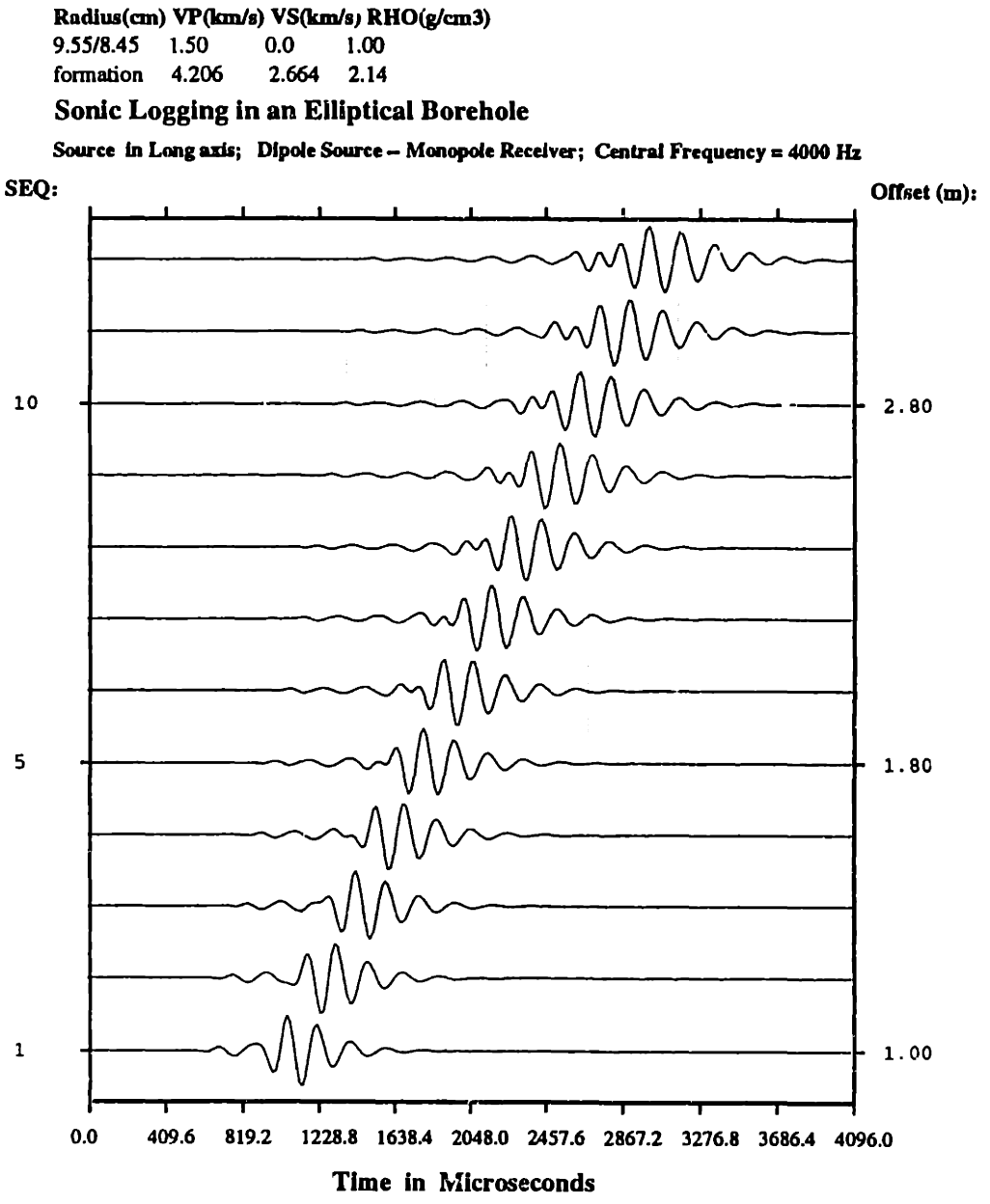

Figure 4-14: Synthetic seismograms in an elliptical borehole for a dipole source and an array of monopole receivers. The dipole source is polarized along the major axis of the borehole shown in Figure 4-2. The formation is Berea sandstone. The central frequency of the source is 4000 Hz. Twelve (12) receivers are evenly distributed at offsets between 1.0 m and 3.2 m from the source. The maximum amplitude is 0.136.

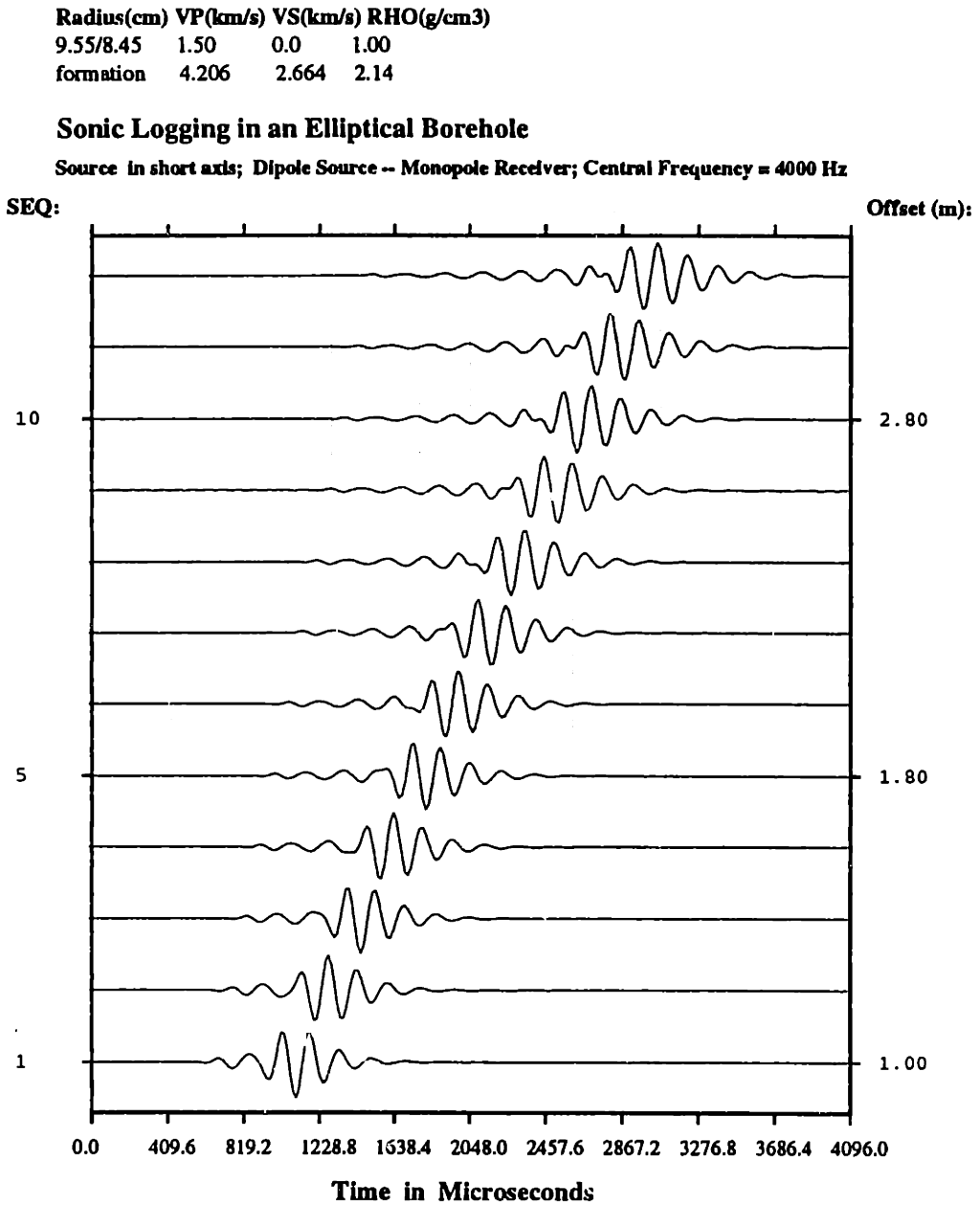

Figure 4-15: Synthetic seismograms in an elliptical borehole for a dipole source and an array of monopole receivers. The dipole source is polarized along the minor axis of the borehole shown in Figure 4-2. The formation is Berea sandstone. The central frequency of the source is 4000 Hz. Twelve (12) receivers are evenly distributed at offsets between 1.0 m and 3.2 m from the source. The maximum amplitude is 0.150.

Chapter 5

Borehole Coupling in a Stratified Formation

In the previous chapters, we have studied the borehole coupling theory, assuming that the formation properties are invariant with depth. As a further development of the theory, in this chapter we consider the case where the fluid-filled borehole is embedded in a stratified formation. The objectives are to understand the scattering of incident elastic energies from the formation into tube waves in the fluid at layer boundaries, and to develop a useful method of computing the hydrophone response in crosswell and vertical seismic profiling surveys.

Numerical simulations of elastic wave propagation in the crosswell and vertical seismic profiling configurations have been extensively studied in recent years (Wyatt, 1981; Temme and Mueller, 1982; Sullivan, 1984; Suprajitno and Greenhalgh, 1986; Schmidt et al., 1986; Aminzadeh, 1989). These methods are primarily for modeling a downhole 3-component geophone data at low frequencies. The borehole is not included in the formulations. These methods are incapable of handling events associated with the borehole fluid and yield erroneous amplitudes for direct and reflected waves refracted at the fluid-solid interface. There is presently an increased demand

for an efficient method of modelling hydrophone VSP and crosshole experiments.

Kurkjian et al. (1992) have reported a method for the modeling of crosswell seismic monopole sensor data. Our method is closely related to their technique, although it was derived independently[1].

This chapter is organized into four sections. In the first section we define the problem, review the fundamentals of borehole coupling theory, and study the propagation characteristics of acoustic waves in the fluid-filled borehole. In the second section we use the global matrix method to compute the pressure in a fluid-filled borehole for a point source in stratified media. Our technique establishes an efficient method for hydrophone data modeling at low frequencies. Its accuracy is validated by an analytical solution for the case where the formation is homogeneous. In the third section, we apply our method to simulate the Kent Cliffs borehole experiment. We find that this method predicts both the propagational and the dynamic characteristics of observed hydrophone data quite well. In the fourth section, we summarize the problem and give some conclusions.

5.1 Theoretical Formulation

5.1.1 Problem Statement

The problem we consider is a vertical fluid-filled borehole in a horizontally layered half-space. As is shown in Figure 5-1, in each layer the formation is a homogeneous elastic medium with density ρ_l, compressional wave speed α_l and shear wave speed

[1] In the 1992 annual meeting of the borehole acoustics and logging consortium, Prof. H. Schmidt (the second author of the above paper, MIT ocean engineering department) gave me a copy of their paper that was about to be presented at the coming SEG meeting in New Orleans. I read the paper and found that their idea was almost the same as my short note that I had prepared as an introduction to parallel computer application in geophysics upon Dr. Charrett's request. In the following week, I sent a copy of that short note to Prof. Schmidt via MIT interdepartmental mail.

β_l, where l denotes the layer number with $1 \leq l \leq N+1$. Here N is the total number of horizontal layers. The half space $z_N < z < \infty$ is denoted as layer $N+1$. The top surface of the l-th layer is at depth z_{l-1} and the bottom is at depth z_l. The borehole is assumed to have a finite length and is filled with a fluid that has density ρ_f and compressional wave speed α_f. Furthermore, the fluid fills only a portion of the borehole from the bottom at depth $z = H$ to the top at depth $z = z_0$ (water table), where $0 \leq z_0 \leq H$. The borehole can be either open, cased, or partially cased. In an open borehole, we use r_b to denote the radius of the borehole. In a cased borehole, there is an additional radial layer around the borehole with an inner radius r_b and an outer radius r_c. The casing is assumed to be homogeneous and elastic with compressional wave speed α_c, shear wave speed β_c, and density ρ_c. The top surface at $z = 0$ in the figure is assumed to be stress free. The goal is to compute the pressure disturbance in the fluid by the elastic wavefields radiated from a source in the formation.

We are interested in the case where the borehole radius is much smaller than the wavelength in the formation, i.e., $r_b \ll \beta_{min}/f$, where β_{min} is the minimum shear velocity in the formation and f is the frequency. For a typical choice of parameters ($r_b = 0.1016\ m$, $\beta_{min} = 2000.0\ m/s$), the frequency of an incident wave needs to be $f < 2000\ Hz$ for which the borehole radius is less than one tenth of the shortest wavelength. This condition satisfies almost all VSP and crosshole experiments (for extreme cases, see Albright et al., 1990; Worthington, 1991).

5.1.2 Borehole Coupling Equation

At low frequencies, the pressure in the fluid is homogeneous across the borehole section and is related to the deformation of an empty borehole by the following borehole coupling equation, written in frequency domain as:

$$\frac{\partial^2 P}{\partial z^2} + \frac{\omega^2}{C_T^2} P = 2\rho_f \omega^2 \epsilon_r^{(inc)}(z, \omega), \tag{5.1}$$

where $P(z,t)$ is the pressure in the fluid, C_T is the tube wave velocity in an open or a cased borehole, and $\epsilon_r^{(inc)}(z) = (\bar{u}_r(r_b,z)/r_b)^{(inc)}$ is the borehole squeeze strain. The overbar denotes an azimuthal average. The derivation has been given in section 3.2.2. In an open borehole, White (1953) gave

$$\epsilon_r^{(inc)}(z,\omega) = \frac{\sigma_{xx}(z,\omega)+\sigma_{yy}(z,\omega)}{E} - \nu\frac{\sigma_{zz}(z,\omega)}{E}, \tag{5.2}$$

where σ_{xx}, σ_{yy} and σ_{zz} are the principal stresses around the vicinity of a borehole when it is actually *absent*. E and ν are the Young's modulus and the Poisson's ratio of the formation, respectively. In a cased borehole, we obtain

$$\epsilon_r^{(inc)}(z,\omega) = \frac{\sigma_{xx}(z,\omega)+\sigma_{yy}(z,\omega)}{E_{\parallel}} - \nu\frac{\sigma_{zz}(z,\omega)}{E_{\perp}}, \tag{5.3}$$

where $E_{\parallel}$ and $E_{\perp}$ are the effective moduli of the cased borehole against radial and vertical deformations, and are given in section 3.2.3. In the case where $r_b = r_c$ or $E_c = E$ and $\nu_c = \nu$, i.e., the casing vanishes, $E_{\parallel}$ and $E_{\perp}$ reduce to E, the Young's modulus of the formation. Thus equation (5.3) reduces to equation (5.2).

5.1.3 Pressure in the Fluid

Given that $\epsilon_r^{(inc)}(z,\omega)$, the borehole squeeze strain, is known, the pressure in the fluid can be obtained from equation (5.1). In a segment of the fluid column that is in the depth range of the m-th layer of the formation, i.e., $z_{m-1} \le z \le z_m$ where z_{m-1} and z_m are the depths of the top and the bottom of the m-th layer respectively, the pressure is determined by

$$P(z,\omega) = A_m e^{-ik_m z} + B_m e^{ik_m z} + \rho_f\omega^2 \int_{z_{m-1}}^{z_m} \epsilon_r^{(inc)}(z',\omega)\ \frac{i}{k_m} e^{-ik_m|z-z'|}dz', \tag{5.4}$$

where $k_m = \omega/C_T$ is the Stoneley wavenumber in the fluid associated with the m-th layer, A_m and B_m are unknown coefficients representing the up-going and down-going energies in the fluid. The Green's function used in deriving this equation can be found in Morse and Feshbach (1953) (pp. 811).

The boundary conditions for determining A_m and B_m are the continuity of pressure between layers m and $m+1$:

$$A_m e^{-ik_m z_m} + B_m e^{ik_m z_m} + w_m(z_m) = A_{m+1} e^{-ik_{m+1} z_m} + B_{m+1} e^{ik_{m+1} z_m} + w_{m+1}(z_m), \quad (5.5)$$

and the continuity of fluid velocity between layers m and $m+1$:

$$\begin{aligned} -ik_m A_m e^{-ik_m z_m} \; + \; ik_m B_m e^{ik_m z_m} + \frac{dw_m(z_m)}{dz} = \\ - \; ik_{m+1} A_{m+1} e^{-ik_{m+1} z_m} + ik_{m+1} B_{m+1} e^{ik_{m+1} z_m} + \frac{dw_{m+1}(z_m)}{dz}, \end{aligned} \quad (5.6)$$

where $w_m(z)$ denotes the third term on the right-hand side of equation (5.4), i.e.,

$$\begin{aligned} w_m(z) &= \rho_f \omega^2 \int_{z_{m-1}}^{z_m} \epsilon_r^{(inc)}(z', \omega) \frac{i}{k_m} e^{-ik_m |z - z'|} dz', \quad (5.7) \\ &= i \frac{\rho_f \omega^2}{k_m} \left[\int_{z_{m-1}}^{z} \epsilon_r^{(inc)}(z', \omega) \; e^{-ik_m (z - z')} dz' + \int_{z}^{z_m} \epsilon_r^{(inc)}(z', \omega) \; e^{+ik_m (z - z')} dz' \right]. \end{aligned}$$

In addition, the stress at the top of the borehole fluid (water table) vanishes:

$$P(z_0, \omega) = 0, \quad (5.8)$$

and the well bottom is assumed to be rigid:

$$\frac{dP(H, \omega)}{dz} = 0. \quad (5.9)$$

As a reminder, z_0 is the depth of the water table and H is the depth of the well bottom.

The boundary conditions yield the following set of linear equations for the unknown coefficients:

$$\underline{\underline{D}} \, \underline{q} = \underline{c}, \quad (5.10)$$

where

$$\underline{\underline{D}} = \begin{pmatrix} e^{-ik_I z_0}, & e^{ik_I z_0}, & & & & & \\ & & e^{-ik_m z_m}, & e^{ik_m z_m}, & -e^{-ik_{m+1} z_m}, & -e^{ik_{m+1} z_m}, & \\ & & -ik_m e^{-ik_m z_m}, & ik_m e^{ik_m z_m}, & ik_{m+1} e^{-ik_{m+1} z_m}, & -ik_{m+1} e^{ik_{m+1} z_m}, & \\ & & & & & -ik_J e^{-ik_J H}, & ik_J e^{ik_J H} \end{pmatrix},$$

$$\underline{q} = (\ A_I, B_I, ..., A_m, B_m, A_{m+1}, B_{m+1}, ..., A_J, B_J\ )^T,$$

and

$$\underline{c} = (-w_I(z_0), ..., w_{m+1}(z_m) - w_m(z_m), \frac{dw_{m+1}(z_m)}{dz} - \frac{dw_m(z_m)}{dz}, ..., -\frac{dw_J(H)}{dz}\ )^T.$$

Here I is the index of the layer in which the water table is (i.e., $z_{I-1} \leq z_0 < z_I$), and J is the index of the layer in which the well bottom is (i.e., $z_{J-1} < H \leq z_J$). It is assumed that $1 \leq I \leq m \leq J \leq N+1$.

5.2 Point Source in a Stratified Formation

In this section we proceed to compute the pressure in the borehole fluid for a point source in a stratified formation. The pressure in the fluid can be easily obtained by solving the matrix equation (5.10) if the borehole squeeze strains are known. To determine the borehole squeeze strain $\epsilon_r^{(inc)}(z,\omega)$ in equation (5.2) for an open borehole, or in equation (5.3) for a cased borehole, we need to compute the stresses at the location of the borehole when it is *absent*. This is a much easier problem than the original one involving a fluid-filled borehole. For a stratified medium, the Thomson-Haskell type propagator matrix method can be used to achieve this goal (Harkrider, 1964; Takeuchi and Saito, 1972; Kennett and Kerry, 1979; Ben-Menahem and Singh, 1981). We adopt an approach that combines the discrete wavenumber method (Bouchon, 1981; Dietrich et al., 1985) with the global matrix method (Chin et al., 1984, Schmidt et al., 1986) to efficiently and accurately compute the stress and displacement fields in a stratified half space.

5.2.1 The Global Matrix Method

Consider a vertically stratified half-space with a source located on the coordinate axis at depth $z = \eta_s$ (see Figure 5-1 without the borehole). In terms of the surface vector

harmonics in the cylindrical coordinate system (R, θ, z), the displacement $\underline{u}$ and traction $\underline{t}$ across a surface perpendicular to the z-axis can be expressed as (Takeuchi and Saito, 1972; Chin et al., 1984):

$$\underline{u}\,(R,\theta,z) = \frac{1}{2\pi}\int_{-\infty}^{\infty} d\omega\, e^{i\omega t}\int_0^{\infty} k\,dk \sum_{m=-\infty}^{\infty} (U\,\mathbf{R_k^m} + V\,\mathbf{S_k^m} + W\,\mathbf{T_k^m}), \qquad (5.11)$$

and

$$\underline{t}\,(R,\theta,z) = \frac{1}{2\pi}\int_{-\infty}^{\infty} d\omega\, e^{i\omega t}\int_0^{\infty} k\,dk \sum_{m=-\infty}^{\infty} (P\,\mathbf{R_k^m} + S\,\mathbf{S_k^m} + T\,\mathbf{T_k^m}), \qquad (5.12)$$

where $\mathbf{R_k^m}, \mathbf{S_k^m}$ and $\mathbf{T_k^m}$ are vector harmonics in a cylindrical coordinate. U, V, W, P, S and T are functions of depth z, horizontal wavenumber k, order of harmonics m, and frequency ω. They are related to each other by a first order matrix equation

$$\frac{\partial}{\partial z}\underline{\mathrm{B}} = \underline{\underline{\mathrm{A}}}\,(z;k,\omega)\,\underline{\mathrm{B}},$$

where $\underline{\mathrm{B}} = (U,\ V,\ P,\ S)^T$ is the displacement-stress vector for a P-SV problem and $\underline{\mathrm{B}} = (W,\ T)^T$ for a SH problem. In this paper we focus our attention to the P-SV problem only. In this case

$$\underline{\underline{\mathrm{A}}}\,(z;k,\omega) = \begin{bmatrix} 0 & k(1-2\gamma) & 1/(\lambda+2\mu) & 0 \\ -k & 0 & 0 & 1/\mu \\ -\rho\omega^2 & 0 & 0 & k \\ 0 & -\rho\omega^2 + 4k^2\mu(1-\gamma) & -k((1-2\gamma) & 0 \end{bmatrix},$$

where $\gamma = \mu/(\lambda+2\mu) = \beta^2/\alpha^2$, λ and μ are the Lamé parameters and ρ is the density. They are dependent on z.

The surface vector harmonics are given by

$$\mathbf{R_k^m} = \underline{e}_z Y_k^m(R,\theta),$$

$$\mathbf{S_k^m} = \frac{1}{k}\nabla_1 Y_k^m(R,\theta),$$

$$\mathbf{T_k^m} = -\frac{1}{k}\underline{e}_z \times \nabla_1 Y_k^m(R,\theta),$$

$$Y_k^m(R,\theta) = J_m(kR)e^{im\theta},$$

$$\nabla_1 = \underline{e}_R \frac{\partial}{\partial R} + \underline{e}_\theta \frac{\partial}{R \partial \theta}.$$

where $\underline{e}_z$, $\underline{e}_R$ and $\underline{e}_\theta$ are the unit vectors in the cylindrical coordinates. $J_m(x)$ is the Bessel function of the first kind (Abramowitz and Stegun, 1965).

For the case where the formation is layered, the elements of matrix $\underline{\underline{A}}$ are piecewise constant such that the resulting equation has constant coefficients in each subinterval as

$$\frac{d}{dz}\underline{B}_l = \underline{\underline{A}}_l \underline{B}_l, \quad z_{l-1} < z < z_l, l = 1, 2, 3, ..., N \tag{5.13}$$

where N is the total number of layers. In forming a global matrix solution to equation (5.13), the continuity of the local solution at an interface is required, i.e.,

$$\underline{B}_l(z_l^-) = \underline{B}_{l+1}(z_l^+), \quad l = 1, 2, ..., N$$

In addition, the free surface condition at $z = 0$ and the radiation condition at $z \to \infty$ must be satisfied. The source is introduced as an equivalent discontinuity in the stress-displacement field across the source plane $z = \eta_s$ (Kennett and Kerry, 1979, Chin et al., 1984):

$$\underline{B}(\eta_s^+) - \underline{B}(\eta_s^-) = \underline{S}^*,$$

where, for a point volume source $\underline{S}^* = (-2, 0, 0, -4\mu k)^T$ (Harkrider, 1964); and for a vertical point force $\underline{S}^* = (0, 0, -\frac{1}{2\pi}, 0)^T$ (Harkrider, 1964; Bouchon, 1981).

Using the spectral decomposition of $\underline{\underline{A}}_l = \underline{\underline{D}}_l \underline{\underline{\Lambda}}_l \underline{\underline{D}}_l^{-1}$, we can rewrite equation (5.13) as

$$\frac{d}{dz}\underline{Q}_l = \underline{\underline{\Lambda}}_l \underline{Q}_l, \quad z_{l-1} < z < z_l, l = 1, 2, ..., N \tag{5.14}$$

where $\underline{Q}_l = \underline{\underline{D}}_l^{-1} \underline{B}_l$. In the P - SV problem the choice of

$$\underline{\underline{D}}_l = \begin{bmatrix} \nu_{\alpha l} & k & \nu_{\alpha l} & k \\ -k & -\nu_{\beta l} & k & \nu_{\beta l} \\ -\mu_l(2k^2 - k_{\beta l}^2) & -2\mu_l k \nu_{\beta l} & \mu_l(2k^2 - k_{\beta l}^2) & 2\mu_l k \nu_{\beta l} \\ 2\mu_l k \nu_{\alpha l} & \mu_l(2k^2 - k_{\beta l}^2) & 2\mu_l k \nu_{\alpha l} & \mu_l(2k^2 - k_{\beta l}^2) \end{bmatrix}$$

leads to

$$\underline{\underline{\Lambda}}_l = \begin{bmatrix} -\nu_{\alpha l} & & & \\ & -\nu_{\beta l} & & \\ & & \nu_{\alpha l} & \\ & & & \nu_{\beta l} \end{bmatrix},$$

where $\nu_{\alpha l} = \sqrt{k^2 - k_{\alpha l}^2}$, $\nu_{\beta l} = \sqrt{k^2 - k_{\beta l}^2}$, $k_{\alpha l} = \omega/\alpha_l$, $k_{\beta l} = \omega/\beta_l$. α_l and β_l are the compressional and shear velocities in the layer l. The choice of branch cuts is $\mathbf{R}(\nu_{\alpha l}) > 0$ and $\mathbf{R}(\nu_{\beta l}) > 0$ for the particular choice of $e^{i\omega t}$ time dependence.

The solution to equation (5.14) can be written in terms of a propagator matrix

$$\underline{\mathbf{Q}}_l(z) = \exp[\underline{\underline{\Lambda}}_l(z - z_{l-1})]\ \underline{\mathbf{Q}}_l(z_{l-1}^+),\ \ z_{l-1} < z < z_l, l = 1, 2, ..., N \qquad (5.15)$$

which relates the wave field at the boundary to that in the interior. Knowing the vector $\underline{\mathbf{Q}}_l(z)$ at the boundaries, the displacement-stress vector $\underline{\mathbf{B}}_l(z)$ can be readily computed by

$$\underline{\mathbf{B}}_l(z) = \underline{\underline{\mathbf{D}}}_l\ \exp[\underline{\underline{\Lambda}}_l(z - z_{l-1})]\ \underline{\mathbf{Q}}_l(z_{l-1}^+). \qquad (5.16)$$

To determine $\underline{\mathbf{Q}}_l(z_{l-1}^+)$, the up-going and down-going amplitudes at the top boundary of the l-th layer, continuities of stress and displacements across the interfaces are imposed in addition to vanishing stresses at the free surface and the radiation condition at infinity. Let's denote

$$\underline{\underline{\mathbf{D}}}_l = \begin{bmatrix} \underline{\underline{\mathbf{M}}}_l^- & \underline{\underline{\mathbf{M}}}_l^+ \\ \underline{\underline{\mathbf{N}}}_l^- & \underline{\underline{\mathbf{N}}}_l^+ \end{bmatrix},$$

$$\exp[\underline{\underline{\Lambda}}_l(z_l - z_{l-1})] = \begin{bmatrix} \underline{\underline{\mathbf{E}}}_l & \\ & \underline{\underline{\mathbf{E}}}_l^{-1} \end{bmatrix},$$

where

$$\underline{\underline{\mathbf{E}}}_l = \begin{bmatrix} \exp(-\nu_{\alpha l}(z_l - z_{l-1})) & 0 \\ 0 & \exp(-\nu_{\beta l}(z_l - z_{l-1})) \end{bmatrix}.$$

Also denote

$$\underline{\mathbf{Q}}_l = \begin{bmatrix} \underline{\mathbf{p}}_l^- \\ \underline{\mathbf{p}}_l^+ \end{bmatrix},$$

where $\underline{\mathbf{p}}_l^- = \begin{bmatrix} p_l^- \\ q_l^- \end{bmatrix}$ corresponds to the down-going amplitude and $\underline{\mathbf{p}}_l^+ = \begin{bmatrix} p_l^+ \\ q_l^+ \end{bmatrix}$ corresponds to the up-going amplitude. Then the interface boundary conditions can be written as

$$\begin{bmatrix} \underline{\underline{\mathbf{M}}}_{l+1}^- & \underline{\underline{\mathbf{M}}}_{l+1}^+ \\ \underline{\underline{\mathbf{N}}}_{l+1}^- & \underline{\underline{\mathbf{N}}}_{l+1}^+ \end{bmatrix} \begin{bmatrix} \underline{\mathbf{p}}_{l+1}^- \\ \underline{\mathbf{p}}_{l+1}^+ \end{bmatrix} - \begin{bmatrix} \underline{\underline{\mathbf{M}}}_l^- & \underline{\underline{\mathbf{M}}}_l^+ \\ \underline{\underline{\mathbf{N}}}_l^- & \underline{\underline{\mathbf{N}}}_l^+ \end{bmatrix} \begin{bmatrix} \underline{\underline{\mathbf{E}}}_l & \\ & \underline{\underline{\mathbf{E}}}_l^{-1} \end{bmatrix} \begin{bmatrix} \underline{\mathbf{p}}_l^- \\ \underline{\mathbf{p}}_l^+ \end{bmatrix} = \underline{\mathbf{0}}, \qquad (5.17)$$

except the source layer $l = s$ at which

$$\begin{bmatrix} \underline{\underline{\mathbf{M}}}_{s+1}^- & \underline{\underline{\mathbf{M}}}_{s+1}^+ \\ \underline{\underline{\mathbf{N}}}_{s+1}^- & \underline{\underline{\mathbf{N}}}_{s+1}^+ \end{bmatrix} \begin{bmatrix} \underline{\mathbf{p}}_{s+1}^- \\ \underline{\mathbf{p}}_{s+1}^+ \end{bmatrix} - \begin{bmatrix} \underline{\underline{\mathbf{M}}}_s^- & \underline{\underline{\mathbf{M}}}_s^+ \\ \underline{\underline{\mathbf{N}}}_s^- & \underline{\underline{\mathbf{N}}}_s^+ \end{bmatrix} \begin{bmatrix} \underline{\underline{\mathbf{E}}}_s & \\ & \underline{\underline{\mathbf{E}}}_s^{-1} \end{bmatrix} \begin{bmatrix} \underline{\mathbf{p}}_s^- \\ \underline{\mathbf{p}}_s^+ \end{bmatrix}$$

$$= \underline{\underline{\mathbf{D}}}_s \exp[\underline{\underline{\Lambda}}(z_s - \eta_s)] \underline{\underline{\mathbf{D}}}_s^{-1} \underline{\mathbf{S}}^*. \qquad (5.18)$$

At $z = 0$, we have the stress free conditions

$$\underline{\underline{\mathbf{N}}}_1^- \underline{\mathbf{p}}_1^- + \underline{\underline{\mathbf{N}}}_1^+ \underline{\mathbf{p}}_1^+ = \underline{\mathbf{0}}, \qquad (5.19)$$

and at $z \to \infty$, we must impose

$$\underline{\mathbf{p}}_{N+1}^+ = \underline{\mathbf{0}}. \qquad (5.20)$$

To cast the boundary conditions into a global matrix equation, we assemble the local coefficients into a global vector

$$\underline{\mathbf{O}} = (\underline{\mathbf{p}}_1^-, \underline{\mathbf{p}}_1^+, ..., \underline{\mathbf{p}}_N^-, \underline{\mathbf{p}}_N^+, \underline{\mathbf{p}}_{N+1}^-)^t,$$

of dimension $4N + 2$, consisting of the amplitudes of down-going and up-going P-SV

waves in individual layers. This vector solves the following linear system

$$\begin{bmatrix}
\underline{\underline{N}}_1^- & \underline{\underline{N}}_1^+ & & & & & \\
\underline{\underline{M}}_1^- \underline{\underline{E}}_1 & \underline{\underline{M}}_1^+ \underline{\underline{E}}_1^- & -\underline{\underline{M}}_2^- & -\underline{\underline{M}}_2^+ & & & \\
\underline{\underline{N}}_1^- \underline{\underline{E}}_1 & \underline{\underline{N}}_1^+ \underline{\underline{E}}_1^- & -\underline{\underline{N}}_2^- & -\underline{\underline{N}}_2^+ & & & \\
 & & & & & & \\
 & & \underline{\underline{M}}_s^- \underline{\underline{E}}_s & \underline{\underline{M}}_s^+ \underline{\underline{E}}_s^- & -\underline{\underline{M}}_{s+1}^- & -\underline{\underline{M}}_{s+1}^+ & \\
 & & \underline{\underline{N}}_s^- \underline{\underline{E}}_s & \underline{\underline{N}}_s^+ \underline{\underline{E}}_s^- & -\underline{\underline{N}}_{s+1}^- & -\underline{\underline{N}}_{s+1}^+ & \\
 & & & & & & \\
 & & & & \underline{\underline{M}}_N^- \underline{\underline{E}}_N & \underline{\underline{M}}_N^+ \underline{\underline{E}}_N^- & -\underline{\underline{M}}_{N+1}^- \\
 & & & & \underline{\underline{N}}_N^- \underline{\underline{E}}_N & \underline{\underline{N}}_N^+ \underline{\underline{E}}_N^- & -\underline{\underline{N}}_{N+1}^-
\end{bmatrix}
\underline{Q} =
\begin{bmatrix}
\underline{0} \\ \underline{0} \\ \underline{0} \\ \\ \underline{\sigma}^- \\ \underline{\sigma}^+ \\ \\ \underline{0} \\ \underline{0}
\end{bmatrix}$$

where

$$\underline{\sigma} = \begin{bmatrix} \underline{\sigma}^- \\ \underline{\sigma}^+ \end{bmatrix} = -\underline{\underline{D}}_s \exp[\underline{\underline{\Lambda}}(z_s - \eta_s)] \underline{\underline{D}}_s^{-1} \underline{S}^*.$$

Remark 1: The following transformation and substitution are employed in the implementation of the global matrix algorithm. Let's define a $(4N+2) \times (4N+2)$ matrix $\underline{\underline{F}}$ as

$$\underline{\underline{F}} = \begin{bmatrix}
\underline{\underline{I}} & & & & \\
 & \underline{\underline{E}}_1 & & \underline{0} & \\
 & & \underline{\underline{I}} & & \\
 & & & \underline{\underline{E}}_2 & \\
 & \underline{0} & & & \underline{\underline{E}}_N \\
 & & & & & \underline{\underline{I}}
\end{bmatrix}$$

where $\underline{\underline{I}}$ is the identity matrix. Then let $\underline{Q} = \underline{\underline{F}}\ \underline{X}$. We can show that $\underline{X}$ satisfies

$$\begin{bmatrix} \underline{\underline{N}}_1^- & \underline{\underline{N}}_1^+ \underline{\underline{E}}_1 & & & & \\ \underline{\underline{M}}_1^- \underline{\underline{E}}_1 & \underline{\underline{M}}_1^+ & -\underline{\underline{M}}_2^- & -\underline{\underline{M}}_2^+ \underline{\underline{E}}_2 & & \\ \underline{\underline{N}}_1^- \underline{\underline{E}}_1 & \underline{\underline{N}}_1^+ & -\underline{\underline{N}}_2^- & -\underline{\underline{N}}_2^+ \underline{\underline{E}}_2 & & \\ & & & & & \\ & \underline{\underline{M}}_s^- \underline{\underline{E}}_s & \underline{\underline{M}}_s^+ & -\underline{\underline{M}}_{s+1}^- & -\underline{\underline{M}}_{s+1}^+ \underline{\underline{E}}_{s+1} & \\ & \underline{\underline{N}}_s^- \underline{\underline{E}}_s & \underline{\underline{N}}_s^+ & -\underline{\underline{N}}_{s+1}^- & -\underline{\underline{N}}_{s+1}^+ \underline{\underline{E}}_{s+1} & \\ & & & & & \\ & & \underline{\underline{M}}_N^- \underline{\underline{E}}_N & \underline{\underline{M}}_N^+ & -\underline{\underline{M}}_{N+1}^- & \\ & & \underline{\underline{N}}_N^- \underline{\underline{E}}_N & \underline{\underline{N}}_N^+ & -\underline{\underline{N}}_{N+1}^- & \end{bmatrix} \underline{X} = \begin{bmatrix} \underline{0} \\ \underline{0} \\ \underline{0} \\ \\ \underline{\sigma}^- \\ \underline{\sigma}^+ \\ \\ \underline{0} \\ \underline{0} \end{bmatrix}$$

In this matrix equation all terms that contain $e^{\nu\alpha h}$ or $e^{\nu\beta h}$ are eliminated. Otherwise, as has been pointed out by Dunkin (1965), they might cause numerical instability in the evanescent region of wavenumbers. ■

Remark 2: In the computation of source term $\underline{\underline{D}}_s^{-1}\ \underline{S}^*$, the following trick makes direct matrix inversion unnecessary. Let

$$\underline{\underline{T}}_s = \begin{bmatrix} \mu_s(2k^2 - k_{\beta_s}^2) & -2\mu_l k\nu_{\beta_s} & \nu_{\beta_s} & -k \\ -2\mu_s k\nu_{\alpha_s} & \mu_s(2k^2 - k_{\beta_s}^2) & -k & \nu_{\alpha_s} \\ \mu_s(2k^2 - k_{\beta_s}^2) & 2\mu_l k\nu_{\beta_s} & -\nu_{\beta_s} & -k \\ -2\mu_s k\nu_{\alpha_s} & -\mu_s(2k^2 - k_{\beta_s}^2) & k & \nu_{\alpha_s} \end{bmatrix},$$

then it is easy to show that

$$\underline{\underline{T}}_s\ \underline{\underline{D}}_s = \mu_s k_{\beta_s}^2 \begin{bmatrix} (\nu_{\beta_s} - \nu_{\alpha_s}) & 0 & -(\nu_{\beta_s} + \nu_{\alpha_s}) & 0 \\ 0 & (\nu_{\beta_s} - \nu_{\alpha_s}) & 0 & -(\nu_{\beta_s} + \nu_{\alpha_s}) \\ -(\nu_{\beta_s} + \nu_{\alpha_s}) & 0 & (\nu_{\beta_s} - \nu_{\alpha_s}) & 0 \\ 0 & -(\nu_{\beta_s} + \nu_{\alpha_s}) & 0 & (\nu_{\beta_s} - \nu_{\alpha_s}) \end{bmatrix}.$$

This matrix is a circulant (Bellman, 1969) and a convolution technique can be employed to obtain its inversion, yielding:

$$\underline{\underline{\mathbf{D}}}_s^{-1}\ \underline{\mathbf{S}}^* = -\frac{1}{4\mu_s k_{\beta_s}^2 \nu_{\beta_s}\nu_{\alpha_s}}((\nu_{\beta_s}-\nu_{\alpha_s}),0,(\nu_{\beta_s}+\nu_{\alpha_s}),0)^T \star \underline{\underline{\mathbf{T}}}_s\ \underline{\mathbf{S}}^*.$$

Remark 3: The global matrix formulation has several advantages over the Thomson-Haskell propagator matrix technique: (1) any number of sources can be conveniently treated because the fields produced by multiple sources are simply superposed; (2) any number of receivers can be treated with only one solution pass since the wavefields are found in all layers simultaneously; (3) time consuming stability problems do not arise as there is no need for an evaluation of the exponential with a positive real argument. Comparisons with the propagator matrix methods developed by Mandal and Mitchell (1986) show that both the global matrix algorithm and the Kennett type propagator matrix algorithm yield identical results for elastic wave propagation in a layered medium. ■

5.2.2 Borehole Squeeze Strain

To evaluate the elastic wave field around the presumed borehole location in the undrilled formation, it is beneficial to change the source coordinates (R,θ,z) used in the above section to the borehole coordinates (r,ϕ,z) with the origin at the center of the borehole, as shown in Figure 5-2. The displacements in the new coordinates are related to those in the old coordinates by a rotation on the horizontal plane, yielding

$$\begin{cases} u_r &= U_R\cos(\theta-\phi)+U_\theta\sin(\theta-\phi), \\ u_\phi &= -U_\theta\cos(\theta-\phi)+U_R\sin(\theta-\phi), \\ u_z &= U_z, \end{cases}$$

where (U_R,U_θ,U_z) is the displacement vector in the source coordinate system (R,θ,z), and (u_r,u_ϕ,u_z) is the same vector in the borehole coordinate system (r,ϕ,z). It is

easy to show that $R = \sqrt{r^2 + r_0^2 - 2rr_0\cos\phi}$, $e^{2i\theta} = (r_0 - re^{i\phi})/(r_0 - re^{-i\phi})$, where r_0 is the horizontal distance between the source and the borehole.

In the borehole coordinate system (r, ϕ, z), using the constitutive relationship relating stress to strain and the geometrical relationship relating strain to displacement, we obtain the normal stresses at $r = r_b$. The results, when being averaged over ϕ in $[0, 2\pi]$, are

$$\sigma_{rr}(r_b,\ z) + \sigma_{\phi\phi}(r_b, z) =$$

$$2\int_0^\infty \left[\frac{\lambda}{\lambda + 2\mu} P(z;\omega,k) - \frac{\mu(3\lambda + 2\mu)}{\lambda + 2\mu} kV(z;\omega,k) \right] J_0(kr_b)J_0(kr_0)\, kdk, \quad (5.21)$$

and

$$\sigma_{zz}(r_b, z) = \int_0^\infty P(z;\omega,k)\ J_0(kr_b)J_0(kr_0)\ kdk. \quad (5.22)$$

Then the borehole squeeze strain in equation (5.2) can be computed by

$$\epsilon_r^{(inc)}(z,\omega) = \int_0^\infty \Gamma(z,\omega,k)\ J_0(kr_b)J_0(kr_0)\ kdk, \quad (5.23)$$

where

$$\Gamma(z,\omega,k) = \frac{\lambda}{2\mu(\lambda + 2\mu)} P(z;\omega,k) - \frac{2(\lambda + \mu)}{\lambda + 2\mu} kV(z;\omega,k)$$

for an open borehole. For a cased borehole, it is

$$\Gamma(z,\omega,k) = \frac{\lambda}{2\mu(3\lambda + 2\mu)} \left[\eta_{||} \frac{4(\lambda + \mu)}{\lambda + 2\mu} - \eta_\perp \right]\ P(z;\omega,k) - \eta_{||} \frac{2(\lambda + \mu)}{\lambda + 2\mu} kV(z;\omega,k).$$

In the above equation, $\eta_{||} = E/E_{||}$ and $\eta_\perp = E/E_\perp$ are the ratio of the effective Young's moduli in an open borehole to those in a cased borehole. They are given by

$$\eta_{||} = \frac{1 + \nu(\frac{\mu_c}{\mu} - 1)(\frac{1}{2} - \gamma_c)(1 - r_b^2/r_c^2)}{1 + (\frac{\mu_c}{\mu} - 1)(1 - \gamma_c)(1 - r_b^2/r_c^2)},$$

and

$$\eta_\perp = \frac{1 + \nu^{-1}(\frac{\mu_c}{\mu} - 1)(\frac{1}{2} - \gamma_c)(1 - r_b^2/r_c^2)}{1 + (\frac{\mu_c}{\mu} - 1)(1 - \gamma_c)(1 - r_b^2/r_c^2)},$$

where μ_c is the shear modulus of the casing, $\gamma_c = \beta_c^2/\alpha_c^2$, r_b and r_c are the inner and outer radii of the cased borehole. As a reminder, $V(z;\omega,k)$ and $P(z;\omega,k)$ in the

above expressions are coefficients in equations (5.11) and (5.12), respectively. They are functions of depth z, frequency ω, and horizontal wavenumber k.

Remark: In deriving these equations, the following identities and approximations have been used (Watson, 1922; Abramowitz and Stegun, 1965; also see Figure 5-2):

$$J_0(kR) = \sum_{m=0}^{\infty} \varepsilon_m J_m(kr_0) J_m(kr) \cos m\phi,$$

$$J_1(kR)\cos\theta = \sum_{m=0}^{\infty} \varepsilon_m \frac{J_{m-1}(kr_0) - J_{m+1}(kr_0)}{2} J_m(kr) \cos m\phi,$$

$$J_1(kR)\sin\theta = \sum_{m=0}^{\infty} \varepsilon_m \frac{J_{m-1}(kr_0) + J_{m+1}(kr_0)}{2} J_m(kr) \sin m\phi,$$

and

$$\frac{J_1(kr_b)}{kr_b} \approx \frac{J_0(kr_b)}{2},$$

and

$$J_1'(kr_b) \approx \frac{J_0(kr_b)}{2},$$

where r_b is the borehole radius, and $\varepsilon_m = \begin{cases} 1 & \text{if } m = 0 \\ 2 & \text{if } m \neq 0 \end{cases}$ is the Newmann factor. The approximations are valid at low frequencies. ■

5.2.3 Discrete Wavenumber Integration

Substituting equation (5.23) into equation (5.7), after a few algebraic manipulations, we get

$$\begin{aligned} w_m(z,\omega) &= i\frac{\rho_f \omega^2}{k_m} \int_0^{\infty} \Big[\underline{\mathbf{k}}_P^T \left(\underline{\mathbf{J}}^+(z;\omega,k) + \underline{\mathbf{J}}^-(z;\omega,k) \right) \\ &- k \underline{\mathbf{k}}_V^T \left(\underline{\mathbf{J}}^+(z;\omega,k) + \underline{\mathbf{J}}^-(z;\omega,k) \right) \Big] J_0(kr_b) J_0(kr_0)\, kdk, \end{aligned}$$

where

$$\underline{\mathbf{k}}_P = \frac{\lambda}{2\mu(3\lambda+2\mu)} \left[\eta_{\parallel} \frac{4(\lambda+\mu)}{\lambda+2\mu} - \eta_{\perp} \right] [0,0,1,0]^T,$$

and

$$\underline{\mathbf{k}}_V = \eta_{\|} \frac{2(\lambda+\mu)}{\lambda+2\mu} [0,1,0,0]^T$$

are two indication vectors that yield $P(z;\omega,k)$ and $V(z;\omega,k)$ from $\underline{\mathbf{B}}(z;\omega,k)$, the displacement-stress vector in the frequency-horizontal wavenumber domain. In the above equation, $\underline{\mathbf{J}}^+(z;\omega,k)$ and $\underline{\mathbf{J}}^-(z;\omega,k)$ are vectors defined as

$$\underline{\mathbf{J}}^+(z;\omega,k) = \int_{z_{m-1}}^{z} \underline{\mathbf{B}}(z;\omega,k)\, e^{-ik_m(z-z')} dz',$$

and

$$\underline{\mathbf{J}}^-(z;\omega,k) = \int_{z}^{z_m} \underline{\mathbf{B}}(z;\omega,k)\, e^{+ik_m(z-z')} dz'.$$

They are explicitly given by

$$\underline{\mathbf{J}}^{\pm}(z;\omega,k) = \underline{\underline{\mathbf{D}}}_m(\omega,k)\ \underline{\underline{\Sigma}}_m^{\pm}(z;\omega,k) \begin{pmatrix} \langle Q_m(z_{m-1}^+)\rangle^- \\ \langle Q_m(z_m^-)\rangle^+ \end{pmatrix} \tag{5.24}$$

where $\langle Q_m(z_{m-1}^+)\rangle^-$ (2 elements) are the down-going amplitudes (P and SV-waves) at the top of layer m and $\langle Q_m(z_m^-)\rangle^+$ (2 elements) are the up-going amplitudes at the bottom of layer m. z is within the layer m, i.e., $z_{m-1} \le z < z_m$. In the derivation, equation (5.16) has been used. The diagonal matrices $\underline{\underline{\Sigma}}_m^+$ and $\underline{\underline{\Sigma}}_m^-$ are given by

$$\underline{\underline{\Sigma}}_m^+(z;\omega,k) = \mathrm{diag} \begin{bmatrix} (e^{-ik_m(z-z_{m-1})} - e^{-\nu\alpha_m(z-z_{m-1})})/(\nu\alpha_m - ik_m) \\ (e^{-ik_m(z-z_{m-1})} - e^{-\nu\beta_m(z-z_{m-1})})/(\nu\beta_m - ik_m) \\ (e^{-\nu\alpha_m(z_m-z)} - e^{-ik_m(z-z_{m-1})-\nu\alpha_m(z_m-z_{m-1})})/(\nu\alpha_m + ik_m) \\ (e^{-\nu\beta_m(z_m-z)} - e^{-ik_m(z-z_{m-1})-\nu\beta_m(z_m-z_{m-1})})/(\nu\beta_m + ik_m) \end{bmatrix}$$

and

$$\underline{\underline{\Sigma}}_m^-(z;\omega,k) = \mathrm{diag} \begin{bmatrix} (e^{-\nu\alpha_m(z-z_{m-1})} - e^{+ik_m(z-z_m)-\nu\alpha_m(z_m-z_{m-1})})/(\nu\alpha_m + ik_m) \\ (e^{-\nu\beta_m(z-z_{m-1})} - e^{+ik_m(z-z_m)-\nu\beta_m(z_m-z_{m-1})})/(\nu\beta_m + ik_m) \\ (e^{+ik_m(z-z_m)} - e^{-\nu\alpha_m(z_m-z)})/(\nu\alpha_m - ik_m) \\ (e^{+ik_m(z-z_m)} - e^{-\nu\beta_m(z_m-z)})/(\nu\beta_m - ik_m) \end{bmatrix}.$$

The integration with respect to the horizontal wavenumber k is carried out first by the discrete wavenumber method (Bouchon and Aki, 1977; Bouchon, 1981), yielding

$$\begin{aligned} w_m(z,\omega) &= \frac{i\pi}{L}\frac{\rho_f\omega^2}{k_m}\sum_{n=0}^{\infty}\varepsilon_n k_n J_0(k_n r_b)J_0(k_n r_0)\left[\underline{\mathbf{k}}_P^T\left(\underline{\mathbf{J}}^+(z;\omega,k_n)+\underline{\mathbf{J}}^-(z;\omega,k_n)\right)\right. \\ &- \left. k_n\underline{\mathbf{k}}_V^T\left(\underline{\mathbf{J}}^+(z;\omega,k_n)+\underline{\mathbf{J}}^-(z;\omega,k_n)\right)\right], \end{aligned} \tag{5.25}$$

where $k_n = 2\pi n/L$. L is the periodicity of the imaginary source arrays, and is chosen such that energies contributed from the virtual sources are out of the time window of observation (Bouchon, 1981).

The derivative of $w_m(z,\omega)$ with respect to z is found to be

$$\begin{aligned} \frac{dw_m(z,\omega)}{dz} &= -\frac{\pi}{L}\rho_f\omega^2\sum_{n=0}^{\infty}\varepsilon_n k_n J_0(k_n r_b)J_0(k_n r_0)\left[\underline{\mathbf{k}}_P^T\left(\underline{\mathbf{J}}^+(z;\omega,k_n)-\underline{\mathbf{J}}^-(z;\omega,k_n)\right)\right. \\ &- \left. k_n\underline{\mathbf{k}}_V^T\left(\underline{\mathbf{J}}^+(z;\omega,k_n)-\underline{\mathbf{J}}^-(z;\omega,k_n)\right)\right]. \end{aligned} \tag{5.26}$$

Summations in the above two equations are truncated when contributions from the next higher order term are negligible in both evaluations. After $w_m(z,\omega)$ and $dw_m(z,\omega)/dz$ are computed, equations (5.10) and (5.4) are used to determine the pressure $P(z,\omega)$ in the fluid. Then an integration with respect to frequency is implemented by FFT to obtain the time response $P(z,t)$ at a given depth.

The additional computation for borehole coupling is found to be significantly less than the computation for the stress field around the borehole by the global matrix method. Thus, this method is as fast as the existing methods that do not include the fluid-filled borehole.

5.2.4 Numerical Examples

To show the accuracy of this technique, we present a comparison with an analytical solution. The degenerated model of Figure 5-1 is a fluid-filled borehole in an unbounded and homogeneous formation. In this case, the pressure in the fluid can be exactly computed for an explosive source in the formation. The exact method

is to express the wave field due to an explosive source as a superposition of plane waves. The coupling of individual plane waves into the borehole fluid is accomplished through the method described in the second chapter. Finally, contributions from all of them are summed. In this example, we compute the pressure in the borehole fluid for a volume source in the formation at a horizontal offset $r_0 = 400$ m. The formation is unbounded and homogeneous with compressional velocity 3000 m/s, shear velocity 2000 m/s, and density 2400 kg/m^3. The fluid in the borehole is ideal water. The borehole is uncased with a 0.10 m radius. The source is at depth $\eta_s = 0$. Its time history is a Kelly wavelet with the central frequency of 50 Hz. We use 21 receivers which equally span a section of the borehole from depths of -400 m to 400 m. Figure 5-3 shows two calculations: one is computed by the exact method, the other by the hybrid method developed in this paper. Up to the resolution in this figure, one can't tell the difference between the calculations by our technique and those by the exact method. Then we take the Fourier transforms of both calculations and pick the spectral amplitudes at the central frequency of 50 Hz. After multiplying by the source receiver distance, i.e., the geometrical spreading correction, we plot the results shown in Figure 5-4 as a function of angle of incidence with respect to the borehole axis. This graphic representation of borehole data is also called the point source reception pattern. In this figure, the open circle is from our numerical method, the solid circle corresponds to the exact solution, the solid triangle shows the pressure disturbance in a full space assuming the borehole is *absent*. The triangles, as expected, are on the unit circle for an explosive source. The circles are bent inward because of the pressure release on the fluid-solid interface at the borehole wall. Again the numerical data agree with the exact solutions in the frequency domain.

In the second example, we choose a configuration where a low velocity layer is embedded in a high velocity half space. The depths of the top and bottom boundaries of the low velocity layer are at 300 m and 500 m, respectively. The borehole (radius $r_b = 0.1$ m) is open and filled with water. It has a finite length of 800 m. The source is at depth 400 m and at offset 400 m. The receivers are in the borehole spanning a

depth range between 0 to 800 m. The source time history is a Kelly wavelet with the central frequency of 100 Hz. The formation parameters for this calculation are given in Table 5.1. Figure 5-5 shows the synthetic seismograms of pressure in the borehole fluid. Obviously, a significant portion of energy is trapped in the low velocity layer. The multiple reflections inside this layer are obvious. The low velocity events are tube waves generated at the interface boundaries as well as at the top and bottom of the borehole. Reflections at the free surface (top) are also discernible. On the free surface the pressure is zero (first trace on the top).

Lithology	*depth* (m)	*P-wave velocity* (m/s)	*S-wave velocity* (m/s)	*density* (g/cm^3)
sandstone	0–300	4206	2664	2.20
shale	300–500	3000	1800	2.00
sandstone	500–	4206	2664	2.20

Table 5.1: medium parameters for the examples in Figures 5-5 and 5-6.

The third example is a calculation for a cased borehole. The configuration and parameters are the same as the second example. The casing is steel with a 2 cm thickness. Figure 5-6 shows the synthetic pressure in the cased borehole. The amplitude of fluid pressure is significantly reduced in a cased borehole. The maximum amplitude in Figure 5-5 is about three times larger than in Figure 5-6. The relative amplitudes of the trapped waves in the depth interval corresponding to the low velocity layer are not as large as those in an open borehole. In the cased borehole, the tube waves from the well head are more evident, as are the P- and S-waves outside the low velocity layer.

An important application of these simulations is the crosshole continuity logging, where the interest is in identifying a low velocity layer sandwiched between surrounding high velocity formations, using trapped energies and tube waves (Krohn, 1992).

5.3 Applications to the Kent Cliffs VSP Experiment

5.3.1 Background

The Kent Cliffs borehole is an approximately 1 km deep test well located in south-eastern New York. The borehole is drilled for the study of the crustal stress regime. Various geophysical and geological data were collected in this borehole, including core samples, well-logs, televiewer survey, hydraulic fracturing stress measurements, and multiple offset VSPs with geophones and hydrophones. Geophysical and lithological data show that the borehole cuts first through fine-to-medium-grained amphibolite; the upper 10-40 meters of the amphibolite is weathered. Below the amphibolite is a gneiss. The transition zone is at a depth of 260 - 271 meters in the borehole. The overall formation shows well developed foliation. The foliations and contact surfaces dip 60^o towards the southeast.

Core logs and downhole televiewer images show that there are two primary shear zones at depth intervals 273 - 275 meters and 511 -513 meters. Fractures of various sizes are found at depths of 232, 286, and 512 meters. Full waveform acoustic logs show that, in the overall depth interval of approximately 1 km, the compressional velocity varies between 5.5 km/s and 6.8 km/s and the shear velocity between 3.3 km/s and 3.6 km/s. The gradient of formation elastic properties with depth is small (see Table 5.2). As a first order approximation, we will ignore the dipping of the formation boundaries in our modeling.

For detailed accounts of this experiment, the reader is referred to the Ph.D theses of Lee (1990) and Cicerone (1991).

5.3.2 Hydrophone VSP Data

The multi-offset hydrophone VSP experiment (Figure 5-7) was carried out using a vertical weight drop as a source. The receivers are an array of six (6) piezo-electric hydrophones separated by a 3.048 meter interval. Four source offsets were used in the experiment. They are at 37.5, 350.5, 288.0, and 518.2 meters away from the well head. In the figure they are referenced as S/P #1, S/P #2, S/P #3, and S/P #4, respectively. Data processing includes raw data demultiplexing, monitor geophone correlation, stacking and bandpass filtering (Lee, 1990).

Figure 5-8 through Figure 5-10 show the hydrophone VSP data at shot points S/P #1, S/P #2, and S/P #3, respectively. A zero phase bandpass filter with a pass band between $100 - 220$ Hz is applied to these data. Evidently, these data show large amplitude tube waves generated at the well head, the shear zones, and the fractures. The direct P- and S-waves are small in amplitude, and are strongly interfered with by large amplitude tube waves. The tube waves originating at the well head are due to the squeeze effect of incident P-, S-, and Rayleigh waves. The tube waves generated at the shear zones and fractures are due to the injection of fluid into the borehole as the incident P-wave and S-wave squeeze the fractures. The latter mechanism is extensively studied in the literature (Beydoun et al., 1985; Circerone, 1991; Toksöz et al., 1992).

5.3.3 Modeling and Comparison

The modeling code developed in this chapter doesn't have the ability to include fractures in its formulation, thus we are unable to model the tube waves generated by them (i.e., the chevron-shaped patterns are absent in our synthetics). Nevertheless, other arrivals, such as P-, S-, and tube waves from the well head, are all included.

We choose a stratified elastic model shown in Table 5.2. The formation P-wave

and S-wave velocity profiles are derived from the sonic logging data, core sample velocity measurements, and near zero offset VSP data. In Table 5.2, the lithology in each layer is also given. In the simulations, we use a vertical force to simulate the actual weight drop. The water table in the borehole is at 14 m from the surface. The well bottom is approximately at 1007 m. Both of these numbers are from actual measurements. We don't attempt to derive the source wavelet by the wavelet estimation scheme (Ziolkowski et al., 1991; Kagansky et al., 1993). Rather, we use a Kelly wavelet as the source time function with the central frequency of 100 Hz. In the numerical simulation, the number of receivers is five times less than that of the field data. That is, we have 65 traces in the simulation instead of the 321 traces in the experiment. Nevertheless, the simulation covers approximately the same depth range as the experiment.

Lithology	*depth* (m)	*P-wave velocity* (m/s)	*S-wave velocity* (m/s)	*density* (g/cm^3)
Amphibolite	0 – 10	5500	3300	2.80
Amphibolite	10 – 85	6246	3700	2.90
Amphibolite	85 – 215	6888	3850	3.10
Transition Zone	215– 270	6189	3590	3.00
Gneiss	270– 425	6197	3530	2.90
Gneiss	425– 470	6197	3500	2.80
Gneiss	470– 770	6197	3530	2.90
Gneiss	770–	6204	3630	2.90

Table 5.2: Medium parameters and lithologies derived from logging data in the Kent Cliffs test borehole.

Figure 5-11 through Figure 5-13 show the synthetic hydrophone pressures for the shot points S/P #1, S/P #2, and S/P #3, respectively. In the synthetic seismograms, the P-, S-, and tube waves from the well head are well modeled. As will be shown later, the synthetic P-waves agree with those in the experiment not only in arrival time, but also in RMS (root mean square) amplitude. There are three tube wave

events generated at the top of borehole (in both the field data and the numerical simulations for S/P #2 and S/P #3): one is due to the squeezing effect of the P-wave, another to that of the S-wave, and the last to the Rayleigh wave (ground roll). The last one tends to have a slightly lower frequency content than the others.

To quantitatively compare the numerical simulations with the field data, we pick the arrival time of the P-wave and measure its RMS amplitude in a window of one period in length, that is,

$$P_{RMS} = \sqrt{\frac{1}{T}\int_{t_0}^{t_0+T} p(t) \times p(t)dt},$$

where t_0 is the P-wave arrival time, T is the period equal to the reciprocal of the central frequency, and $p(t)$ is the hydrophone pressure data. We then plot both t_0 and P_{RMS} as functions of depth. The results are shown in Figure 5-14 through Figure 5-17.

Figure 5-14a shows the P-wave traveltime versus depth for both the synthetic data and the field data for the shot point S/P #1 (37.5 m horizontal offset). The solid line is the traveltime measured from the field data, the + symbol is that from the synthetics. The agreement is excellent. Actually, the velocity model is partly based on information from this particular offset. In Figure 5-14b and Figure 5-14c, we show the P-wave traveltime for the shot points S/P #2 (350 m horizontal offset) and S/P #3 (288 m horizontal offset). At these shot points, the traveltimes in the synthetics are slightly different from those in the field data, which is attributed to the fact that the formation is actually tilded towards the southeast. Seismic rays tend to find the shortest traveltime pathes, some of them may not be permissible in our stratified model.

More importantly, our simulation can predict the dynamic behavior of a downhole hydrophone measurement as well. In Figure 5-15, we plot the P-wave RMS amplitude versus depth for the shot point S/P #1. In this plot, the solid line is the RMS amplitude of the synthetic data, the + symbol is that of the field data. The integrated

RMS amplitude in the depth interval 304.8−990.6 m is used to scale the synethtic and the field data. There is an excellent agreement between the synthetic amplitude and the observed one, except at locations where tube waves are generated and interfere with the P-wave. This kind of agreement also exists for the other two shot points– S/P #2 and S/P #3– as shown in Figure 5-16 and Figure 5-17. The observed data points tend to shift away from the synthetic prediction at shallow depths, due partly to the tube wave interference and partly to the assumption of laterally homogeneous velocity model for synthetic computations. Note that complicated inhomogeneities around the surface were not included in the modeling. Also the S-wave amplitudes in Figure 5-12 are larger than the observed data in Figure 5-9. This is because the S-wave energy is affected strongly both by the anelastic attenuation for wave propagation across a large distance and by the radiation pattern of the weight-drop source, and these factors are not taken into account properly in the numerical modeling.

5.4 Discussions and Conclusions

In this chapter, an efficient and accurate method is proposed to model hydrophone VSP data in a stratified formation. This method incorporates the borehole coupling theory into the global matrix algorithm by dividing the problem into two parts: propagation from the source to the presumed borehole location by the global matrix algorithm, and coupling the resulting stresses into the borehole fluid by a low frequency approximation. This approach greatly reduces the difficulties of the original problem involving two sets of interfaces perpendicular to each other. It yields a very accurate result at a frequency below 2 kHz. This is demonstrated by a comparison with an analytical solution. The method is as fast as other existing ones in modeling elastic wave propagation in a layered medium.

This method has been applied to model the Kent Cliffs hydrophone VSP data. Using a stratified model derived from both the sonic logging data and the near-zero

offset VSP survey, we are able to predict the traveltime and rms amplitude of the P-wave arrival in the hydrophone data, especially for the first shot point S/P #1. There are systematic, although small, discrepancies between predictions and observations in the other two shot points (S/P #2 and S/P #3). They might be attributed to the dipping of the formation (dip angle 60° toward the southeast, see Lee, 1990), an issue that will be addressed in the next chapter.

Besides applications to hydrophone VSP data simulation, this method can be used to model crosshole continuity logging data, if proper source borehole effects are taken into account (Ben-Menahem and Kostek, 1991; Kurkjian et al., 1992). One limitation of this method would be the transmission of high frequency signals through large distances, because the computation time increases linearly with both frequency and the maximum distance between the source and the receivers. However, this can be offset by the utilization of fast computers.

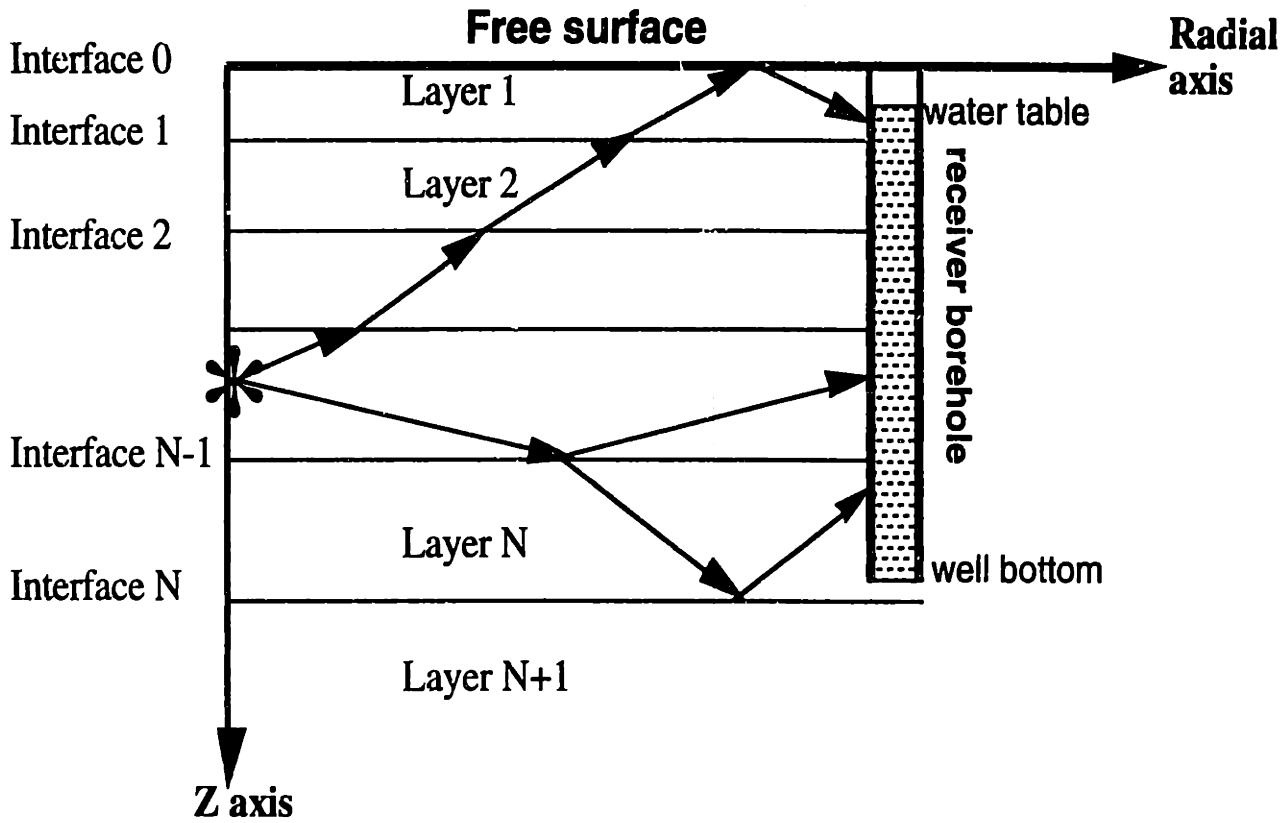

Figure 5-1: A borehole in a stratified half space. In each layer, the formation is homogeneous and elastic with compressional velocity α_n, shear velocity β_n, and density ρ_n. A seismic source is either on the free surface (VSP geometry) or inside the formation (Crosswell geometry). An array of hydrophones are in the borehole. The borehole has a finite length and may be partially filled with fluid.

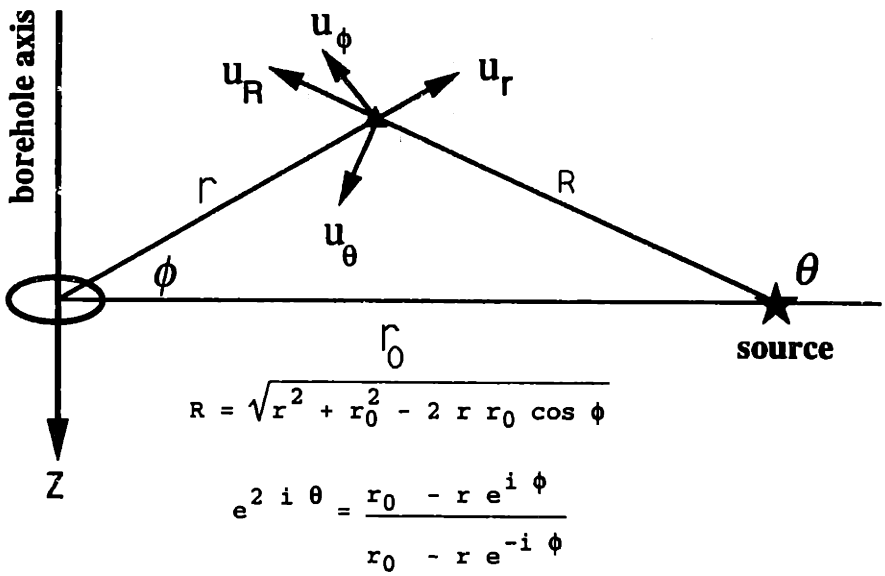

Figure 5-2: A schematic diagram showing the transformation from the source coordinate ($\mathbf{R}$, θ, $\mathbf{z}$) to the borehole coordinate ($\mathbf{r}$, ϕ, $\mathbf{z}$). The distance between the seismic source and the center of borehole is r_0.

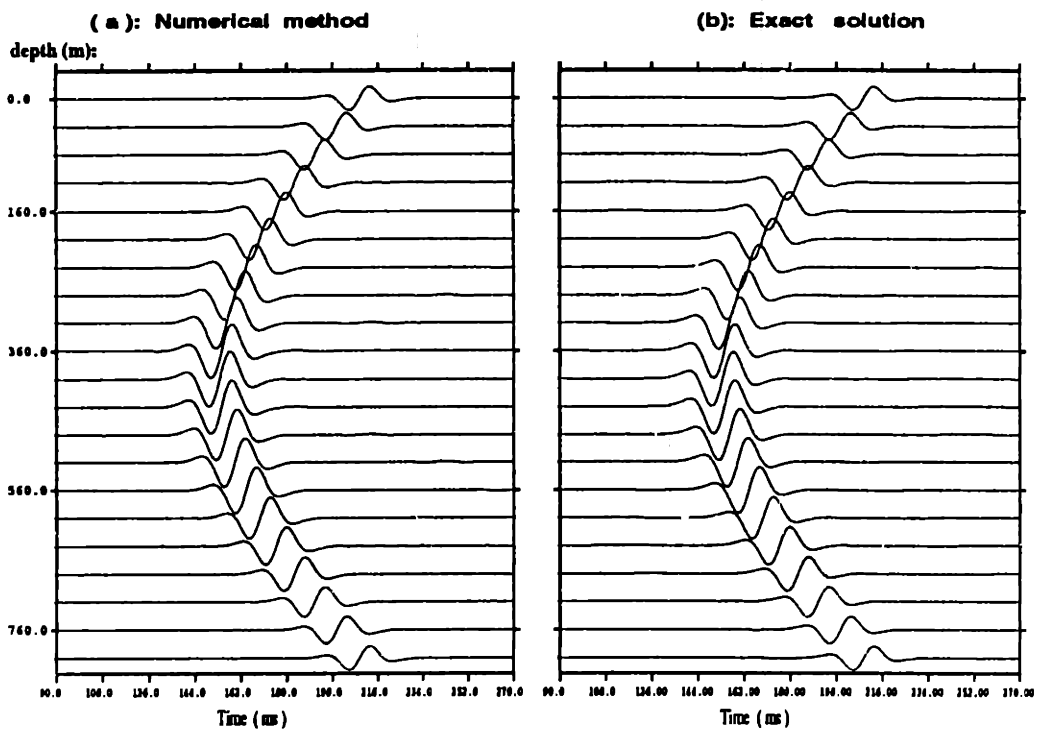

Figure 5-3: Synthetic hydrophone pressures in the borehole fluid for an explosive source inside a homogeneous and unbounded formation: (a) by the numerical method proposed in this chapter, and (b) by an exact method. The parameters in these calculations are: $r_0 = 400$ m, $\alpha = 3000$ m/s, $\beta = 2000$ m/s, $\rho = 2400$ kg/m^3. The borehole radius is 0.10 m. The source time history is a Kelly wavelet with the central frequency 50 Hz. The depth of the source is 400 m. A total of 21 traces are plotted, spanning a depth range from 0 to 800 m.

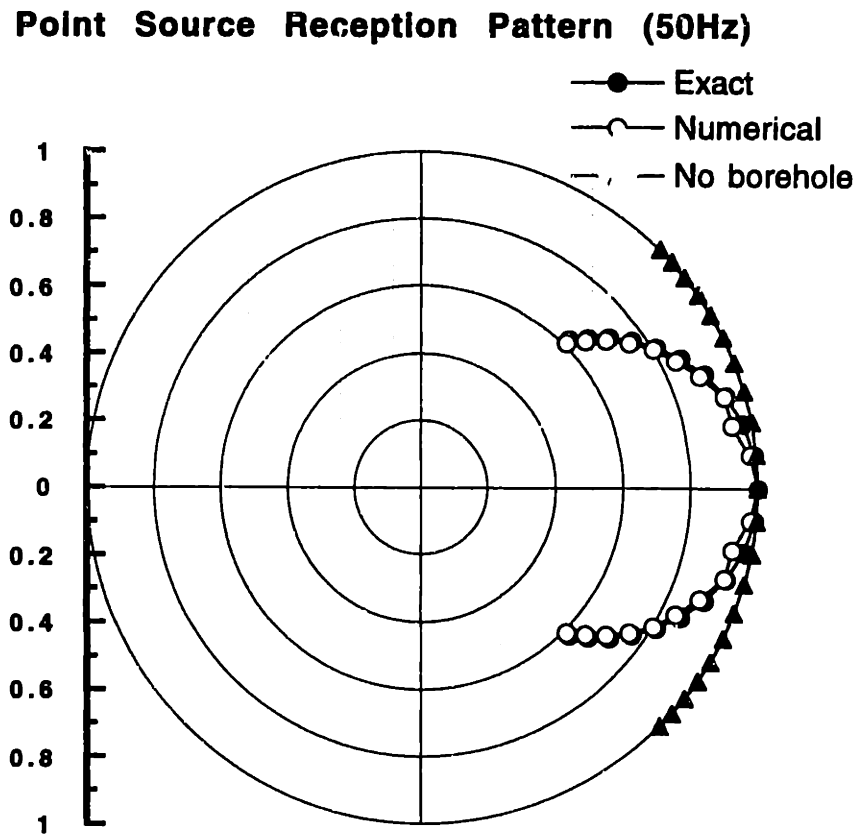

Figure 5-4: Borehole point source reception pattern for the example shown in Figure 5-3. The solid circles are data from the exact method. The open circles are data from the numerical method proposed in this chapter. The solid triangles show the isotropic radiation from an explosive source in a homogeneous and unbounded medium. The data are individually normalized. The reception pattern of a fluid-filled borehole shows a lobe at normal incidence.

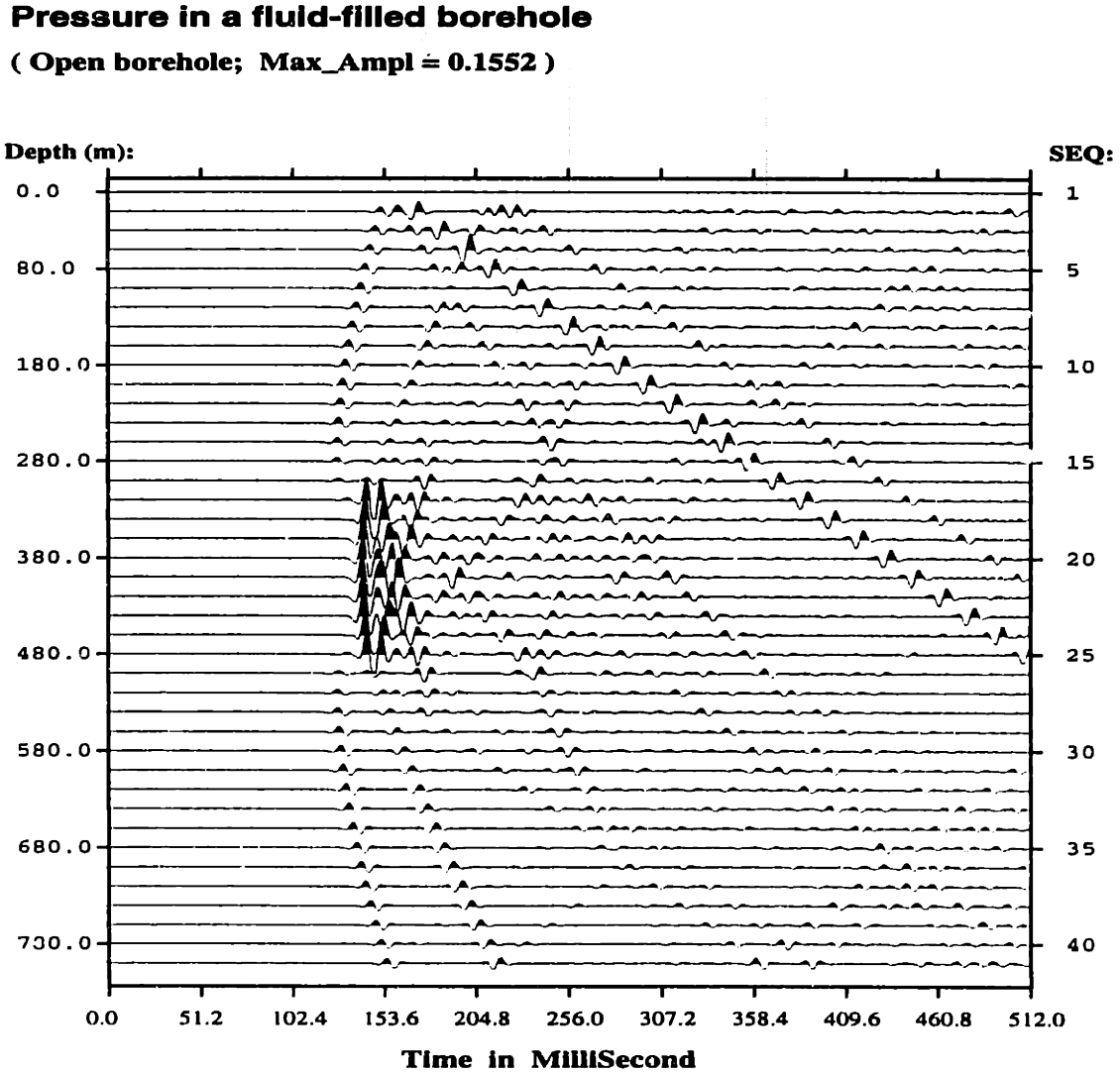

Figure 5-5: Synthetic hydrophone pressures in an open borehole for an explosive source in the formation. The source is inside a low velocity layer embedded in a high velocity halfspace. Its time history is a Kelly wavelet with the central frequency 100 Hz. The source-borehole offset is 400 m. The borehole radius is 0.10 m. Other parameters used in this calculation are given in Table 5.1. The maximum amplitude in this data set is 0.1552.

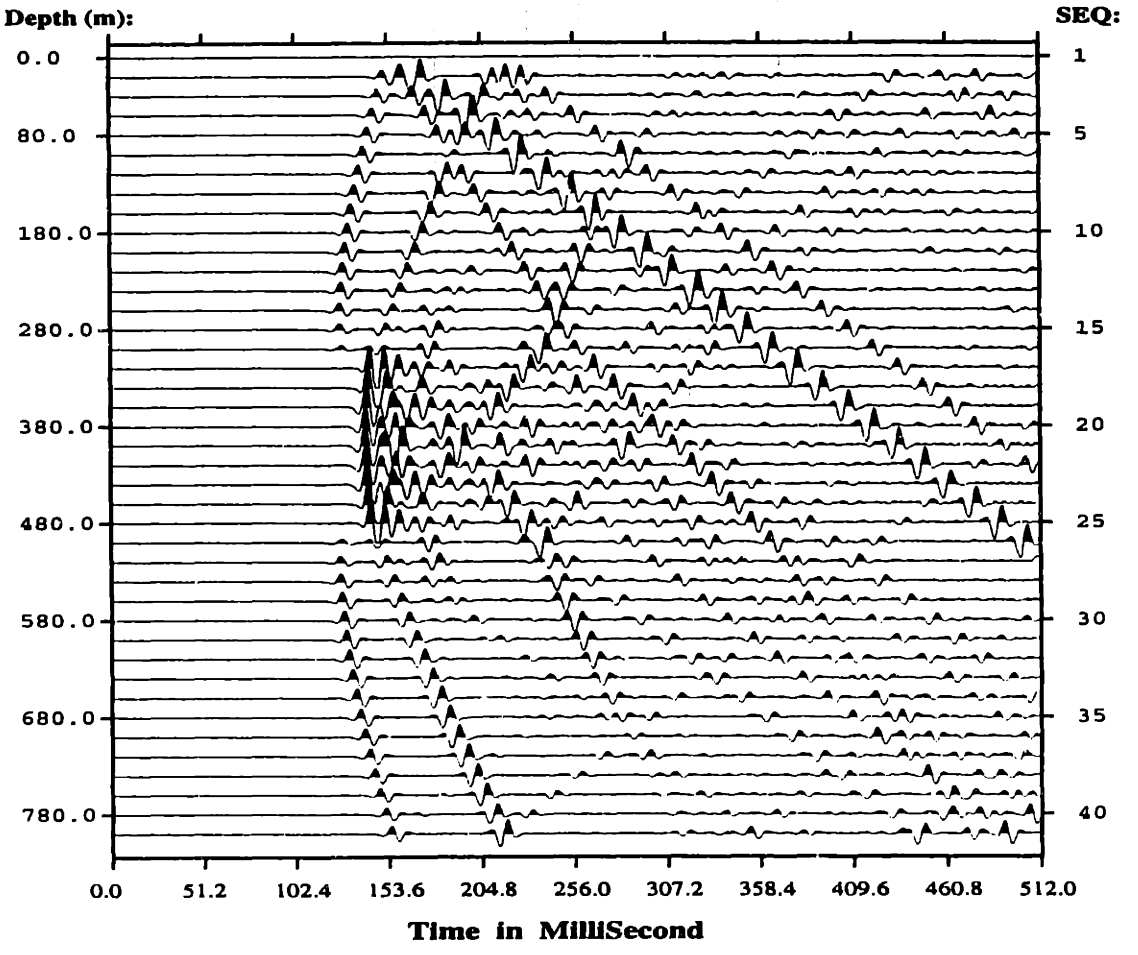

Figure 5-6: Synthetic hydrophone pressures in a cased borehole for an explosive source in the formation. The source is inside a low velocity layer embedded in a high velocity halfspace. Its time history is a Kelly wavelet with the central frequency 100 Hz. The source-borehole offset is 400 m. The casing is steel. The inner radius of the casing is 0.10 m, the outer radius is 0.12 m. Other parameters used in this calculation are given in Table 5.1. The maximum amplitude in this data set is 0.0520.

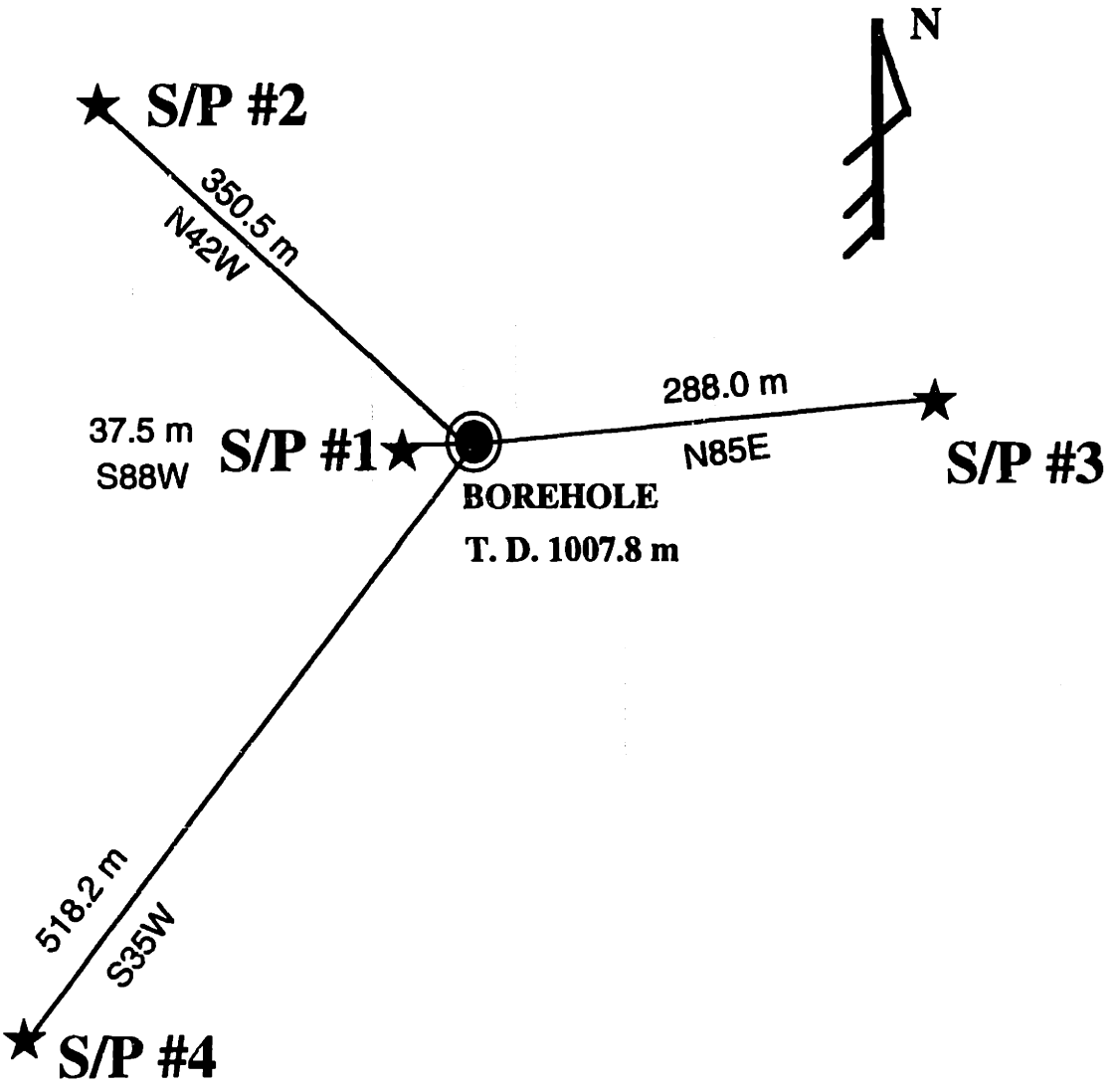

Figure 5-7: A map showing the Kent Cliffs hydrophone VSP experiment. A total of four (4) shot points around the borehole were used in the experiment. The borehole has a depth about 1 kilometer and is slightly deviated toward SE by about 30 meters in the east direction and 70 meters in the south direction. The formation in this region is amphibolite and gneiss in the top and bottom portions of the borehole respectively, and is tilded toward the SE by as much as 60° (Courtesy of Dr. J. M. Lee)

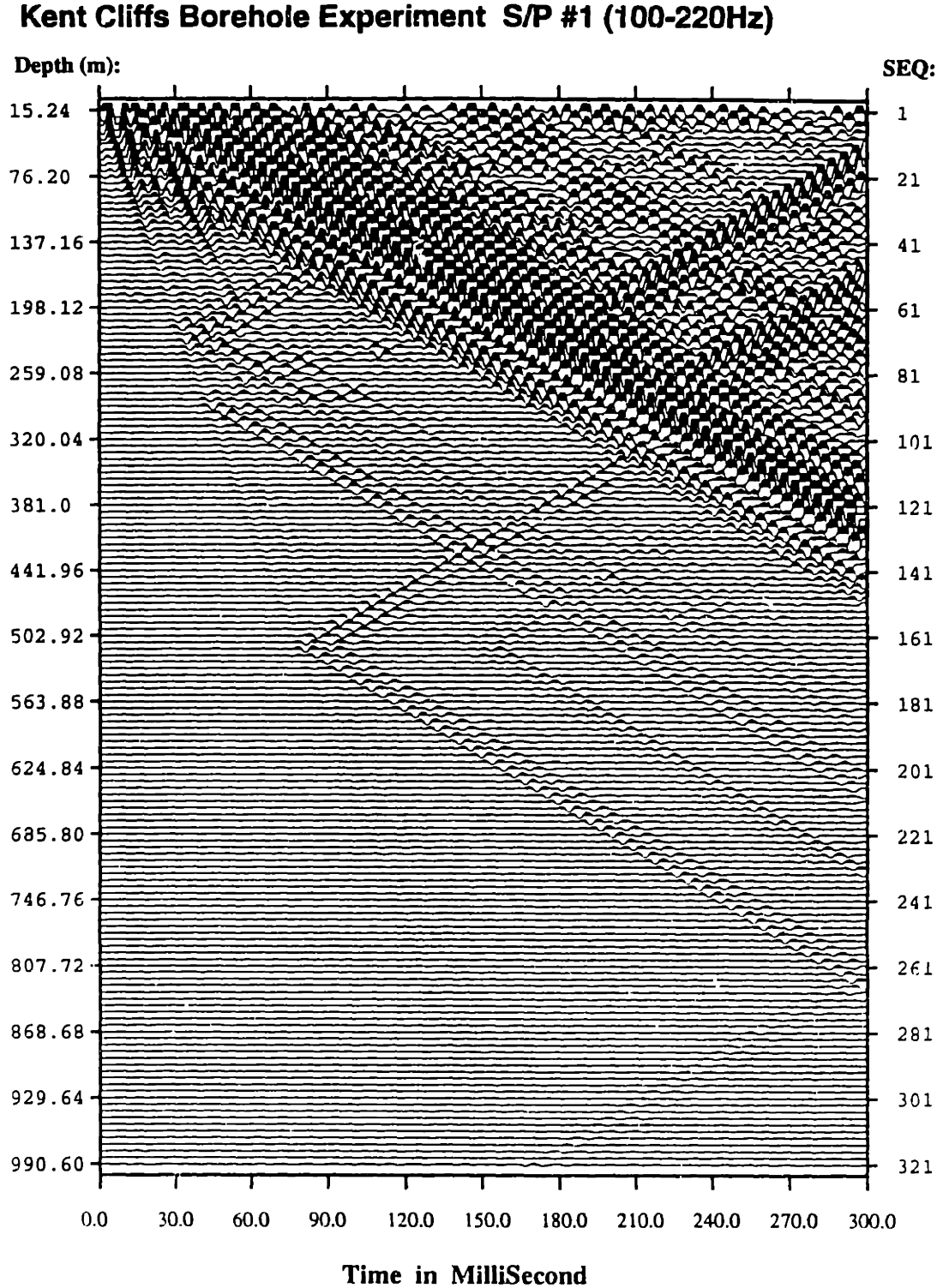

Figure 5-8: Hydrophone VSP data for the shot point S/P #1. The source offset is 37.5 m in the direction S88°W. The first hydrophone is at depth 15.25 m, slightly below the water table. The last hydrophone is at 990.6 m, slightly above the well bottom. A bandpass filter is applied to this data with a pass band between 100 Hz and 220 Hz.

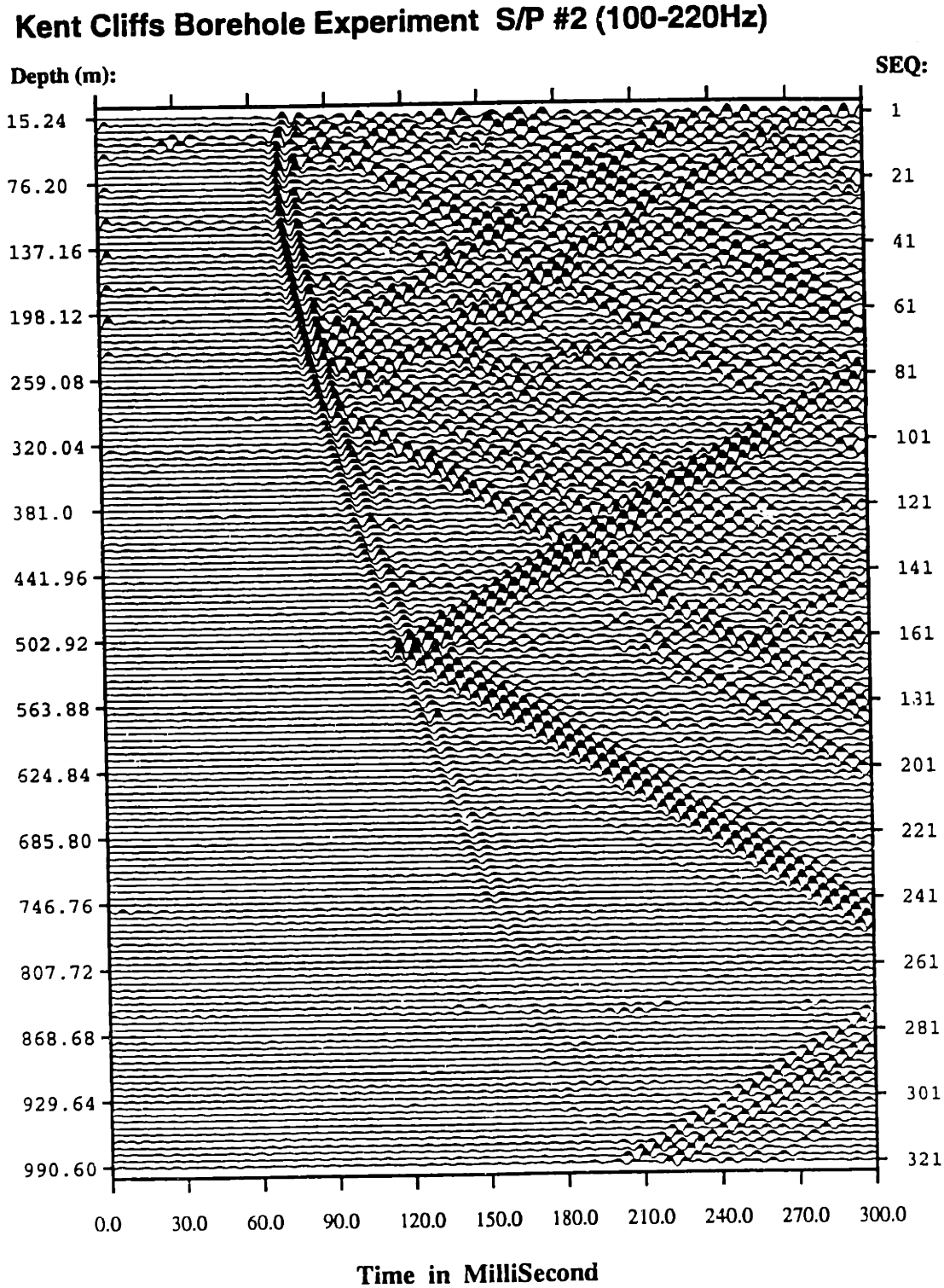

Figure 5-9: Hydrophone VSP data for the shot point S/P #2. The source offset is 350.5 m in the direction N42°W. The first hydrophone is at depth 15.25 m, slightly below the water table. The last hydrophone is at 990.6 m, slightly above the well bottom. A bandpass filter is applied to this data with a pass band between 100 Hz and 220 Hz.

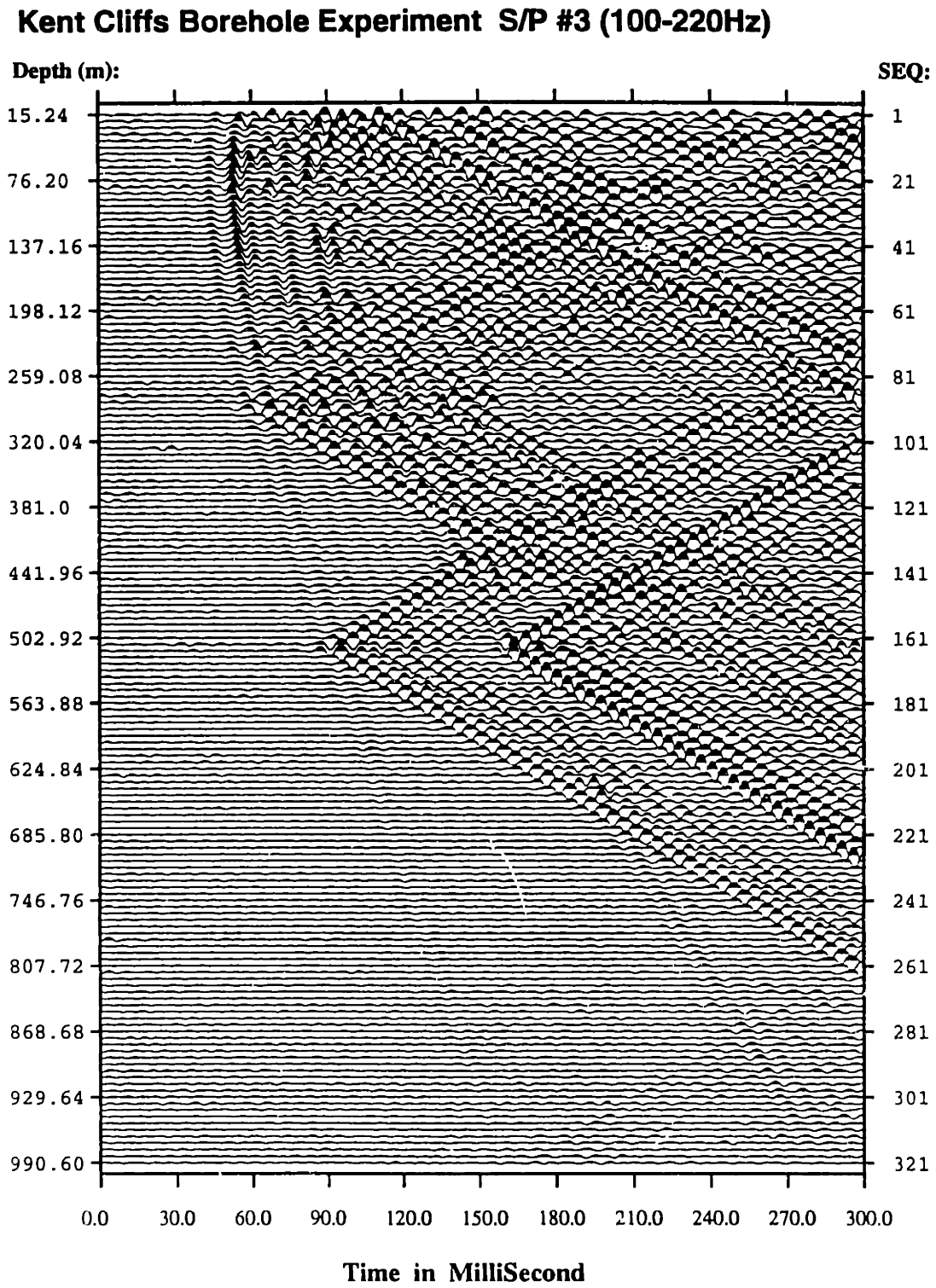

Figure 5-10: Hydrophone VSP data for the shot point S/P #3. The source offset is 288.0 m in the direction N85°E. The first hydrophone is at depth 15.25 m, slightly below the water table. The last hydrophone is at 990.6 m, slightly above the well bottom. A bandpass filter is applied to this data with a pass band between 100 Hz and 220 Hz.

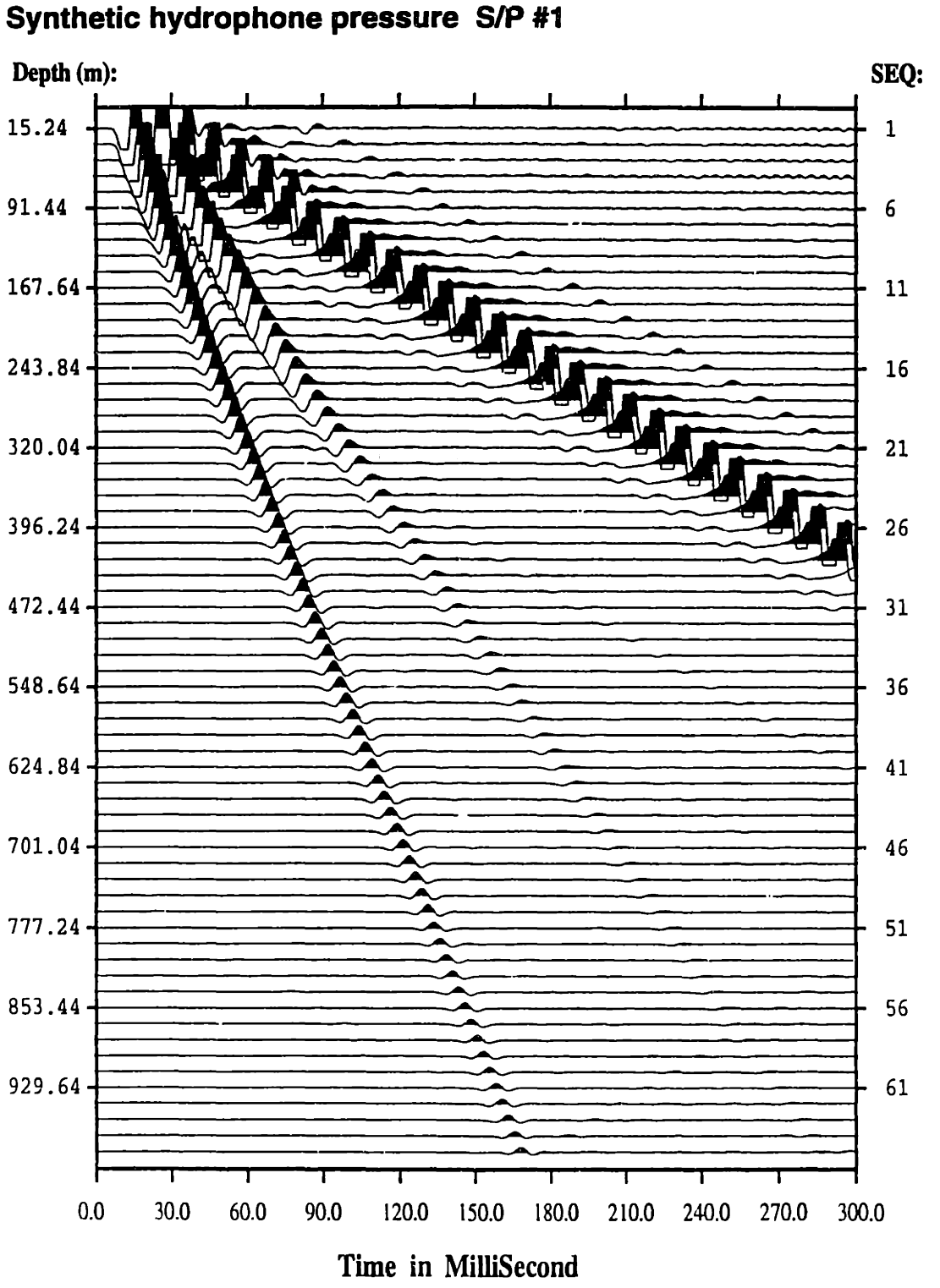

Figure 5-11: Synthetic hydrophone VSP data for the shot point S/P #1, computed with a stratified model for the formation. The source is a vertical force near the free surface, simulating the actual weight drop. Its time history is a Kelly wavelet with the central frequency 100 Hz. Others parameters are given in Table 5.2.

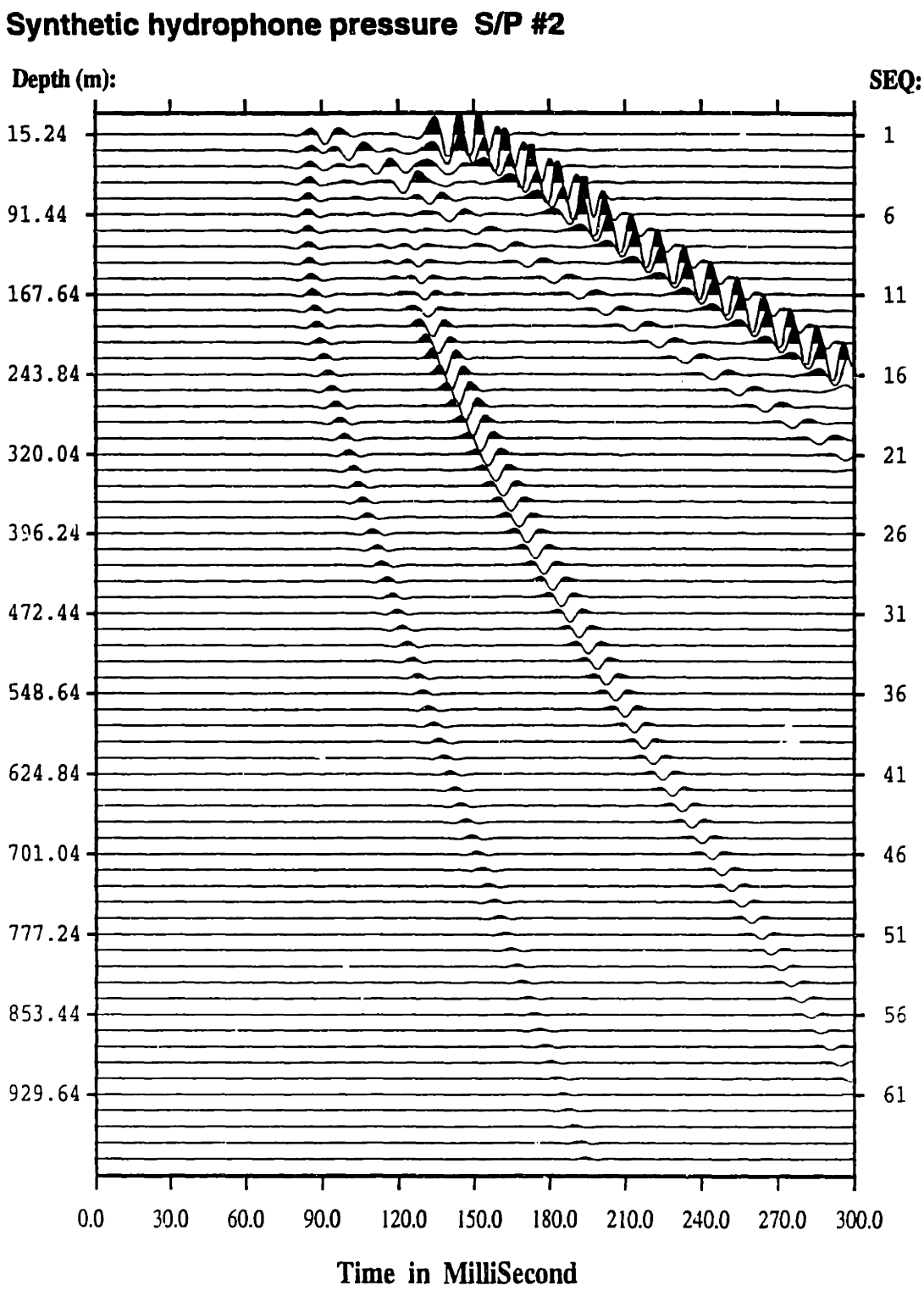

Figure 5-12: Synthetic hydrophone VSP data for the shot point S/P #2, computed with a stratified model for the formation. The source is a vertical force near the free surface, simulating the actual weight drop. Its time history is a Kelly wavelet with the central frequency 100 Hz. Others parameters are given in Table 5.2.

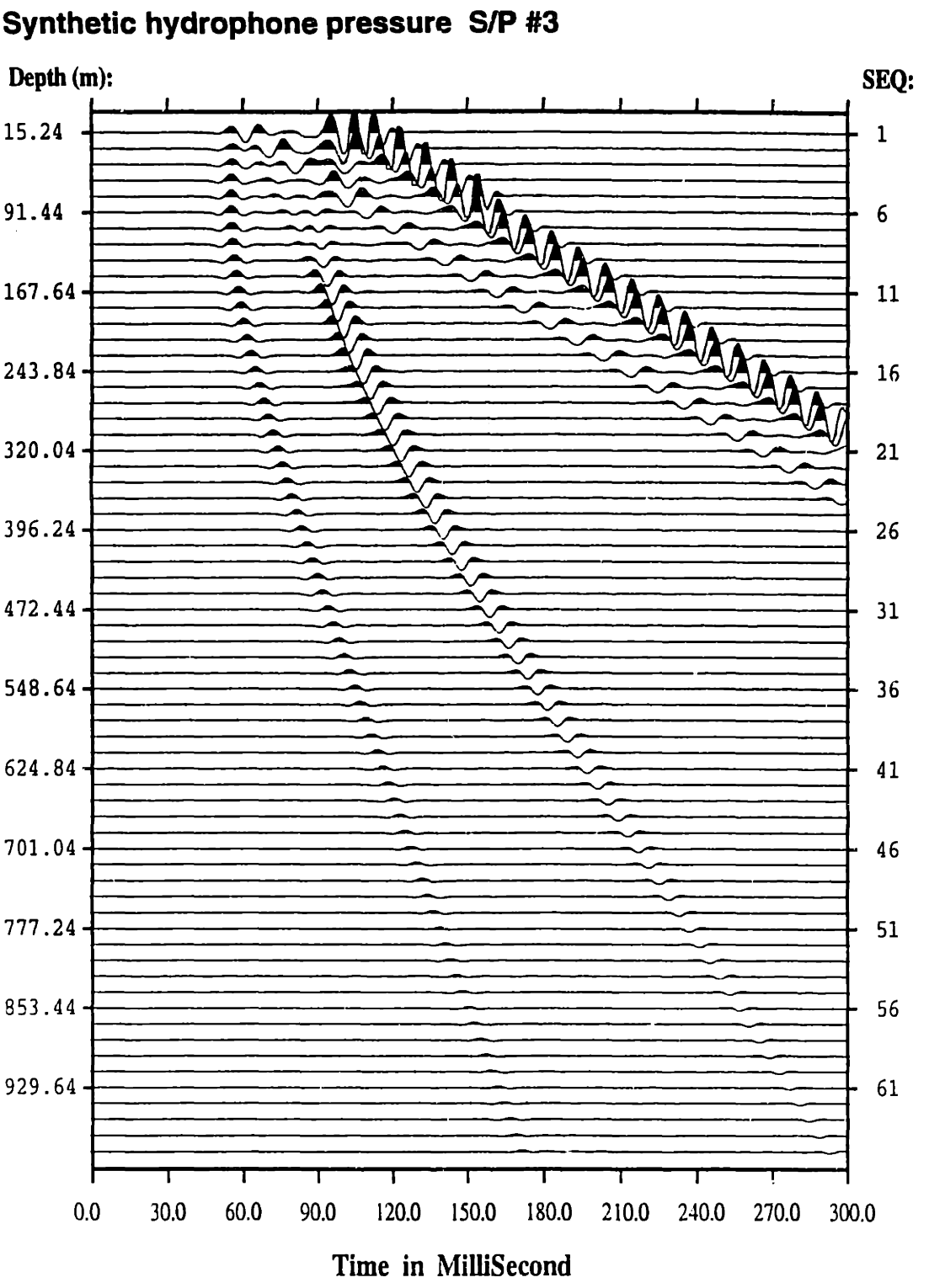

Figure 5-13: Synthetic hydrophone VSP data for the shot point S/P #3, computed with a stratified model for the formation. The source is a vertical force near the free surface, simulating the actual weight drop. Its time history is a Kelly wavelet with the central frequency 100 Hz. Others parameters are given in Table 5.2.

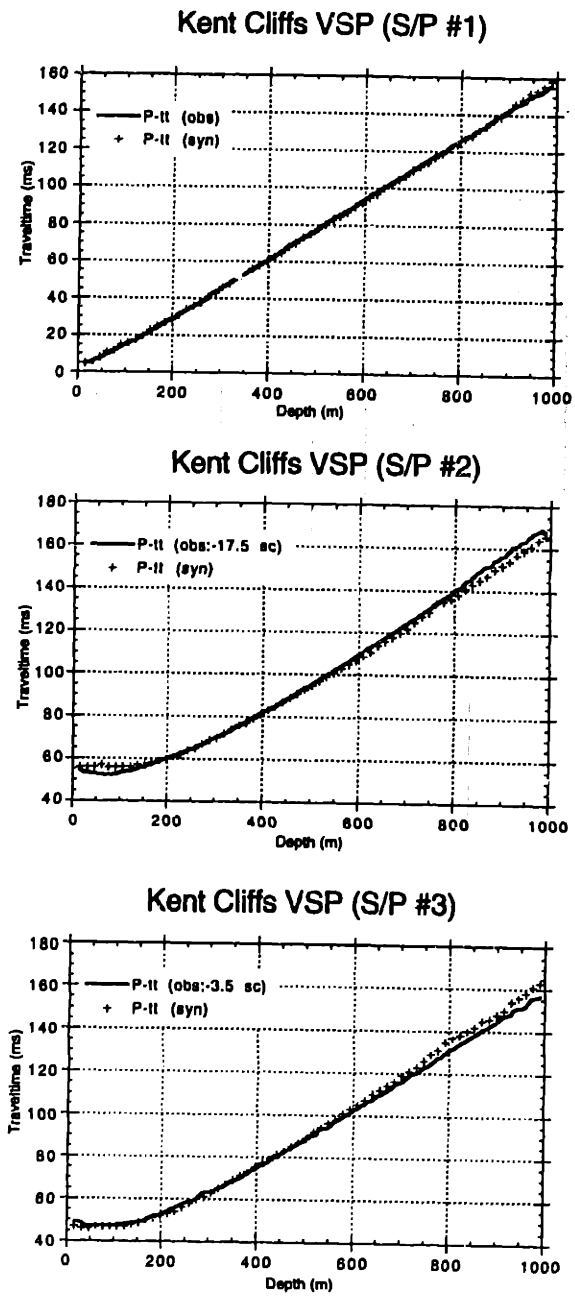

Figure 5-14: P-wave traveltimes for the shot points S/P #1 (a), S/P #2 (b), and S/P #3 (c) . The solid line is the traveltime picked from the field hydrophone measurements shown in Figure 5-8 to Figure 5-10. The plus (+) symbol is the one picked from the synthetic hydrophone pressure shown in Figure 5-11 to Figure 5-13. The horizontal axis is the depth of receivers in meters. The vertical axis is the traveltime in miliseconds.

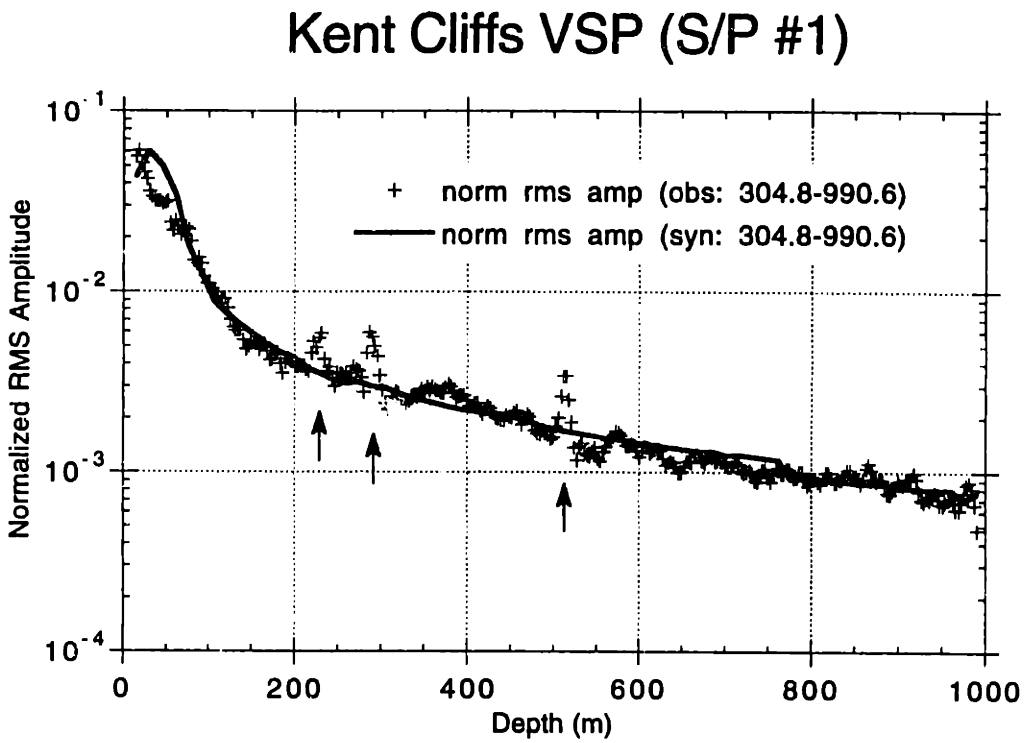

Figure 5-15: RMS (root mean square) amplitudes of the first arrival (P-wave) for the shot points S/P #1. The solid line is the RMS amplitude computed from the synthetic hydrophone pressure shown in Figure 5-11. The plus (+) symbol is the one derived from the field hydrophone measurement shown in Figure 5-8. A constant factor derived from data in the depth range between 304.8 m and 990.6 m is used to normalize the synthetic and field data. The horizontal axis is the depth of receivers in meters. The vertical axis is the normalized RMS amplitude in a logarithmic scale. The arrows indicate locations where tube waves generated by fractures interfere with the P-wave signals.

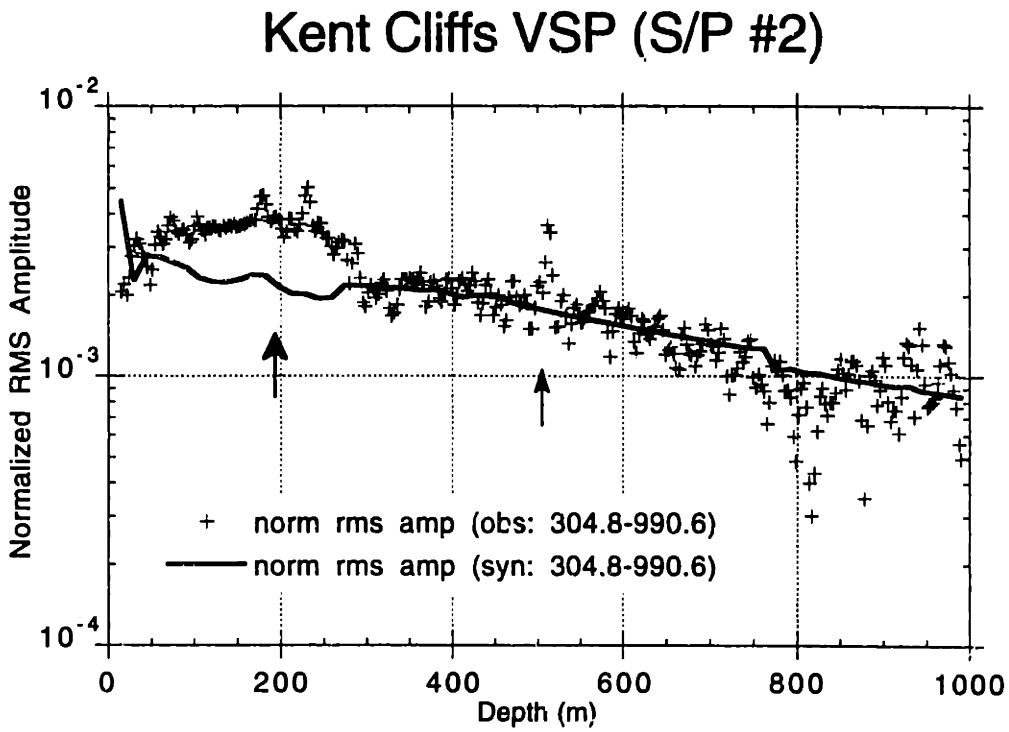

Figure 5-16: RMS (root mean square) amplitude of the first arrival (P-wave) for the shot point S/P #2. The solid line is the RMS amplitude computed from the synthetic hydrophone pressure shown in Figure 5-12. The plus (+) symbol is the one derived from the field hydrophone measurement shown in Figure 5-9. A constant factor derived from data in the depth range between 304.8 m and 990.6 m is used to normalize the synthetic and field data. The horizontal axis is the depth of receivers in meters. The vertical axis is the normalized RMS amplitude in a logarithmic scale. The arrows indicate locations where tube waves interfere with the P-wave signals.

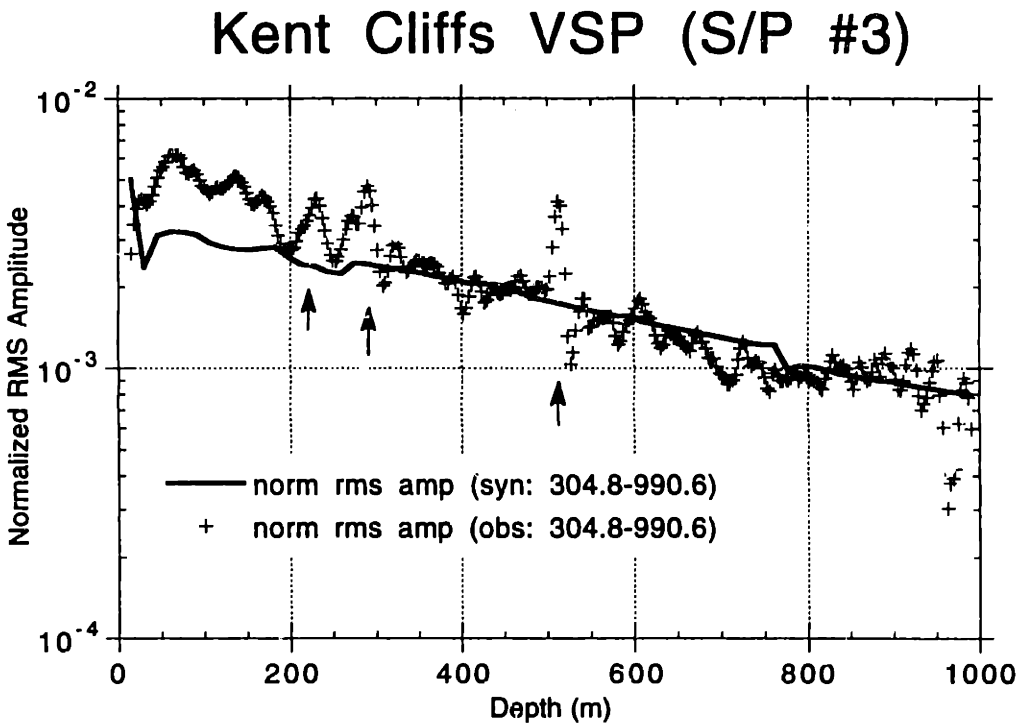

Figure 5-17: RMS (root mean square) amplitude of the first arrival (P-wave) for the shot point S/P #3. The solid line is the RMS amplitude computed using the synthetic hydrophone pressure shown in Figure 5-13. The plus (+) symbol is the one derived from the field hydrophone measurement shown in Figure 5-10. A constant factor derived from data in the depth range between 304.8 m and 990.6 m is used to normalize the synthetic and field data. The horizontal axis is the depth of receivers in meters. The vertical axis is the normalized RMS amplitude in a logarithmic scale. The arrows indicate locations where tube waves interfere with the P-wave signals.

Chapter 6

Borehole Coupling in a Laterally Imhomogeneous Formation

The objective of this chapter is to develop a method of computing pressure in a fluid-filled borehole for a source in a laterally inhomogeneous formation. This method is of practical importance because it aids in both modelling and interpretation of downhole seismic data when the formations adjacent to the borehole are neither homogeneous nor stratified.

There are a variety of techniques in the literature that are capable of computing complete synthetic seismograms for acoustic and elastic wave propagation in heterogeneous media. Among them are the boundary integral equation method and the closely related boundary element method (Kawase, 1988; Dong et al., 1992; Bouchon, 1993, among others), as well as the finite difference method (Stephen et al., 1985; Charrette, 1991; Cheng et al., 1992; Carcione et al., 1992; Kostek, 1993). The boundary integral equation method, using the integral formulation of the wave equation, is well developed for two dimensional wave scattering by irregular interfaces, where only the boundaries are discretized and wave propagation between them is handled by an appropriate Green's function (Kawase, 1988; Bouchon, 1993). On the

other hand, the finite difference method works directly on the differential form of the wave equation by discretizing the whole medium and approximating the differential equations by difference ones. Although the amount of grid points in the boundary integral equation method is, in general, one dimension less than that in the finite difference method, the amount of floating point computation is larger by at least the same factor. Therefore, in terms of cost of memory and CPU time, the two methods are very comparable. The finite difference method, however, has the advantage of simplicity and robustness, and is much easier to adapt to 3-D modeling. To the best of our knowledge, there is no report of applying the boundary integral equation method to the study of elastic wave propagation in a general 3-D medium.

The ability to model wave propagation in a 3-D heterogeneous medium using the finite difference method has become practical only in recent years, thanks to the advent of massively parallelized supercomputers (Fox et al., 1988; Baker et al., 1988; Charrette, 1991; Mora et al., 1992). The parallel computer currently running at the Earth Resources Laboratory of the Massachusetts Institute of Technology has 512 nodes connected by high bandwidth communication channels. Each node is attached to 4 Mbytes in-core memory, which, in total, allow us to run a fairly large size 3-D model in a reasonably short time. Without this machine, it would be inconceivable to solve the problem dealt with in this chapter.

However, directly solving the elastic wave propagation over large distances in a 3-D heterogeneous medium that includes a fluid-filled borehole is neither economical nor feasible for the currently available parallel computers, because of the scale difference between the borehole diameter and the seismic wavelength. The borehole diameter is on the order of 20 cm, while the seismic wavelength is commonly on the order of 20 m. One can not afford to use a grid size of centimeters to model elastic wave propagation through hundreds of meters. The method we use to circumvent this difficulty is to decompose the problem into two distinct parts: compute the stress fields in the vicinity of presumed borehole locations, and apply the borehole coupling theory thereafter to obtain the pressure in the borehole fluid. This approach is in

line with the method employed in chapter 5, where the accuracy is justified by a comparison with an exact solution.

This chapter is organized into four sections. In the first section, we give an outline of a 3-D elastic finite difference formulation. Several issues are addressed, including its properties, accuracy, and implementation. In the second section, we present our discovery of a type of optimal absorbing boundary condition that is especially suited to 3-D finite difference modelling. In the third section, we propose a hybrid technique to compute the pressure in a fluid-filled borehole, given that the stress field around the borehole is already calculated by the finite difference method. An application is also given in this section. In the last section, we give a summary and some conclusions.

6.1 The Finite Difference Method

6.1.1 The Basic Equation

The wave equation for a linear, elastic, isotropic, and heterogeneous medium can be written, using the stress-velocity formulations (Virieux, 1986), as

$$\rho \frac{\partial}{\partial t} V_x = \frac{\partial}{\partial x}\tau_{xx} + \frac{\partial}{\partial y}\tau_{xy} + \frac{\partial}{\partial z}\tau_{xz}, \tag{6.1a}$$

$$\rho \frac{\partial}{\partial t} V_y = \frac{\partial}{\partial x}\tau_{xy} + \frac{\partial}{\partial y}\tau_{yy} + \frac{\partial}{\partial z}\tau_{yz}, \tag{6.1b}$$

$$\rho \frac{\partial}{\partial t} V_z = \frac{\partial}{\partial x}\tau_{xz} + \frac{\partial}{\partial y}\tau_{yz} + \frac{\partial}{\partial z}\tau_{zz}, \tag{6.1c}$$

and

$$\frac{\partial}{\partial t}\tau_{xx} = (\lambda + 2\mu)\ \frac{\partial}{\partial x} V_x + \lambda\ \frac{\partial}{\partial y} V_y + \lambda\ \frac{\partial}{\partial z} V_z, \tag{6.2a}$$

$$\frac{\partial}{\partial t}\tau_{yy} = \lambda\ \frac{\partial}{\partial x} V_x + (\lambda + 2\mu)\ \frac{\partial}{\partial y} V_y + \lambda\ \frac{\partial}{\partial z} V_z, \tag{6.2b}$$

$$\frac{\partial}{\partial t}\tau_{zz} = \lambda\ \frac{\partial}{\partial x} V_x + \lambda\ \frac{\partial}{\partial y} V_y + (\lambda + 2\mu)\ \frac{\partial}{\partial z} V_z, \tag{6.2c}$$

$$\frac{\partial}{\partial t}\tau_{xy} = \mu\,(\frac{\partial}{\partial y}V_x + \frac{\partial}{\partial x}V_y), \tag{6.2d}$$

$$\frac{\partial}{\partial t}\tau_{xz} = \mu\,(\frac{\partial}{\partial z}V_x + \frac{\partial}{\partial x}V_z), \tag{6.2e}$$

$$\frac{\partial}{\partial t}\tau_{yz} = \mu\,(\frac{\partial}{\partial z}V_y + \frac{\partial}{\partial y}V_z), \tag{6.2f}$$

where the first three are the equations of motion and the last six are the equations of constitutive laws. (V_x, V_y, V_z) is the particle velocity vector, $(\tau_{xx}, \tau_{yy}, \tau_{zz}, \tau_{xy}, \tau_{yz}, \tau_{xz})$ is the stress tensor. ρ is the density, λ and μ are the Lamé's parameters.

A three dimensional staggered grid is built upon these stress-velocity equations. The structure is analogous to Virieux (1986) for 2-D modeling. The layout of the grid upon a computational domain is shown in Figure 6-1. At each grid point, the particle velocity vector is half-grid shifted along the three coordinate axes. Normal stresses are defined at the vertices, while the shear stresses are half-grid shifted along both directions in their action planes. The elastic parameters are defined at locations where they are actually used. Such a staggered grid ensures that all the difference approximations are properly centered.

In the finite difference approximations to the differential equations, a scheme is used that has second order accuracy in time and fourth order accuracy in space (Levander, 1988; Cheng et al., 1992). The advantage of the fourth order scheme over the second order one is well-known (e.g., Fornberg, 1987). We prefer the fourth order scheme to both the higher order ones and the spectral method, because the fourth order scheme seems to be a trade-off between the grid dispersion and the amount of floating-point computations (Sei, 1993), and is much easier to implement on a parallel computer.

Another aspect that is crucial to finite difference modeling is the choice of proper absorbing boundary conditions. Absorbing boundary conditions are needed to minimize artificial reflections from the edges of the domain of computation. Viscous damping (Cerjan et al., 1985) is not suitable to 3-D elastic modelling, where the in-core memory is very limited, and thus, valuable. Paraxial approximation by Clayton

and Engquist (1977) tends to be unstable for some combinations of elastic parameters, and is not easy to parallelize. A scheme that is stable, effective, and easy to realize on a parallel computer is desirable. Although the absorbing boundary conditions developed by Reynolds (1978), Liao et al. (1984) and Higdon (1986, 1990) are candidates in this search, none has proven optimal in the sense that it achieves a maximum absorbing effect with a minimum amount of computation and storage on the boundaries. We discovered an effective way to find this class of optimal absorbing boundary conditions. As a major contribution to this chapter, we present our optimal absorbing boundary conditions in the next section.

6.1.2 Accuracy and Performance

To study its accuracy and performance, we compare the 3-D finite difference technique with the classical discrete wavenumber – (propagator) global matrix method (Harkrider, 1964; Bouchon, 1981; Chin et al., 1984). The problem is to model elastic wave propagation in a stratified isotropic medium with a free surface at the top boundary. A crosswell configuration is used in this simulation. A source is at depth 300 m. There are 41 receivers distributed equally at depths from 0 to 600 m. The horizontal offset between the source and the receivers is 300 m. In the 3-D finite difference calculation, the cubic volume is discretized into $100 \times 100 \times 200$ grid points. The grid size is 4 m, which is about one tenth of the shortest shear wavelength. The source is an explosion. Its time history is a Kelly wavelet with the central frequency of 50 Hz. The time sampling interval is 0.2 ms. The top surface is stress free. Symmetric boundary conditions are used at the surfaces $x = 0$ and $y = 0$. The optimal absorbing boundary condition is applied to the remaining boundaries. In the discrete wavenumber – (propagator) global matrix method, the same explosive source is used. Excessive wavenumber summation is undertaken to ensure accuracy of the results (for details, see the previous chapter).

Table 6.1 lists the physical parameters for the calculation. Both the compressional

and shear velocities increase with depth with an exception at the 400 m – 500 m interval. The source is located right on the interface at 300 m. Figure 6-2 and Figure 6-3 show the horizontal and vertical components of particle velocity computed by both the discrete wavenumber – global matrix method (dashed line) and the 3-D finite difference technique developed in this chapter (solid line). In these figures, the first events are the direct P-waves, which are followed by converted S-waves. The free surface reflections are discernible. The two calculations are almost identical. Some slight disagreement can be found, which is attributed to the cumulative grid dispersion in the finite difference modeling, especially at high frequencies. This comparison confirms that the finite difference technique is accurate.

depth (m)	*P-wave velocity* (m/s)	*S-wave velocity* (m/s)	*density* (g/cm^3)
0–100	3000	2000	2.00
100–200	3500	2400	2.20
200–300	4000	2600	2.30
300–400	4500	3000	2.50
400–500	4300	2800	2.40
500–∞	4500	3000	2.50

Table 6.1: medium parameters for the examples in Figures 6-2 and 6-3.

The performance of our code is also very good in terms of the efficiency of the concurrent computation. For a 3-D cube as large as this example (approximately 96 Mbytes in-core memory) and 2000 time steps (about 1.32 Teraflops), it takes about 40 minutes on 128 nodes nCUBE-2. Each node of nCUBE-2 is about 3/4 times slower than a personal DECstation 5000/25 machine. Taking this factor into account, we find that this problem would run 63 hours on the DECstation, assuming that the in-core memory allows it.

6.2 Optimal Absorbing Boundary Conditions

Absorbing boundary conditions are widely used in the numerical modeling of wave propagation in unbounded media to reduce reflections from artificial boundaries (Lindman, 1975; Clayton and Engquist, 1977; Reynolds, 1978; Liao et al., 1984; Cerjan et al., 1985; Higdon, 1986; Randall, 1988; Higdon, 1991). The absorbing boundary condition one chooses should allow for a maximum absorbing effect with a minimum amount of computation and storage, and should be easily implemented. These requirements are necessary because of the computational efficiency. In this section, we present an algorithm to design a class of optimal absorbing boundary conditions for a given operator length where only grid points perpendicular to the boundary are used. As in Liao et al. (1984) and Higdon (1986), we employ directly a discrete formulation of extrapolation on a finite difference grid. The major motivation behind this decision is that the reflection coefficient of a discretized absorbing boundary condition differs from the corresponding continuous one by $O(\omega\Delta t, \omega/\alpha\Delta x)$, which is not small for a typical computer simulation with $\omega/\alpha\Delta x = 2\pi/10 \sim 0.628$ (i.e., 10 grid points per wavelength), where ω denotes frequency, α is the medium velocity, Δt the time step, and Δx the grid size (Higdon, 1986). We will show that for an absorbing boundary condition to be optimal, the zeros and poles of the reflection coefficients in a complex plane must lie on specific locations of the unit circle. A fast algorithm will be given to design useful absorbing boundary conditions.

6.2.1 Problem Statement

Let $v^n(i,j,k)$ denote a wavefield at $(x = i\Delta x,\ y = j\Delta y,\ z = k\Delta z)$ and at time $t = n\Delta t$. In the interior of a finite difference domain, v is updated according to the difference approximations of wave equations. On the artificial boundaries, extrapolation based on values at previous time steps and/or interior grids is needed to minimize unwanted reflections.

Let us write $v^{n+1}(0,j,k)$ on the artificial boundary, e.g., $x = 0$ (see Figure 6-4), as a linear combination of fields at previous time steps and at $x \geq 0$ as:

$$\begin{aligned} v^{n+1}(0,j,k) &= a_{01}v^{n+1}(1,j,k) + a_{02}v^{n+1}(2,j,k) \\ &+ a_{10}v^{n}(0,j,k) + a_{11}v^{n}(1,j,k) + a_{12}v^{n}(2,j,k) \\ &+ a_{20}v^{n-1}(0,j,k) + a_{21}v^{n-1}(1,j,k) + a_{22}v^{n-1}(2,j,k), \end{aligned} \tag{6.3}$$

where the coefficients $\{a_{ij}\}(a_{00} \equiv 0)$ are chosen such that reflections from the artificial boundary at $x = 0$ are as small as possible. In acoustic cases, equation (6.3) is applied directly to the pressure field on the artificial boundary. When used to absorb elastic energy, equation (6.3) is applied to the individual component of an elastic wave. In this scheme, only grid points perpendicular to the boundary are used in the extrapolation process. The extrapolation operator is two steps in both time and space grids, i.e., a (2,2) scheme where the first number refers to the steps in time and the second in space. A more general formulation will be given at the end of this section. The (2,2) schemes are used often in the literature (Clayton and Engquist, 1977; Reynolds, 1978; Higdon, 1990) because it is very efficient in both computation and memory, and is easy to code.

6.2.2 Plane Wave Reflection Coefficients

Assume the elastic potentials of incident and reflected plane waves in the (x,z) plane are

$$\Phi = \Phi_0 \exp(i\omega t + ik_\alpha \cos\theta x + ik_\alpha \sin\theta z) + R_p \exp(i\omega t - ik_\alpha \cos\theta x + ik_\alpha \sin\theta z),$$

$$\Psi = \Psi_0 \exp(i\omega t + ik_\beta \cos\phi x + ik_\beta \sin\phi z) + R_s \exp(i\omega t - ik_\beta \cos\phi x + ik_\beta \sin\phi z),$$

where Φ is a dilatation potential and Ψ is the y-component of a rotational potential. Φ_0 and Ψ_0 are the amplitudes of the incident P- and S-waves, respectively. In the case where $\Phi_0 = 1$ and $\Psi_0 = 0$, R_p and R_s are the P–P and P–S reflection coefficients, respectively, and are subsequently referenced to as R_{pp} and R_{ps}. Similarly, in the case

where $\Phi_0 = 0$ and $\Psi_0 = 1$, R_p and R_s are the S–P and S–S reflection coefficients, respectively, and are subsequently referenced to as R_{sp} and R_{ss}. In the above equations, ω denotes wave frequency; $k_\alpha = \omega/\alpha$ is the compressional wavenumber; $k_\beta = \omega/\beta$ is the shear wavenumber. θ and ϕ are the angles of incidence of the P- and S-waves, respectively, and are related by

$$\frac{\sin\theta}{\alpha} = \frac{\sin\phi}{\beta}$$

the Snell's law.

The displacements in the x and z directions are related to these potentials by the following expressions (Ewing et al., 1957)

$$u = \frac{\partial\Phi}{\partial x} - \frac{\partial\Psi}{\partial z},$$
$$w = \frac{\partial\Phi}{\partial z} + \frac{\partial\Psi}{\partial x},$$

where u is the horizontal displacement and w is the vertical displacement.

Let $\mathrm{z} = \exp(i\omega\Delta t)$ be a one-step shift in time, $\mathrm{z}_a = \exp(ik_\alpha \cos\theta\Delta x)$ be a one-step shift in space with an apparent compressional velocity, and $\mathrm{z}_b = \exp(ik_\beta \cos\phi\Delta x)$ be a one-step shift in space with an apparent shear velocity. By expressing the displacements on the finite difference grid in terms of z, z_a and z_b, and substituting them into the boundary condition (6.3), we obtain the elastic reflection coefficients as

$$R_{pp} = \frac{\xi-\eta}{\xi+\eta}\,\frac{\Omega_0+\Omega_1\mathrm{z}_a+\Omega_2\mathrm{z}_a^2}{\Omega_0+\Omega_1\mathrm{z}_a^{-1}+\Omega_2\mathrm{z}_a^{-2}}, \tag{6.4}$$

$$R_{ps} = \frac{2\xi\eta}{\xi+\eta}\,\frac{\Omega_0+\Omega_1\mathrm{z}_a+\Omega_2\mathrm{z}_a^2}{\Omega_0+\Omega_1\mathrm{z}_b^{-1}+\Omega_2\mathrm{z}_b^{-2}}, \tag{6.5}$$

$$R_{sp} = -\frac{2}{\xi+\eta}\,\frac{\Omega_0+\Omega_1\mathrm{z}_b+\Omega_2\mathrm{z}_b^2}{\Omega_0+\Omega_1\mathrm{z}_a^{-1}+\Omega_2\mathrm{z}_a^{-2}}, \tag{6.6}$$

$$R_{ss} = \frac{\xi-\eta}{\xi+\eta}\,\frac{\Omega_0+\Omega_1\mathrm{z}_b+\Omega_2\mathrm{z}_b^2}{\Omega_0+\Omega_1\mathrm{z}_b^{-1}+\Omega_2\mathrm{z}_b^{-2}}, \tag{6.7}$$

where R_{pp} and R_{ps} are the P–P and P–S reflection coefficients, and R_{sp} and R_{ss} are the S–P and S–S reflection coefficients, respectively. In equations (6.4)–(6.7),

$$\Omega_0 = a_{00}\mathrm{z} + a_{10} + a_{20}\mathrm{z}^{-1} - \mathrm{z}, \tag{6.8}$$

$$\Omega_1 = a_{01}z + a_{11} + a_{21}z^{-1}, \tag{6.9}$$

$$\Omega_2 = a_{02}z + a_{12} + a_{22}z^{-1}, \tag{6.10}$$

are the **z-transforms** along columns of the coefficient matrix $\{a_{ij}\}$. $\xi = \frac{\beta}{\alpha}\cos\theta/\sin\phi$ and $\eta = \frac{\beta}{\alpha}\sin\theta/\cos\phi$ are two factors independent of the finite difference grid. Note that equations (6.4)–(6.7) agree with Higdon (1990) in the continuous limit $\Delta t \to 0, \Delta x \to 0$ and $\Delta t/\Delta x$ finite.

The reflection coefficients on a finite difference grid have neat structures. For instances, the numerator is a space z-transform associated with the incident wave; the denominator is another space z-transform associated with the reflected wave; the coefficients Ω_0, Ω_1, and Ω_2 are z-transforms with respect to time; the numerator represents a wave propagating toward an artificial boundary, therefore it is a polynomial of positive power of z; the denominator represents a wave reflected backward into the finite difference domain and is a polynomial of the negative power of z.

6.2.3 Transfer Functions Analogy

Using electrical engineering terminology, the reflection coefficients in equations (6.4)–(6.7) (e.g., R_{pp}) can be regarded as the combined transfer functions of two cascaded subsystems shown in the block diagram of Figure 6-5. The input $\mathrm{x}(n)$ is passed to the inverse of a delayed feed-backward subsystem. In turn, the intermediate result $\mathrm{w}(n)$ is fed into an advanced feed-forward subsystem to generate the system output $\mathrm{y}(n)$. These two cascaded subsystems can be represented by a pair of difference equations (Oppenheim et al., 1989):

$$\Omega_0\mathrm{w}(n) + \Omega_1\mathrm{w}(n-1) + \Omega_2\mathrm{w}(n-2) = \mathrm{x}(n), \tag{6.11}$$

$$\Omega_0\mathrm{w}(n) + \Omega_1\mathrm{w}(n+1) + \Omega_2\mathrm{w}(n+2) = \mathrm{y}(n), \tag{6.12}$$

with the first a causal system and the second an anticausal system.

The transfer functions of these two difference equations, obtained by z_a-transforming

both sides of the above difference equations, are

$$D_{-}(z_a) = \frac{1}{\Omega_0 + \Omega_1 z_a^{-1} + \Omega_2 z_a^{-2}}, \tag{6.13}$$

$$D_{+}(z_a) = \frac{1}{\Omega_0 + \Omega_1 z_a + \Omega_2 z_a^{2}}, \tag{6.14}$$

respectively. By eliminating the z_a-transform of $w(n)$, the transfer function of the entire system is

$$H(z_a) = \frac{D_{-}(z_a)}{D_{+}(z_a)}.$$

By inspection, we find that R_{pp}, the P–P reflection coefficient, is related to $H(z_a)$ by

$$R_{pp} = \frac{\xi - \eta}{\xi + \eta} H(z_a), \tag{6.15}$$

and similar relationships exist for the other reflection coefficients.

We also note that: (1) for the first subsystem to be stable, the poles of $D_{-}(z_a)$ must be inside the unit circle $| z_a | = 1$ in a complex z_a plane (Robinson and Treitel, 1980; Oppenheim et al., 1989); (2) for the same reason, the pole of $D_{+}(z_a)$ must be outside the unit circle. We can draw the following conclusions for the derived reflection coefficients in equations (6.4)–(6.7):

- The poles of the reflection coefficients must be on or inside the unit circle.
- The zeros of the reflection coefficients must be on or outside the unit circle.

We include the unit circle as a permissible position for both the zeros and the poles because, as will be shown later, z_a is defined only on a small segment of the unit circle for an angle of incidence from 0^o up to 90^0.

6.2.4 Design of Optimal Absorbing Boundary Conditions

Summation identity: The first identity is

$$\sum_{i=0,j=0}^{2} a_{ij} = 1, \tag{6.16}$$

i.e., summation of the coefficients on the right-hand side of equation (6.3) must be one.

There are many ways to prove equation (6.16). Taking the limit of $\Delta t \to 0$ and $\Delta x \to 0$, the wave field around the boundary should be the same in the tiny region $(x = 0, x+2\Delta x)$ and $(t-\Delta t, t+\Delta t)$, which yields equation (6.16) from equation (6.3). Imagining that $\Delta t \to 0$ and $\Delta x \to 0$, i.e., $(z, z_a, z_b) \to (1, 1, 1)$, we have the reflection coefficients, e.g., R_{pp},

$$R_{pp} \to \frac{\xi - \eta}{\xi + \eta}$$

for $\Omega_0 + \Omega_1 + \Omega_2 \neq 0$. If this is true, R_{pp} will be finite at almost all angles of incidence. This case fails to achieve our objective of finding appropriate coefficients that minimize the reflection coefficients. For that, we must have $\Omega_0 + \Omega_1 + \Omega_2 = 0$ when $\Delta t \to 0$ and $\Delta x \to 0$, which also yields equation (6.16).

Differentiation identities: The second and third identities are

$$\sum_{j=0}^{2}(a_{0j} - a_{2j}) = 1, \tag{6.17}$$

and

$$\sum_{i=0}^{2}(a_{i0} - a_{i2}) = 1, \tag{6.18}$$

where equation (6.17) is true if no $\partial/\partial t$ term exists in the equivalent differential form of (6.3), and equation (6.18) is true also if no $\partial/\partial x$ term exists.

Equations (6.17) and (6.18) are also the consequence of

$$R_{pp}(\Delta t, \Delta x) = R_{pp}(0, 0) + O[(\Delta t)^2, (\Delta x)^2]$$

as $\Delta t \to 0$ and $\Delta x \to 0$. That is, the rate of convergence should be at least as fast as $O((\Delta t)^2, (\Delta x)^2)$. A simple Taylor expansion of the numerator and denominator of the reflection coefficient in terms of Δt and Δx is enough to obtain equations (6.17) and (6.18).

Minimum energy wavelet: As we will show later, there is a degree of freedom in choosing coefficients in equation (6.3) for a given optimal absorbing ability other than the above three constraints. For this reason, we impose the energy minimization constraint to the coefficients $\{a_{ij}\}$ as,

$$\sum_{i=0,j=0}^{2} a_{ij}^2 = \text{minimum}. \tag{6.19}$$

$\Delta t \to 0$ **paradox:** Suppose $\Delta t \to 0$ and Δx finite. Then,

$$\text{Im}(\Omega_0) \to 0,$$

$$\text{Im}(\Omega_1) \to 0,$$

$$\text{Im}(\Omega_2) \to 0,$$

where $\text{Im}(\cdot)$ denotes the imaginary part of a quantity in the bracket.

Under these conditions, for all $z_a = \exp(ik_\alpha \cos\theta \Delta x)$ on the unit circle we have

$$\| \frac{\Omega_0 + \Omega_1 z_a + \Omega_2 z_a^2}{\Omega_0 + \Omega_1 z_a^{-1} + \Omega_2 z_a^{-2}} \| \to 1.$$

This observation has two implications: (1) keeping Δt very small reduces the effectiveness of an absorbing boundary, although interior time integration is more accurate; and (2) the optimal absorbing condition exists only where $\alpha \Delta t / \Delta x$ is finite.

6.2.5 Zeros and Poles

Recall that

$$z_a = \exp(ik_\alpha \cos\theta \Delta x),$$

where θ is the angle of incidence of a plane wave impinging on a boundary. As θ varies from 0^o to 90^o, in the complex plane, z_a lies between $(\cos(k_\alpha \Delta x), \sin(k_\alpha \Delta x))$ and $(1, 0)$ along the unit circle. In terms of the phase angle ϑ (measured from the real axis), z_a lies on a segment of the unit circle with

$$0 \le \vartheta_a \le k_\alpha \Delta x.$$

Similarly, z_b, the one-step shift with the apparent shear velocity, is on a segment of the unit circle with

$$0 \leq \vartheta_b \leq k_\beta \Delta x.$$

It is easy to show that $\vartheta_a < \vartheta_b$ since $\alpha > \beta$.

The reflection coefficients, e.g. R_{pp}, have two zeros and two poles in the complex z plane. The zeros are at

$$z_c^{\pm} = -\frac{\Omega_1 \pm \sqrt{\Omega_1^2 - 4\Omega_0\Omega_2}}{2\Omega_2}, \tag{6.20}$$

and the poles are at

$$z_p^{\pm} = -\frac{\Omega_1 \pm \sqrt{\Omega_1^2 - 4\Omega_0\Omega_2}}{2\Omega_0}. \tag{6.21}$$

Note that the difference between the zeros and poles is just a factor of Ω_0/Ω_2.

The location of the zeros and poles determines the reflection coefficients. For example, the magnitude of the reflection coefficient R_{pp} is proportional to the ratio of

$$\frac{|\, z_a - z_c^+ \,|\, |\, z_a - z_c^- \,|}{|\, z_a - z_p^+ \,|\, |\, z_a - z_p^- \,|},$$

where the terms inside the vertical bars are distances between z_a and the zeros or the poles, as shown in Figure 6-6.

Requirements for the location of the zeros and poles are: (1) the zeros are on or outside the unit circle; (2) the poles are on or inside the unit circle; and (3) for an optimal boundary condition, both of the zeros are on the segment of the unit circle where z_a is defined such that there is an optimal cancellation in the numerators of the reflection coefficients. Since the poles are dependent on the zeros, their locations inside or on the unit circle are not arbitrary. Optimal locations of the zeros and poles do exist where the reflection coefficients have local minima.

6.2.6 Relationships Between Zeros and Poles

Suppose the two zeros of the reflection coefficient R_{pp}, $z_c^{\pm}$, are given, the two poles are determined by

$$z_p^{\pm} = \frac{1}{z_c^{\mp}}, \tag{6.22}$$

i.e., the zeros are paired with the poles in such a way that one is the inverse of the other. The proof is straightforward by making use of $\Omega_1/\Omega_2 = -(z_c^+ + z_c^-)$ and $\Omega_0/\Omega_2 = z_c^+ z_c^-$.

The implications of equation (6.22) are: (1) if the zeros are outside the unit circle, the poles must be inside the unit circle; (2) the magnitude of a pole is the inverse of that of a zero, and the phase of a pole is the negative of that of a zero; (3) if the zeros are on the unit circle, so are the poles. More important, in the last case, the phase angles of the zeros determine the properties of the reflection coefficients.

6.2.7 Properties of Optimal Absorbing Boundary Conditions

We state that "for an absorbing boundary condition to be optimal, the zeros of the reflection coefficients must be on the unit circle, and if $k_\alpha \Delta x < \frac{\pi}{2}$, the zeros must be in the first quadrant." Here, $k_\alpha \Delta x < \frac{\pi}{2}$ comes from the requirement that at least five grid points per wavelength are needed to reduce grid dispersion for the commonly used fourth-order differentiation scheme (Virieux, 1986; Levander, 1988).

To prove this statement, we rewrite the reflection coefficient (acoustic case) as

$$R_{pp} = \frac{(z_a - z_c^+)(z_a - z_c^-)}{(z_a^{-1} - z_c^+)(z_a^{-1} - z_c^-)}, \tag{6.23}$$

using equation (6.22) in the derivation. As a reminder, the domain of z_a is on a segment of the unit circle with a phase angle between $(0, k_\alpha \Delta x]$.

Let $z_c^+ = r_+ e^{i\vartheta_+}$, $z_c^- = r_- e^{i\vartheta_-}$, the statement says that for fixed ϑ_+ and ϑ_- in

$(0, k_\alpha \Delta x]$, the minimum magnitude of R_{pp} occurs at $r_+ = r_- = 1$. Analytical proof is mathematically involved. A graphic proof is shown in Figure 6-7, where the open circle represents one of the two zeros of the reflection coefficient in equation (6.23), and the two solid circles represent z_a and z_a^{-1}, respectively. As the zero of equation (6.23) moves toward infinity in the first quadrant, the ratio of $\mid z_a - z_c^{\pm} \mid / \mid z_a^{-1} - z_c^{\pm} \mid$ increases monotonically to one. A minimum exists only at $\mid z_c^{\pm} \mid = 1$.

6.2.8 A Fast Algorithm

Advantages can be gained by making use of the properties of an optimal absorbing boundary condition. We propose the following algorithm to design a useful optimal boundary condition to absorb artificial reflections. The inputs to the algorithm are: (1) two physical angles of incidence, θ^+ and θ^-, at which either R_{pp} or R_{ss} (depending on the user's choice) is zero; and (2) the dimensionless time step, $\widetilde{\Delta t} = \omega \Delta t$, and grid size, $\widetilde{\Delta x} = \omega / \alpha \Delta x$ for maximum P-wave absorption, or $\widetilde{\Delta x} = \omega / \beta \Delta x$ for maximum S-wave absorption, where ω is the central frequency of a source wavelet in the calculation. The phase angles, ϑ_+ and ϑ_-, of the two zeros are related to the physical angles of incidence, $\theta^{\pm}$, by

$$\vartheta_{\pm} = \widetilde{\Delta x} \cos \theta^{\pm}. \tag{6.24}$$

It is easy to show that

$$\frac{a_{00} z + a_{10} + a_{20} z^{-1} - z}{a_{02} z + a_{12} + a_{22} z^{-1}} = \cos(\vartheta_+ + \vartheta_-) + i \sin(\vartheta_+ + \vartheta_-), \tag{6.25}$$

and

$$\frac{a_{01} z + a_{11} + a_{21} z^{-1}}{a_{02} z + a_{12} + a_{22} z^{-1}} = -(\cos \vartheta_+ + \cos \vartheta_-) - i(\sin \vartheta_+ + \sin \vartheta_-), \tag{6.26}$$

where equations (6.8)– (6.10) are used, and $z = \exp(i \widetilde{\Delta t})$.

The above two equations offer four constraints on the coefficients $\{a_{ij}\}$ where eight are unknown ($a_{00} \equiv 0$). The other four constraints come from the three identities in equations (6.16), (6.17) and (6.18), and the minimum energy criterion in equation (6.19). The algorithm to compute $\{a_{ij}\}$ is presented in Appendix E. The

absorbing boundary condition designed with this algorithm is guaranteed to be optimal in the sense that the artificial reflections are at least local minima.

For a practical problem with $\alpha = 3000$ m/s, $\beta = 2000$ m/s, $\Delta t = 0.0005$ s, $\Delta x = 10$ m, and $\omega = 2\pi \times 20$ Hz, choosing the design parameters $\theta^+ = 40.40^o$ and $\theta^- = 11.32^o$ for maximum P-wave absorptions (Peng and Toksöz, 1993c), we obtain the coefficients $\{a_{ij}\}$, shown in Table 6.2, of an optimal absorbing boundary condition whose properties are to be discussed in the following texts.

a_{ij}	j=0	j=1	j=2
i = 0	0.0000000000	-0.0893569160	-0.6916645269
i = 1	1.6376375943	0.2867676972	1.6376375943
i = 2	-0.6916645269	-0.0893569160	-1.0000000000

Table 6.2: List of coefficients of the optimal absorbing boundary whose zero-pole plot is shown in Figure 6-8a.

6.2.9 Analysis of Results

Figure 6-8a shows, in a complex z-plane, the zeros and poles of the optimal absorbing boundary condition in Table 6.2. For comparison, we also compute the zeros and poles of Reynolds' absorbing condition (Figure 6-8b) using his equation (18c) (Reynolds, 1978) and of Higdon's absorbing condition (Figure 6-8c) using his equation (12) with ($\beta_1 = 1$, $\beta_2 = \alpha/\beta = 1.5$) (Higdon, 1991). We find that, for the optimal absorbing boundary condition, the two zeros are located exactly on the segment of the unit circle where z_a is defined for an angle of incidence between 0^o and 90^o. Reynolds' and Higdon's absorbing boundary conditions do not have this property. There is only one zero on the unit circle slightly above the real axis for Reynolds' boundary condition, while two zeros remain outside the unit circle for Higdon's absorbing condition. The two poles of the optimal absorbing condition are also located on the unit circle at the

conjugated positions of the two zeros. For Reynolds' boundary condition, one pole is almost on the unit circle and slightly below the real axis, very close to the domains of z_a and z_b. Reynolds' boundary condition behaves poorly as $\Delta t \rightarrow 0$, because this particular pole comes increasingly closer to the real axis.

The reflection coefficients of the optimal, Reynolds', and Higdon's absorbing boundary conditions in the acoustic case are plotted in Figure 6-9. The horizontal axis is the angle of incidence and the vertical axis is $20 \log_{10}(\mid R_{pp} \mid + \epsilon)$, where $\epsilon = 10^{-20}$ is a small positive number for avoiding the singularity of the log function. The reflection coefficient of the optimal absorbing boundary condition has two zeros and is generally 10-20 dB less in magnitude than Higdon's absorbing boundary condition, which in turn has a better performance by about 10 dB (less) over Reynolds' boundary condition. An exception occurs at an angle near grazing incidence, where Reynolds' absorbing boundary condition has a smaller reflection. Comparing the plots in the three studies (i.e., Reynolds (1978), Higdon (1991), and this study), we find that the reflection coefficients on a discrete finite difference grid are different from those derived from an analytical boundary condition. For example, in the continuous case, the acoustic reflection coefficient in both Reynolds' and Higdon's absorbing boundary conditions is zero at normal incidence $\theta = 0^o$, while on a discrete finite difference lattice this is not the case.

Now let us look at the reflection coefficients with the absorbing condition in equation (6.3) applied to each elastic wave component. Figure 6-10a shows the P – P reflection coefficients for the three absorbing boundary conditions discussed in previous examples. We find that, besides the two zeros at $z_a = z_c^{\pm}$, there is a physical zero in R_{pp} where $\xi = \eta$ such that there is no P-wave reflection. On the average, the optimal absorbing boundary condition out performs other boundary conditions by approximately 10–20 dB.

Figure 6-10b shows the P – S reflection coefficients for the optimal, Reynolds', and Higdon's absorbing boundary conditions. R_{ps} is generally small for all three bound-

ary conditions, although again the optimal is better than the Higdon and Reynolds formulae.

In Figure 6-11, we plot the S – P and S – S reflection coefficients, respectively, for the three absorbing boundary conditions. For our choice of parameters, Reynolds' boundary condition behaves poorly for $\mid R_{sp} \mid > 1$ at an angle of incidence $\phi \sim \sin^{-1} \beta/\alpha$. Our analysis confirms Mahrer's (1986) finding that the smaller the time step Δt and β/α are, the more unstable the Reynolds absorbing boundary condition. Therefore, for a general-purpose finite difference modeling code, Reynolds' absorbing boundary condition is not a good choice for absorbing artificial reflections. (The instability of Clayton and Engquist's (1977) absorbing boundary condition was also reported by Mahrer (1986) and Emerman and Stephen (1983)).

There is a physical zero in R_{ss} corresponding to the case where no S-wave reflection exists. The optimal absorbing boundary condition has two additional zeros in R_{ss} at angles of incidence corresponding to $z_b = z_c^{\pm}$. At small incidence angles, Higdon's boundary condition has smaller R_{sp} and R_{ss} reflection coefficients because it is designed to absorb a normal incident S-wave. At large angles of incidence, the optimal absorbing boundary condition is better. This does not mean, however, that the Higdon (1991) absorbing boundary condition is better at absorbing normal-incident S-waves, because the optimal absorbing boundary condition in this particular example is designed for a maximum absorption of the incident P-wave. By properly locating the zeros on the unit circle, we can have better S-wave absorption with some sacrifice of the P-wave absorption. As a matter of fact, using the fast algorithm given in the previous section, we can compute the coefficients $\{a_{ij}\}$ for any given locations of the zeros on the unit circle.

6.2.10 Numerical Examples

The example we choose for actual computation is a 3-D elastic finite difference modeling of wave propagation in a homogeneous cube. The objective is to compare the optimal, Higdon's, and Reynolds' absorbing boundary conditions with a realistic simulation. We use the stress-velocity formulation of Virieux (1986) and Levander (1988) on a staggered grid. The scheme has fourth-order accuracy in space and second-order accuracy in time. Dispersion analysis suggests that the shortest wavelengths in the model be sampled at five grid points per wavelength. The code is optimized to minimize internode communications and I/O on a parallel computer. For 3-D elastic modeling with $100 \times 100 \times 100$ grids and 2000 time steps, it takes about 42 minutes on a 64-node nCUBE-2 at the Earth Resources Laboratory of the Massachusetts Institute of Technology.

In this example, we simulate the elastic wave propagation in a medium with compressional velocity $\alpha = 3000\ m/s$, shear velocity $\beta = 2000\ m/s$, and density $\rho = 2000\ kg/m^3$. We use an explosive source. The source function is a delayed Ricker wavelet [$s(t) = (2\pi^2 f_0^2 (t - t_0)^2 - 1) e^{-\pi^2 f_0^2 (t-t_0)^2}$] with central frequency $f_0 = 20\ Hz$ and a time delay $t_0 = f_0^{-1}$. The cube is 960 m in each dimension. The time step chosen is $\Delta t = 0.0005\ s$ and the grid size is $\Delta x = 10\ m$. The source is at coordinate $(z_s, y_s, x_s) = (240\ m, 240\ m, 240\ m)$. All six surfaces are absorbing boundaries with either the optimal, Reynolds', or Higdon's boundary condition.

Figure 6-12 presents three snapshots taken at a propagation time 0.30 second. The one on the top-left (a) is a simulation using Reynolds' absorbing boundary condition; the top-right one (b) is that using Higdon's absorbing boundary condition; and the one on the bottom-left (c) is that using the optimal absorbing boundary condition in Table 6.2. Shown in these snapshots are the vertical components of particle velocity in the x-z plane at y= 240 m. They are blown up by a factor of ten (10) to make reflections from the artificial boundaries visible. Only the first arrival is physical; all others are artificial reflections from boundaries. In the simulation with the

Reynolds' absorbing boundary condition, artificial reflection is about one-tenth the incident wave and is clearly visible in the amplified snapshots (Figure 6-12, top-left). The artificial reflection is much smaller in the simulation with Higdon's absorbing boundary condition, which is about one-thirtieth of the incident wave (Figure 6-12, top-right) . The simulation with the optimal absorbing boundary condition (Figure 6-12, bottom-left) has a smaller artificial reflection than both the Higdon and Reynolds absorbing boundary conditions.

6.2.11 Generalization to (m, m) Schemes

We have thus far focused our attention on the (2,2) scheme, i.e., the extrapolation on the artificial boundary has two steps "deep" in both time and space grids. Generalization to a scheme that has m steps "deep" in both time and space grids can be derived. The results are:

$$R_{pp} = \frac{\xi - \eta}{\xi + \eta} \frac{\sum_{j=0}^{m} \Omega_j z_a^j}{\sum_{j=0}^{m} \Omega_j z_a^{-j}}, \tag{6.27}$$

$$R_{ps} = -\frac{2\xi\eta}{\xi + \eta} \frac{\sum_{j=0}^{m} \Omega_j z_a^j}{\sum_{j=0}^{m} \Omega_j z_b^{-j}}, \tag{6.28}$$

$$R_{sp} = \frac{2}{\xi + \eta} \frac{\sum_{j=0}^{m} \Omega_j z_b^j}{\sum_{j=0}^{m} \Omega_j z_a^{-j}}, \tag{6.29}$$

$$R_{ss} = \frac{\xi - \eta}{\xi + \eta} \frac{\sum_{j=0}^{m} \Omega_j z_b^j}{\sum_{j=0}^{m} \Omega_j z_b^{-j}}, \tag{6.30}$$

where

$$\Omega_j = \sum_{i=0}^{m} a_{ij} z^{1-i} - \delta_{j0} z. \tag{6.31}$$

Here, $\delta_{j0} = \begin{cases} 1 & j = 0 \\ 0 & \text{otherwise} \end{cases}$ is the Kronecker's delta. The properties of the (m, m) scheme are similar to those of the (2,2) scheme discussed previously. For example, for an (m, m) scheme to be optimal, the m zeros of the reflection coefficients must be on the segment of the unit circle with phase angles between $(0, k_\alpha \Delta x]$, and the poles are at the conjugated positions of the zeros.

6.3 A Hybrid Method for Borehole Coupling in a Heterogeneous Formation

Directly employing a borehole as a part of the finite difference formulation proves impractical due to the scale difference between the borehole diameter and the seismic wavelength. At low frequencies, however, the problem can be separated into two parts: propagation by the 3-D elastic finite difference technique, and coupling into fluid by an appropriate borehole coupling theory. This section outlines the method of computing pressure in a fluid-filled borehole, in which the 3-D elastic finite difference technique and the borehole coupling theory are hybridly combined. This approach enables one to simulate a hydrophone measurement in a heterogeneous formation.

6.3.1 Basic Equations

As is shown in the previous chapters (equations (3.12) and (5.3)), the pressure in a fluid-filled borehole satisfies, at a low frequency approximation, the following borehole coupling equation:

$$\left[\frac{\partial^2}{\partial t^2} - C_T^2 \frac{\partial^2}{\partial z^2}\right] P(z,t) = 2\ \rho_f C_T^2 \frac{\partial^2}{\partial t^2}\epsilon_r(z,t), \tag{6.32}$$

where ϵ_r is the borehole squeeze strain. It is related to the stress fields computed by the 3-D elastic finite difference method at the absence of the fluid-filled borehole, according to the following equation

$$\epsilon_r(z,t) = \frac{\sigma_{xx}(z,t) + \sigma_{yy}(z,t)}{E_{\|}} - \frac{\nu\sigma_{zz}(z,t)}{E_{\perp}}, \tag{6.33}$$

where $E_{\|} = E_{\perp} = E$ in an open borehole. In a cased borehole, as shown in section 3.2.3, $E_{\|}$ is larger than $E_{\perp}$.

We define

$$Q(z,t) = 2\ \rho_f C_T^2(z)\ \epsilon_r(z,t) \tag{6.34}$$

as the *borehole squeeze pressure*. The borehole squeeze pressure possesses the right dimension of pressure. It serves as a secondary source for the pressure in the fluid. Taking into account the stress free boundary condition at the well head and the rigid boundary condition at the well bottom, we obtain a set of equations for the pressure in the borehole fluid as

$$\left[\frac{\partial^2}{\partial t^2} - C_T^2(z)\,\frac{\partial^2}{\partial z^2}\right] P(z,t) = \frac{\partial^2}{\partial t^2} Q(z,t), \tag{6.35a}$$

$$P(z, t=0) = 0, \tag{6.35b}$$

$$\frac{\partial}{\partial t} P(z, t=0) = 0, \tag{6.35c}$$

$$P(z = z_0, t) = 0, \tag{6.35d}$$

$$\frac{\partial}{\partial z} P(z = z_H, t) = 0. \tag{6.35e}$$

The initial conditions are set to zero to ensure causality. In the above equations, z_0 is the depth of the water table, z_H is the depth of the well bottom.

6.3.2 Integral Equation Method

Solving equations (6.35a)–(6.35e) by low order finite differences with respect to the z derivative (e.g., 2nd order or 4th order differentiation) is found to be less accurate due to the fact that Δz between two consecutive receivers in the finite difference calculation is usually large. Therefore, it is preferable to use a long differentiation operator with the operator length typically on the order of 32 or 64. The impulse response of the differentiation operator can be accurately designed by the Remez exchange algorithm using the Chebyshev approximation, a method developed by McClellan, Parks and Rabiner (1973).

Let's denote $h(z)$ the impulse response of the second order differentiation operator $\partial^2/\partial z^2$, i.e.,

$$\frac{\partial^2 P(z,t)}{\partial z^2} = \int_{-\infty}^{\infty} h(z - z_0)\, P(z_0, t)\, dz_0.$$

To obtain an integral expression for the pressure in the fluid, we rewrite equation (6.35a) and integrate it twice with respect to time. This procedure yields

$$P(z,t) = C_T^2(z) \int_{-\infty}^{\infty} h(z-z_0) \left[\int_0^t ds \int_0^s P(z_0,\tau)d\tau\right] dz_0 + Q(z,t), \qquad (6.36)$$

where the boundary conditions have been incorporated into the differentiator. Also we have taken it for granted that, at $t = 0$, the borehole squeeze pressure and its time derivative are zero.

The integral equation (6.36) can be explicitly solved using the following approximations

$$\tilde{P}(z_0, t+\Delta t) \equiv \int_0^{t+\Delta t} ds \int_0^s P(z_0,\tau)d\tau \approx \tilde{P}(z_0,t) + \Delta t\ \hat{P}(z_0,t) + O(\Delta t)^2,$$

and

$$\hat{P}(z_0,t) \equiv \int_0^t P(z_0,\tau)d\tau \approx \hat{P}(z_0,t-\Delta t) + \Delta t\ P(z_0,t) + O(\Delta t)^2,$$

with truncation errors the same as the 2nd order time difference commonly employed in finite difference techniques, where Δt is the time step size. This approach enables us to compute $P(z,t)$ by an explicit forward marching procedure. It is found that, numerically, this method is stable as long as[1]

$$C_T \frac{\Delta t}{\Delta z} \leq \frac{1}{\sqrt{2}}.$$

In the computer program written by McClellan, Park and Rabiner (1979), only the impulse response $h_a(z)$ of first order differential operators $\partial/\partial z$ is available. To compute the impulse response $h(z)$ of the second order differential operators $\partial^2/\partial z^2$, we cascade two first order derivative operators by a simple convolution. Table 6.3 lists the coefficients of the second order differentiation operators. Its frequency spectrum (spatial or temporal) is very close to ω^2 with a relative error of less than 1%.

[1]If this condition is violated, before applying the technique, an appropriate time upsampling in the borehole squeeze pressure is the best way to circumvent the instability.

6.3.3 Numerical Examples

In the following numerical examples, we compare the pressures in an open fluid-filled borehole calculated by the hybrid technique proposed in this chapter (finite difference method in conjunction with borehole coupling theory) with those calculated by the global matrix method with borehole coupling theory in Chapter 5. The latter technique has already been validated by an analytical solution. The formation is stratified and its properties are given in Table 5.1. Different from the second example in section 5.2.4 (Figure 5-5), in this example the source-borehole offset is 200 m rather than 400 m, the central frequency of the source wavelet is 50 Hz rather than 100 Hz, and the borehole spans a depth of 600 m rather than 800 m. The size of the problem is limited by the in-core memory for an 3-D finite difference calculation.

Figure 6-13 shows two calculations: the solid line is the pressure in the borehole computed by the 3-D finite difference method plus the borehole coupling theory, and the dashed line is the same data computed by the global matrix method plus the borehole coupling theory. The agreement between these two techniques is excellent, although the phases of tube waves is slightly off at a later time. Since the source (at depth 400 m) is inside the low velocity layer, a significant amount of energy is trapped in this layer, as is evident in both calculations. Direct P-wave and S-wave, as well as reflections from the free surface and interfaces, are discernible. The low velocity tube waves generated at the free surface, the internal interfaces, and the well bottom are also visible.

6.3.4 The Kent Cliffs VSP Experiment: Revisited

In Chapter 5, we computed the synthetic hydrophone seismograms for the Kent Cliff borehole experiment, assuming that the formation is stratified. Using the simplified model, we were able to predict the hydrophone data for the small offset shot point S/P #1 extremely well. However, there are systematic, although small, discrepancies

in both traveltime and rms amplitude for the other two shot points at large offsets. The geophysical and geological data collected in this borehole reveal that the formations actually dip 60° toward southeast (Zoback, 1986; Lee, 1990). We believe that the focusing and defocusing effects of the dipping layers might explain the discrepancies. In the following examples, we recompute the synthetic hydrophone pressures at the Kent Cliffs borehole using the hybrid method developed in this chapter with a geological model shown in Figure 6-14. In this model, the layers are dipping toward southeast with a strike of N55°E and a dip angle of 60°. Also illustrated in this figure are the averaged sonic velocity profiles derived from logging data and the layout of the experiment (Zoback, 1986; Lee, 1990).

In the calculations, the source is simulated by a vertical force. Its time history is a Kelly wavelet with the central frequency of 75 Hz. The receivers span a depth range from the surface to 990.6 m. The 3-D volume is discretized into 100×100 ×200 grid points. The grid size is 6 m. The time step size is 0.1 ms. Figure 6-15 shows the synthetic hydrophone data for the shot point S/P #3 at offset 288 m in the N85°E direction. The first trace is right at the depth of water table, thus is zero. Otherwise, the synthetic seismograms are very similar to Figure 5-13 (the calculation with a stratified earth model). In Figure 6-15, the direct P-wave, S-wave, and the tube waves from the free surface are clearly visible. The S-waves are less accurately modeled because of the cumulative error due to grid dispersion for wave propagation over a large distance.

Figure 6-16 and Figure 6-17 show the rms (root mean square) amplitudes of the first arrival (P-wave) for the shot point S/P #3 and the other two shot points, respectively. The solid lines are the data from the synthetic hydrophone pressures, the plus (+) symbols are the data derived from the field hydrophone measurements. The agreement between the synthetic P-wave amplitude and the observed one is excellent, except at locations where the tube waves from fractures interfere with the P-wave, and at the shallow depth where media are most inhomogeneous and weathered (This factor is not taken into account in the simulation). Detailed comparisons show that

the traveltime and rms amplitude of the P-wave in Figure 6-15 (as well as the other computation for S/P #2) agree with field hydrophone data better than the previous calculations (Figure 5-16 and Figure 5-17) using a stratified earth model. This demonstrates that a better geological model does indeed improve our theoretical predictions of the field data, although a complete knowledge about the subsurface structures is, of course, not feasible.

6.4 Discussions and Conclusions

In this chapter, we formulated a 3-D elastic finite difference algorithm to model wave propagation in a heterogeneous medium. The optimal absorbing boundary condition was incorporated into the finite difference code, which significantly reduces reflections from an artificial boundary without increasing the amount of additional computation and storage on the boundary. We developed a hybrid method for computing the pressure in a fluid-filled borehole by cascading the 3-D elastic finite difference algorithm with the borehole coupling equations.

We compared the 3-D finite difference method with the classic discrete wavenumber – global matrix method for elastic wave propagation in a stratified medium, and found an excellent agreement between the two methods. The 3-D finite difference method was successfully applied to a variety of problems of acoustic/elastic wave propagation in 3-D media, such as elastic wave scattering in a three dimensional random medium, seismo/acoustic propagation through sea mountains, ocean trench, and the continental shelf, and elastic wave scattering through a salt dome, as well as acoustic logging in a dipping formation. These applications were not included in this thesis since they were beyond our scope.

We demonstrated that it was possible to design optimal absorbing boundary conditions to model acoustic and elastic wave propagation in 2-D and 3-D media using

the finite difference method. At a given time step, the field on an artificial boundary was expressed as a linear combination of the field at previous time steps and interior grid points. The reflection coefficients were found to be identical to the transfer functions of two cascaded systems—the inverse of a causal and delayed feed-backward system, and an anticausal and advanced feed-forward system. The reflection from an artificial boundary was determined by the locations of the zeros and the poles of the reflection coefficients in a complex z plane. It was found that for an absorbing boundary condition to be optimal, the zeros of the reflection coefficients must be on the segment of the unit circle with phase angles between $(0, k_\alpha \Delta x)$. A fast algorithm was given to compute the unknown coefficients in the boundary extrapolation scheme. The optimal absorbing boundary condition we designed yields reflection coefficients that are about 10 dB smaller than the Higdon's absorbing boundary condition, and about 20 dB smaller than the Reynolds' absorbing boundary condition. The simulations of 3-D elastic wave propagation using finite differences showed that the optimal absorbing boundary condition had a smaller artificial reflection than the Reynolds and Higdon absorbing boundary conditions.

We also showed that the hybrid method for computing the pressure in a fluid-filled borehole agreed with the method given in the previous chapter. With a 3-D model including dipping formations, this method was applied to simulate the Kent Cliffs hydrophone VSP data. The synthetic P-wave amplitude matches the field data better than the simulation with a stratified model.

The hybrid method is very general, and in principal it can be applied to a variety of heterogeneous models. Two aspects limit this method somewhat: the borehole coupling theory is valid at low frequencies (the borehole diameter is less than one tenth of the shortest wavelength); and, although the finite difference method is very robust, the amount of computation goes as a cubic power of the size of the model such that it becomes unfeasible even to currently available massively parallelized supercomputer for applications where large offsets between the source and receivers are involved.

The contributions of this chapter are threefold. (1) The 3-D finite difference technique developed in this chapter offers a useful tool for modeling elastic wave propagation in a heterogeneous three dimensional medium. Its accuracy is tested against both analytic solutions and the classic discrete wavenumber – propagator matrix method. (2) The discovery of a class of optimal absorbing boundary conditions and the methodology in finding them make our work unique in the numerous publications on finite difference methods. We pose the problem as locating the zeros and poles of the reflection coefficients in a complex plane so as to minimize the reflection coefficients. We prove that the optimal locations of the zeros and poles are on the unit circle, with the zeros in the first quadrant and the poles in the fourth quadrant. The optimal absorbing boundary condition is incorporated into our 3-D finite difference program. Numerical tests show that it greatly reduces reflections from an artificial boundary. (3) A hybrid method is proposed to compute pressure in a fluid-filled borehole due to a source in a heterogeneous formation. Direct inclusion of the borehole into the finite difference modeling is unfeasible to currently available parallel computers. We circumvent this difficulty by dividing the whole problem into two parts: propagation from the source to the borehole location by the finite difference method and coupling into the fluid by applying the borehole coupling equations (in either an open or a cased borehole). This approach proves to be accurate. Using this hybrid method, we are able to predict the dynamical behaviors of the Kent Cliffs hydrophone data better.

2nd Order Digital Differentiator
Filter Length = 63
Filter Coefficients:

h(1)	=	0.15661932E-04	=	h(63)	h(17)	=	0.25463600E-01	=	h(47)
h(2)	=	-0.42795040E-04	=	h(62)	h(18)	=	-0.23341786E-01	=	h(46)
h(3)	=	0.50450635E-04	=	h(61)	h(19)	=	0.16933490E-01	=	h(45)
h(4)	=	-0.48960021E-04	=	h(60)	h(20)	=	-0.16943144E-01	=	h(44)
h(5)	=	0.56255794E-04	=	h(59)	h(21)	=	0.18808344E-01	=	h(43)
h(6)	=	-0.68359135E-04	=	h(58)	h(22)	=	-0.21924412E-01	=	h(42)
h(7)	=	0.85265965E-04	=	h(57)	h(23)	=	0.26451327E-01	=	h(41)
h(8)	=	-0.10842194E-03	=	h(56)	h(24)	=	-0.32947831E-01	=	h(40)
h(9)	=	0.14052757E-03	=	h(55)	h(25)	=	0.42538606E-01	=	h(39)
h(10)	=	-0.18639435E-03	=	h(54)	h(26)	=	-0.57401560E-01	=	h(38)
h(11)	=	0.25483879E-03	=	h(53)	h(27)	=	0.82116038E-01	=	h(37)
h(12)	=	-0.36360382E-03	=	h(52)	h(28)	=	-0.12767360E+00	=	h(36)
h(13)	=	0.55397506E-03	=	h(51)	h(29)	=	0.22615658E+00	=	h(35)
h(14)	=	-0.94651891E-03	=	h(50)	h(30)	=	-0.50759161E+00	=	h(34)
h(15)	=	0.20804049E-02	=	h(49)	h(31)	=	0.20274291E+01	=	h(33)
h(16)	=	-0.12364591E-01	=	h(48)	h(32)	=	-0.33343613E+01	=	h(32)

Table 6.3: The FIR (Finite Impulse Response) coefficients of the second order digital differentiator designed with the McClellan, Parks and Rabiner method. This filter has a linear phase.

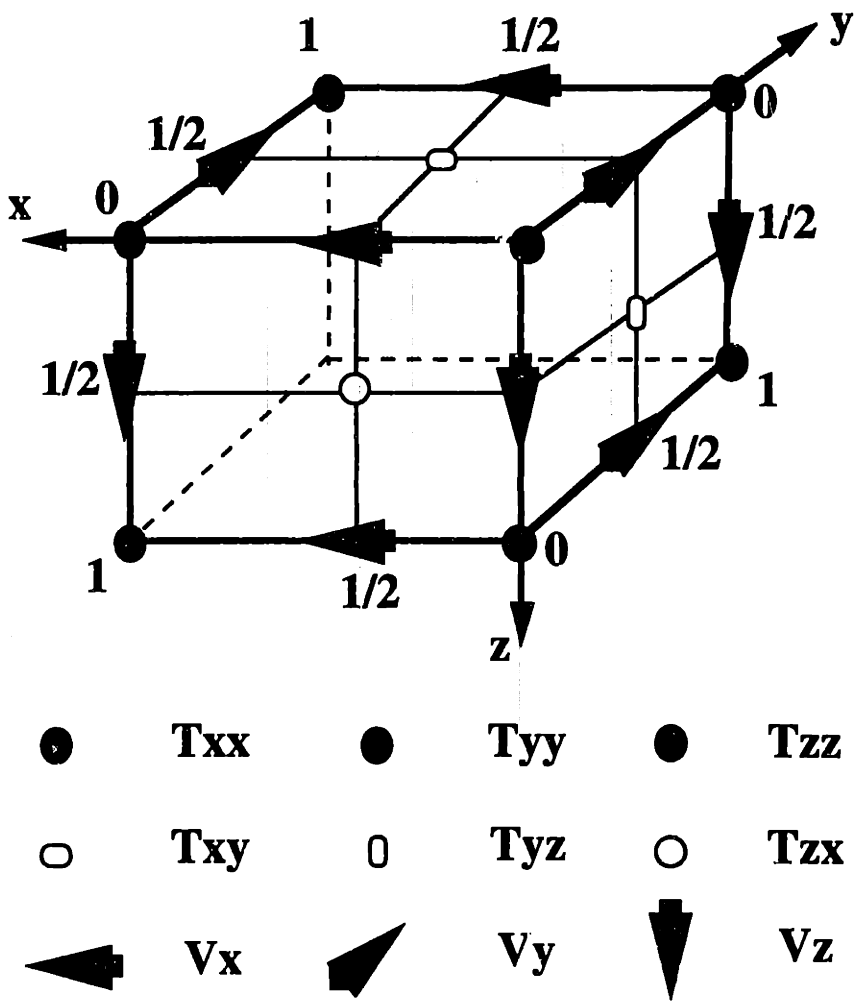

Figure 6-1: A three dimensional staggered grid for elastic wave modeling by the finite difference method. The layout of this grid is as follows: the three particle velocity components (V_x, V_y, V_z) are half-grid shifted along their corresponding directions; the normal stresses $(\tau_{xx}, \tau_{yy}, \tau_{zz})$ are defined at the vertices; the shear stresses $(\tau_{xy}, \tau_{yz}, \tau_{xz})$ are half-grid shifted along both directions in their action planes. The elastic parameters are defined at locations where they are used.

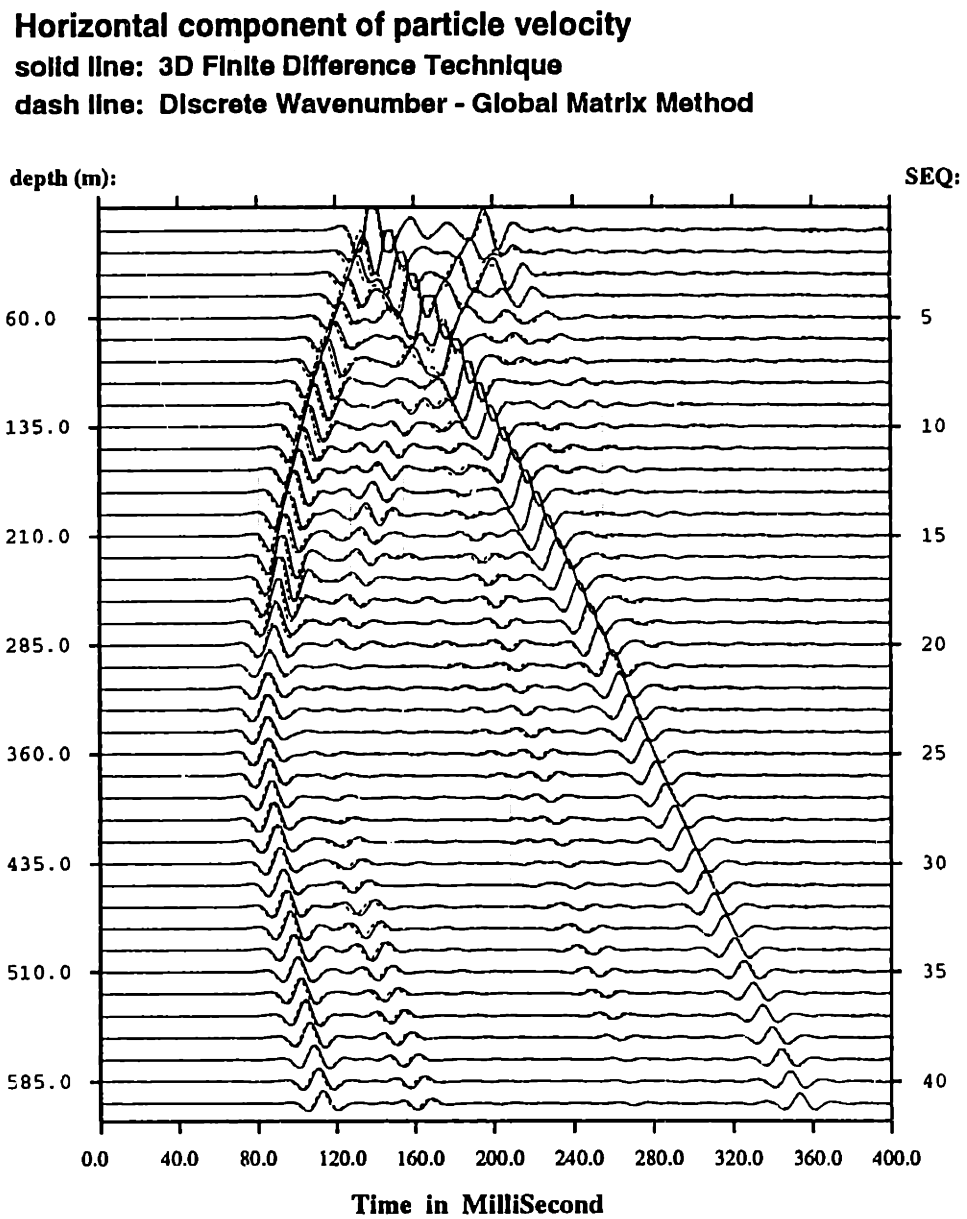

Figure 6-2: Horizontal component of the particle velocity computed by the discrete wavenumber–global matrix method (dashed line) and by the 3-D finite difference method (solid line). In this calculation, the source is at depth 300 m below the stress free surface, and is at 300 m offset from the vertical array of receivers, mimicking a crosswell geometry. The receivers span a depth range from the surface to 600 m. The formation velocity profiles are given in Table 6.1. The source is an explosion. Its time history is a Kelly wavelet with the central frequency 50 Hz. In the finite difference computation, the cubic volume is discretized into $100 \times 100 \times 200$ grid points. The grid size is 4 m. The time step size is 0.2 ms.

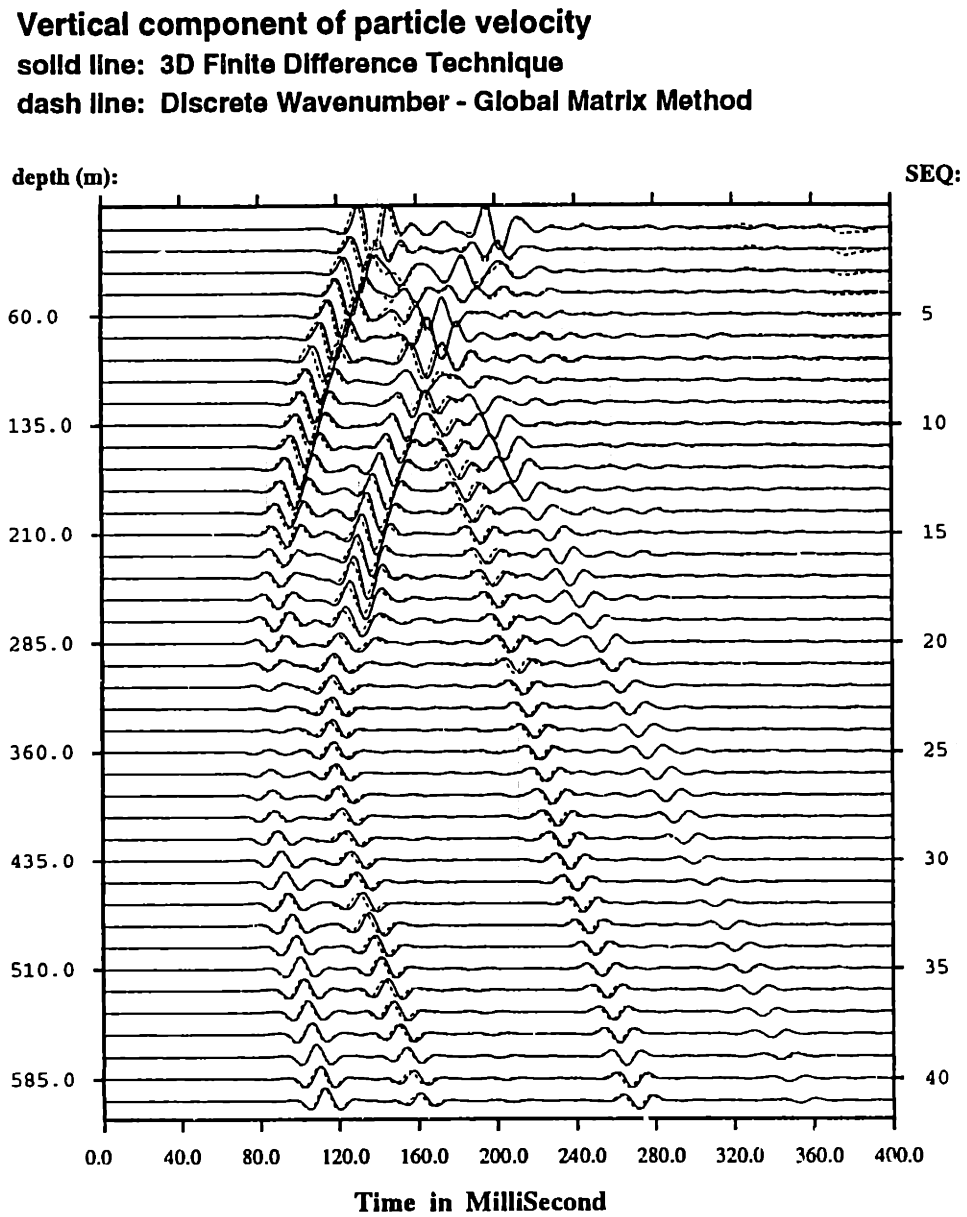

Figure 6-3: Vertical component of the particle velocity computed by the discrete wavenumber–global matrix method (dashed line) and by the 3-D finite difference method (solid line). In this calculation, the source is at depth 300 m below the stress free surface, and is at 300 m offset from the vertical array of receivers, mimicking a crosswell geometry. The receivers span a depth range from the surface to 600 m. The formation velocity profiles are given in Table 6.1. The source is an explosion. Its time history is a Kelly wavelet with the central frequency 50 Hz. In the finite difference computation, the cubic volume is discretized into 100×100 ×200 grid points. The grid size is 4 m. The time step size is 0.2 ms.

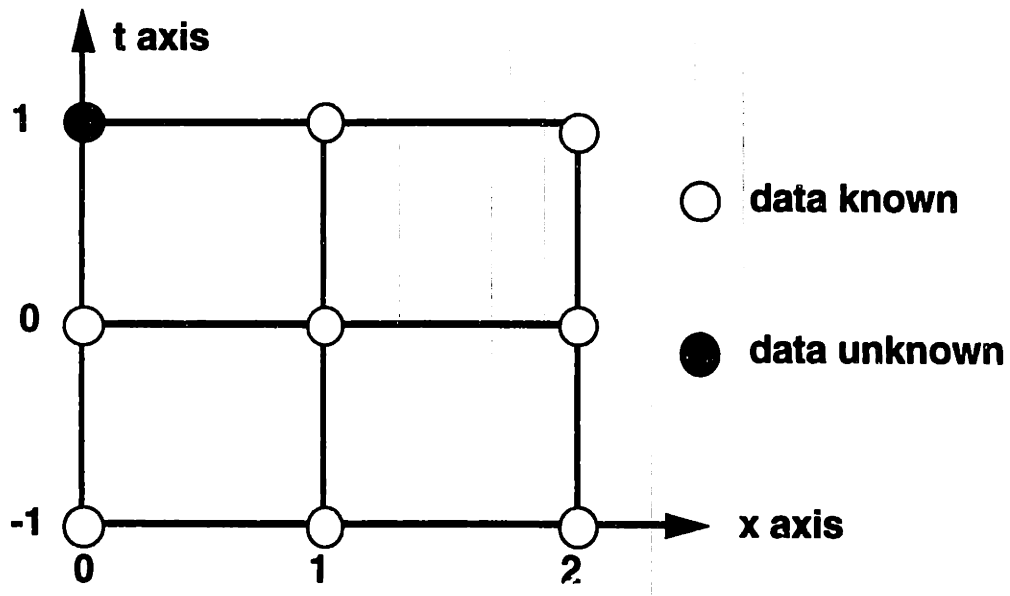

Figure 6-4: A stencil for updating a boundary grid at $x = 0$ for the finite difference method. The unknown data (solid circle) is computed by the eight(8) known values (open circle) according to equation (6.3).

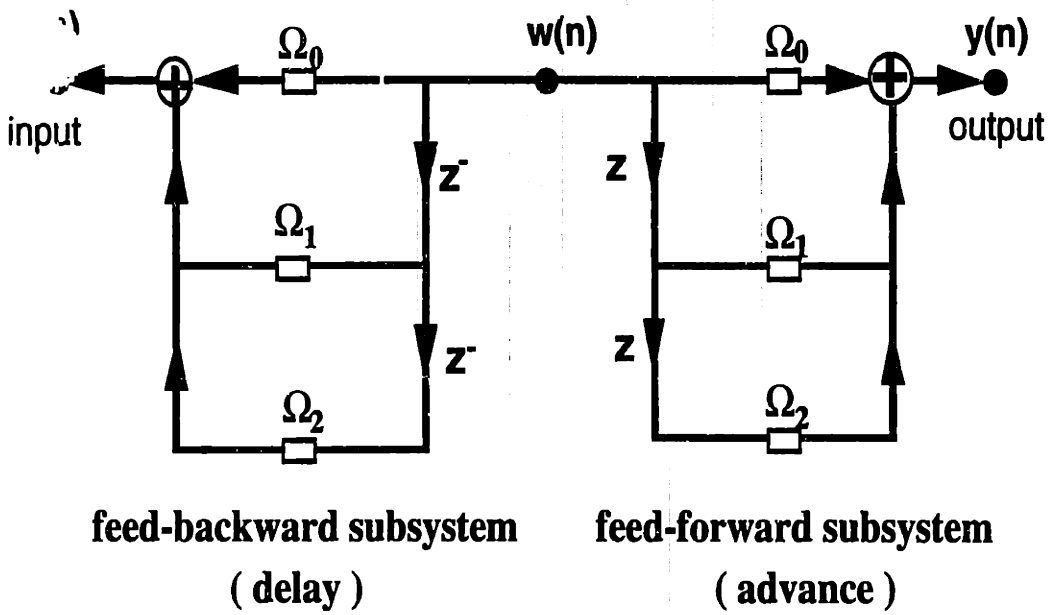

Figure 6-5: The reflection coefficient, e.g. R_{pp}, is identical with the transfer function of two cascaded systems. The first is the inverse of a causal feed-backward system with delay. The second is an anticausal feed-forward system with advance.

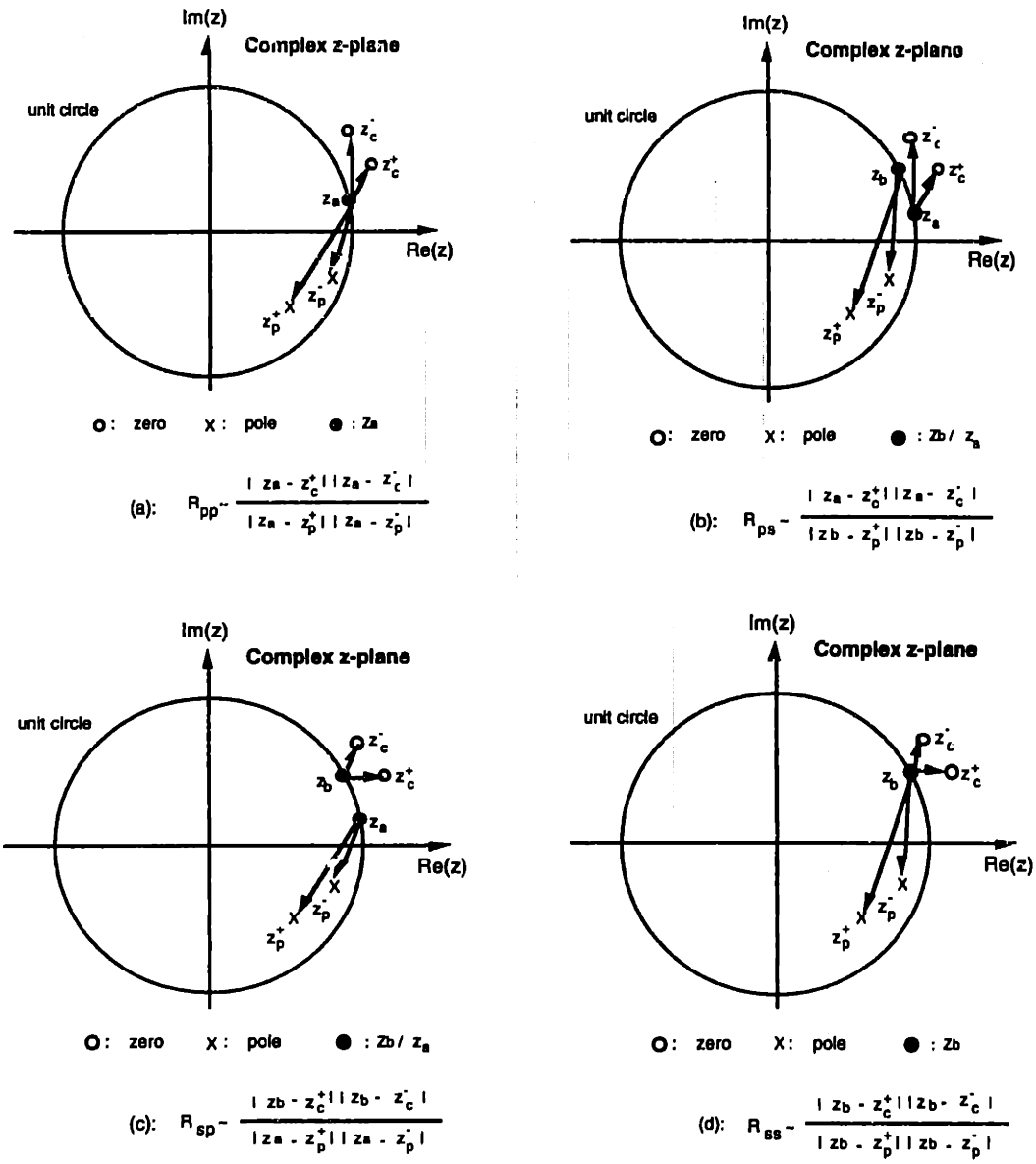

Figure 6-6: Geometrical representations in a complex z plane of the elastic reflection coefficients from an artificial boundary: (a) R_{pp}; (b) R_{ps}; (c) R_{sp}; and (d) R_{ss}. In these figures, the open circles are the zeros; the crosses are the poles; the solid circles are the unit shift operators.

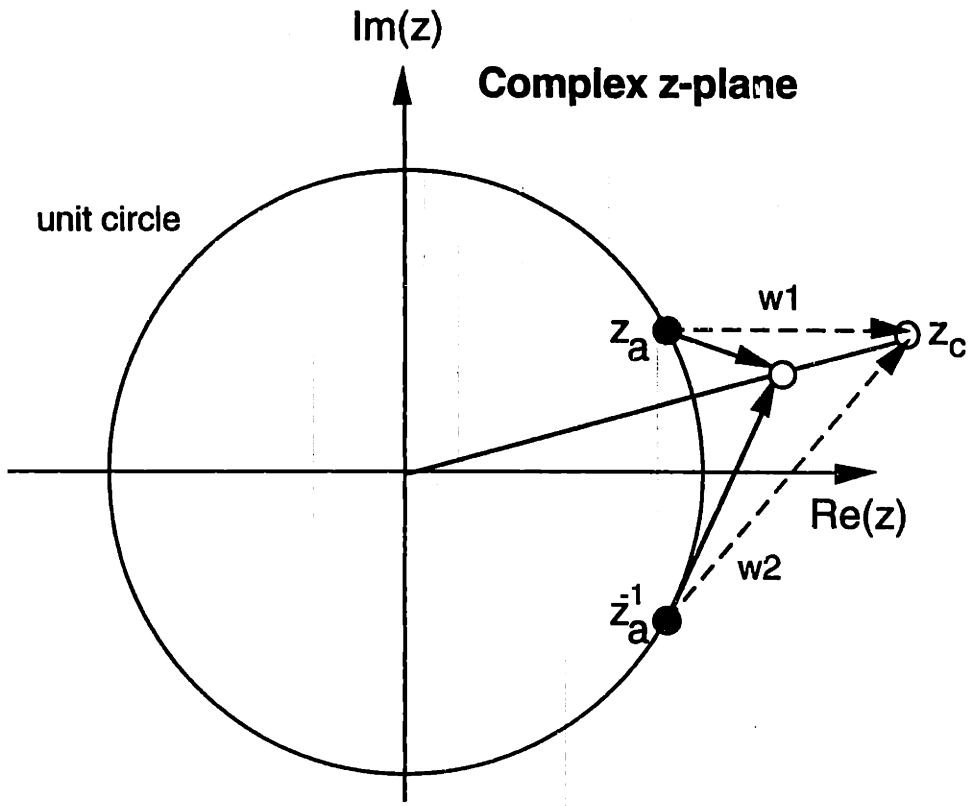

w1/w2 is minimum if the zero is on the unit circle, as the phase angle being fixed.

Figure 6-7: A graphic proof of the statement that the zeros of an optimal absorbing boundary condition are on the unit circle. It is obvious that $w_1 = \mid z_a - z_c \mid$ increases faster than $w_2 = \mid z_a^{-1} - z_c \mid$ as $z_c \rightarrow \infty$ in the first quadrant.

(a) Optimal Absorbing Boundary Condition

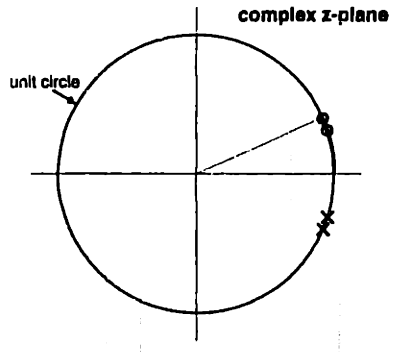

zeros: (0.9495712,0.3135886) (0.9168157,0.3992748)
poles: (0.9168419,-0.3992862) (0.9496491,-0.3135813)

(b) Reynolds Absorbing Boundary Condition

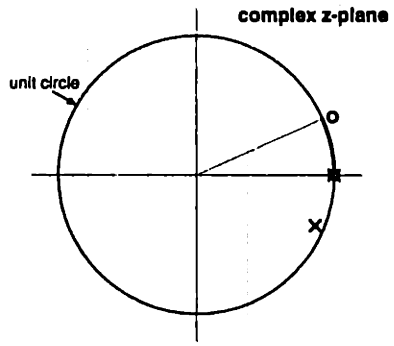

zeros: (0.9868580,0.4183922) (0.9980288,6.2758043E-02)
poles: (0.9980288,-6.2758066E-02) (0.8589286,-0.3641548)

(c) Higdon's Absorbing Boundary Condition

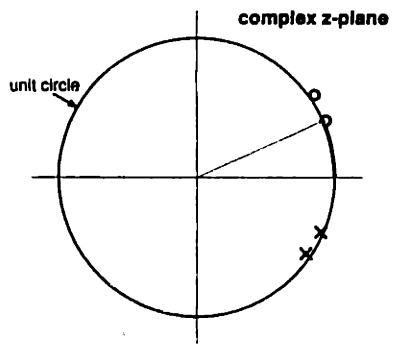

zeros: (0.9341828,0.4081899) (0.8548074,0.5026366)
poles: (0.7900883,-0.5477669) (0.8988435,-0.3927484)

Figure 6-8: Zeros and poles in a complex z plane of the optimal (a), Reynolds' (b) and Higdon's (c) absorbing boundary conditions. In these figures, the open circles are the zeros; the crosses are the poles.

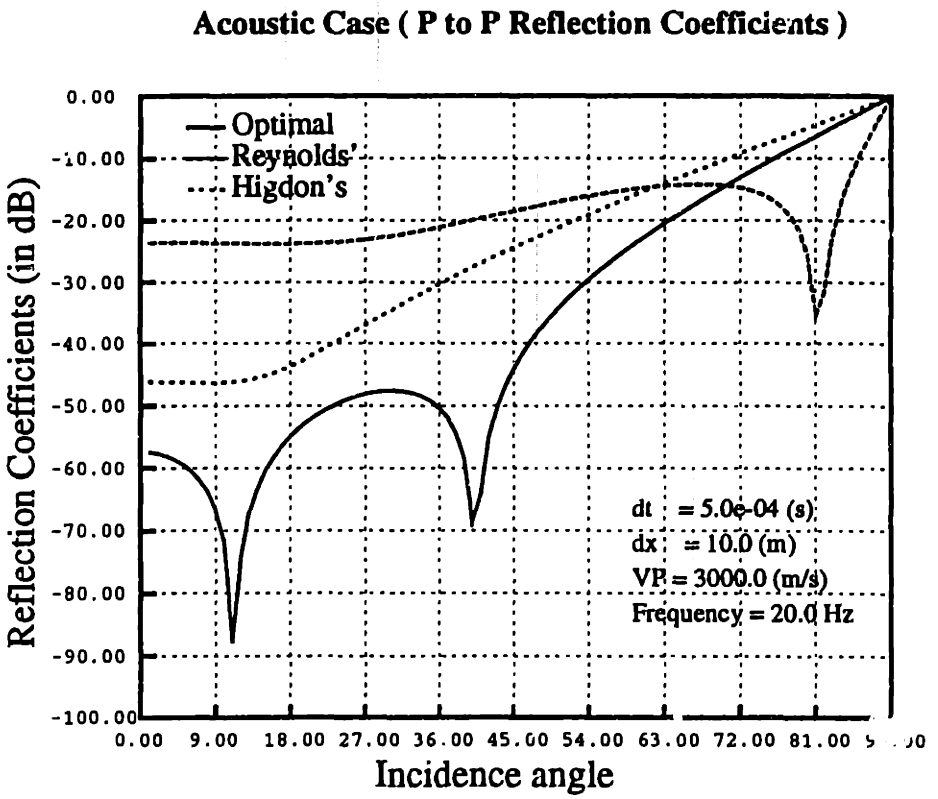

Figure 6-9: Acoustic reflection coefficients as a function of angle of incidence for the optimal (solid line), Reynolds' (long dash) and Higdon's (short dash) absorbing boundary conditions. The angle of incidence is defined such that zero corresponds to normal incidence and 90° to grazing incidence. The vertical axis is the magnitudes of the reflection coefficients in dB. The parameters are listed at the low right corner of this figure.

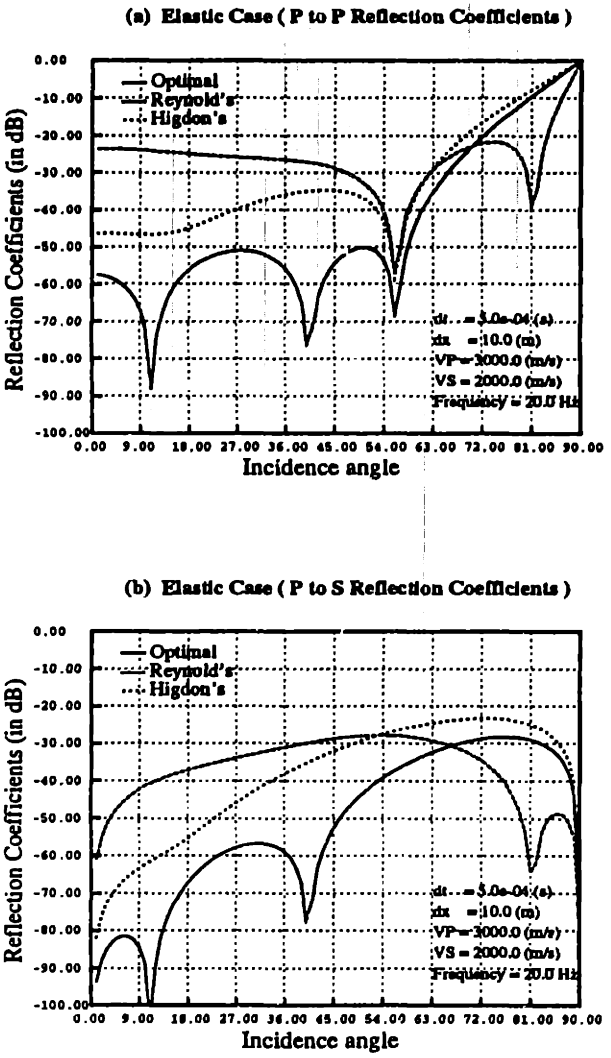

Figure 6-10: Elastic reflection coefficients R_{pp} (a) and R_{ps} (b) as a function of angle of incidence for the optimal (solid line), Reynolds' (long dash) and Higdon's (short dash) absorbing boundary conditions. The angle of incidence is defined such that zero corresponds to normal incidence and 90° to grazing incidence. The vertical axis is the magnitudes of the reflection coefficients in dB. The parameters are: (grid size) $\Delta x = 10$ m, (time step size) $\Delta t = 5 \times 10^{-4}$ s, (compressional velocity) $\alpha = 3000$ m/s, and (shear velocity) $\beta = 2000$ m/s. The source frequency is 20 Hz.

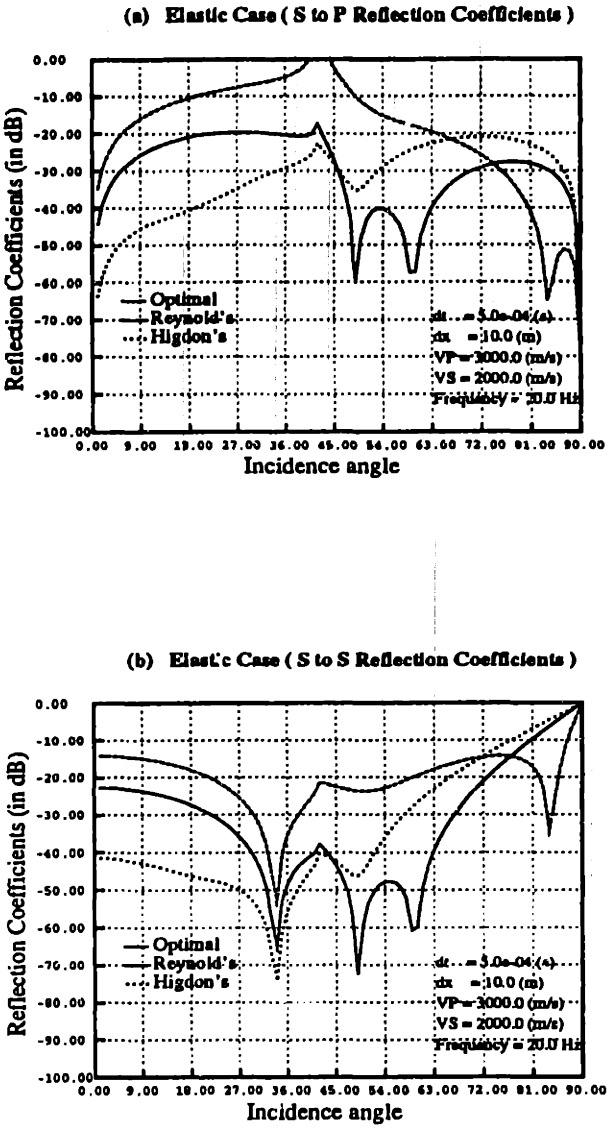

Figure 6-11: Elastic reflection coefficients R_{sp} (a) and R_{ss} (b) as a function of angle of incidence for the optimal (solid line), Reynolds' (long dash) and Higdon's (short dash) absorbing boundary conditions. The angle of incidence is defined such that zero corresponds to normal incidence and 90° to grazing incidence. The vertical axis is the magnitudes of the reflection coefficients in dB. The parameters are: (grid size) $\Delta x = 10$ m, (time step size) $\Delta t = 5 \times 10^{-4}$ s, (compressional velocity) $\alpha = 3000$ m/s, and (shear velocity) $\beta = 2000$ m/s. The source frequency is 20 Hz.

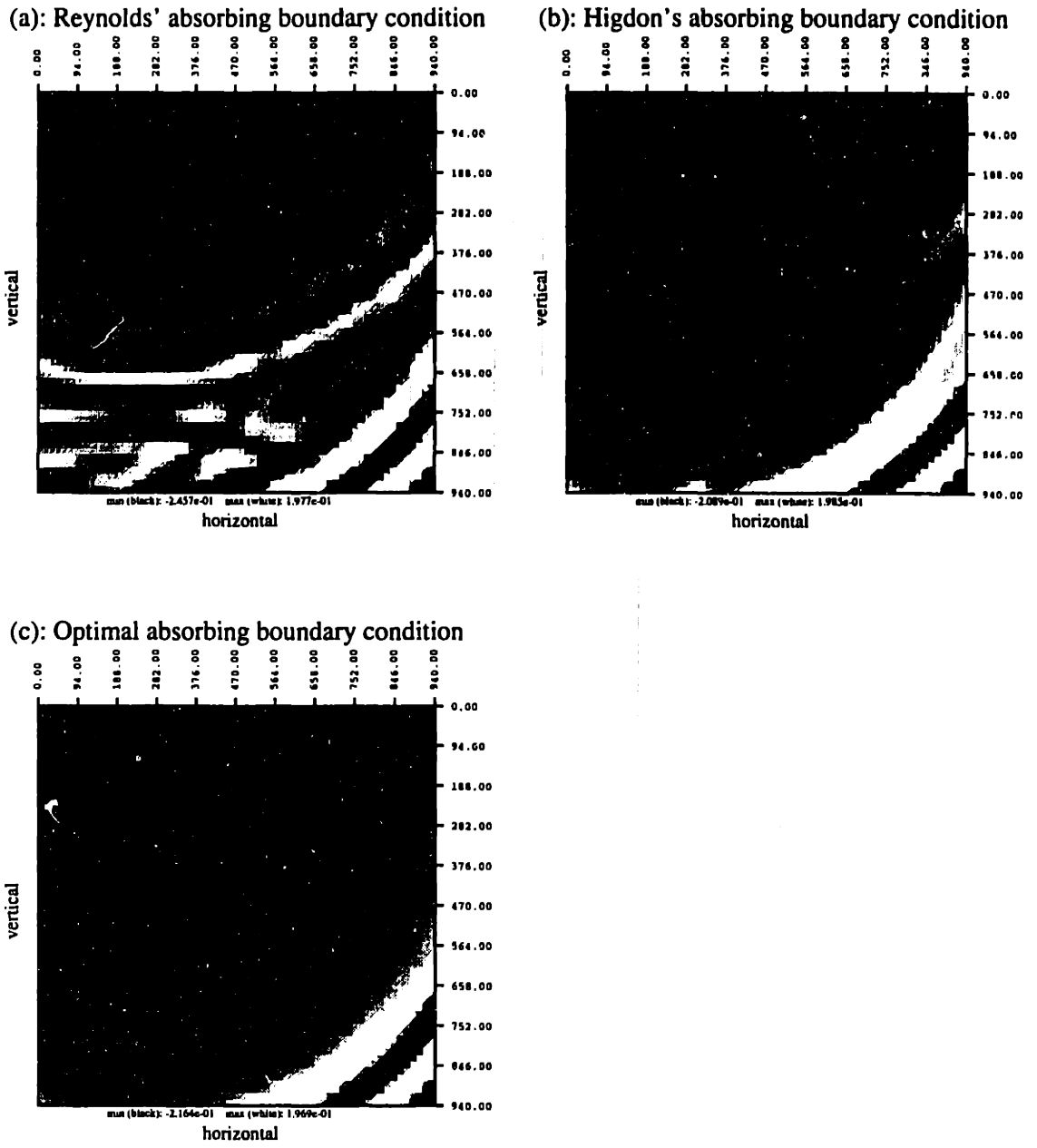

Figure 6-12: Snapshots of an 3-D elastic finite difference simulation on an nCUBE parallel computer with Reynolds' (top-left), Higdon's (top-right), and the optimal (bottom-left) absorbing boundary conditions. Shown in the snapshots are the vertical components of particle velocity. The snapshots are taken at a propagational time 0.30 s, and are blown up by a factor of ten ($\times$ 10).

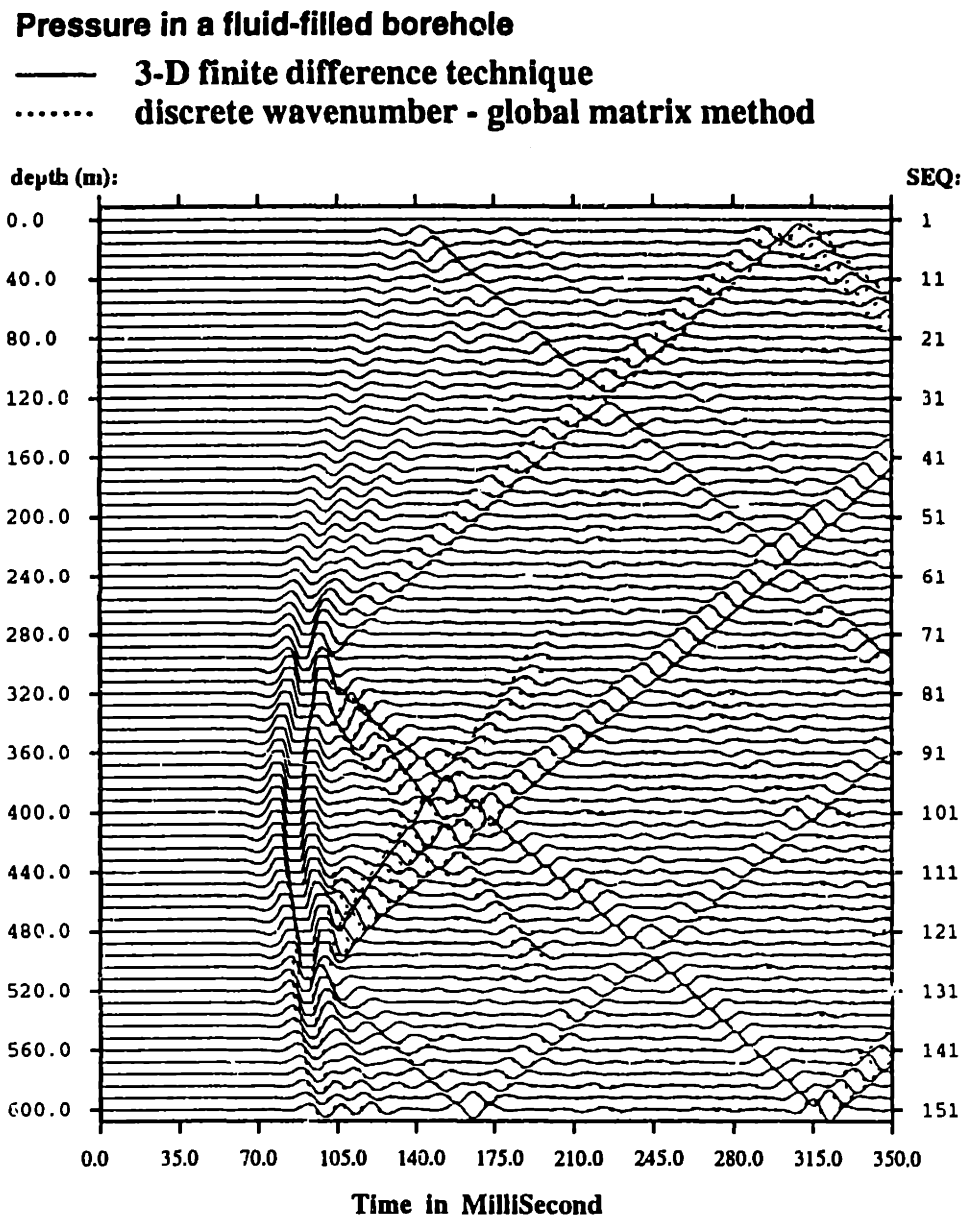

Figure 6-13: Synthetic hydrophone pressures in an open borehole for an explosive source in the formation. The solid line shows the computation by the hybrid method developed in this chapter. The dashed line is the computation by the method developed in chapter 5. The source is inside a low velocity layer embedded in a high velocity halfspace (see Table 5.1 for detailed parameters). Its time history is a Kelly wavelet with the central frequency 50 Hz. The source-borehole offset is 200 m. The borehole radius is 0.10 m.

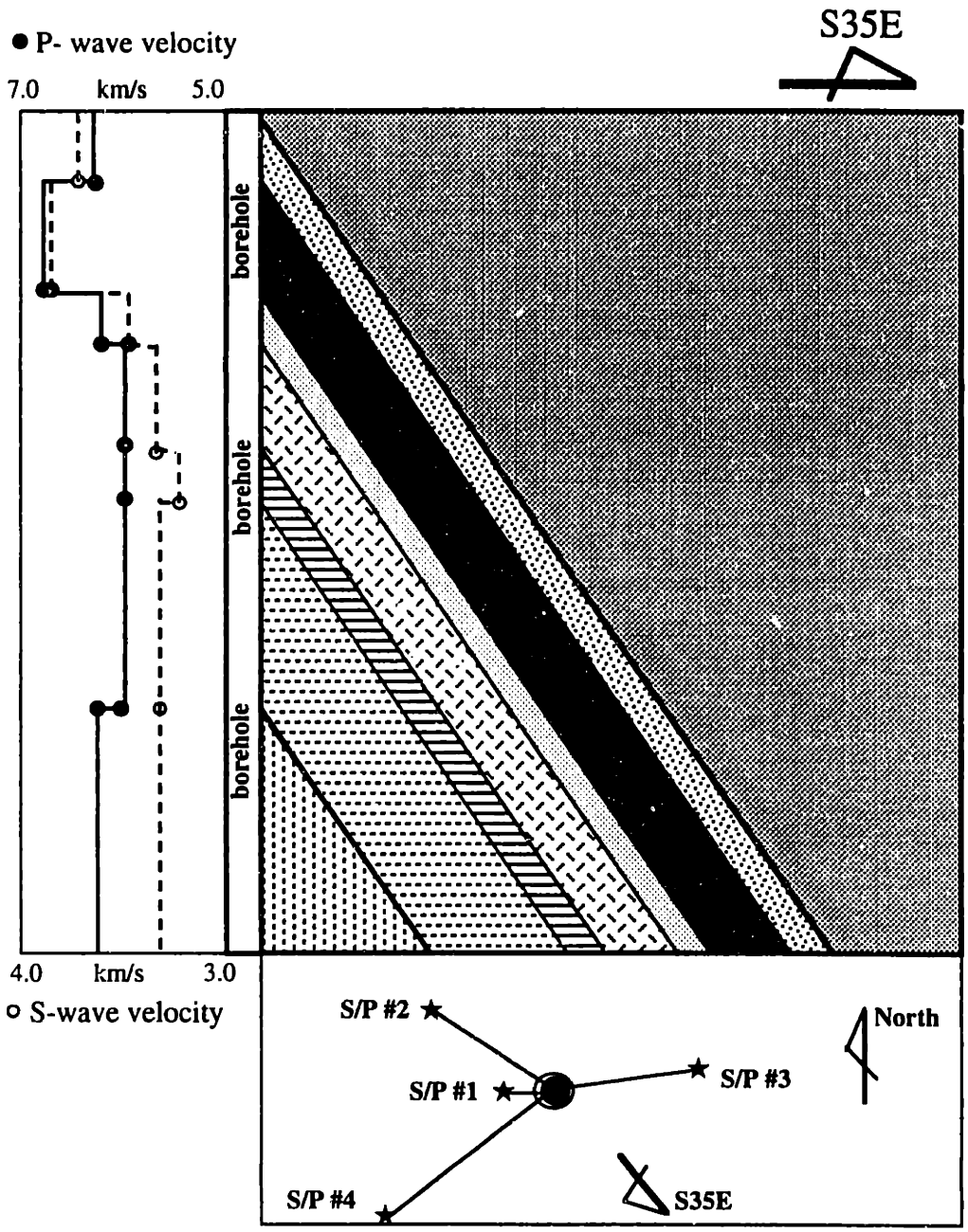

Figure 6-14: A geological model for the Kent Cliffs borehole experiment site including dipping layers. The model is constructed using sonic logging data and downhole televiewer images from the borehole in addition to core sample information. The formation is tilded toward the southeast direction with an uniform dipping angle equal to 60°. The left panel in this figure shows the averaged P-wave and S-wave velocity profiles. The bottom panel is the layout of the experiment.

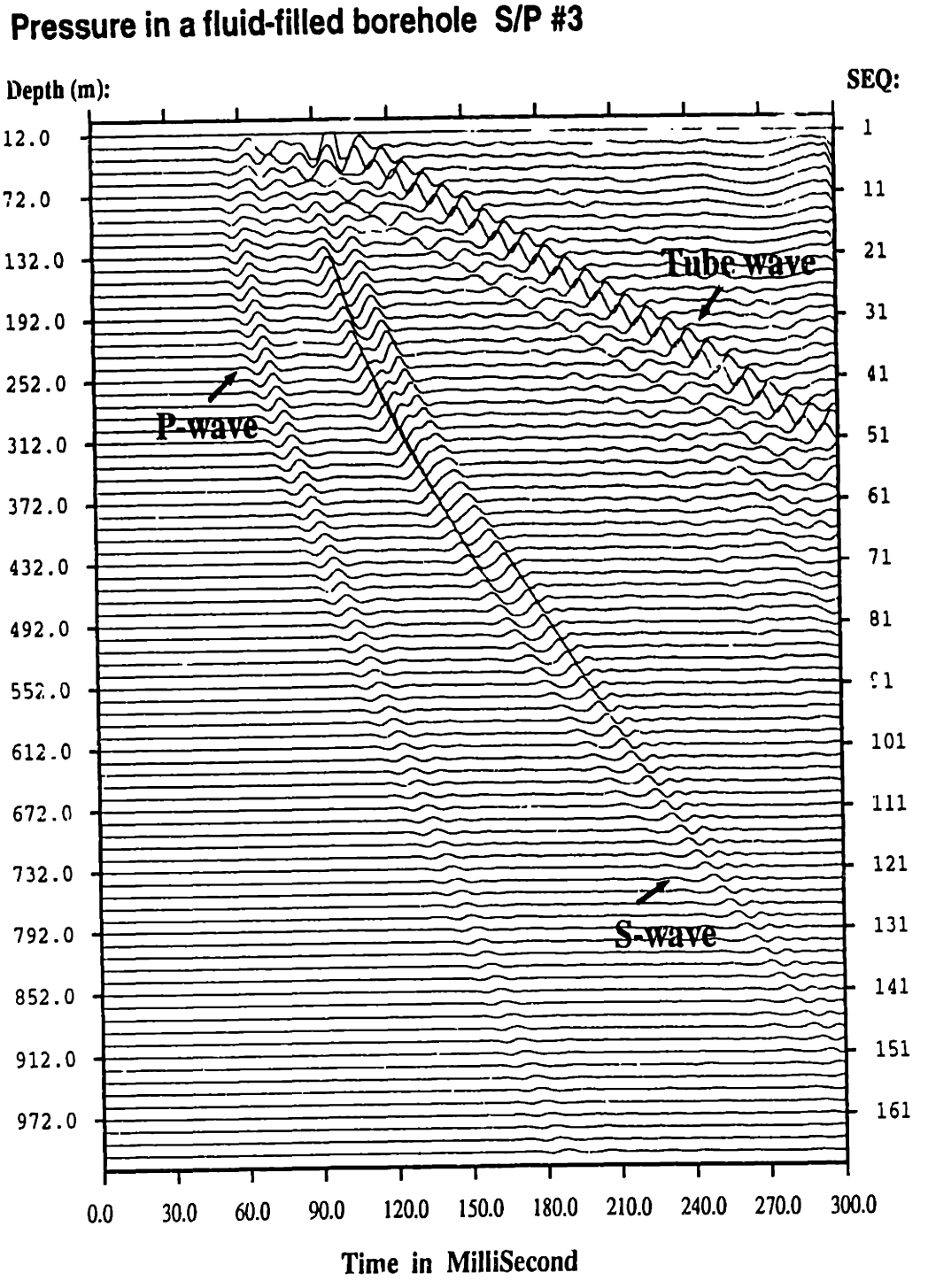

Figure 6-15: Synthetic hydrophone VSP data for the shot point S/P #3 computed by the hybrid method developed in this chapter. In this calculation, the source is simulated by a vertical force at offset 288 m in the N85°E direction. Its time history is a Kelly wavelet with the central frequency 75 Hz. The receivers spans a depth range from the surface to 990.6 m. The geological model is shown in Figure 6-14. The cubic volume is discretized into $100 \times 100 \times 200$ grid points. The grid size is 6 m. The time step size is 0.1 ms. A static time delay of 20 ms due to the source wavelet is not applied in this plot.

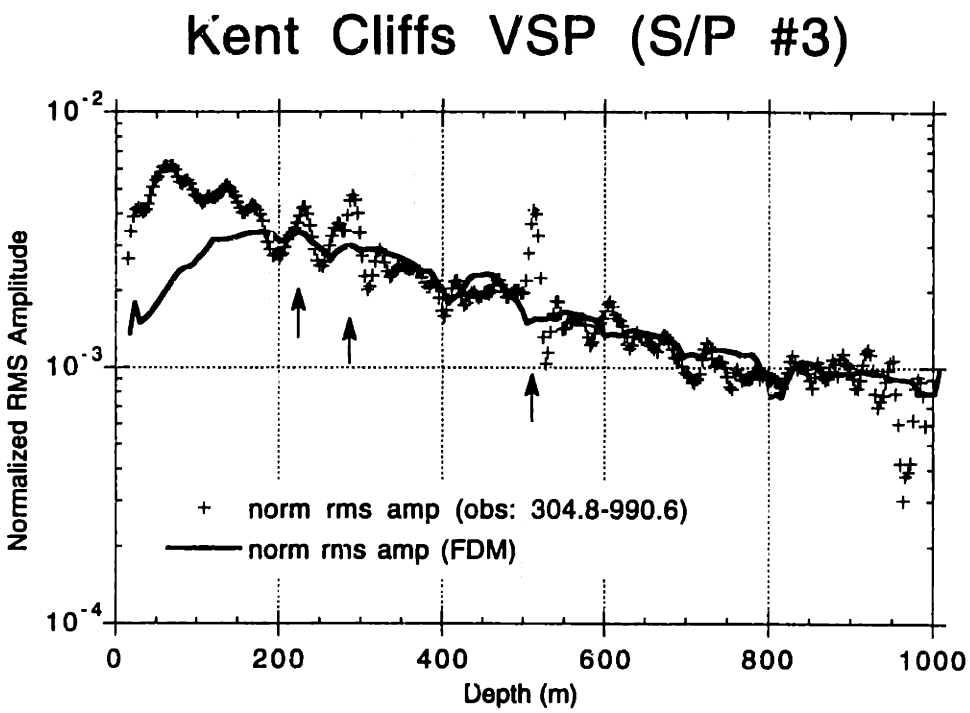

Figure 6-16: RMS (root mean square) amplitude of the first arrival (P-wave) for the shot point S/P #3. The solid line shows the values computed from the synthetic hydrophone pressures. The plus (+) symbols are the data derived from the field hydrophone measurements shown in Figure 5-10. A constant factor derived from data in the depth range from 304.8 m to 990.6 m is used to normalize the synthetic and field data. The horizontal axis is the depth of receivers in meters. The vertical axis is the normalized RMS amplitude in a logarithmic scale. The arrows indicate locations where tube waves are generated by fractures.

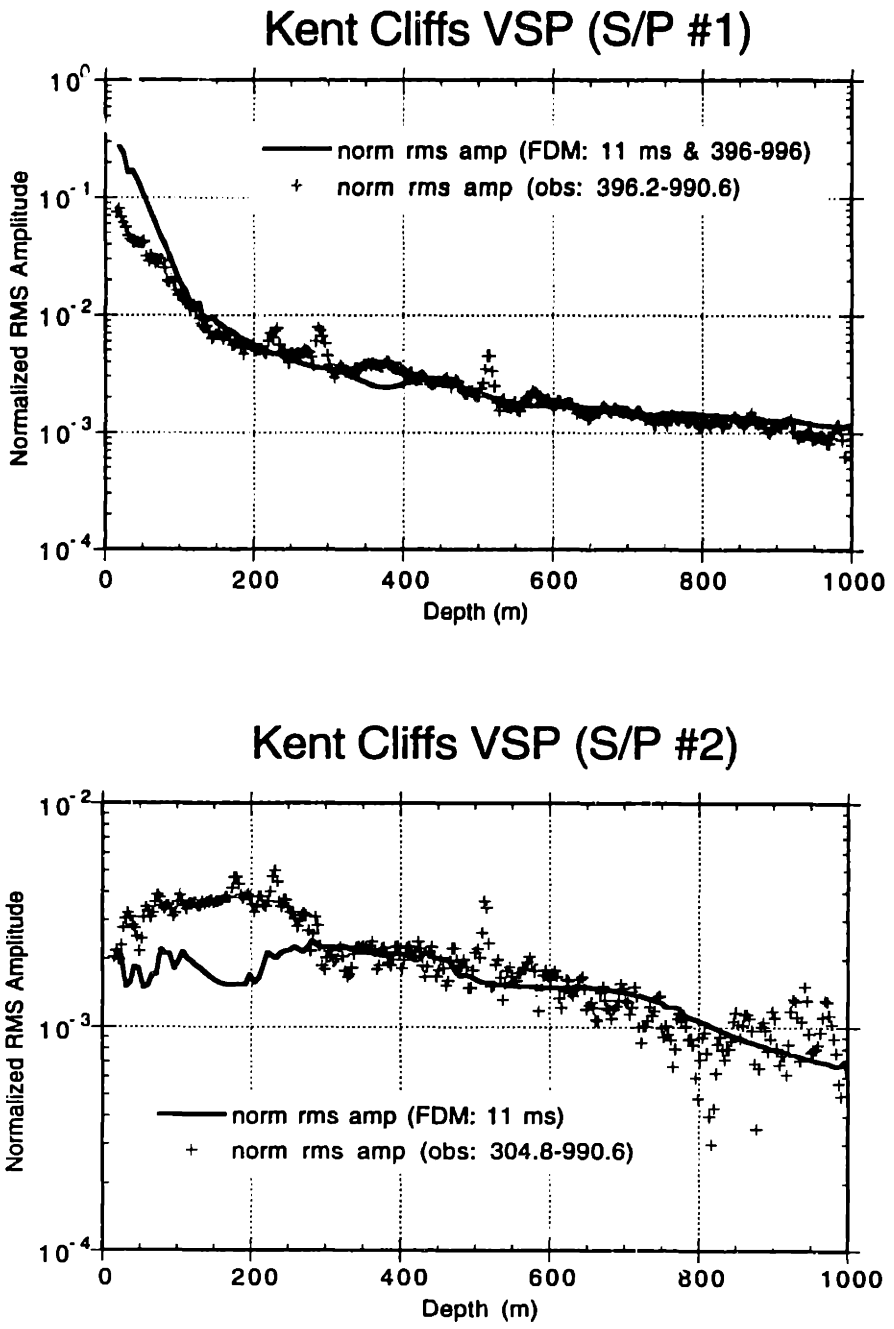

Figure 6-17: RMS (root mean square) amplitude of the first arrival (P-wave) for the shot points S/P #1 (top) and S/P #2 (bottom). The solid line is the data computed using the synthetic hydrophone pressures. The plus (+) symbols are the data derived from the field hydrophone measurements. A constant factor derived from data in the depth range from 304.8 m to 990.6 m is used to normalize the synthetic and field data. The horizontal axis is the depth of receivers in meters. The vertical axis is the normalized RMS amplitude in a logarithmic scale.

Chapter 7

Removal of Borehole Effects from Downhole Seismic Measurements

The primary goal of this chapter is to develop a processing method for removing the borehole effect from downhole hydrophone data. After applying this method, the data should resemble the incident wave field when the borehole is absent. Obviously, this method should possess the ability to reject events associated with tube waves, and to yield the true amplitudes of incident P- and S-waves which are refracted at the solid-fluid interface. Conventional fan filters can not be used to achieve this goal. A physical filter derived from the borehole coupling mechanism is desirable.

Marzetta (1992) recently proposed using the inverse borehole coupling theory to reject the tube waves from hydrophone vertical seismic profiling data. Apparently realizing the usefulness of an old but elegant analysis of White (1953, 1983), Marzetta showed in his paper that a physically meaningful quantity called the *borehole squeeze strain* can be obtained from an array of hydrophone data. Marzetta's method applies only to open boreholes. Also, unlike familiar quantities such as pressure, particle displacements and particle velocities, the borehole squeeze strain is an uncomfortable 'monster' to deal with.

In this chapter we first develop an inverse borehole coupling theory that is applicable to both open and cased boreholes. Then we introduce a mapping scheme which converts the borehole squeeze strain to pressure and particle displacement of the incident elastic wave in an undisturbed formation. The merit of our technique is that the borehole effect is removed from downhole measurements after these processing techniques. The data are then well-suited for use in further analyses such as amplitude studies, diffraction tomography, or true amplitude migration.

This chapter is divided into five sections. The first section presents an algorithm to compute the borehole squeeze pressure from hydrophone VSP or crosswell data. This method is valid for both open and cased boreholes. The second section is devoted to a technique to transform the borehole squeeze pressure into the pressure of the incident wave in the formation. Synthetic data calculated by the hybrid technique given in Chapter 6 are used to test its accuracy. Field data from the Kent Cliffs borehole experiment are also processed using this technique, and those results are given in the third section. In the fourth section, we address more advanced topics such as mapping hydrophone data into geophone responses, provided that an accurate formation velocity profile along the borehole is available. The last section of this chapter contains some discussions and conclusions.

7.1 Borehole Squeeze Pressure

An alternative form of the borehole coupling equation, given that pressure in the fluid is known, is (Marzetta, 1992; rewriting equation (6.35a))

$$\frac{\partial^2}{\partial t^2} Q(z,t) = \frac{\partial^2}{\partial t^2} P(z,t) - C_T^2(z)\, \frac{\partial^2}{\partial z^2} P(z,t), \tag{7.1a}$$

$$Q(z, t=0) = 0, \tag{7.1b}$$

$$\frac{\partial}{\partial t} Q(z, t=0) = 0, \tag{7.1c}$$

where $P(z,t)$ is the fluid pressure at time t and depth z, and $Q(z,t)$ is the borehole squeeze pressure. The borehole squeeze pressure is related to the stresses of the incident waves by

$$Q(z,t) = 2\ \rho_f C_T^2(z)\ \left[\frac{\sigma_{xx}(z,t)+\sigma_{yy}(z,t)}{E}\ -\nu\frac{\sigma_{zz}(z,t)}{E}\right],$$

in an open borehole, and by

$$Q(z,t) = 2\ \rho_f C_T^2(z)\ \left[\frac{\sigma_{xx}(z,t)+\sigma_{yy}(z,t)}{E_{\|}}\ -\nu\frac{\sigma_{zz}(z,t)}{E_{\perp}}\right],$$

in a cased borehole. The notations can be found in section 6.3.1 and section 3.2.3.

Upon double integrations with respect to time, equation (7.1a) becomes

$$Q(z,t) = P(z,t) - C_T^2(z)\ \int_{-\infty}^{\infty} h(z-z_0)\left[\int_0^t ds \int_0^s P(z_0,\tau)d\tau\right] dz_0, \qquad (7.2)$$

where $h(z)$ is the impulse response of the second order differentiator (see section 6.3.2). An example of this impulse response has been given in Table 6.3. Successively shorter operators (of lengths 32, 16, 8, 4, and 2) are used near the top and bottom edges. Proper boundary conditions for $P(z,t)$ are used to minimize the edge effects.

Remark 1: This process removes tube waves from the pressure measurements $P(z,t)$, and partially compensates for the borehole effect on the amplitudes of the P- and S-waves. This can be easily seen in the frequency-wavenumber domain, where the borehole squeeze pressure is a filtered version of the hydrophone data with the filter identically zero at the tube wave wavenumbers $k_z = \pm\omega/C_T$. ■

Remark 2: The filter in the (ω, k_z) plane is a notch filter. This filter may not be as effective as the conventional fan filters at removing tube waves from the data. However, since it is based on the physics of the borehole coupling process, it yields a quantity that bears direct information about the incident wave in the formation. This filter can also be combined with the conventional F-K processing to both effectively eliminate tube waves and transform the hydrophone pressure into the borehole squeeze pressure. ■

Remark 3: Although the borehole squeeze pressure is directly related to the stresses of the incident waves in formation, it is still not a very useful quantity for later processing such as amplitude analysis, tomographic inversion using full waveforms, or true amplitude migration. For this reason, in the next sections, we develop a few techniques which map the borehole squeeze pressure into the pressure and the individual displacement component of the incident wave. ■

Two examples are given in this section as demonstrations. In the first example we process the synthetic hydrophone data shown in Figure 6-13 using the above procedure. Recall that this data set is computed for a stratified earth model given in Table 5.1. In the processing, the free surface boundary condition at the well top and the rigid boundary condition at the well bottom are used in differentiating the hydrophone data. Figure 7-1 shows the borehole squeeze pressure derived from the synthetic hydrophone data. One can see, by comparing Figure 7-1 with Figure 6-13, that events traveling with the tube wave speed are effectively eliminated by the inversion process. The amplitude of the P- and S-waves are partially compensated. Some edge effects in the first trace (zero hydrophone pressure trace) are also visible.

Shown in Figure 7-2 is another example of applying this procedure to the hydrophone data set in Figure 6-15. The latter figure shows the synthetic hydrophone data for the Kent Cliffs hydrophone experiment at shot point S/P#3, where dipping formations are properly handled. In the processing the nonreflecting boundary condition is used in differentiating the hydrophone data at both the top and the bottom edges (for 1-D absorbing boundary condition, see Higdon, 1990). One can see, by comparing Figure 7-2 with Figure 6-15, that the tube waves are removed and the P- and S-waves are well preserved.

7.2 Pressures of Incident Compressional Waves

In this section we describe a method of transforming the pressure in the fluid (hydrophone measurement) into the *pressure of the incident wave* in the formation, assuming that the data is comprised of compressional waves only. We first derive a partial differential equation relating the pressure of an incident P-wave to the borehole squeeze pressure. Then we proceed to solve this equation and show the accuracy of this method, using synthetic examples where the true 'pressure' of the incident wave is known.

7.2.1 Inverse Borehole Coupling Equation

In the frequency-wavenumber (ω - k_z) domain, a plane P-wave in the (x, z) plane can be expressed as

$$\begin{pmatrix} u_x \\ u_z \end{pmatrix} = \begin{pmatrix} ik_p \\ ik_z \end{pmatrix} \exp(ik_z z + ik_p x), \tag{7.3}$$

where u_x and u_z are the horizontal and vertical displacements, respectively. k_z, k_p and $k_\alpha = \omega/\alpha$ are the vertical, horizontal, and compressional wavenumbers, respectively. They are related by $k_z^2 + k_p^2 = k_\alpha^2$. The spheric component of the stress tensor of the incident wave, or, simply put the *pressure*, by definition, is defined by

$$\begin{aligned} P_0(k_z,\omega) &\equiv \frac{1}{3}(\sigma_{xx} + \sigma_{yy} + \sigma_{zz}), \\ &= -\rho\omega^2 \left(1 - \frac{4}{3}\frac{\beta^2}{\alpha^2}\right) \exp(ik_z z + ik_p x), \end{aligned} \tag{7.4}$$

where σ_{xx}, σ_{yy} and σ_{zz} are the three principal stresses of the incident wave. They are derived from equation (7.3) using the stress–strain and strain–displacement relationships (e.g., Ewing et al., 1957). The borehole squeeze pressure $Q(k_z,\omega)$ can be computed using equations (6.33) and (6.34) as

$$Q(k_z,\omega) = 2\rho_f C_T^2 \left[\frac{\sigma_{xx} + \sigma_{yy}}{E_\parallel} - \nu\frac{\sigma_{zz}}{E_\perp}\right],$$

$$= -2\rho_f\omega^2\frac{C_T^2}{\alpha^2}\frac{\eta_\parallel-\nu^2\eta_\perp}{(1+\nu)(1-2\nu)}\left\{1-2\frac{\beta^2}{\alpha^2}\frac{(1-\nu)(\eta_\parallel+\nu\eta_\perp)}{\eta_\parallel-\nu^2\eta_\perp}\cos^2\delta\right\}$$
$$\cdot\exp(ik_z z+ik_p x), \tag{7.5}$$

where $\cos\delta = k_z/(\omega/\alpha)$. Here δ is the inclination angle of the incident plane P-wave with respect to the vertical axis. The notations have been given in section 5.2.2 and section 3.2.

The ratio of the borehole squeeze pressure to the pressure of the incident wave is found by dividing equation (7.5) by equation (7.4), yielding

$$\frac{Q(k_z,\omega)}{P_0(k_z,\omega)} = \frac{2\rho_f}{\rho(1-\frac{4}{3}\frac{\beta^2}{\alpha^2})}\frac{C_T^2}{\alpha^2}\frac{\eta_\parallel-\nu^2\eta_\perp}{(1+\nu)(1-2\nu)}\left\{1-\frac{2\beta^2}{\alpha^2}\frac{(1-\nu)(\eta_\parallel+\nu\eta_\perp)}{\eta_\parallel-\nu^2\eta_\perp}\cos^2\delta\right\}. \tag{7.6}$$

The right hand side of the above equation can be considered as the transfer function of a 2-D filter whose output is the borehole squeeze pressure and whose input is the pressure of the incident wave. However, we are interested in the inverse problem of estimating $P_0(k_z,\omega)$ given $Q(k_z,\omega)$. Direct inversion of equation (7.6) proves to be problematic due to the existence of poles in the inverse filter. Equation (7.6) also lacks the ability to handle spatial variations of the elastic parameters. For a better formulation, we make use of the following mappings from $(\omega - k_z)$ domain to $(t - z)$ domain:

$$ik_z \leftrightarrow \partial/\partial z \qquad -k_z^2 \leftrightarrow \partial^2/\partial z^2$$
$$ik_p \leftrightarrow \partial/\partial x \qquad -k_p^2 \leftrightarrow \partial^2/\partial x^2$$
$$-i\omega \leftrightarrow \partial/\partial t \qquad -\omega^2 \leftrightarrow \partial^2/\partial t^2 \quad .$$

From equation (7.6) with $\cos\delta = k_z/(\omega/\alpha)$, we obtain a partial differential equation for the pressure of the incident wave, written in the time and space domain as

$$\frac{\partial^2}{\partial t^2}P_0(z,t) - \gamma^2\frac{\partial^2}{\partial z^2}P_0(z,t) = \varrho^2\frac{\partial^2}{\partial t^2}Q(z,t), \tag{7.7}$$

where

$$\gamma^2 = 2\beta^2\frac{(1-\nu)(\eta_\parallel+\nu\eta_\perp)}{\eta_\parallel-\nu^2\eta_\perp},$$

and

$$\varrho^{-2} = \frac{2\rho_f}{\rho(1-\frac{4}{3}\frac{\beta^2}{\alpha^2})}\frac{C_T^2}{\alpha^2}\frac{\eta_\parallel-\nu^2\eta_\perp}{(1+\nu)(1-2\nu)}.$$

The inverse borehole coupling theory, as stated in equation (7.7), reveals the following: (1) the acceleration of borehole squeeze pressure acts as the source in the inversion for pressure of an incident wave and (2) the pressure of the incident wave satisfies an inhomogeneous wave equation with traveling speed $\gamma = \sqrt{2}\beta$ in an open borehole and $\gamma > \sqrt{2}\beta$ in a cased borehole.

A null initial condition can be used in solving the partial differential equation (7.7) to ensure causality. However, proper boundary conditions are required to accommodate the spatial derivative with respect to depth z. Since measurements are available only in the depth range $z_0 \leq z \leq z_H$, where z_0 is the depth of the shallowest hydrophone and z_H is that of the deepest, no information exists for the ranges $z < z_0$ and $z > z_H$. Naturally, we can assume $Q(z < z_0, t) \equiv 0$ and $Q(z > z_H, t) \equiv 0$, which corresponds to the zero padding practice in the frequency-wavenumber (F-K) processing (Robinson et al., 1986). This implies that no secondary source for $P_0(z,t)$ exists outside the depth range $z_0 \leq z \leq z_H$. Thus the proper boundary conditions for equation (7.7) are the absorbing boundary conditions which permit only outgoing energy at $z = z_0$ and $z = z_H$. They can be written mathematically as

$$(\frac{\partial}{\partial t} + \gamma \frac{\partial}{\partial z})P_0(z,t) = 0, \qquad z = z_0, \tag{7.8}$$

and

$$(\frac{\partial}{\partial t} - \gamma \frac{\partial}{\partial z})P_0(z,t) = 0, \qquad z = z_H. \tag{7.9}$$

Equation (7.7), together with its initial and boundary conditions, is solved using the same technique described in section 6.3.2.

Remark 1: This process fully compensates for the effect of a borehole on the amplitude of an incident P-wave. However, an incident S-wave is misinterpreted as a compressional wave arriving at a smaller angle of incidence according to

$$\cos\delta_p = \frac{\alpha}{\beta}\cos\delta_s,$$

where δ_s is the angle of incidence of the plane S-wave, and δ_p is that of the 'misinterpreted' plane P-wave. Since $\cos\delta_p$ is larger than $\cos\delta_s$, it is evident from equa-

tion (7.6) that this event is awarded a larger amplitude compensation than the true P-waves. Therefore, we expect that events associated with S-waves will become more prominent in the data after processing using this technique. ■

Remark 2: The inversion for the pressure of the incident wave is not uniquely determined. This is because, in the frequency-wavenumber domain, the filter has poles at $k_z = \pm\omega/\gamma$, as is evident from equation (7.7) after a F-K transform. Noise traveling with these particular wavenumbers will be amplified. Mathematically, equation (7.7) admits a solution of the form

$$P_0(z,t) = P_0'(z,t) + \mathcal{N}(z \pm \gamma t),$$

where the spurious events $\mathcal{N}(z \pm \gamma t)$ have no effects on the borehole squeeze pressure $Q(z,t)$. ■

Remark 3: The spurious events $\mathcal{N}(z \pm \gamma t)$ in the solution to equation (7.7) prove to be troublesome, even in tests using synthetic data. To effectively attenuate the noise events associated with the poles at $k_z = \pm\omega/\gamma$, we add a damping term to equation (7.7)

$$\frac{\partial^2}{\partial t^2}P_0(z,t) + \epsilon\frac{\partial}{\partial t}P_0(z,t) - \gamma^2\,\frac{\partial^2}{\partial z^2}P_0(z,t) = \varrho^2\,\frac{\partial^2}{\partial t^2}Q(z,t). \qquad (7.10)$$

In this equation, no pole exists in the entire frequency-wavenumber plane. The choice of ϵ should be such that events traveling with the P-wave velocity or faster are not seriously affected, which requires

$$\epsilon \ll \mid 1 - 2\beta^2/\alpha^2 \mid \omega_c \sim \frac{\omega_c}{3},$$

where ω_c is the central circular frequency. Typically, $\epsilon = \frac{\omega_c}{30} \sim \frac{\omega_c}{100}$ is a good choice.

In implementation equation (7.10) is solved using the same technique as equation (7.7) except that at each time step an attenuation factor $(1+\epsilon t)^{-1}$ is applied. Although this procedure greatly reduces the amplitude of the spurious events, it also causes attenuation of useful signals. Therefore, a compensation gain is applied to

restore the amplitude of useful signals to the case where $\epsilon = 0$. It turns out that, unless ϵ is very small, the gain function is dependent on the frequency and wavenumber contents of the data. One empirical gain function derived from both conjectures and numerical simulations is

$$gain \approx \frac{\exp(\epsilon t)}{1 + \xi\,(\epsilon t)^3}.$$

This gain function is used in our examples with $\xi \approx 0.025$, but this value is problem dependent. ■

7.2.2 Numerical examples

The examples in this section compare the pressures of incident waves with those obtained by applying the inverse borehole coupling theory to borehole hydrophone data. We use synthetic examples where both the pressure of incident waves in formation and hydrophone pressure in fluid are available.

We apply our technique to the synthetic hydrophone data shown in Figure 6-15 (see section 6.3.4 for a detailed account of the model and parameters). The borehole squeeze pressure $Q(z,t)$ shown in Figure 7-2 is the input to the inversion for $P_0(z,t)$, the pressure of the incident wave. Two cases are to be presented: $\epsilon = 0$ and $\epsilon = 16\ \mathrm{s}^{-1}$. Figure 7-3 shows the inverted pressure of the incident wave with $\epsilon = 0$ (i.e., no damping is used). As one might expect, the most energetic events in this figure are the spurious events traveling with a speed of $\gamma = \sqrt{2}\beta$ (both upgoing and downgoing). Figure 7-4 shows the inverted pressure of the incident wave with $\epsilon = 16\ \mathrm{s}^{-1}$. In this case the spurious events are greatly attenuated. The P-wave and S-wave (mistaken as P-wave in this processing) are clearly distinguishable. Slowly traveling spurious events are also visible, but they are much easier to remove using a velocity filter than those in Figure 7-3.

Figure 7-5 shows the 'true' pressure of the incident waves computed by the 3D finite difference method using the relationship $P_0 = (\sigma_{xx} + \sigma_{yy} + \sigma_{zz})/3$. Only the

P-wave is salient. The Rayleigh wave on the free surface (top) is also discernible, but its amplitude decays rapidly with depth. The important point to note is that the first arrival P-wave in Figure 7-3 agrees with that of Figure 7-5 in both amplitude and phase. To show this, we plot in Figure 7-6 the rms amplitude of both incident P-waves as a function of depth. A 7.5 ms window length was used to compute the rms amplitudes. The solid line (labeled as FD3D, which stands for 3D Finite Difference computation) displays the rms amplitudes from Figure 7-5. The + symbol (labeled as IBCF, which stands for Inverse Borehole Coupling Filter) denotes the rms amplitudes from Figure 7-3. Both sets of amplitudes agree very well.

An attenuation correction is needed to compensate for the effect of the nonzero ϵ–term on P-wave amplitude in Figure 7-4. After trying several gain functions, experience has shown that an exponential gain of $\exp(\epsilon t)$ causes excess gain correction at large depth (later arrival time), and that a gain function of $\exp(\epsilon/2t)$ causes under-compensation. However, using the empirical gain function given at the end of section 7.2.1 with $\xi = 0.025$, we obtain a good estimate of the gain compensation (Figure 7-7). It should be pointed out that the gain function can be derived precisely through the following approach: (1) construct noise-free signals such that they have the same frequency content and moveouts as the desired signal (usually the first P-wave arrival); (2) apply equation (7.10) to those noise-free signals twice with $\epsilon \neq 0$ and $\epsilon = 0$, respectively. The amplitude ratio of these signals gives the precise gain function.

7.3 Application to Kent Cliffs Hydrophone Data

In this section we apply the techniques developed in the previous two sections to the Kent Cliffs hydrophone data shown in Figure 5-9 and Figure 5-10. The procedure is as follows: we use the method in section 7.1 to compute the borehole squeeze pressure $Q(z,t)$ using the field hydrophone data $P(z,t)$ as input. We then feed the borehole squeeze pressures into equation (7.10) to estimate the pressure of the incident P-

waves $P_0(z,t)$. Our objective in this section is to demonstate the usefulness of our techniques with field examples.

The velocity information along the borehole is derived from the sonic logging data (averaged over depth), and linear interpolation is used to obtain the compressional and shear velocities as well as density at the location of each hydrophone. The tube wave velocity is computed using the zero frequency approximation of Boit (1952) and White (1953). Figure 7-8 shows the borehole squeeze pressure for shot point S/P #2. By comparing Figure 7-8 with the hydrophone data in Figure 5-9, one can see that tube waves generated at fractures, shear zones, and free surface are significantly attenuated in the borehole squeeze pressure data. Residual tube waves at certain depths (e.g., 513 m) are still visible, but they are small in amplitude compared to the P-waves. The S-waves are clearly discernible in the borehole squeeze pressure data, while they are overwhelmed by the tube waves in the hydrophone data. Improvement in borehole squeeze pressure data quality is quite appreciable. Figure 7-9 shows the borehole squeeze pressure for shot point S/P #3. Compared with the hydrophone data in Figure 5-10, one can see that, once again, tube waves are significantly reduced in the borehole squeeze pressure data, and residual tube waves are small in amplitude compared to both the P- and S-waves. The S-waves are very prominent in this particular example. The data quality, after applying this processing, is greatly enhanced.

Given the newly obtained borehole squeeze pressure $Q(z,t)$, we then proceed to compute the pressure of the incident P-waves $P_0(z,t)$ using the inverse borehole coupling filter in equation (7.10). We choose $\epsilon = 16\ s^{-1}$ and apply a F-K filter (using the PROMAX[1] software package) to reject the spurious events since these events travel at a velocity less than one half of the P-wave velocity (making them perfect targets for F-K filtering). The empirical gain formula given in the previous section is applied afterwards. Figure 7-10 and Figure 7-11 show the pressures of incident waves

[1]PROMAX is the trademark of Advance Geophysical, Inc..

in the formation for shot points S/P #2 and S/P #3, respectively. These results are derived from the borehole squeeze pressure data shown in Figure 7-8 and Figure 7-9. The first arrival P-waves are clearly the largest amplitude events. The S-waves are also evident; however, they are not properly handled by the algorithms. Residual noises are visible, but their amplitudes are relatively small. Based on the numerical examples shown in the previous section, we believe that the first arrival P-waves in these figures should closely resemble the pressure of the incident wave. They can be used as input for imaging and inversion schemes in which the borehole is not included as a part of formulation.

7.4 Hydrophone to Geophone Mapping

By hydrophone to geophone mapping, we mean that one can estimate a downhole geophone response from an array of hydrophone measurements, given that both P-wave and S-wave velocity profiles in the borehole are known (e.g., from sonic well logging). Without the medium velocity information, it is impossible to map a hydrophone data (1 component) to the corresponding geophone measurements (2 components). However, when the sonic well logging profiles are available, we have two inputs for two unknowns, and then the hydrophone to geophone mapping is indeed feasible. The assumptions we make are: (1) the formation is isotropic; (2) the data are comprised of compressional waves only. The proper handling of S-waves is beyond the scope of this study. This analysis should not discourage the downhole geophysical practices using 3-component geophones.

7.4.1 Basic Equations

Using equations (7.3) and (7.5), the ratio of the borehole squeeze pressure $Q(k_z, \omega)$ and the vertical particle displacement of the incident P-wave $u_z(k_z, \omega)$ can be written

as

$$\frac{Q(k_z,\omega)}{u_z(k_z,\omega)} = -2\rho_f \frac{C_T^2}{\alpha^2}\,\frac{\omega^2}{ik_z}\,\frac{\eta_{\|}-\nu^2\eta_{\perp}}{(1+\nu)(1-2\nu)}\left\{1-\frac{2\beta^2}{\alpha^2}\frac{(1-\nu)(\eta_{\|}+\nu\eta_{\perp})}{\eta_{\|}-\nu^2\eta_{\perp}}\cos^2\delta\right\}.$$

The equivalent form in the (z,t) domain is obtained using the mapping procedure outlined in section (7.2.1), which yields

$$\left[\frac{\partial^2}{\partial t^2}-\gamma^2\,\frac{\partial^2}{\partial z^2}\right]u_z(z,t) = \varrho_0^2\,\frac{\partial}{\partial z}Q(z,t), \tag{7.11}$$

where

$$\varrho_0^{-2} = 2\rho_f\frac{C_T^2}{\alpha^2}\,\frac{\eta_{\|}-\nu^2\eta_{\perp}}{(1+\nu)(1-2\nu)}.$$

This equation can be solved using the same technique as that for equations (7.7) and (7.10). Similarly, one can obtain an equation for the horizontal particle displacement $u_r(z,t)$ as

$$\left[\frac{\partial^2}{\partial t^2}-\gamma^2\,\frac{\partial^2}{\partial z^2}\right]\,u_r(z,t) = \varrho_0^2\,\frac{\partial}{\partial x}Q(z,t). \tag{7.12}$$

In equation (7.12), a complication occurs due to the term $\partial/\partial x\ Q(z,t)$, which is not directly available from the borehole squeeze pressure itself. Although it is possible to estimate this quantity using the paraxial approximation of wave equation (Claerbout, 1985; Bamberger et al., 1988, among others), we will restrict our attention to equation (7.11) only.

7.4.2 Numerical examples

In this section we demonstrate the hydrophone–geophone mapping procedure by applying it to the synthetic example given in section 6.3.4 (see Figure 6-14 for the model and geometry). Figure 7-12 shows the vertical component of particle velocity computed by the 3D finite difference method when the borehole is absent. In this figure the P-wave, S-wave, and Rayleigh wave on the surface are evident. Figure 7-13 shows the vertical component of particle velocity $u_z(z,t)$ derived from the z-derivative of the borehole squeeze pressure (Figure 7-2) using equation (7.11). This particular example has a damping factor $\epsilon = 16\ s^{-1}$, although a series of ϵ values have been

tried. In Figure 7-13 both the P-wave and S-wave are discernible, as well as some slowly travelling spurious events inherent in the inverse filter. The gain compensation is not applied in this plot, which is the reason that the P-wave amplitude decays faster with depth compared with Figure 7-12.

In Figure 7-14 three traces at depths 156 m (the 25-th trace), 456 m (the 75-th trace), and 756 m (the 125-th trace) are shown. The solid lines are the true vertical component of particle velocity (in Figure 7-12) computed by the 3D finite difference method. The dashed lines are the estimated vertical components (in Figure 7-13) from the borehole squeeze pressure using the inverse borehole coupling equations. In this figure $\epsilon = 0$ instead of $\epsilon = 16\ s^{-1}$. Strong spurious energies are observable because $\epsilon = 0$ is used in the processing. Nevertheless, we see that the first P-waves overlay very well in both amplitude and phase. Figure 7-15 shows the rms amplitude of the first arrival P-wave as a function of depth. We used a 12.5 ms time window in the computation. The solid line in this figure is the amplitude of P-wave (vertical component) from the 3D finite difference simulation. The plus symbols are the same data from the $u_z(z,t)$ obtained from the hydrophone data. Overall agreement is significant, although some discrepancies at shallow depths are visible.

7.5 Discussions and Conclusions

A new procedure for processing hydrophone VSP and crosswell data is proposed in this chapter. This procedure consists of three steps using three techniques. In the first step we apply the technique developed in section 7.1 to convert hydrophone pressure data $P(z,t)$ to borehole squeeze pressure data $Q(z,t)$. This processing significantly attenuates the tube waves and partially compensates the P- and S-waves for the effects of a borehole on their amplitudes. This processing can be also combined with the F-K velocity filter to completely reject the tube waves and other noises. In the second step we apply the technique proposed in section 7.2 to transform the borehole squeeze

pressure data $Q(z,t)$ into the pressure of the incident P-wave $P_0(z,t)$. This process yields an excellent estimation of the incident P-wave in the formation, although the S-waves are improperly handled and some spurious events inherent in the inverse filter might be troublesome. In the third step (more theoretical at this point) we apply the technique developed in section 7.4 to map the hydrophone data in the borehole fluid to the solid displacement in the formation. To do so, we need both the P-wave and S-wave velocity profiles along the borehole. Numerical tests show that this technique yields good estimation of the vertical component of a geophone response. The estimation of the horizontal component of the geophone response is more difficult, although not impossible, due to the inavailablity of the horizontal derivative of the borehole squeeze pressure. The first two steps have been successfully applied to the Kent Cliffs hydrophone data.

These processing techniques are very fast and robust. For the Kent Cliffs examples, where 321 traces are used and each trace has 2002 time samples, it takes about 15 minutes on a DECstation 5000/25 to complete the first step, and about 25 minutes to finish the second and third steps, respectively, including the time for disk input and output. Since these processings are implemented in the (z-t) domain, the depth variations of medium parameters are properly handled. One should beware of instability if the requirement of $\gamma\Delta t/\Delta x < 1/\sqrt{2}$ in the second and third steps are not satisfied (see section 6.3.2). This instability is easily overcome by upsampling the borehole squeeze pressure data by a suitable factor (i.e., decrease Δt). Taking proper care of the poles in the second and third steps is also important for successes on field data. It is always advisable to use a nonzero damping factor, the larger the better. A proper gain compensation for the useful signals is also needed after the processing. It is possible to derive the precise gain function using the method outlined in section 7.2.2 if the empirical gain function given in section 7.2.1 is not satisfactory.

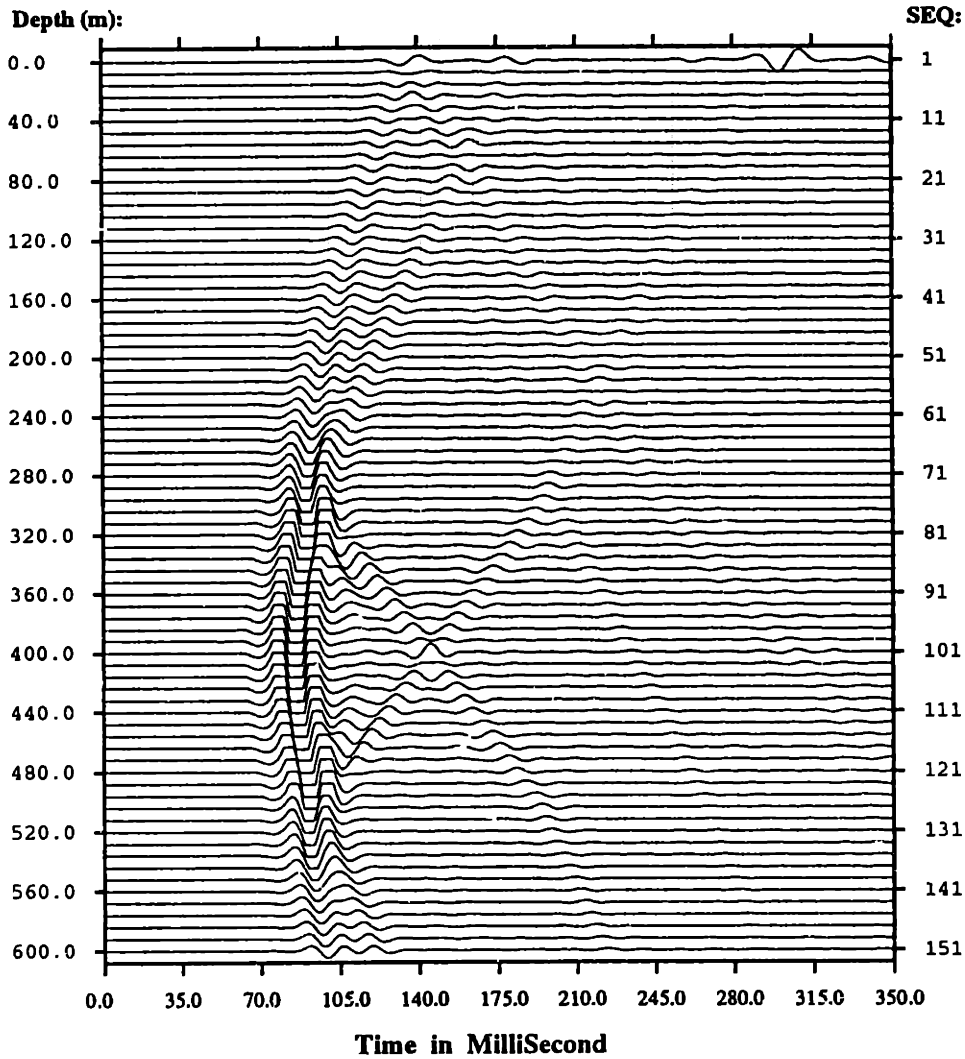

Figure 7-1: Borehole squeeze pressure derived from the synthetic hydrophone data shown in Figure 6-13, using the inverse borehole coupling equation (7.1a). The stress free boundary condition at the top and the rigid boundary condition at the bottom are used to differentiate the hydrophone pressure. The first trace shows some edge effects. Note that the tube waves are eliminated.

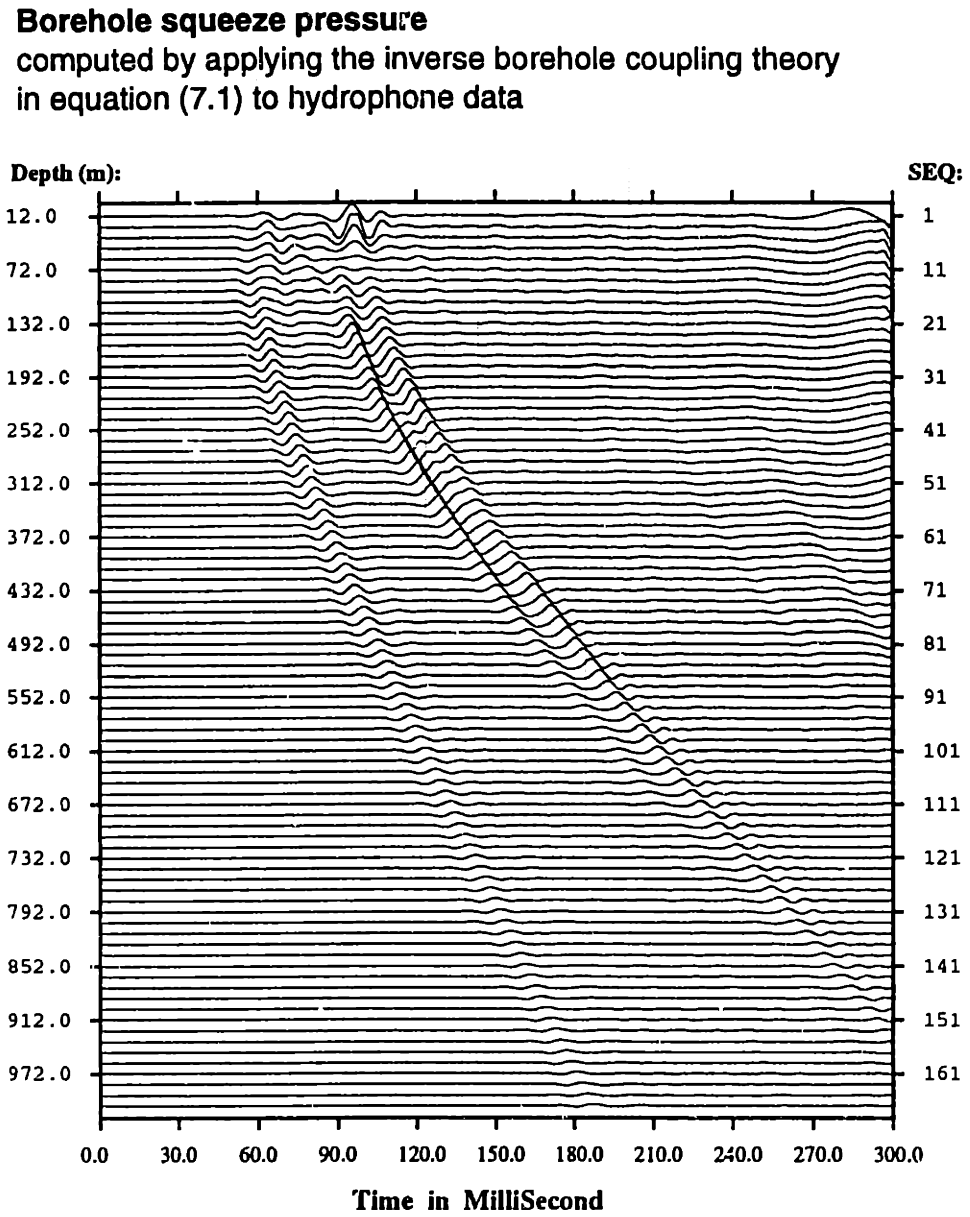

Figure 7-2: Borehole squeeze pressure derived from the synthetic hydrophone data shown in Figure 6-15, using the inverse borehole coupling equation (7.1a). Recall that this data is a simulation of the Kent Cliffs hydrophone VSP measurements at shot point S/P #3. A nonreflecting boundary condition at the top and a rigid boundary condition at the bottom are used in differentiating the hydrophone pressure. The tube waves are obviously attenuated.

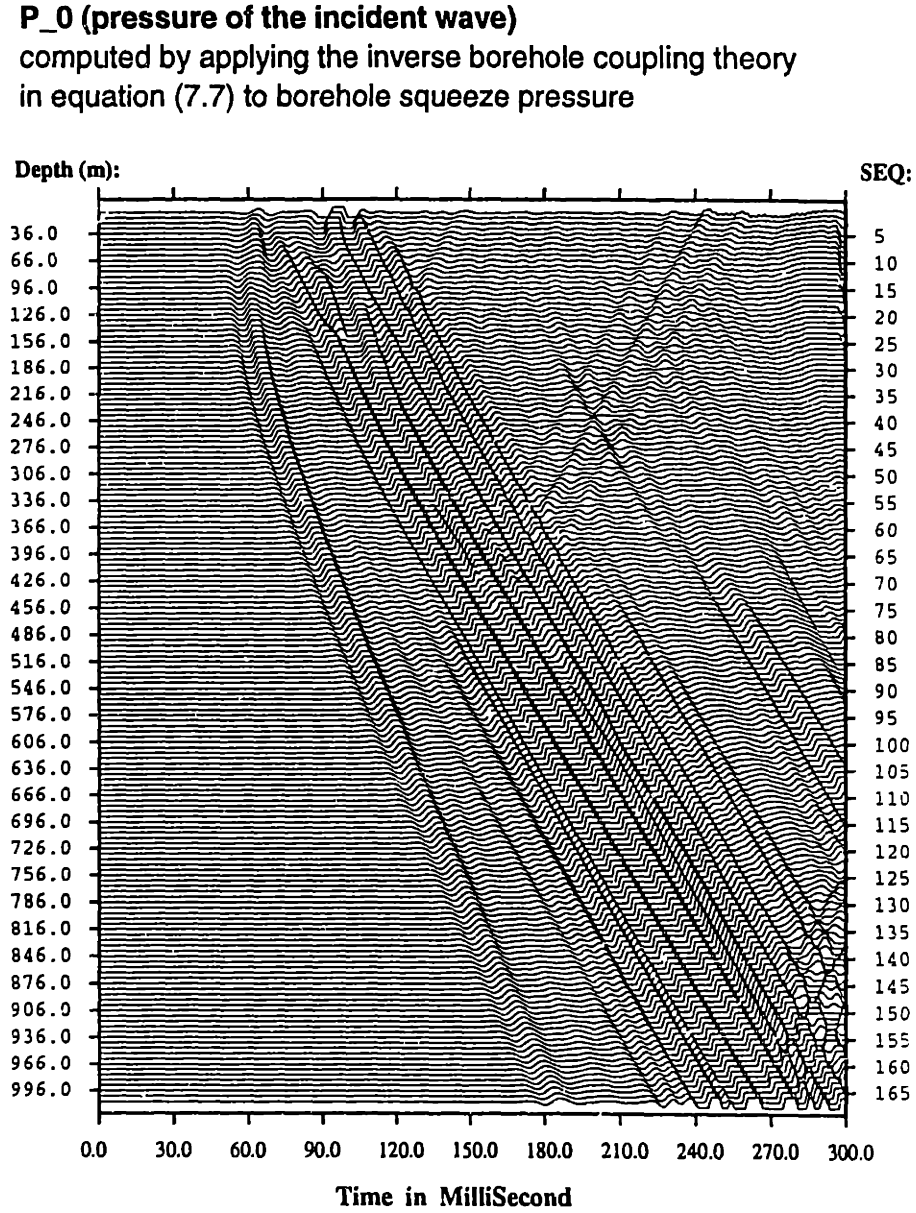

Figure 7-3: Pressure of the incident wave derived from the borehole squeeze pressure shown in Figure 7-2, using the inverse borehole coupling equation (7.7). The first break in this figure is the P-wave arrival. The most energetic events are noises traveling with a speed of γ; these are associated with the poles in the inverse borehole coupling filter. $\epsilon = 0$ is used in the processing.

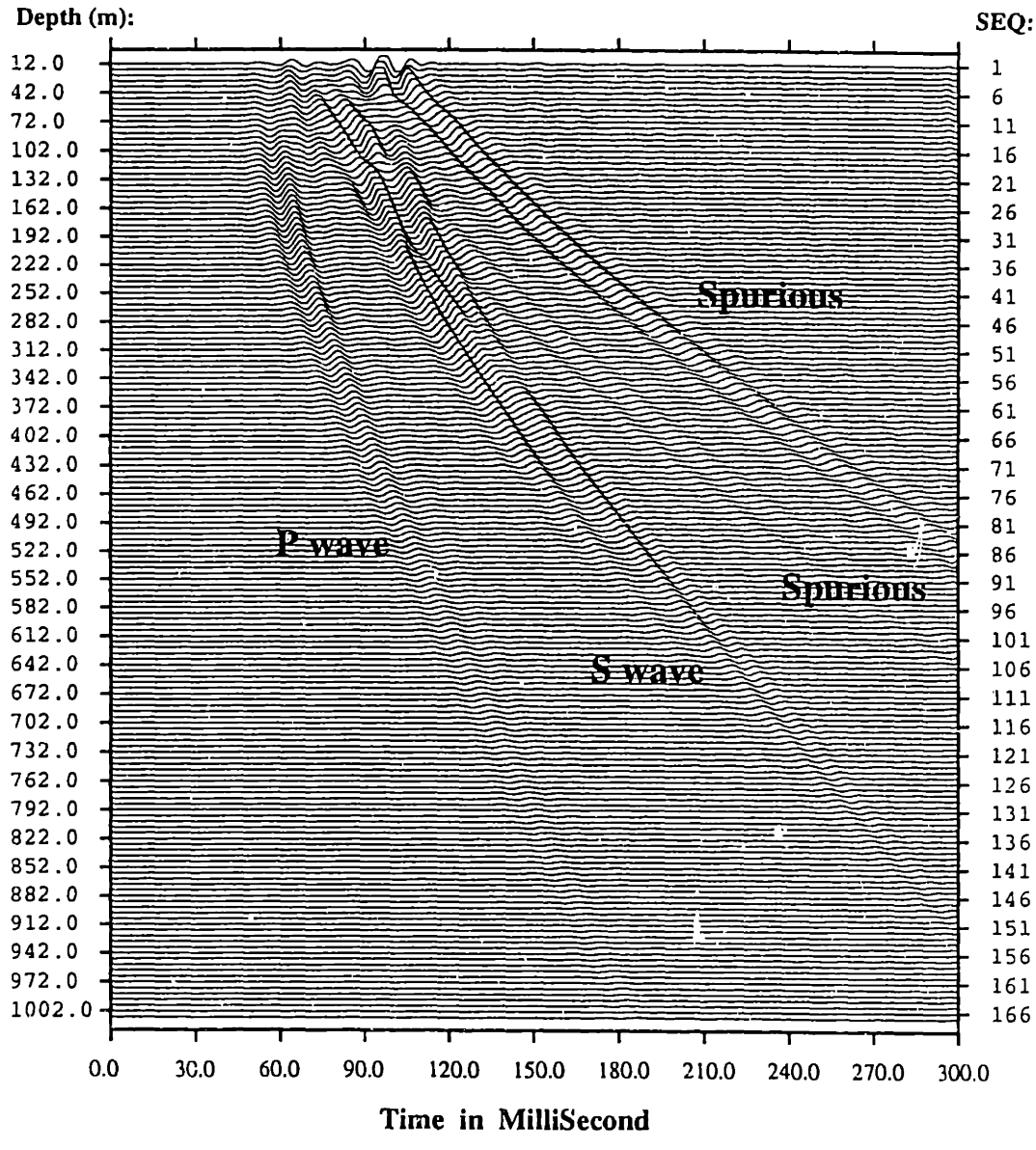

Figure 7-4: Pressure of the incident wave derived from the borehole squeeze pressure shown in Figure 7-2, using the inverse borehole coupling equation (7.7). $\epsilon = 16$ per second is used in the processing. No gain compensation is applied in this figure. The spurious events in Figure 7-4 are greatly reduced.

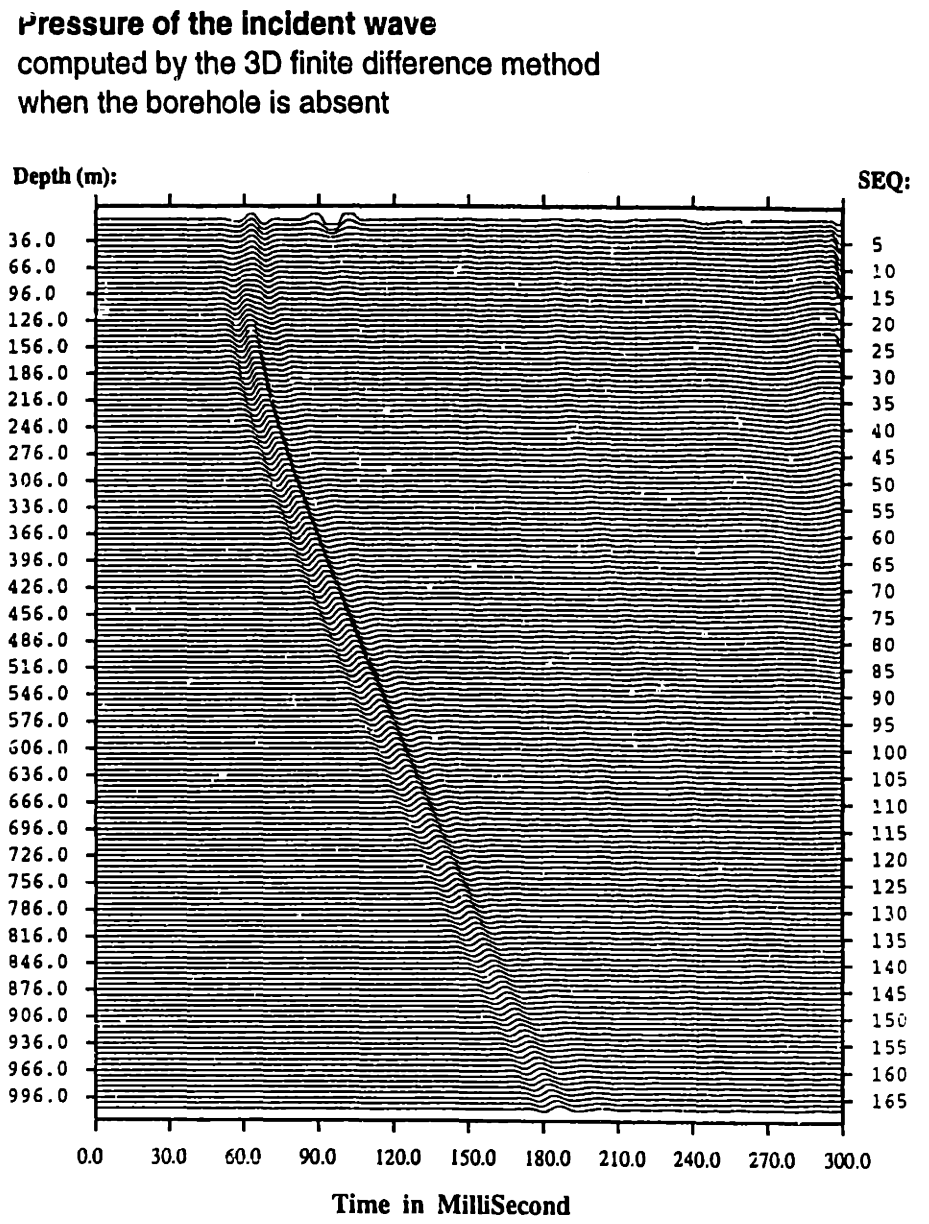

Figure 7-5: Pressure of the incident wave computed by the 3D elastic finite difference method in the absence of the fluid-filled borehole, using the geological model at the Kent Cliffs borehole test site shown in Figure 6-14.

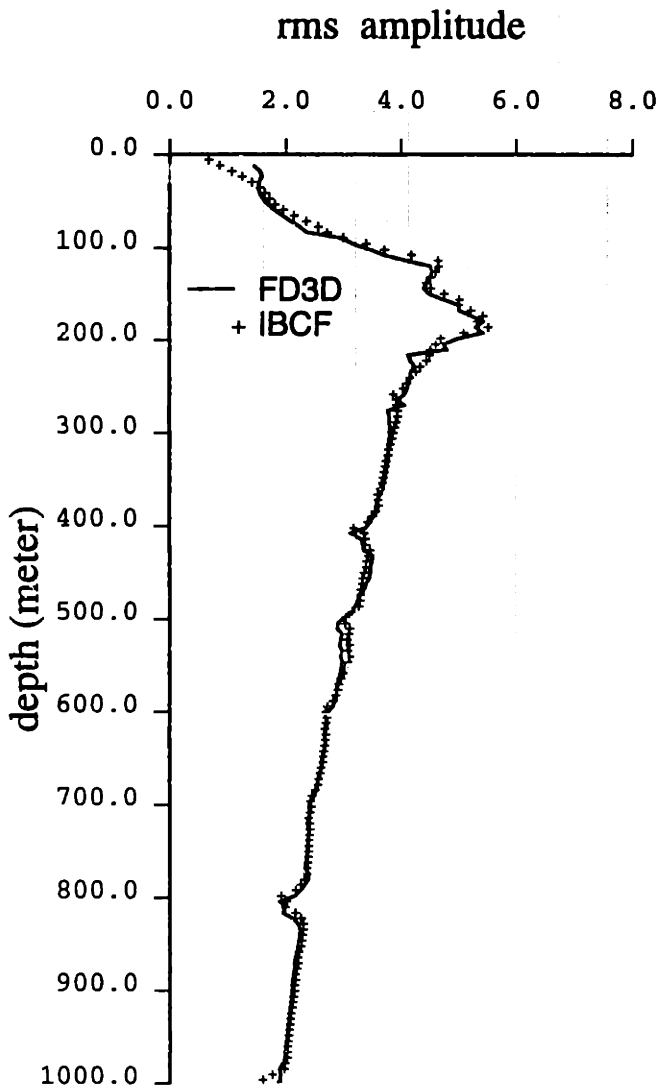

Figure 7-6: RMS (root mean square) amplitudes of the first P-wave arrival in Figure 7-3 and Figure 7-5 as a function of depth. A window of 7.5 ms is used in computing the rms amplitudes. The solid line in this figure is the rms amplitude of the P-wave in Figure 7-5 (labeled as FD3D in the figure). The plus (+) symbols in this figure come from the P-wave in Figure 7-3 (labeled as IBCF in the figure).

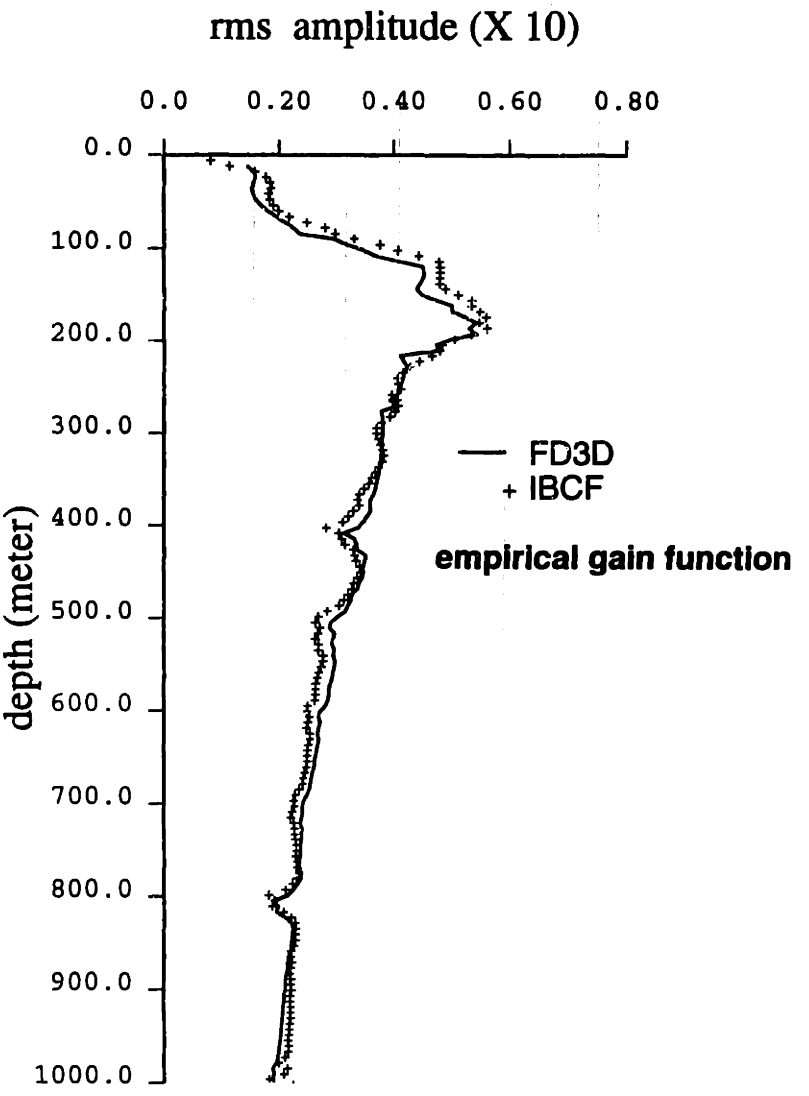

Figure 7-7: RMS (root mean square) amplitude of the first P-wave arrival in Figure 7-4 and Figure 7-5 as a function of depth. A window of 7.5 ms is used to compute the rms amplitudes, and the empirical gain function is applied to the data from Figure 7-4.

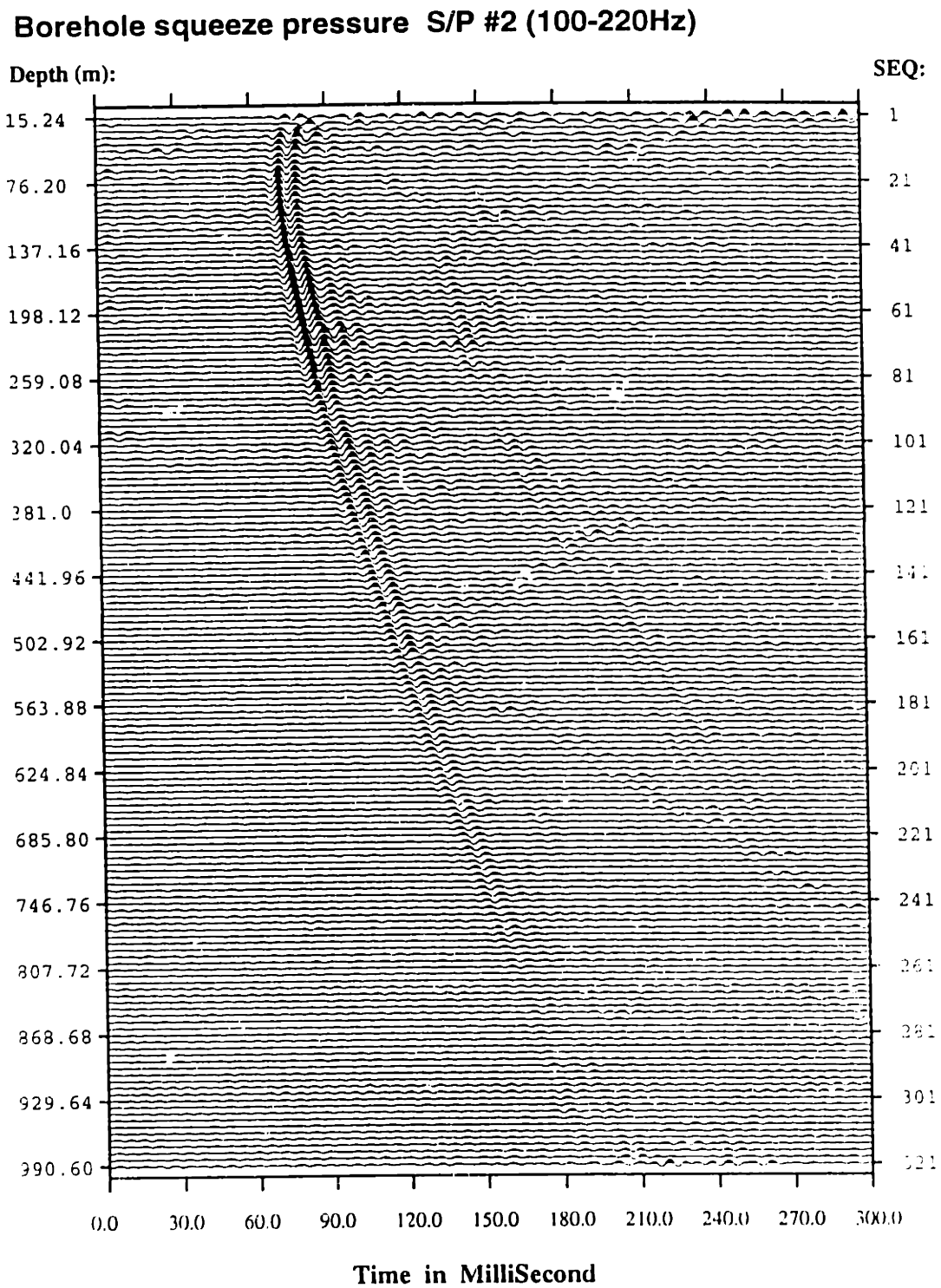

Figure 7-8: Borehole squeeze pressure derived from the Kent Cliffs hydrophone data shown in Figure 5-9, using the inverse borehole coupling equation (7.1a). The non-reflecting boundary condition is applied at both the top and the bottom edges. The tube wave velocity profile is obtained via shear wave sonic logging data using a low frequency formula. The tube waves are greatly attenuated in the borehole squeeze pressure data.

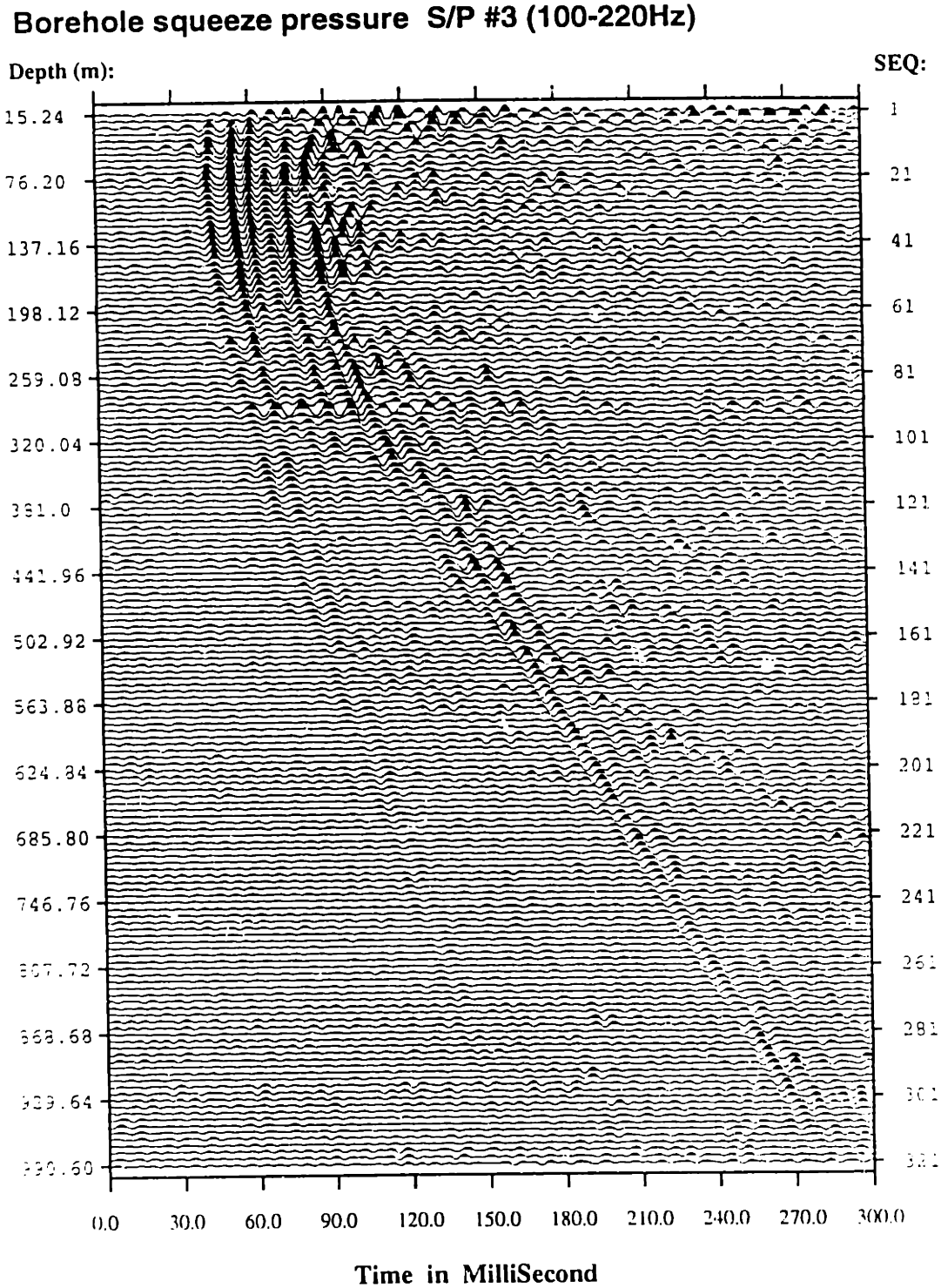

Figure 7-9: Borehole squeeze pressure derived from the Kent Cliffs hydrophone data shown in Figure 5-10, using the inverse borehole coupling equation (7.1a). The non-reflecting boundary condition is applied at both the top and the bottom edges. The tube wave velocity profile is obtained via shear wave sonic logging data using a low frequency formula. The tube waves are greatly attenuated in the borehole squeeze pressure data.

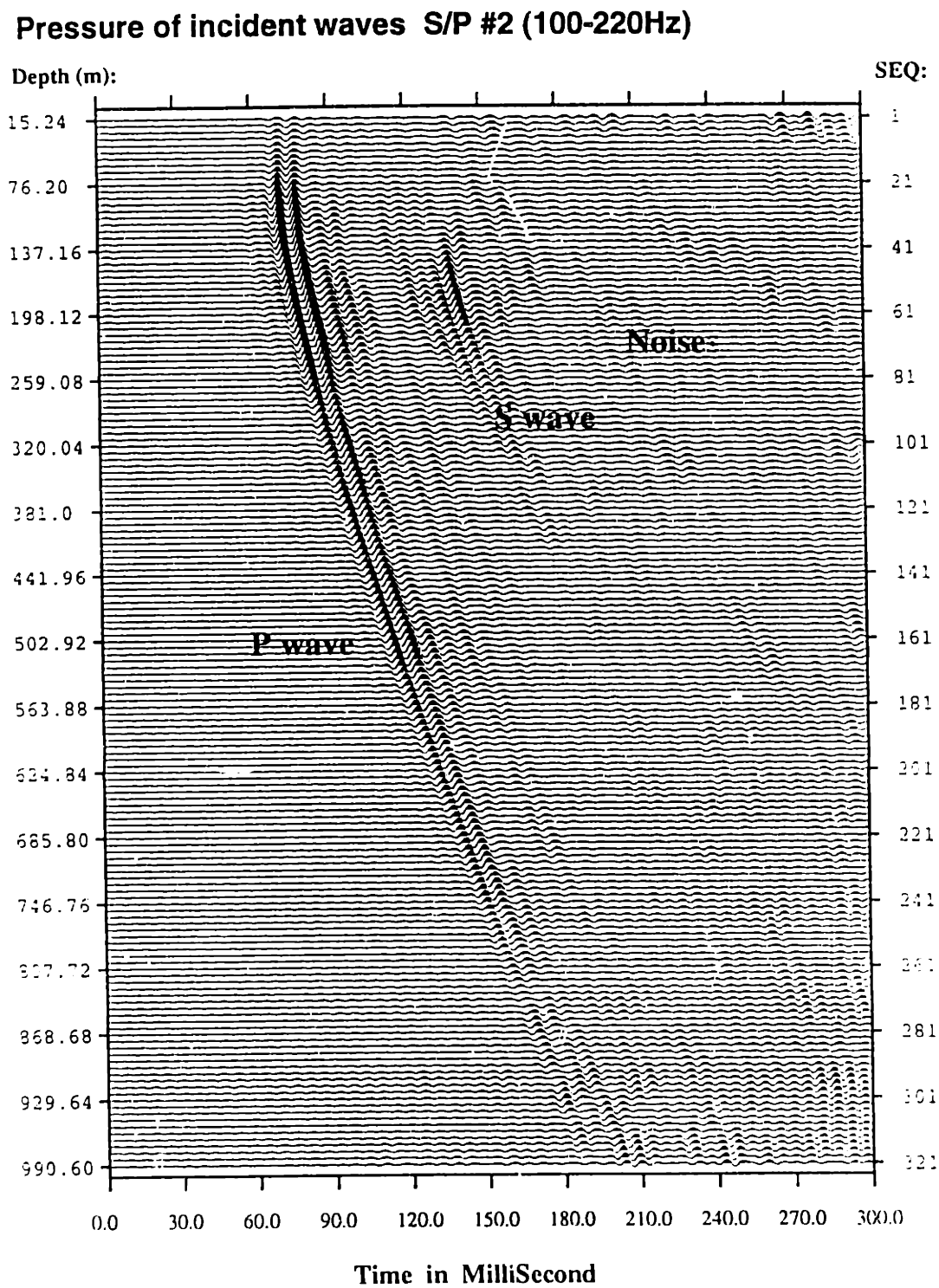

Figure 7-10: Pressure of the incident wave derived from the borehole squeeze pressure shown in Figure 7-8, using the inverse borehole coupling equation (7.7). $\epsilon = 16\ s^{-1}$ is used in the processing, and the empirical gain compensation is applied. An additional F-K filter is also employed to reject the spurious events traveling at much lower velocity than the signals.

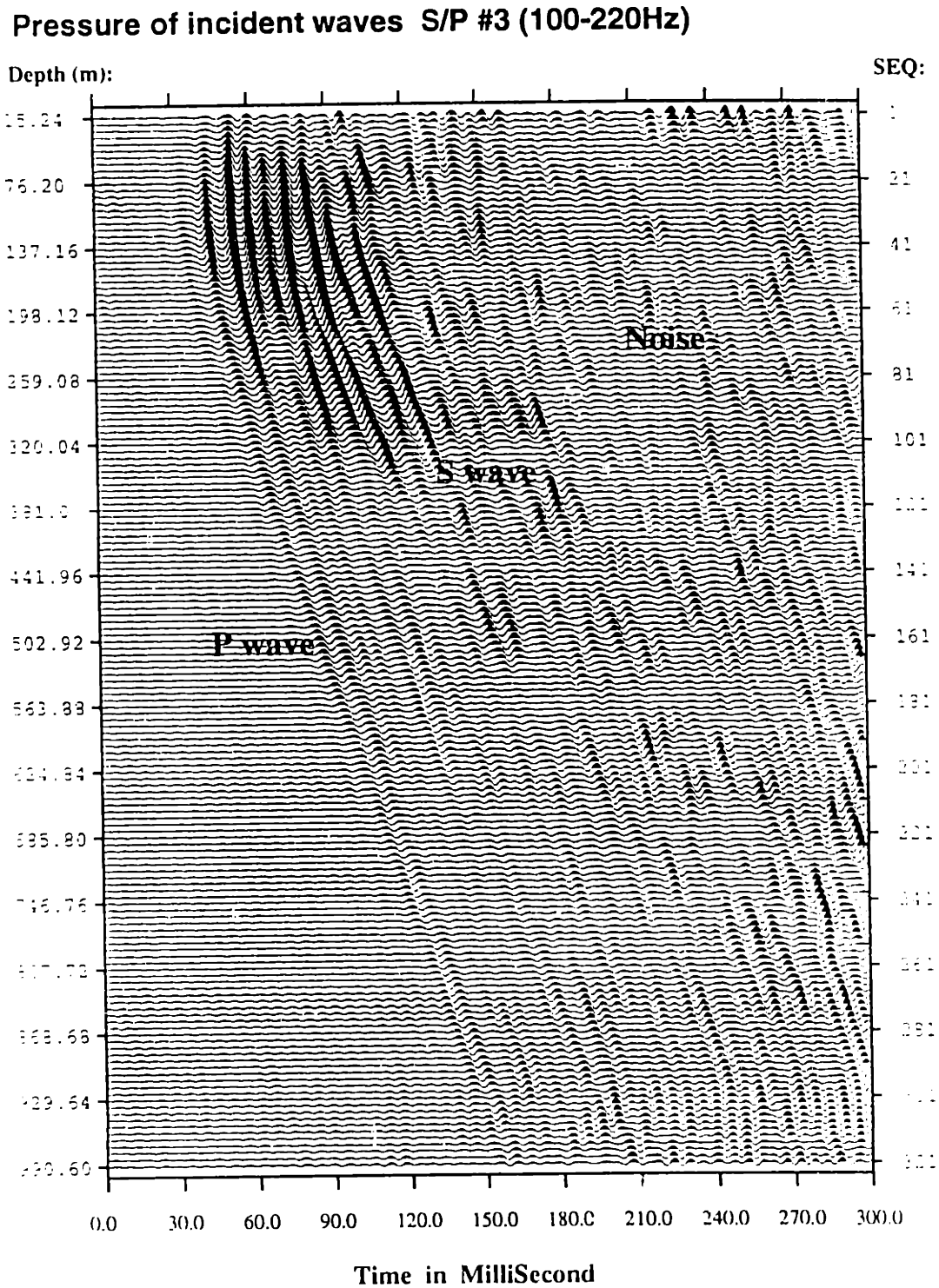

Figure 7-11: Pressure of the incident wave derived from the borehole squeeze pressure shown in Figure 7-9, using the inverse borehole coupling equation (7.7). $\epsilon = 16\ s^{-1}$ is used in the processing, and the empirical gain compensation is applied. An additional F-K filter is also employed to reject the spurious events traveling at much lower velocity than the signals.

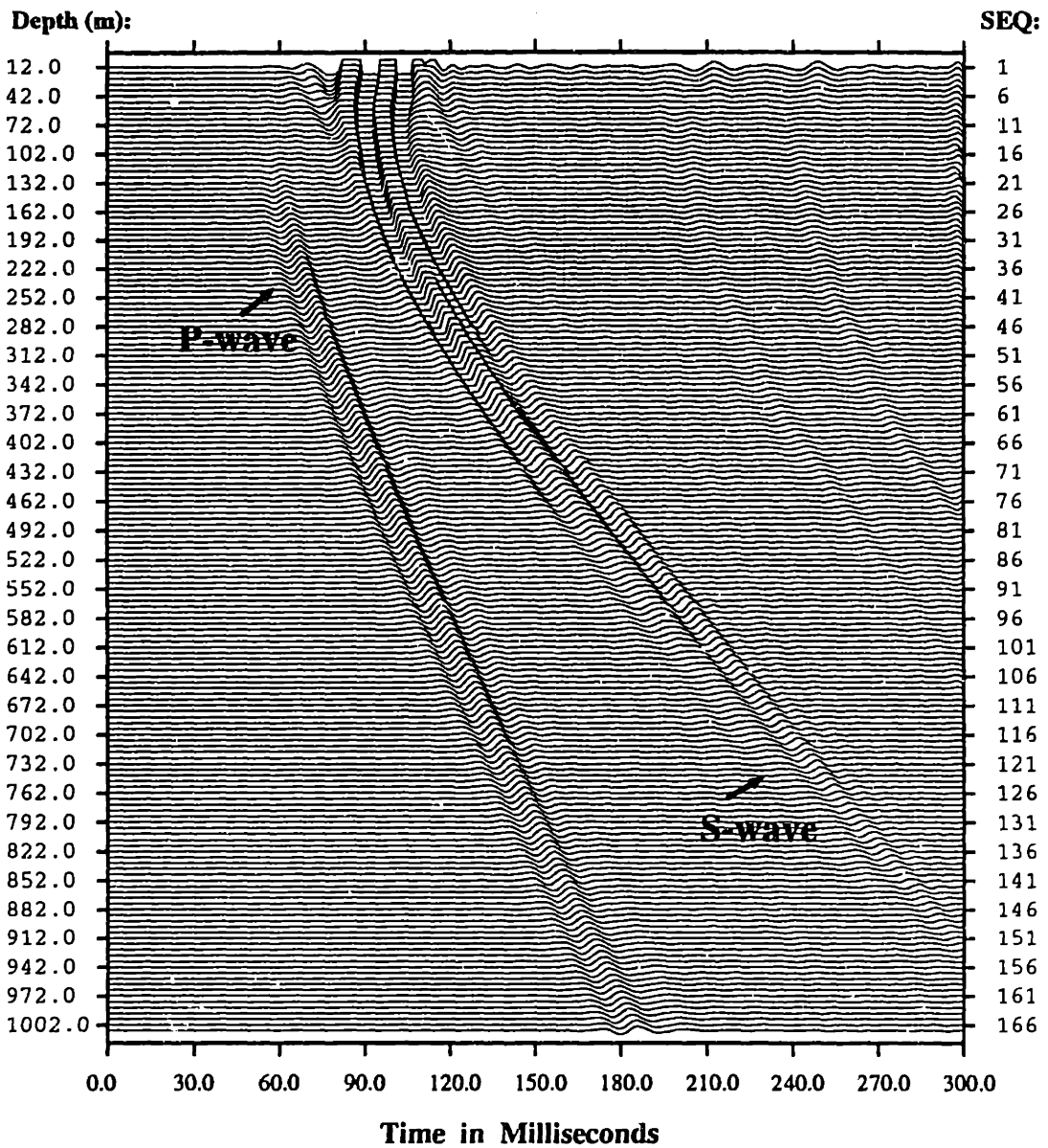

Figure 7-12: Vertical component of particle velocity of the incident wave computed by the 3D elastic finite difference method in the absence of the fluid-filled borehole, using the geological model at the Kent Cliffs borehole test site shown in Figure 6-14.

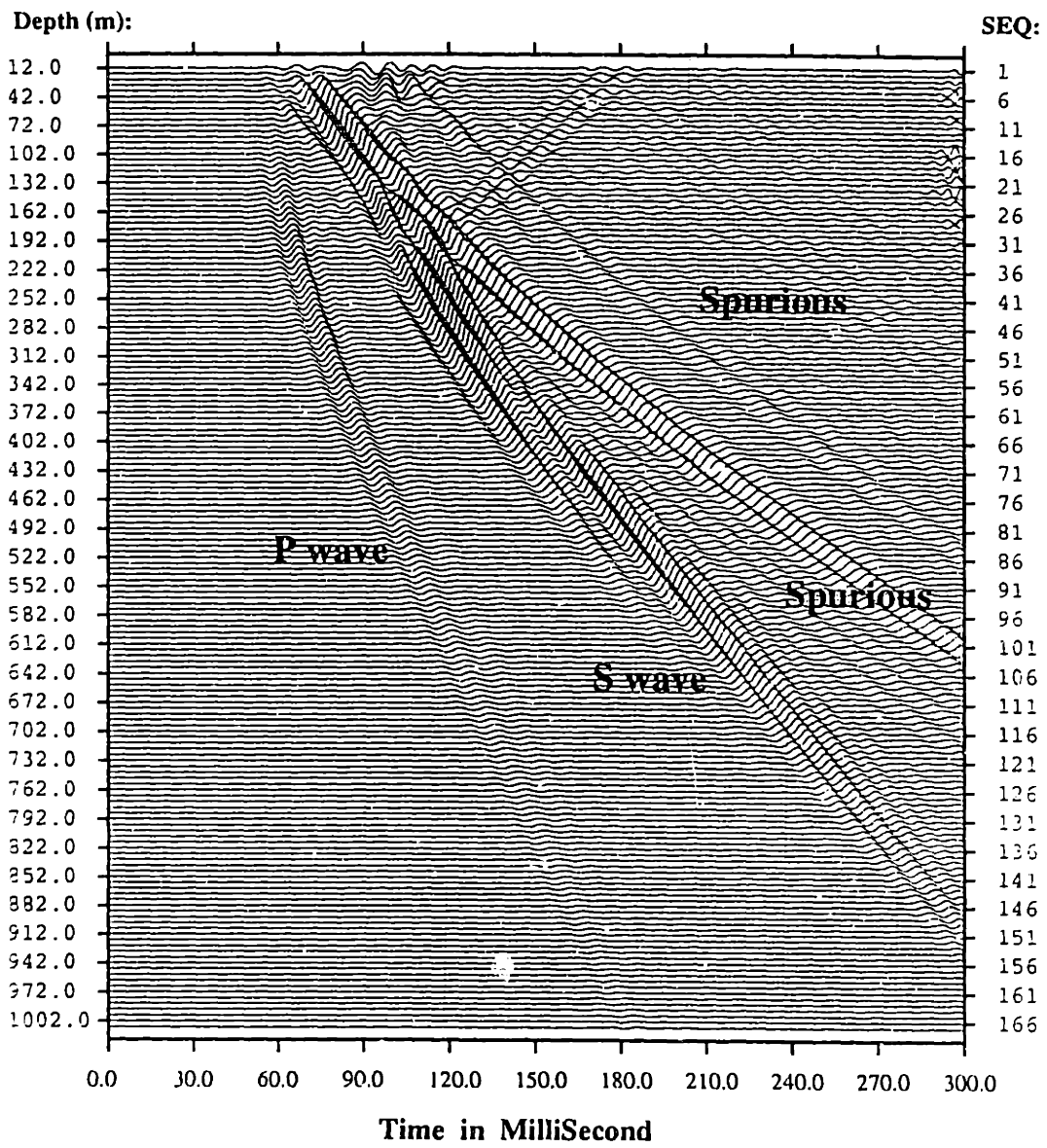

Figure 7-13: Vertical component of particle velocity of the incident wave derived from the borehole squeeze pressure shown in Figure 7-2, using the inverse borehole coupling equation (7.11). $\epsilon = 16\ s^{-1}$ is used in the processing. No gain compensation is applied in this figure. The spurious events are marked.

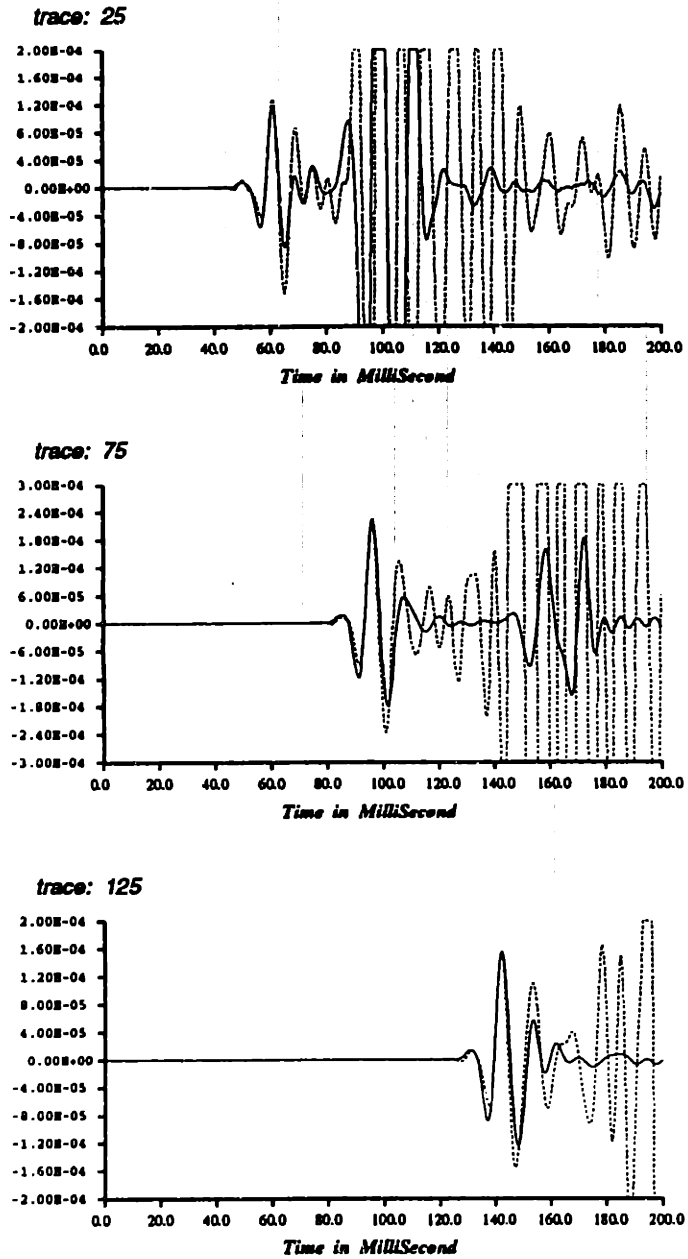

Figure 7-14: Three representative traces in Figure 7-12 are plotted on top of those derived from the hydrophone data via the inverse borehole coupling equations for comparison of the first P-wave arrival in both phase and amplitude. In these figures, the solid lines are the true vertical component of particle velocity of the incident wave. The dashed lines are the estimated vertical components from the hydrophone data using the inverse borehole coupling equations. Strong spurious energies are observable because $\epsilon = 0$ is used in the processing.

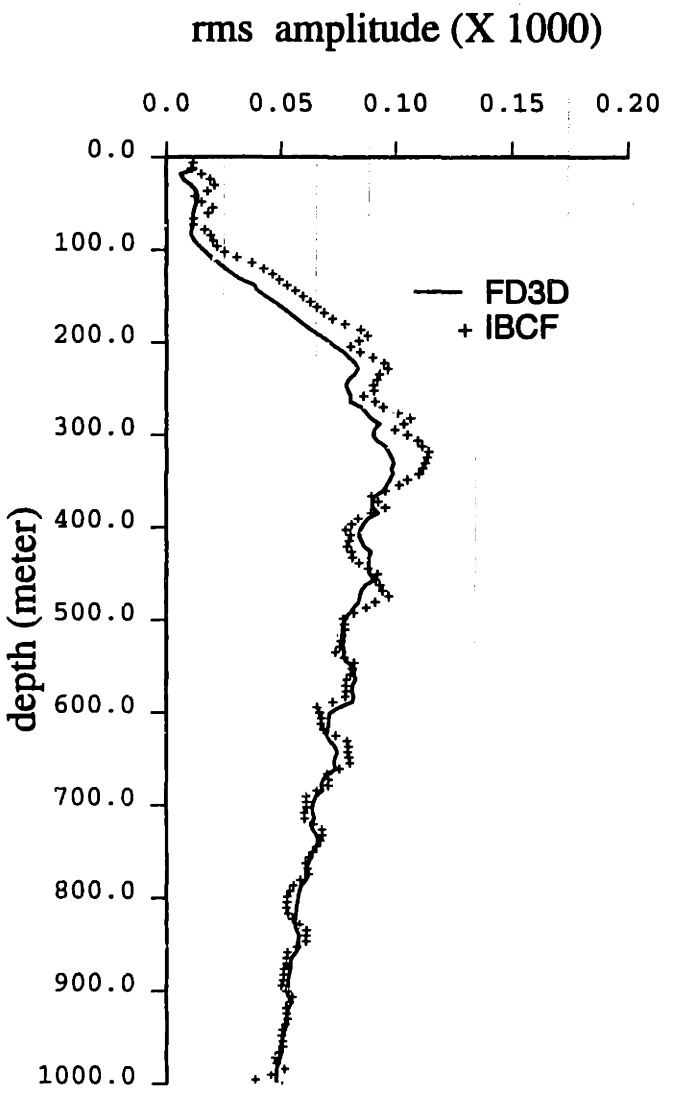

Figure 7-15: RMS (root mean square) amplitude of the first P-wave arrivals in Figure 7-12 and Figure 7-13 ($\epsilon = 0$ is used instead) as a function of depth. A window of 12.5 ms is used in computing the rms amplitudes.

Chapter 8

Summary and Conclusions

In this thesis, a complete and systematic investigation was carried out on the borehole coupling theory, modeling techniques for VSP and crosswell surveys, and downhole hydrophone data processing. By starting with a model of an open borehole in a homogeneous formation, an exact formulation for elastic wave coupling in the fluid-filled borehole, which is valid for all frequencies and all azimuthally symmetric and nonsymmetric components, was given. Plane compressional wave and shear wave incidences were considered. The borehole reception patterns for both the pressure in the fluid and the solid displacement on the borehole wall were computed. The particle motion properties of downhole geophone measurements and the effect of geophone orientation were investigated in detail.

The interaction of an incident elastic wave with a cased borehole was also considered, where both approximate and exact solutions were obtained. The approximate solutions are simple and explicit, and are useful in the study of cased borehole coupling as well as radiation at a low frequency. The exact formulation employs the global matrix method to compute the wave field in each annulus by imposing the continuity of displacements and stresses across annulus boundaries. The cased borehole effects on hydophone and geophone data were extensively studied for both plane P-wave

and S-wave incidences. A laboratory experiment was carried out to demonstrate the resonance phenomena due to a SV-wave incidence from a soft formation.

As a further development, the coupling of an incident elastic wave into a borehole of irregular cross-section was investigated, in order to quantify the effect of borehole irregularity on downhole seismic measurements. The mode-matching method was used to solve the problem in which the Reichel et al. algorithm was incorporated, achieving both accuracy and computational speed. Using this method, we computed the fluid pressure in both elliptical and highly irregular boreholes, as well as the solid displacement in the formation. The method was also applied to calculate the synthetic sonic logging seismograms in an elliptical borehole, where several examples were used to show the cross-mode coupling phenomena associated with a borehole of irregular shape.

Also considered was the case where the fluid-filled borehole was embedded in a stratified formation. A method for computing the pressure in the borehole fluid for a source in the stratified formation was proposed, in which the borehole coupling theory was hybridly combined with the discrete wavenumber–global matrix algorithm. This approach greatly reduces the difficulties of the original problem and yields accurate results at low frequencies (< 2 kHz). Using a stratified geological model for the Kent Cliffs borehole experiment site, we were able to predict, through calculation of the complete synthetic seismograms, the traveltime and RMS amplitude of the hydrophone data.

When the formations adjacent to the borehole were neither homogeneous nor stratified, we developed a method to calculate the pressure in the fluid-filled borehole by cascading the 3-D elastic finite difference formulation with the borehole coupling theory. An optimal absorbing boundary condition was discovered and incorporated into the 3-D finite difference algorithm. This algorithm was parallelized on the massively-parallelized supercomputer nCUBE. Directly including the borehole in the finite difference model is not feasible even for the currently available parallel computer. This

difficulty was circumvented by dividing the whole problem into two parts: propagation from the source to the presumed borehole location by the finite difference method, and coupling into the fluid by applying the borehole coupling equations. With a geological model including dipping formations, this method was used to simulate the Kent Cliffs hydrophone VSP data. The theoretic predictions were indeed improved as compared to the previous modelling with a stratified medium.

The studies on borehole coupling mechanism also lead us to a method of removing the borehole effects from downhole hydrophone data by applying inverse borehole coupling filters. Using this method, the hydrophone VSP and crosswell data were transformed into the borehole squeeze pressures, where the tube waves were effectively eliminated and the P-wave and S-wave were partially compensated for the borehole effects on their amplitudes. A follow-up procedure was then employed to convert the borehole squeeze pressure to either the pressure or the displacement of an incident wave in the formation. The processed data could be directly used as inputs for the imaging and inversion schemes that do not include the receiver borehole in their formulations.

Through these extensive investigations and modeling, we have reached the following conclusions:

- A significant fluid resonance exists in both open and cased boreholes when the formation is very soft (i.e., the formation shear wave velocity is less than the speed of the tube wave) and when the incident wave is of the SV-type. This resonance is associated with the excitation of a tube wave in the fluid. In an open borehole, it only prevails at low frequencies. However, in a cased borehole it is also prominent at a very high frequency because the tube wave velocity is raised well above the formation shear wave speed by the steel pipe.

- Correction of the borehole effects on downhole geophone measurements should be made for frequencies above 500 Hz in the hard formation. In the soft for-

mation, if the angle of incidence differs significantly from the resonance angle for SV-wave incidence, no borehole correction is needed for frequencies below 300 Hz. For downhole experiments with frequency above 1000 Hz, boreholes can significantly alter the particle motion direction, thus data-based horizontal components rotation is unreliable. These findings apply to both open and cased boreholes.

- In a cased borehole, for plane P-wave incidence at low frequencies, the pressure in the fluid vanishes at a particular angle of incidence if the casing thickness exceeds a critical value – the cased borehole screening effect. This behavior prevails in both hard and soft formations. The critical angles for both the fluid resonance and the screening effect are well predicted by simple and explicit formulae.

- In a borehole of irregular cross-section, the pressure in the fluid is sensitive to the irregularity, while the solid displacement in the formation is much less affected. The fluid pressure splits into two distinct branches with the larger one associated with incident waves propagating along the effective minor axis, and the smaller one along the effective major axis. The difference in amplitude is on the order of the borehole ellipticity. If a monopole source is placed at the center of the fluid, dipole motions characteristic of the tube waves are excited; conversely, if a dipole source is used, monopole motions characteristic of the flexural waves are generated. The cross-mode coupling phenomena might be mistakenly attributed to the formation anisotropy if the borehole irregularity effect is not properly taken into account.

- The hybrid method for computing the pressure in a fluid-filled borehole embedded in either a stratified or a heterogeneous formation is accurate and efficient. In the former case, this method incorporates the borehole coupling equations into the discrete wavenumber – global matrix formulation. In the latter case, it combines the 3-D elastic finite difference technique with the borehole coupling theory. Using this method, we are able to predict, both in traveltime and in rms

amplitude, the Kent Cliffs hydrophone VSP data reasonably well. This method is robust in handling open, cased, or partially cased boreholes, and allows for a borehole of finite length.

- The 3-D finite difference technique developed in this thesis offers a powerful tool for modeling elastic wave propagation in a heterogeneous three-dimensional medium. Employing the optimal absorbing boundary condition in the formulation reduces the artificial reflections from boundaries. The discovery of the class of optimal boundary conditions and the methodology in finding them make our work unique.

- The new procedure for hydrophone data processing is based on the borehole coupling mechanism. It consists of three steps using three different techniques. The first step of this procedure greatly attenuates the tube wave and partially compensates the P-wave and S-wave for the borehole effects on their amplitudes. The second and third steps map the borehole squeeze pressure, which is the output of the first step, into the pressure and the displacement of the incident wave in the formation, respectively. This procedure is successfully applied to process the Kent Cliffs hydrophone VSP data.

8.1 Practical Applications and Implications

The results presented in this thesis have many applications and implications relating to the design, processing, and modelling of a downhole seismic experiment. A knowledge of borehole effects on the measurements can be helpful in choosing an appropriate source frequency for the planned experiment and using an appropriate tool (i.e., a downhole geophone or hydrophone) since, depending on the formation properties and the source frequencies, different tools respond to an incident wave differently. If the source frequency is curtailed by the seismic resolution or the size of the object to be explored, it will be important to know to what extent the measure-

ment portrays the incident wave in the formation. At high frequencies, the particle motion direction derived from the measurement may be significantly different from the polarization of the incident wave, implying that the data-based horizontal component rotation is very unreliable and the direction of measured polarization does not coincide with the direction of the incident wave, especially in a cased borehole. Since the borehole acts as an antenna whose response, although being linear, is frequency and wavenumber dependent, an appropriate inverse filter reciprocal to the response function is desirable in the subsequent data processing. However, such an inverse filter is not without a problem: i.e., the very existence of poles suggests that, strictly speaking, the coupling process is irreversible.

The inverse borehole coupling filters developed in this thesis clearly offer a promising way for hydrophone data processing, as is demonstrated with the Kent Cliffs hydrophone VSP data. Such an advancement should promote the downhole data acquisition using a hydrophone where both the cost and the time for surveying are significantly less compared to the borehole experiment using a geophone, excluding the particular applications, e.g., anisotropy analyses, that require 3-component geophone data. It should be pointed out that the transformation from the hydrophone pressure data into the borehole squeeze pressure data is well-posed. The latter is directly associated with the stress field of the incident wave, suggesting that it could be used in full-waveform inversion, diffraction tomography, and true-amplitude migration schemes if these schemes are properly formulated in terms of the borehole squeeze pressure.

The methods for computing the pressure in a receiver borehole are of practical use in the interpretation of the VSP and crosswell data. Through modelling, the events in the observed seismograms are better understood; the interpreted subsurface structures can be justified, improved, or corrected. For a model with stratified formations, the method can be used to simulate VSP and crosswell experiments across large offsets. For application to heterogeneous formations, the method might be restricted to small offsets because of the in-core memory limitation for the 3-D elastic finite difference

computation. These modeling abilities were essentially unavailable previously.

8.2 Future Work

Borehole coupling is a complex problem for many reasons. First of all, it is a 3-D problem of elastic wave propagation, involving a three-dimensional source and a three-dimensional medium (e.g., a vertical interface corresponding to the borehole/formation boundary in addition to a few horizontal interfaces in the formation). The second complication arises from the scale difference between the seismic wavelength and the borehole diameter, which inhibits any grid-based numerical method for a complete solution. Since the problem is nonsymmetric, the measurement using a geophone will also depend on the tool location on the borehole wall, which is unknown in a downhole survey due to cable twisting and tool rotation. This complicates later data processing and interpretation. If the elastic anisotropy of the formation is also taken into account, the problem might be beyond the reach of our present means of analyses.

The method we have developed in this thesis for hydrophone data modeling employs a low frequency approximation, requiring a seismic wavelength at least ten times larger than the borehole diameter. For a formation of predominantly crystalline rock, it might not be a problem for borehole seismic experiments whose frequences are on the order of one kilohertz or less. However, in very soft sediments and for a high frequency experiment, this method might yield erroneous results for shear waves. Obviously, a computationally feasible method accurate at high frequencies would be the goal of future research.

In a crosswell seismic survey, two boreholes are involved in the data acquisition: one acts as the source borehole, the other as the receiver borehole. Both the radiation into the elastic formation emanating from a downhole source and the coupling of an

impinging elastic wave into the borehole fluid need to be taken into account, in order to model the crosswell data set. The radiation problem has been well studied by Meredith (1990), Gibson (1993), and others for a borehole in a homogeneous formation, and by Dong et al. (1992) and Bouchon (1993) for a borehole in a vertically stratified medium. Including these excellent research results in the modeling code developed in this thesis will be a topic of on-going research.

As far as the data processing for removing the effects of a borehole is concerned, difficulties still exist for downhole seismic data at high frequencies. An inverse borehole coupling filter that is dependent on tool location is necessary in this case, since at high frequencies, the pressure in the fluid and the solid displacement on the borehole wall are functions of the tool location. In addition, this filter is a complicated function of frequency, wavenumber, and borehole radius, in which evaluations of the Bessel functions are involved. Nevertheless, these difficulties can be overcome if information about the tool position is available.

Bibliography

Abramowitz, M. and I. A. Stegun, *Handbook of mathematical functions,* Dover Publication Inc., New York, 1965.

Aki, K. and P. G. Richards, *Quantitative seismology: theory and methods, volume 1,* W.H. Freeman and Company, New York, 1980.

Albright, J. N. and P. A. Johnson, Cross-borehole observation of mode conversion from borehole Stoneley waves to channel waves at a coal layer, *Geophys. Prosp., 38,* 607–620, 1990.

Aminzadeh, F., Applications of elastic modeling in processing and interpretation of VSP data: a case study, *Geophys. Prosp., 37,* 893–906, 1989.

Baker, L. J., Hypercube performance for 2-D seismic finite difference modeling, in *The 3rd conference on hypercube concurrent computers and application,* pp. 1146–1156, 1988.

Balch, A. and M. N. Lee, *Vertical seismic profiling technique, applications, and case histories,* D. Reidel, 1984.

Bamberger, A., B. Engquist, L. Halpern, and P. Joly, Higher order paraxial wave equation approximations in heterogeneous media, *SIAM J. Appl. Math, 48,* 129–154, 1988.

Bellman, R., *Introduction to matrix computation,* McGraw-Hill, New York, 1969.

Ben-Menahem, A. and S. Kostek, The equivalent force system of a monopole source in a fluid-filled open borehole, *Geophysics, 56,* 1477–1481, 1991.

Ben-Menahem, A. and S. J. Singh, *Seismic waves and sources,* Springer-Verlag, New York, 1981.

Beydoun, W. B., C. H. Cheng, and M. N. Toksöz, Detection of open fractures with vertical seismic profiling, *J. Geophys. Res., 90,* 4557–4566, 1985.

Beydoun, W. B., Tube wave filtering from pressure-particle velocity measurements, in *Vertical Seismic Profiling: 14B, M. N. Toksöz and R. R. Stewart (ed.),* pp. 302–314, Geophysical Press, 1984.

Biot, M., Propagation of elastic waves in a cylindrical borehole containing a fluid, *J. Appl. Phys., 23,* 997–1009, 1952.

Blair, D. P., Rise times of attenuated seismic pulse detected in both empty and fluid-filled cylindrical boreholes, *Geophysics, 49,* 398–410, 1984.

Bleistein, N., On the imaging of reflectors in the earth, *Geophysics, 52,* 931–942, 1987.

Bouchon, M. and K. Aki, Discrete wavenumber representation of seismic-source wave fields, *Bull. Seis. Soc. Am., 67,* 259–277, 1977.

Bouchon, M., A simple method to calculate Green's function for elastic layered media, *Bull. Seis. Soc. Am., 71,* 959–971, 1981.

Bouchon, M., A numerical simulation of the acoustic and elastic wavefields radiated by a source on a fluid-filled borehole embedded in a layered medium, *Geophysics, 58,* 475–481, 1993.

Bregman, N. D., R. C. Bailey, and C. H. Chapman, Crosshole seismic tomography, *Geophysics, 54,* 200–215, 1989.

Cao, D., W. B. Beydoun, S. C. Singh, and A. Tarantola, A simultaneous inversion for background velocity and impedance maps, *Geophysics, 55,* 458–469, 1990.

Carcione, J. M., D. Kosloff, A. Behle, and G. Serian, A spectral scheme for wave propagation simulation in 3-D elastic-anisotropic media, *Geophysics, 57,* 1593–1607, 1992.

Castagna, J. P., Petrophysical imaging using AVO, *The Leading Edge, 12,* 172–178, 1993.

Cerjan, C., D. Kosloff, R. Kosloff, and M. Reshef, A nonreflecting boundary condition for discrete acoustic and elastic wave equations, *Geophysics, 50,* 705–708, 1985.

Charrette, E. E., *Elastic wave scattering in laterally inhomogeneous media,* PhD thesis, M.I.T., Cambridge, Massachusetts, 1991.

Cheng, C. H. and M. N. Toksöz, Elastic wave propagation in a fluid-filled borehole and synthetic acoustic logs, *Geophysics, 46,* 1042–1053, 1981.

Cheng, N., Z. Zhu, C. H. Cheng, and M. N. Toksöz, Experimental and finite difference modeling of borehole Mach waves, submitted to Geophys. Prosp., 1992.

Chin, R. C. Y., G. W. Hedstrom, and L. Thigpen, Matrix methods in synthetic seismograms, *Geophys. J. R. Astr. Soc., 77,* 483–502, 1984.

Cicerone, R. D., *Detection and characterization of in-situ fractures in the Earth from vertical seismic profiling data,* PhD thesis, M.I.T., Cambridge, Massachusetts, 1991.

Claerbout, J. F., *Imaging the Earth's interior,* Blackwell Scientific Publications, Boston, 1985.

Clayton, R. and B. Engquist, Absorbing boundary conditions for acoustic and elastic wave equations, *Bull. Seis. Soc. Am., 67,* 1529–1540, 1977.

Clayton, R. and R. H. Stolt, A Born WKBJ inversion method for acoustic reflection data, *Geophysics, 46,* 1559–1567, 1981.

Cormier, V. F. and M. H. Mullen, Application of asymptotic ray theory to synthetic vertical seismic profiling, in *Vertical Seismic Profiling: 14B, M. N. Toksöz and R. R. Stewart (ed.),* pp. 28–44, Geophysical Press, 1984.

Crase, E., C. Wideman, M. Noble, and A. Tarantola, Nonlinear elastic inversion of land seismic reflection data, *J. Geophys. Res., 97,* 4685–4705, 1992.

Dart, R. L. and M. L. Zoback, Wellbore breakout stress analysis within the central and eastern continental United States, *The Log Analyst, 30,* 12–25, 1989.

Devaney, A. J., Geophysical diffraction tomography, *IEEE Transactions on Geoscience and Remote Sensing, 22,* 3–13, 1984.

Dickey, J. W. and H. Überall, Surface wave resonances in sound scattering from elastic cylinders, *J. Acoust. Soc. Am., 63,* 319–320, 1978.

Dietrich. M. and M. Bouchon, Synthetic vertical seismic profiles in elastic media, *Geophysics, 50,* 224–234, 1985.

DiSiena, J., B. Byan, J. Fix, and J. Gaiser, F-K analysis and tube wave filtering, in *Vertical Seismic Profiling: 14B, M. N. Toksöz and R. R. Stewart (ed.)*, pp. 288–301, Geophysical Press, 1984.

Dong, W., M. Bouchon, and M. N. Toksöz, Modeling downhole source radiation by boundary element and discrete wave number method, in *62th Ann. Internat. Mtg., Soc. Expl. Geophys., Expanded Abstracts*, pp. 1337–1340, 1992.

Du Toit, C. F., The numerical computation of Bessel functions of the first and second kind for integer orders and complex arguments, *IEEE Trans. Antena and Propagation, 38*, 1341–1349, 1990.

Du Toit, C. F., Evaluation of some algorithms and programs for the computation of integer-order Bessel functions of the first and second kind with complex arguments, *IEEE Antennas and Propagation Magazine, 35*, 19–25, 1993.

Dunkin, J. W., Computation of modal solutions in layered, elastic media at high frequencies, *Bull. Seis. Soc. Am., 55*, 335–358, 1965.

Ellefsen, K. J., *Elastic wave propagation along a borehole in an anisotropic medium*, PhD thesis, M.I.T., Cambridge, Massachusetts, 1990.

Emerman, S. H. and R. A. Stephen, Comment on absorbing boundary conditions for acoustic and elastic wave equations by Clayton and Engquist, *Bull. Seis. Soc. Am., 73*, 661–665, 1983.

Esmersoy, C., Polarization analysis, rotation and velocity estimation in three component VSP, in *Vertical Seismic Profiling: 14B, M. N. Toksöz and R. R. Stewart (ed.)*, pp. 236–255, Geophysical Press, 1984.

Ewing, W. M., W. S. Jardetzky, and F. Press, *Elastic waves in layered media*, McGraw-Hill, New York, 1957.

Flax, L. and W. G. Neubauer, Acoustic reflection from layered elastic absorptive cylinders, *J. Acoust. Soc. Am., 61*, 307–312, 1977.

Fokkema, J. T. and P. M. van den Berg, *Seismic applications of acoustic reciprocity*, Elsevier, Amsterdam, 1993.

Fornberg, B., The pseudospectral method: comparisons with finite differences for the elastic wave equation, *Geophysics, 52,* 483–501, 1987.

Fox, G., M. Johnson, G. Lyzenga, S. Otto, J. Salmon, and D. Walker, *Solving problems on concurrent processors, vol. I,* Prentice Hall, Englewood Cliffs, New Jersey, 1988.

Gaunaurd, G. C. and H. Überall, Theory of resonant scattering from spherical cavities in elastic and viscoelastic media, *J. Acoust. Soc. Am., 63,* 1699–1721, 1978.

Gibson, R. L. and C. Peng, Low and high frequency radiation from seismic sources in cased boreholes, submitted to Geophysics, 1993.

Gibson, R. L., Radiation from seismic sources in cased and cemented boreholes, submitted to Geophysics, 1993.

Greenfield, R. J., Seismic radiation from a point source on the surface of a cylindrical cavity, *Geophysics, 43,* 1071–1082, 1978.

Grenander, U. and G. Szego, *Toeplitz forms and their applications,* Chelsea Publishing Company, New York, 1984.

Hardge, B. A., An examination of tube wave noise in vertical seismic profiling data, *Geophysics, 46,* 892–903, 1981.

Harkrider, D. G., Surface waves in multilayered elastic media I. Rayleigh and Love waves from buried sources in a multilayered elastic halfspace, *Bull. Seis. Soc. Am., 54,* 627–679, 1964.

Harris, J. M., Cross-well seismic measurements in sedimentary rocks, in *58th Ann. Internat. Mtg., Soc. Expl. Geophys., Expanded abstracts,* pp. 147–150, 1988.

Hatchell, P. J. and C. S. Cowles, Flexural borehole modes and measurement of shear-wave azimuthal anisotropy, in *62th Ann. Internat. Mtg., Soc. Expl. Geophys., Expanded abstracts,* pp. 201–204, 1992.

Heelan, P., *The theory of head wave propagation along a plane interface separating two solid media,* PhD thesis, University of St. Louis, 1952.

Heelan, P., Radiation from a cylindrical source of finite length, *Geophysics, 18,* 685–696, 1953.

Higdon, R. L., Absorbing boundary conditions for difference approximations to the multi-dimensional wave equation, *Math. Comp., 47,* 437–459, 1986.

Higdon, R. L., Radiation boundary conditions for elastic wave propagation, *SIAM J. Numerical Analysis, 27,* 831–870, 1990.

Higdon, R. L., Absorbing boundary conditions for elastic waves, *Geophysics, 56,* 231–241, 1991.

Hilchie, D. W., Caliper logging–theory and practice, *The Log Analyst, 9,* 3–12, 1968.

Huang, C. F. and J. A. Hunter, The correlation of 'tube wave' events with open fractures in fluid-filled boreholes, in *Current Research, Part A,* pp. 361–376, Geol. Surv. Can., 1981.

Kagansky, A. and D. Loewenthal, Estimation of a point source wavelet in elastic media, *Geophysics, 58,* 1195–1199, 1993.

Kawase, H., Time-domain response of a semicircular canyon for incident SV, P and Rayleigh waves calculated by the discrete wavenumber boundary element method, *Bull. Seis. Soc. Am., 78,* 1415–1437, 1988.

Kennett, B. L. N. and N. J. Kerry, Seismic waves in a stratified halfspace, *Geophys. J. R. Astr. Soc., 57,* 557–583, 1979.

Kostek, S., *Linear and nonlinear wave propagation in a fluid-filled borehole,* PhD thesis, M.I.T., Cambridge, Massachusetts, 1993.

Krohn, C. E., Cross-well continuity logging using guided seismic waves, *The Leading Edge, July,* 39–45, 1992.

Kurkjian, A. L., H. Schmidt, J. E. White, C. Chouzenoux, and T. L. Marzetta, Numerical modeling of cross well seismic monopole sensor data, in *62th Ann. Internat. Mtg., Soc. Expl. Geophys., Expanded abstracts,* pp. 141–144, 1992.

Kurkjian, A. L., Numerical computation of individual far-field arrivals excited by an acoustic source in a borehole, *Geophysics, 50,* 852–866, 1985.

Lee, M. N. and A. Balch, Theoretical seismic wave radiation from a fluid-filled borehole, *Geophysics, 47,* 1308–1314, 1982.

Lee, M. N., Particle displacement on the wall of a borehole from incident plane wave, *Geophysics, 52,* 1290–1296, 1987.

Lee, J. M., *In situ seismic anisotropy and its relationship to crack and rock fabrics,* PhD thesis, the Pennsylvania State University, 1990.

Levander, A. R., Fourth-order finite difference P-SV seismograms, *Geophysics, 53,* 1425–1436, 1988.

Liao, Z. P., H. L. Wong, B. P. Yang, and Y. F. Yuan, A transmitting boundary for transient wave analysis, *Scintia Sinica (Series A), 27,* 1063–1076, 1984.

Lindman, E. L., Free-space boundary conditions for the time dependent wave equation, *J. Comput Phys., 18,* 66–78, 1975.

Liu, H. and C. J. Randall, Synthetic waveforms in noncircular boreholes using a boundary integral equation method, in *61th Ann. Internat. Mtg., Soc. Expl. Geophys., Expanded Abstracts,* pp. 843–845, 1991.

Love, A. E. H., *A treatise on the mathematical theory of elasticity,* Dover Publications, New York, 1944.

Lovell, J. R. and B. E. Hornby, Borehole coupling at sonic frequencies, *Geophysics, 55,* 806–814, 1990.

Mahrer, K. D., An empirical study of instability and improvement of absorbing boundary conditions for the elastic wave equation, *Geophysics, 51,* 1499–1501, 1986.

Mandal, B. and B. J. Mitchell, Complete seismogram synthesis for transversely isotropic media, *J. Geophys., 59,* 149–156, 1986.

Marzetta, T. L. and M. Schoenberg, Tube waves in cased boreholes, in *55th Ann. Internat. Mtg., Soc. Expl. Geophys., Expanded Abstracts,* pp. 34–36, 1985.

Marzetta, T, L., M. Orton, A. Krampe, L. K. Johnston, and P. C. Wuenschel, A hydrophone vertical seismic profiling experiment, *Geophysics, 53,* 1437–1444, 1988.

Marzetta, T. L., Inverse borehole coupling theory and its application to hydrophone vertical seismic profiling, in *62th Ann. Internat. Mtg., Soc. Expl. Geophys., Expanded Abstracts,* pp. 145–147, 1992.

Matarese, J. R., *Nonlinear traveltime tomography,* PhD thesis, M.I.T., Cambridge, Massachusetts, 1993.

McClellan, J. H., T. W. Parks, and L. R. Rabiner, A computer program for designing optimum FIR linear phase digital filters, *IEEE Trans. Audio and Electroacoustics, AU-21,* 506–526, 1973.

McMechan, G. A., Synthetic finite-offset vertical seismic profiling for laterally varying media, *Geophysics, 50,* 627–636, 1985.

Meredith, J. A., *Numerical and analytical modeling of downhole seismic sources: the near and far field,* PhD thesis, M.I.T., Cambridge, Massachusetts, 1990.

Mora, P., Elastic wavefield inversion of reflection and transmission data, *Geophysics, 53,* 750–759, 1988.

Mora, P., The seismic simulation project, in *Institute de Physique du Globe de Paris, annual report,* 1992.

Morse, P. and H. Feshbach, *Methods of theoretical physics, Part I,* McGraw-Hill, New York, 1953.

Norris, A., The speed of a tube wave, *J. Acoust. Soc. Am., 87,* 414–417, 1990.

Okuno, Y., The mode-matching method, in *Analysis Methods for Electromagnetic Wave Propagation,* edited by Yamashita, E., Artech House Inc., Norwood, Massachusetts, 1990.

Oppenheim, A. V. and R. W. Schafer, *Discrete-time signal processing,* Prentice Hall, Englewood Cliffs, New Jersey, 1989.

Ostrander, J., Plane-wave reflection coefficients for gas sands at non-normal angles of incidence, *Geophysics, 49,* 1637–1648, 1984.

Paillet, F. L. and C. H. Cheng, *Acoustic waves in boreholes–the theory and application of acoustic full-waveform logs,* CRC Press, 1991.

Peng, C. and M. N. Toksöz, Optimal absorbing boundary conditions for finite difference modelings of acoustic and elastic wave propagation, J. Acoust. Soc. Am., in press.

Peng, C., C. H. Cheng, and M. N. Toksöz, Borehole effect on downhole seismic measurements, *Geophys. Prosp., 41,* 883–912, 1993a.

Peng, C., C. H. Cheng, and M. N. Toksöz, Cased borehole effect on downhole seismic measurements, in *Expanded Abstracts, 55th EAEG annual meeting, Stavager, Norway,* 1993b, C054.

Peng, C., C. H. Cheng, and M. N. Toksöz, Cased borehole effects on downhole seismic measurements, in *Borehole Acoustics and Logging Consortium Annual Report,* pp. 137–214, M.I.T., 1993d.

Pratt, R. G. and N. R. Goulty, Combining wave-equation imaging with traveltime tomography to form high-resolution images from crosshole data, *Geophysics, 56,* 208–224, 1991.

Pratt, R. G. and M. H. Worthington, The application of diffraction tomography to cross-hole seismic data, *Geophysics, 53,* 1284–1294, 1988.

Press, W. H., B. P. Flannery, S. A. Teukolsky, and W. T. Vetterling, *Numerical Recipes: the art of scientific computing,* Cambridge University Press, Cambridge, United Kingdom, 1989.

Randall, C. J., Absorbing boundary condition for the elastic wave equation, *Geophysics, 53,* 611–624, 1988.

Randall, C. J., Modes of noncircular fluid-filled boreholes in elastic formations, *J. Acoust. Soc. Am., 89,* 1002–1016, 1991.

Randall, C. J., Multiple acoustic waveforms in nonaxisymmetric boreholes and formations, *J. Acoust. Soc. Am., 90,* 1620–1631, 1991.

Rechtien, R. D. and K. L. Hambacker, A high-frequency sparker source for the borehole environment, *Geophysics, 58,* 660–669, 1993.

Reichel, L., G. S. Ammar, and W. B. Gragg, Discrete least squares approximation by trigonometric polynomials, *Math. Comp., 57,* 273–289, 1991.

Reynolds, A. C., Boundary conditions for the numerical solution of wave propagation problems, *Geophysics, 43,* 1099–1110, 1978.

Robinson, E. A. and S. Treitel, *Geophysical signal analysis,* Prentice Hall, Englewood Cliffs, New Jersey, 1980.

Robinson, E. A. and S. Treitel, *Geophysical signal processing,* Prentice Hall, Englewood Cliffs, New Jersey, 1986.

Rosenbaum, J. H., Synthetic microseismograms–logging in porous formations, *Geophysics, 39,* 14–32, 1974.

Schleicher, J., M. Tygel, and P. Hubral, 3-D true-amplitude finite offset migration, *Geophysics, 58,* 1112–1126, 1993.

Schmidt, H. and G. Tango, Efficient global matrix approach to the computation of synthetic seismograms, *Geophys. J. R. Astr. Soc., 84,* 331–359, 1986.

Schmitt, D. P., Shear wave logging in elastic formations, *J. Acoust. Soc. Am., 84,* 2215–2229, 1988.

Schoenberg, M., T. L. Marzetta, J. Aron, and R. Porter, Space-time dependence of acoustic waves in a borehole, *J. Acoust. Soc. Am., 70,* 1496–1507, 1981.

Schoenberg, M., Fluid and solid motion on the neighborhood of a fluid-filled borehole due to the passage of a low frequency elastic plane wave, *Geophysics, 51,* 1191–1205, 1986.

Sei, A., Computational cost of finite-difference elastic waves modeling, in *63th Ann. Internat. Mtg., Soc. Expl. Geophys., Expanded abs tracts,* pp. 1065–1068, 1993.

Stephen, R. A., F. Pardo-Casas, and C. H. Cheng, Finite-difference synthetic acoustic logs, *Geophysics, 50,* 1588–1609, 1985.

Sullivan, M. F., Finite element modeling of VSP data, in *Vertical Seismic Profiling: 14B, M. N. Toksöz and R. R. Stewart (ed.),* pp. 45–62, Geophysical Press, 1984.

Suprajitno, M. and S. A. Greenhalgh, Theoretical vertical seismic profiling seismograms, *Geophysics, 51,* 1252–1265, 1986.

Takeuchi, H. and M. Saito, Seismic surface waves, in *Method of Computational Physics II,* edited by Bolt, B. A., pp. 217–295, Academic Press, New York, 1972.

Temme, P. and G. Muller, Numerical simulation of vertical seismic profiling, *J. Geophys., 50,* 177–188, 1982.

Thompson, D. R., *Nonlinear waveform tomography: theory and application to cross-hole seismic data,* PhD thesis, M.I.T., Cambridge, Massachusetts, 1993.

Thomsen, L., Weak elastic anisotropy, *Geophysics, 51,* 1954–1966, 1986.

Timoshenko, S. and J. N. Goodier, *Theory of Elasticity,* McGraw-Hill, New York, 1951.

Toksöz, M. N., C. H. Cheng, and M. E. Willis, Seismic waves in a borehole–a review, in *Vertical Seismic Profiling: 14B, M. N. Toksöz and R. R. Stewart (ed.),* pp. 256–275, Geophysical Press, 1984.

Toksöz, M. N., C. H. Cheng, and R. D. Cicerone, Fracture detection and characterization from hydrophone vertical seismic profiling data, in *Fauli Mechanics and Transport Properties of Rocks,* edited by Evans, B. and T. Wong, pp. 389–414, Academic Press, New York, 1992.

Tubman, K., C. H. Cheng, and M. N. Toksöz, Synthetic full-waveform acoustic logs in cased boreholes, *Geophysics, 49,* 1051–1059, 1984.

Tubman, K., *Full waveform acoustic logs in radially layered boreholes,* PhD thesis, M.I.T., Cambridge, Massachusetts, 1984.

Ugincius, P. and H. Überall, Creeping wave analysis of acoustic scattering by elastic cylindrical shells, *J. Acoust. Soc. Am., 43,* 1025–1035, 1968.

Virieux, J., P-SV wave propagation in heterogeneous media: velocity-stress finite-difference method, *Geophysics, 51,* 889–901, 1986.

Watson, G. N., *A treatise on the theory of Bessel functions,* Cambridge University Press, Cambridge, United Kingdom, 1922.

White, J. E. and E. Welsh, Borehole coupling of seismic waves in a permeable solid, *Geophys. Prosp., 36,* 417–429, 1988.

White, J. E. and R. E. Zechman, Computed response of an acoustic logging tool, *Geophysics, 33,* 302–310, 1968.

White, J. E., Signals in a borehole due to plane waves in the solid, *J. Acoust. Soc. Am., 25,* 906–915, 1953.

White, J. E., Use of reciprocity theorem for computation of low frequency radiation patterns, *Geophysics, 25,* 613–624, 1960.

White, J. E., *Underground Sound: Application of Seismic Waves,* Elsevier, 1983.

Winbow, G. A., Seismic sources in open and cased boreholes, *Geophysics, 56,* 1040–1050, 1991.

Worthington, M. H., Cross-well continuity logging using stoneley waves at the Whitchester borehole test site, in *Expanded Abstracts, 53th EAEG annual meeting, Florence, Italy,* 1991, B039.

Wu, R. S. and M. N. Toksöz, Diffraction tomography and multi-source holography applied to seismic imaging, *Geophysics, 52,* 11–25, 1987.

Wyatt, K. D., Synthetic vertical seismic profiles, *Geophysics, 46,* 880–891, 1981.

Zimmerman, R. W., Compressibility of two-dimensional cavities of various shapes, *J. Appl. Mech., 108,* 500–504, 1986.

Ziolkowski, A. M., Why don't we measure seismic signatures ?, *Geophysics, 56,* 190–201, 1991.

Zoback, M. D., In-situ stress measurements in the Kent Cliffs research well, Kent Cliffs borehole research project: a determination of magnitude and orientation of tectonic stress in southeastern New York state EP 84-27, Woodward-Clyde consultants research report, 1986.

Appendix A

Basic Equations in a Cylindrical Coordinate System

A-1 Expressions for Stresses and Displacements

In terms of the four potentials ϕ_f, ϕ, ξ and ψ, the displacement and stress in both fluid and solid in cylindrical coordinates can be written as (Aki and Richards, 1980; White, 1983; Meredith, 1990)

$$\begin{aligned}
\vec{u}_f &= \hat{e}_r \frac{\partial \phi_f}{\partial r} + \hat{e}_\theta \frac{1}{r} \frac{\partial \phi_f}{\partial \theta} + \hat{e}_z \frac{\partial \phi_f}{\partial z} \\
u_r &= \frac{\partial \phi}{\partial r} + \frac{\partial^2 \xi}{\partial r \partial z} + \frac{1}{r} \frac{\partial \psi}{\partial \theta} \\
u_\theta &= \frac{1}{r} \frac{\partial \phi}{\partial \theta} + \frac{1}{r} \frac{\partial^2 \xi}{\partial \theta \partial z} - \frac{\partial \psi}{\partial r} \\
u_z &= \frac{\partial \phi}{\partial z} + \frac{\partial^2 \xi}{\partial z^2} - \nabla^2 \xi
\end{aligned}$$

and

$$\sigma_{rr} = -\rho\omega^2\varphi - 2\rho\beta^2 \left[\left(\frac{1}{r} \frac{\partial \phi}{\partial r} + \frac{1}{r^2} \frac{\partial^2 \phi}{\partial \theta^2} + \frac{\partial^2 \phi}{\partial z^2} \right) + \frac{\partial}{\partial z} \left(\frac{\omega^2}{\beta^2} \xi + \frac{1}{r} \frac{\partial \xi}{\partial r} + \frac{1}{r^2} \frac{\partial^2 \xi}{\partial \theta^2} + \frac{\partial^2 \xi}{\partial z^2} \right) \right.$$

$$+\frac{1}{r^2}\frac{\partial\psi}{\partial\theta}-\frac{1}{r}\frac{\partial^2\psi}{\partial r\partial\theta}]$$

$$\sigma_{rz} = 2\rho\beta^2\,[\frac{\partial^2\phi}{\partial r\partial z}+\frac{\partial}{\partial r}(\frac{\omega^2}{2\beta^2}\xi+\frac{\partial^2\xi}{\partial z^2})+\frac{1}{2r}\frac{\partial^2\psi}{\partial z\partial\theta}]$$

$$\sigma_{r\theta} = 2\rho\beta^2\,[\frac{\partial}{\partial\theta}(\frac{1}{r}\frac{\partial\phi}{\partial r}-\frac{\phi}{r^2})+\frac{\partial^2}{\partial z\partial\theta}(\frac{1}{r}\frac{\partial\xi}{\partial r}-\frac{\xi}{r^2})+\frac{1}{r^2}\frac{\partial^2\psi}{\partial\theta^2}+\frac{1}{r}\frac{\partial\psi}{\partial r}+\frac{1}{2}(\frac{\omega^2}{\beta^2}\psi+\frac{\partial^2\psi}{\partial z^2})]$$

and

$$\sigma_{zz} = \rho(\alpha^2-2\beta^2)\nabla^2\phi+2\rho\beta^2\,[\frac{\partial^2\phi}{\partial z^2}+\frac{\partial}{\partial z}(\frac{\partial^2\xi}{\partial z^2}-\nabla^2\xi)]$$

$$\sigma_{z\theta} = 2\rho\beta^2\,[\frac{2}{r}\frac{\partial^2\phi}{\partial z\partial\theta}+\frac{1}{r}\frac{\partial}{\partial\theta}(2\frac{\partial^2\xi}{\partial z^2}-\nabla^2\xi)-\frac{\partial^2\psi}{\partial r\partial z}]$$

$$\sigma_{\theta\theta} = \rho(\alpha^2-2\beta^2)\nabla^2\phi+2\rho\beta^2\,[\frac{1}{r^2}\frac{\partial^2\phi}{\partial\theta^2}+\frac{1}{r}\frac{\partial\phi}{\partial r}+\frac{1}{r}\frac{\partial}{\partial z}(\frac{1}{r}\frac{\partial^2\xi}{\partial\theta^2}+\frac{\partial\xi}{\partial r})-\frac{1}{r}\frac{\partial^2\psi}{\partial r\partial\theta}+\frac{1}{r^2}\frac{\partial\psi}{\partial\theta}].$$

A-2 Additional Expressions

Given below are expressions for the displacement and stress components that are not included in the text:

$$u_\theta^f = \mathcal{V}_0^{(f)}(r)A_0+2\sum_{n=1}^{\infty}i^n\mathcal{V}_n^{(f)}(r)\,(-A_n\sin n\theta+A_n^{'}\cos n\theta)$$

$$u_\theta^\phi = \mathcal{V}_0^{(\phi)}(r)B_0+2\sum_{n=1}^{\infty}i^n\mathcal{V}_n^{(\phi)}(r)\,(-B_n\sin n\theta+B_n^{'}\cos n\theta)$$

$$u_\theta^\xi = \mathcal{V}_0^{(\xi)}(r)C_0+2\sum_{n=1}^{\infty}i^n\mathcal{V}_{\theta n}^{(\xi)}(r)\,(-C_n\sin n\theta+C_n^{'}\cos n\theta)$$

$$u_\theta^\psi = \mathcal{V}_0^{(\psi)}(r)D_0^{'}+2\sum_{n=1}^{\infty}i^n\mathcal{V}_n^{(\psi)}(r)\,(-D_n\sin n\theta+D_n^{'}\cos n\theta)$$

$$u_z^f = \mathcal{W}_0^{(f)}(r)A_0+2\sum_{n=1}^{\infty}i^n\mathcal{W}_n^{(f)}(r)\,(A_n\cos n\theta+A_n^{'}\sin n\theta)$$

$$u_z^\varphi = \mathcal{W}_0^{(\phi)}(r)B_0+2\sum_{n=1}^{\infty}i^n\mathcal{W}_n^{(\phi)}(r)\,(B_n\cos n\theta+B_n^{'}\sin n\theta)$$

$$u_z^{\xi} = \mathcal{W}_0^{(\xi)}(r)C_0 + 2\sum_{n=1}^{\infty} i^n \mathcal{W}_n^{(\xi)}(r)\ (C_n \cos n\theta + C_n' \sin n\theta)$$

$$u_z^{\psi} = 0$$

and

$$\sigma_{zz}^{\phi} = \mathcal{L}_0^{(\phi)}(r)B_0 + 2\sum_{n=1}^{\infty} i^n \mathcal{L}_n^{(\phi)}(r)\ (B_n \cos n\theta + B_n' \sin n\theta)$$

$$\sigma_{zz}^{\xi} = \mathcal{L}_0^{(\xi)}(r)C_0 + 2\sum_{n=1}^{\infty} i^n \mathcal{L}_n^{(\xi)}(r)\ (C_n \cos n\theta + C_n' \sin n\theta)$$

$$\sigma_{zz}^{\psi} = 0$$

$$\sigma_{\theta\theta}^{\phi} = \mathcal{M}_0^{(\phi)}(r)B_0 + 2\sum_{n=1}^{\infty} i^n \mathcal{M}_n^{(\phi)}(r)\ (B_n \cos n\theta + B_n' \sin n\theta)$$

$$\sigma_{\theta\theta}^{\xi} = \mathcal{M}_0^{(\xi)}(r)C_0 + 2\sum_{n=1}^{\infty} i^n \mathcal{M}_n^{(\xi)}(r)\ (C_n \cos n\theta + C_n' \sin n\theta)$$

$$\sigma_{\theta\theta}^{\psi} = \mathcal{M}_0^{(\psi)}(r)D_0 + 2\sum_{n=1}^{\infty} i^n \mathcal{M}_n^{(\psi)}(r)\ (D_n \cos n\theta + D_n' \sin n\theta)$$

$$\sigma_{z\theta}^{\phi} = \mathcal{N}_0(r)^{(\phi)}B_0' + 2\sum_{n=1}^{\infty} i^n \mathcal{N}_n^{(\phi)}(r)\ (-B_n \sin n\theta + B_n' \cos n\theta)$$

$$\sigma_{z\theta}^{\xi} = \mathcal{N}_0(r)^{(\xi)}C_0' + 2\sum_{n=1}^{\infty} i^n \mathcal{N}_n^{(\xi)}(r)\ (-C_n \sin n\theta + C_n' \cos n\theta)$$

$$\sigma_{z\theta}^{\psi} = \mathcal{N}_0^{(\psi)}(r)D_0' + 2\sum_{n=1}^{\infty} i^n \mathcal{N}_n^{(\psi)}(r)\ (-D_n \sin n\theta + D_n' \cos n\theta).$$

A-3 Lists of Coefficients

We list the coefficients of the stresses and displacements in the harmonic expansions as follows:

$$\mathcal{U}_n^{(f)}(r) = \alpha_f k_f J_n'(k_f r), \qquad \mathcal{V}_n^{(f)}(r) = \alpha_f \tfrac{k_f}{k_f r} n J_n(k_f r), \qquad \mathcal{W}_n^{(f)}(r) = \alpha_f i k_z J_n(k_f r)$$

$$\mathcal{U}_n^{(\phi)}(r) = \alpha k_p H_n^{(1)\prime}(k_p r), \quad \mathcal{U}_n^{(\xi)}(r) = -\beta \tfrac{k_z k_s}{k_\beta} H_n^{(1)\prime}(k_s r), \quad \mathcal{U}_n^{(\psi)}(r) = \beta \tfrac{k_s}{k_s r} n H_n^{(1)}(k_s r)$$

$$\mathcal{V}_n^{(\phi)}(r) = \alpha \tfrac{k_p}{k_p r} n H_n^{(1)}(k_p r), \quad \mathcal{V}_n^{(\xi)}(r) = -\beta \tfrac{k_z}{k_\beta r} n H_n^{(1)}(k_s r), \quad \mathcal{V}_n^{(\psi)}(r) = \beta k_s H_n^{(1)\prime}(k_s r)$$

$$\mathcal{W}_n^{(\phi)}(r) = \alpha i k_z H_n^{(1)}(k_p r), \quad \mathcal{W}_n^{(\xi)}(r) = \beta i \tfrac{k_z^2}{k_\beta} H_n^{(1)}(k_s r), \quad \mathcal{W}_n^{(\psi)}(r) = 0$$

$$\mathcal{R}_n^{(f)}(r) = -\rho_f \alpha_f \omega^2 J_n(k_f r)$$

$$\mathcal{R}_n^{(\phi)}(r) = -\rho\alpha[(\omega^2 - 2\beta^2 k_z^2) H_n^{(1)}(k_p r) + \tfrac{2\beta^2 k_p^2}{k_p r}(H_n^{(1)\prime}(k_p r) - \tfrac{n^2}{k_p r} H_n^{(1)}(k_p r))]$$

$$\mathcal{R}_n^{(\xi)}(r) = 2\rho\beta^3 \tfrac{k_z k_s^2}{k_\beta}[H_n^{(1)}(k_s r) + \tfrac{1}{k_s r} H_n^{(1)\prime}(k_s r) - \tfrac{n^2}{k_s^2 r^2} H_n^{(1)}(k_s r)]$$

$$\mathcal{R}_n^{(\psi)}(r) = -2\rho\beta^3 k_s^2 n[\tfrac{1}{k_s^2 r^2} H_n^{(1)}(k_s r) - \tfrac{1}{k_s r} H_n^{(1)\prime}(k_s r)]$$

$$\mathcal{T}_n^{(\phi)}(r) = -2\rho\alpha\beta^2 k_p^2 n[\tfrac{1}{k_p^2 r^2} H_n^{(1)}(k_p r) - \tfrac{1}{k_p r} H_n^{(1)\prime}(k_p r)]$$

$$\mathcal{T}_n^{(\xi)}(r) = 2\rho\beta^3 \tfrac{k_z k_s^2}{k_\beta} n[\tfrac{1}{k_s^2 r^2} H_n^{(1)}(k_s r) - \tfrac{1}{k_s r} H_n^{(1)\prime}(k_s r)]$$

$$\mathcal{T}_n^{(\psi)}(r) = -\rho\beta^3 k_s^2[H_n^{(1)}(k_s r) + \tfrac{2}{k_s r} H_n^{(1)\prime}(k_s r) - \tfrac{2n^2}{k_s^2 r^2} H_n^{(1)}(k_s r)]$$

$$\mathcal{Z}_n^{(\phi)}(r) = 2i\rho\alpha\beta^2 k_z k_p H_n^{(1)\prime}(k_p r)$$

$$\mathcal{Z}_n^{(\xi)}(r) = -i\rho\beta^3 \tfrac{(k_z^2 - k_s^2) k_s}{k_\beta} H_n^{(1)\prime}(k_s r)$$

$$\mathcal{Z}_n^{(\psi)}(r) = i\rho\beta^3 k_z \tfrac{k_s}{k_s r} n H_n^{(1)}(k_s r)$$

$$\mathcal{L}_n^{(\phi)}(r) = -\rho\alpha[\omega^2 - 2\beta^2(k_\alpha{}^2 - k_z^2)] H_n^{(1)}(k_p r)$$

$$\mathcal{L}_n^{(\xi)}(r) = -2\rho\beta^3 \tfrac{k_z}{k_\beta}(k_\beta{}^2 - k_z^2) H_n^{(1)}(k_s r)$$

$$\mathcal{L}_n^{(\psi)}(r) = 0$$

$$\mathcal{M}_n^{(\phi)}(r) = -\rho\alpha[(\alpha^2 - 2\beta^2) k_\alpha{}^2 H_n^{(1)}(k_p r) - 2\beta^2 \tfrac{k_p^2}{k_p r} H_n^{(1)\prime}(k_p r) + 2\beta^2 \tfrac{k_p^2}{k_p^2 r^2} n^2 H_n^{(1)}(k_p r)]$$

$$\mathcal{M}_n^{(\xi)}(r) = -2\rho\beta^3 \tfrac{k_z}{k_\beta}[\tfrac{k_s^2}{k_s r} H_n^{(1)\prime}(k_s r) - \tfrac{k_s^2}{k_s^2 r^2} n^2 H_n^{(1)}(k_s r)]$$

$$\mathcal{M}_n^{(\psi)}(r) = 2\rho\beta^3 k_s^2 n[\tfrac{1}{k_s^2 r^2} H_n^{(1)}(k_s r) - \tfrac{1}{k_s r} H_n^{(1)\prime}(k_s r)]$$

$$\mathcal{N}_n^{(\phi)}(r) = 2i\rho\alpha\beta^2 \frac{k_z k_p}{k_p r} n H_n^{(1)}(k_p r)$$

$$\mathcal{N}_n^{(\xi)}(r) = i\rho\beta^3 \frac{k_\beta{}^2 - 2k_z^2}{k_s r} \frac{k_s}{k_\beta} n H_n^{(1)}(k_s r)$$

$$\mathcal{N}_n^{(\psi)}(r) = i\rho\beta^3 k_z k_s H_n^{(1)\prime}(k_s r)$$

where, as a reminder, $k_\alpha = \frac{\omega}{\alpha}$, $k_\beta = \frac{\omega}{\beta}$, $k_p = \sqrt{k_\alpha{}^2 - k_z^2}$, $k_s = \sqrt{k_\beta{}^2 - k_z^2}$ and $k_f = \sqrt{\frac{\omega^2}{\alpha_f^2} - k_z^2}$. The vertical wavenumber $k_z = k_\alpha \cos\delta$ for plane P wave incidence and $k_z = k_\beta \cos\delta$ for plane shear wave incidence. δ is the angle of incidence.

A-4 Expressions for Incident Plane Waves

For a plane P-wave traveling in the direction $\hat{\vec{k}} = (\sin\delta\cos\nu, \sin\delta\sin\nu, \cos\delta)$, where δ is the angle of incidence with respect to the borehole axis and ν is the azimuth angle, the displacement potential can be written as (omitting the $e^{i(k_z z - \omega t)}$ dependence)

$$\begin{aligned} \phi_P &= -\frac{\alpha V(\omega)}{\omega^2} \exp[ik_p r\cos(\theta - \nu)] \qquad \text{(A.1)} \\ &= -\frac{\alpha V(\omega)}{\omega^2} [J_0(k_p r) + 2\sum_{n=1}^{\infty} i^n(\cos n\nu\cos n\theta + \sin n\nu \sin n\theta) J_n(k_p r)]. \end{aligned}$$

In addition to the displacement and stress components given in equations (2.12a)-(2.14d), we have

$$\begin{aligned} u_\theta^P &= \mathcal{V}_0^{(P)}(r) + 2\sum_{n=1}^{\infty} i^n \mathcal{V}_n^{(P)}(r)\ (-\cos n\nu \sin n\theta + \sin n\nu\cos n\theta) \\ u_z^P &= \mathcal{W}_0^{(P)}(r) + 2\sum_{n=1}^{\infty} i^n \mathcal{W}_n^{(P)}(r)\ (\cos n\nu\cos n\theta + \sin n\nu \sin n\theta). \end{aligned}$$

If the incident plane wave is of SV-type, the displacement potential will be

$$\begin{aligned} \xi_{SV} &= -\frac{i\beta^2 V(\omega)}{\omega^3} \frac{1}{\sin\delta} \exp[ik_s r\cos(\theta - \nu)] \qquad \text{(A.2)} \\ &= -\frac{i\beta^2 V(\omega)}{\omega^3} \frac{k_\beta}{k_s} [J_0(k_s r) + 2\sum_{n=1}^{\infty} i^n(\cos n\nu\cos n\vartheta + \sin n\nu \sin n\theta) J_n(k_s r)] \end{aligned}$$

and

$$u_\theta^{SV} = \mathcal{V}_0^{(SV)}(r) + 2\sum_{n=1}^{\infty} i^n \mathcal{V}_n^{(SV)}(r)\ (-\cos n\nu \sin n\theta + \sin n\nu \cos n\theta)$$

$$u_z^{SV} = \mathcal{W}_0^{(SV)}(r) + 2\sum_{n=1}^{\infty} i^n \mathcal{W}_n^{(SV)}(r)\ (\cos n\nu \cos n\theta + \sin n\nu \sin n\theta).$$

Similarly, for a plane SH-wave incidence we have

$$\psi_{SH} = -\frac{\beta v(\omega)}{\omega^2}\frac{1}{\sin\delta}\exp[ik_s r\cos(\theta-\nu)] \tag{A.3}$$

$$= -\frac{\beta v(\omega)}{\omega^2}\frac{k\beta}{k_s}\left[J_0(k_s r) + 2\sum_{n=1}^{\infty} i^n(\cos n\nu\cos n\theta + \sin n\nu \sin n\theta)J_n(k_s r)\right]$$

and

$$u_\theta^{SH} = \mathcal{V}_0^{(SH)}(r) + 2\sum_{n=1}^{\infty} i^n \mathcal{V}_n^{(SH)}(r)\ (\cos n\nu\cos n\theta + \sin n\nu\sin n\theta)$$

$$u_z^{SH} = 0.$$

The coefficients are given below

$$\mathcal{U}_n^{(P)}(r) = \alpha k_p J_n'(k_p r), \qquad \mathcal{V}_n^{(P)}(r) = \alpha\tfrac{k_p}{k_p r} n J_n(k_p r), \qquad \mathcal{W}_n^{(P)}(r) = i\alpha k_z J_n(k_p r)$$

$$\mathcal{U}_n^{(SV)}(r) = -\beta k_z J_n'(k_s r), \quad \mathcal{V}_n^{(SV)}(r) = -\beta\tfrac{k_z}{k_s r} n J_n(k_s r), \quad \mathcal{W}_n^{(SV)}(r) = i\beta k_s J_n(k_s r)$$

$$\mathcal{U}_n^{(SH)}(r) = \beta\frac{k\beta}{k_s r} n J_n(k_s r), \quad \mathcal{V}_n^{(SH)}(r) = -\beta k_\beta J_n'(k_s r), \quad \mathcal{W}_n^{(SH)}(r) = 0$$

$$\mathcal{R}_n^{(P)}(r) = -\rho\alpha[(\omega^2 - 2\beta^2 k_z^2)J_n(k_p r) + 2\beta^2\tfrac{k_p^2}{k_p r}(J_n'(k_p r) - \tfrac{n^2}{k_p r}J_n(k_p r))]$$

$$\mathcal{T}_n^{(P)}(r) = -2\rho\alpha\beta^2 k_p^2 n[\tfrac{1}{k_p^2 r^2}J_n(k_p r) - \tfrac{1}{k_p r}J_n'(k_p r)]$$

$$\mathcal{Z}_n^{(P)}(r) = 2i\rho\alpha\beta^2 k_z k_p J_n'(k_p r)$$

$$\mathcal{R}_n^{(SV)}(r) = 2\rho\beta^3 k_z k_s[J_n(k_s r) + \tfrac{1}{k_s r}J_n'(k_s r) - \tfrac{n^2}{k_s^2 r^2}J_n(k_s r)]$$

$$\mathcal{T}_n^{(SV)}(r) = -2\rho\beta^3 k_s k_z n[\tfrac{1}{k_s r}J_n'(k_s r) - \tfrac{1}{k_s^2 r^2}J_n(k_s r)]$$

$$\mathcal{Z}_n^{(SV)}(r) = i\rho\beta^3(k_s^2 - k_z^2)J_n'(k_s r)$$

$$\mathcal{R}_n^{(SH)}(r) = 2\rho\beta^3 k_s^2 n[\tfrac{1}{k_s r} J_n'(k_s r) - \tfrac{1}{k_s^2 r^2} J_n(k_s r)]$$

$$\mathcal{T}_n^{(SH)}(r) = \rho\beta^3 k_s^2 [J_n(k_s r) + \tfrac{2}{k_s r} J_n'(k_s r) - \tfrac{2n^2}{k_s^2 r^2} J_n(k_s r)]$$

$$\mathcal{Z}_n^{(SH)}(r) = i\rho\beta^3 k_s k_z \tfrac{n}{k_s r} J_n(k_s r).$$

Appendix B

Coefficients for Displacements and Stresses in a Cased Borehole

B-1 Lists of Coefficients

The matrix D in equation (3.24) is given by

$$\mathrm{D} = \begin{bmatrix} \mathcal{U}_n^{\phi(1)}(r) & \mathcal{U}_n^{\phi(2)}(r) & \mathcal{U}_n^{\xi(1)}(r) & \mathcal{U}_n^{\xi(2)}(r) & \mathcal{U}_n^{\psi(1)}(r) & \mathcal{U}_n^{\psi(2)}(r) \\ \mathcal{V}_n^{\phi(1)}(r) & \mathcal{V}_n^{\phi(2)}(r) & \mathcal{V}_n^{\xi(1)}(r) & \mathcal{V}_n^{\xi(2)}(r) & \mathcal{V}_n^{\psi(1)}(r) & \mathcal{V}_n^{\psi(2)}(r) \\ \mathcal{W}_n^{\phi(1)}(r) & \mathcal{W}_n^{\phi(2)}(r) & \mathcal{W}_n^{\xi(1)}(r) & \mathcal{W}_n^{\xi(2)}(r) & \mathcal{W}_n^{\psi(1)}(r) & \mathcal{W}_n^{\psi(2)}(r) \\ \mathcal{R}_n^{\phi(1)}(r) & \mathcal{R}_n^{\phi(2)}(r) & \mathcal{R}_n^{\xi(1)}(r) & \mathcal{R}_n^{\xi(2)}(r) & \mathcal{R}_n^{\psi(1)}(r) & \mathcal{R}_n^{\psi(2)}(r) \\ \mathcal{T}_n^{\phi(1)}(r) & \mathcal{T}_n^{\phi(2)}(r) & \mathcal{T}_n^{\xi(1)}(r) & \mathcal{T}_n^{\xi(2)}(r) & \mathcal{T}_n^{\psi(1)}(r) & \mathcal{T}_n^{\psi(2)}(r) \\ \mathcal{Z}_n^{\phi(1)}(r) & \mathcal{Z}_n^{\phi(2)}(r) & \mathcal{Z}_n^{\xi(1)}(r) & \mathcal{Z}_n^{\xi(2)}(r) & \mathcal{Z}_n^{\psi(1)}(r) & \mathcal{Z}_n^{\psi(2)}(r) \end{bmatrix}$$

where

$$\mathcal{U}_n^{\phi(1)}(r) = \alpha k_p H_n^{(1)\prime}(k_p r), \qquad \mathcal{U}_n^{\phi(2)}(r) = \alpha k_p H_n^{(2)\prime}(k_p r)$$

$$\mathcal{U}_n^{\xi(1)}(r) = -\beta \frac{k_z k_s}{k_\beta} H_n^{(1)\prime}(k_s r), \quad \mathcal{U}_n^{\xi(2)}(r) = -\beta \frac{k_z k_s}{k_\beta} H_n^{(2)\prime}(k_s r)$$

$$\mathcal{U}_n^{\psi(1)}(r) = \beta \frac{k}{k_s} n H_n^{(1)}(k_s r), \quad \mathcal{U}_n^{\psi(2)}(r) = \beta \frac{k_s}{k_s r} n H_n^{(2)}(k_s r)$$

$$\mathcal{V}_n^{\phi(1)}(r) = \alpha\frac{k_p}{k_p r} n H_n^{(1)}(k_p r), \qquad \mathcal{V}_n^{\phi(2)}(r) = \alpha\frac{k_p}{k_p r} n H_n^{(2)}(k_p r)$$
$$\mathcal{V}_n^{\xi(1)}(r) = -\beta\frac{k_z}{k_\beta r} n H_n^{(1)}(k_s r), \quad \mathcal{V}_n^{\xi(2)}(r) = -\beta\frac{k_z}{k_\beta r} n H_n^{(2)}(k_s r)$$
$$\mathcal{V}_n^{\psi(1)}(r) = \beta k_s H_n^{(1)\prime}(k_s r), \qquad \mathcal{V}_n^{\psi(2)}(r) = \beta k_s H_n^{(2)\prime}(k_s r)$$

$$\mathcal{W}_n^{\phi(1)}(r) = i\alpha k_z H_n^{(1)}(k_p r), \quad \mathcal{W}_n^{\phi(2)}(r) = i\alpha k_z H_n^{(2)}(k_p r)$$
$$\mathcal{W}_n^{\xi(1)}(r) = i\beta\frac{k_s^2}{k_\beta} H_n^{(1)}(k_s r), \quad \mathcal{W}_n^{\xi(2)}(r) = i\beta\frac{k_s^2}{k_\beta} H_n^{(2)}(k_s r)$$
$$\mathcal{W}_n^{\psi(1)}(r) = 0, \qquad \mathcal{W}_n^{\psi(2)}(r) = 0$$

$$\mathcal{R}_n^{\phi(1)}(r) = -\rho\alpha[(\omega^2 - 2\beta^2 k_z^2) H_n^{(1)}(k_p r) + \tfrac{2\beta^2 k_p^2}{k_p r}(H_n^{(1)\prime}(k_p r) - \tfrac{n^2}{k_p r} H_n^{(1)}(k_p r))]$$
$$\mathcal{R}_n^{\phi(2)}(r) = -\rho\alpha[(\omega^2 - 2\beta^2 k_z^2) H_n^{(2)}(k_p r) + \tfrac{2\beta^2 k_p^2}{k_p r}(H_n^{(2)\prime}(k_p r) - \tfrac{n^2}{k_p r} H_n^{(2)}(k_p r))]$$
$$\mathcal{R}_n^{\xi(1)}(r) = 2\rho\beta^3\frac{k_z k_s^2}{k_\beta}[H_n^{(1)}(k_s r) + \tfrac{1}{k_s r} H_n^{(1)\prime}(k_s r) - \tfrac{n^2}{k_s^2 r^2} H_n^{(1)}(k_s r)]$$
$$\mathcal{R}_n^{\xi(2)}(r) = 2\rho\beta^3\frac{k_z k_s^2}{k_\beta}[H_n^{(2)}(k_s r) + \tfrac{1}{k_s r} H_n^{(2)\prime}(k_s r) - \tfrac{n^2}{k_s^2 r^2} H_n^{(2)}(k_s r)]$$
$$\mathcal{R}_n^{\psi(1)}(r) = -2\rho\beta^3 k_s^2 n[\tfrac{1}{k_s^2 r^2} H_n^{(1)}(k_s r) - \tfrac{1}{k_s r} H_n^{(1)\prime}(k_s r)]$$
$$\mathcal{R}_n^{\psi(2)}(r) = -2\rho\beta^3 k_s^2 n[\tfrac{1}{k_s^2 r^2} H_n^{(2)}(k_s r) - \tfrac{1}{k_s r} H_n^{(2)\prime}(k_s r)]$$

$$\mathcal{T}_n^{\phi(1)}(r) = -2\rho\alpha\beta^2 k_p^2 n[\tfrac{1}{k_p^2 r^2} H_n^{(1)}(k_p r) - \tfrac{1}{k_p r} H_n^{(1)\prime}(k_p r)]$$
$$\mathcal{T}_n^{\phi(2)}(r) = -2\rho\alpha\beta^2 k_p^2 n[\tfrac{1}{k_p^2 r^2} H_n^{(2)}(k_p r) - \tfrac{1}{k_p r} H_n^{(2)\prime}(k_p r)]$$
$$\mathcal{T}_n^{\xi(1)}(r) = 2\rho\beta^3\frac{k_z k_s^2}{k_\beta} n[\tfrac{1}{k_s^2 r^2} H_n^{(1)}(k_s r) - \tfrac{1}{k_s r} H_n^{(1)\prime}(k_s r)]$$
$$\mathcal{T}_n^{\xi(2)}(r) = 2\rho\beta^3\frac{k_z k_s^2}{k_\beta} n[\tfrac{1}{k_s^2 r^2} H_n^{(2)}(k_s r) - \tfrac{1}{k_s r} H_n^{(2)\prime}(k_s r)]$$
$$\mathcal{T}_n^{\psi(1)}(r) = -\rho\beta^3 k_s^2[H_n^{(1)}(k_s r) + \tfrac{2}{k_s r} H_n^{(1)\prime}(k_s r) - \tfrac{2n^2}{k_s^2 r^2} H_n^{(1)}(k_s r)]$$
$$\mathcal{T}_n^{\psi(2)}(r) = -\rho\beta^3 k_s^2[H_n^{(2)}(k_s r) + \tfrac{2}{k_s r} H_n^{(2)\prime}(k_s r) - \tfrac{2n^2}{k_s^2 r^2} H_n^{(2)}(k_s r)]$$

$$\mathcal{Z}_n^{\phi(1)}(r) = 2i\rho\alpha\beta^2 k_z k_p H_n^{(1)'}(k_p r)$$

$$\mathcal{Z}_n^{\phi(2)}(r) = 2i\rho\alpha\beta^2 k_z k_p H_n^{(2)'}(k_p r)$$

$$\mathcal{Z}_n^{\xi(1)}(r) = -i\rho\beta^3 \frac{(k_z^2 - k_s^2)k_s}{k_\beta} H_n^{(1)'}(k_s r)$$

$$\mathcal{Z}_n^{\xi(2)}(r) = -i\rho\beta^3 \frac{(k_z^2 - k_s^2)k_s}{k_\beta} H_n^{(2)'}(k_s r)$$

$$\mathcal{Z}_n^{\psi(1)}(r) = i\rho\beta^3 k_z k_s \frac{n}{k_s r} H_n^{(1)}(k_s r)$$

$$\mathcal{Z}_n^{\psi(2)}(r) = i\rho\beta^3 k_z k_s \frac{n}{k_s r} H_n^{(2)}(k_s r)$$

In the above expressions, α, β and ρ are compressional velocity, shear velocity and density in the each layer respectively. Variables involving wavenumbers are $k_\alpha = \frac{\omega}{\alpha}$, $k_\beta = \frac{\omega}{\beta}$, $k_p = \sqrt{k_\alpha{}^2 - k_z^2}$, $k_s = \sqrt{k_\beta{}^2 - k_z^2}$ and $k_f = \sqrt{\frac{\omega^2}{\alpha_f^2} - k_z^2}$. The vertical wavenumber k_z will be preserved upon reflection or refraction according to the Snell's law, and $k_z = k_\alpha \cos\delta$ for a plane P wave incidence and $k_z = k_\beta \cos\delta$ for a plane shear wave incidence. δ is the angle of incidence with respect to the borehole axis (i.e., $\delta = 90°$ corresponds to normal incidence on the borehole).

B-2 Displacement–Stress Vector of an Incident Wave

The displacement-stress vector $\vec{\mathrm{w}}(r)$ of the incident wave can be easily computed from the displacement potentials in Appendix A-4. The n-th harmonic component can be written as

$$\vec{\mathrm{w}}(r) = \left[\mathcal{U}_n^{(P)}(r), \mathcal{V}_n^{(P)}(r), \mathcal{W}_n^{(P)}(r), \mathcal{R}_n^{(P)}(r), \mathcal{T}_n^{(P)}(r), \mathcal{Z}_n^{(P)}(r)\right]^T$$

for a plane P-wave incidence, and

$$\vec{\mathrm{w}}(r) = \left[\mathcal{U}_n^{(SV)}(r), \mathcal{V}_n^{(SV)}(r), \mathcal{W}_n^{(SV)}(r), \mathcal{R}_n^{(SV)}(r), \mathcal{T}_n^{(SV)}(r), \mathcal{Z}_n^{(SV)}(r)\right]^T$$

for a plane SV-wave incidence and

$$\vec{\mathrm{w}}(r) = \left[\mathcal{U}_n^{(SH)}(r), \mathcal{V}_n^{(SH)}(r), \mathcal{W}_n^{(SH)}(r), \mathcal{R}_n^{(SH)}(r), \mathcal{T}_n^{(SH)}(r), \mathcal{Z}_n^{(SH)}(r)\right]^T$$

for a plane SH-wave incidence. The entities in the above expressions have been given in Appendix A-4.

B-3 Static Displacement

In this appendix, we outline the methods of deriving the effective moduli $E_{\parallel}$ and $E_{\perp}$ of a cased borehole. First consider an empty cased borehole subject to a stress state at infinity: $\sigma_{rr} = \sigma_{\theta\theta} = \sigma_0$ and $\sigma_{zz} = 2\nu\sigma_0$. The radial displacement on the borehole wall can be obtained by using the Airy function method (Love, 1944), yielding

$$u_r/r_b = \frac{2(1-\nu^2)}{E} \frac{\sigma_0}{1 + (\frac{\mu_c}{\mu} - 1)(1-\gamma_c)(1-\frac{r_b^2}{r_c^2})} .$$

where r_b and r_c are the inner and outer radii of the casing. E and ν are the Young's modulus and the Poisson's ratio of the formation, respectively. μ and μ_c are the formation and casing shear rigidities. $\gamma_c = \beta_c^2/\alpha_c^2$ is a parameter of the casing. Next consider a stress state at infinity: $\sigma_{rr} = \sigma_{\theta\theta} = 0$ and $\sigma_{zz} = \sigma_0$. In this case, the radial displacement on the borehole wall is found to be

$$u_r/r_b = -\frac{\sigma_0 \left[\nu + \nu_c(\frac{\mu_c}{\mu} - 1)(1-\gamma_c)(1-\frac{r_b^2}{r_c^2})\right]}{E \left[1 + (\frac{\mu_c}{\mu} - 1)(1-\gamma_c)(1-\frac{r_b^2}{r_c^2})\right]}.$$

Comparisons with equation (3.16) lead to the expressions for $E_{\parallel}$ and $E_{\perp}$ given in the text.

Appendix C

Expressions for the Elements of the Coefficient Matrices in Section 4.1.2

In this appendix, we give a list of the elements of coefficient matrices $\underline{\underline{a_{11}}}$, $\underline{\underline{a_{12}}}$, ..., $\underline{\underline{t_{22}}}$ which are the integrals of the corresponding modal functions along the fluid-solid boundary. In the following expressions, $\epsilon_l = \begin{cases} 2 & \text{if } l = 0 \\ 1 & \text{if } l \geq 1 \end{cases}$ and $\varepsilon_n = \begin{cases} 1 & \text{if } n = 0 \\ 2 & \text{if } n \geq 1 \end{cases}$. φ is the angle between the normal to the boundary and the radial axis of the cylindrical coordinate system, and is a function of θ. The function $\mathcal{U}_n^{(f)}$, for example, is the radial dependence of the fluid displacement of the n-th harmonic mode, and has been given in Appendix A-3.

$$\begin{Bmatrix} \left(\underline{\underline{a_{11}}}\right)_{ln} \\ \left(\underline{\underline{a_{21}}}\right)_{ln} \end{Bmatrix} = \frac{i^n \varepsilon_n}{\pi \epsilon_l} \int_0^{2\pi} \left\{ \mathcal{U}_n^{(f)}[r(\theta)] \cos n\theta \cos\varphi - \mathcal{V}_n^{(f)}[r(\theta)] \sin n\theta \sin\varphi \right\} \begin{Bmatrix} \cos l\theta \\ \sin l\theta \end{Bmatrix} d\theta \qquad \text{(C.1a)}$$

$$\left\{ \begin{array}{c} (\underline{\underline{a_{12}}})_{ln} \\ (\underline{\underline{a_{22}}})_{ln} \end{array} \right\} = \frac{i^n \varepsilon_n}{\pi \epsilon_l} \int_0^{2\pi} \left\{ \mathcal{U}_n^{(f)}[r(\theta)] \sin n\theta \cos\varphi + \mathcal{V}_n^{(f)}[r(\theta)] \cos n\theta \sin\varphi \right\} \left\{ \begin{array}{c} \cos l\theta \\ \sin l\theta \end{array} \right\} d\theta \tag{C.1b}$$

$$\left\{ \begin{array}{c} (\underline{\underline{b_{11}}})_{ln} \\ (\underline{\underline{b_{21}}})_{ln} \end{array} \right\} = \frac{i^n \varepsilon_n}{\pi \epsilon_l} \int_0^{2\pi} \left\{ \mathcal{U}_n^{(\phi)}[r(\theta)] \cos n\theta \cos\varphi - \mathcal{V}_n^{(\phi)}[r(\theta)] \sin n\theta \sin\varphi \right\} \left\{ \begin{array}{c} \cos l\theta \\ \sin l\theta \end{array} \right\} d\theta \tag{C.2a}$$

$$\left\{ \begin{array}{c} (\underline{\underline{b_{12}}})_{ln} \\ (\underline{\underline{b_{22}}})_{ln} \end{array} \right\} = \frac{i^n \varepsilon_n}{\pi \epsilon_l} \int_0^{2\pi} \left\{ \mathcal{U}_n^{(\phi)}[r(\theta)] \sin n\theta \cos\varphi + \mathcal{V}_n^{(\phi)}[r(\theta)] \cos n\theta \sin\varphi \right\} \left\{ \begin{array}{c} \cos l\theta \\ \sin l\theta \end{array} \right\} d\theta \tag{C.2b}$$

$$\left\{ \begin{array}{c} (\underline{\underline{c_{11}}})_{ln} \\ (\underline{\underline{c_{21}}})_{ln} \end{array} \right\} = \frac{i^n \varepsilon_n}{\pi \epsilon_l} \int_0^{2\pi} \left\{ \mathcal{U}_n^{(\xi)}[r(\theta)] \cos n\theta \cos\varphi - \mathcal{V}_n^{(\xi)}[r(\theta)] \sin n\theta \sin\varphi \right\} \left\{ \begin{array}{c} \cos l\theta \\ \sin l\theta \end{array} \right\} d\theta \tag{C.3a}$$

$$\left\{ \begin{array}{c} (\underline{\underline{c_{12}}})_{ln} \\ (\underline{\underline{c_{22}}})_{ln} \end{array} \right\} = \frac{i^n \varepsilon_n}{\pi \epsilon_l} \int_0^{2\pi} \left\{ \mathcal{U}_n^{(\xi)}[r(\theta)] \sin n\theta \cos\varphi + \mathcal{V}_n^{(\xi)}[r(\theta)] \cos n\theta \sin\varphi \right\} \left\{ \begin{array}{c} \cos l\theta \\ \sin l\theta \end{array} \right\} d\theta \tag{C.3b}$$

$$\left\{ \begin{array}{c} (\underline{\underline{d_{11}}})_{ln} \\ (\underline{\underline{d_{21}}})_{ln} \end{array} \right\} = \frac{i^n \varepsilon_n}{\pi \epsilon_l} \int_0^{2\pi} \left\{ \mathcal{U}_n^{(\psi)}[r(\theta)] \cos n\theta \cos\varphi - \mathcal{V}_n^{(\psi)}[r(\theta)] \sin n\theta \sin\varphi \right\} \left\{ \begin{array}{c} \cos l\theta \\ \sin l\theta \end{array} \right\} d\theta \tag{C.4a}$$

$$\left\{ \begin{array}{c} \left(\underline{\underline{d_{12}}}\right)_{ln} \\ \left(\underline{\underline{d_{22}}}\right)_{ln} \end{array} \right\} = \frac{i^n \varepsilon_n}{\pi \epsilon_l} \int_0^{2\pi} \left\{ \mathcal{U}_n^{(\psi)}[r(\theta)] \ \sin n\theta \cos\varphi + \mathcal{V}_n^{(\psi)}[r(\theta)] \ \cos n\theta \sin\varphi \right\}$$

$$\left\{ \begin{array}{c} \cos l\theta \\ \sin l\theta \end{array} \right\} d\theta \qquad \text{(C.4b)}$$

$$\left\{ \begin{array}{c} \left(\underline{\underline{e_{11}}}\right)_{ln} \\ \left(\underline{\underline{e_{21}}}\right)_{ln} \end{array} \right\} = \frac{i^n \varepsilon_n}{\pi \epsilon_l} \int_0^{2\pi} \mathcal{R}_n^{(f)}[r(\theta)] \ \cos n\theta \left\{ \begin{array}{c} \cos l\theta \\ \sin l\theta \end{array} \right\} d\theta \qquad \text{(C.5a)}$$

$$\left\{ \begin{array}{c} \left(\underline{\underline{e_{12}}}\right)_{ln} \\ \left(\underline{\underline{e_{22}}}\right)_{ln} \end{array} \right\} = \frac{i^n \varepsilon_n}{\pi \epsilon_l} \int_0^{2\pi} \mathcal{R}_n^{(f)}[r(\theta)] \ \sin n\theta \left\{ \begin{array}{c} \cos l\theta \\ \sin l\theta \end{array} \right\} d\theta \qquad \text{(C.5b)}$$

$$\left\{ \begin{array}{c} \left(\underline{\underline{f_{11}}}\right)_{ln} \\ \left(\underline{\underline{f_{21}}}\right)_{ln} \end{array} \right\} = \frac{i^n \varepsilon_n}{\pi \epsilon_l} \int_0^{2\pi} \left\{ \mathcal{R}_n^{(\phi)}[r(\theta)] \ \cos n\theta \cos^2\varphi - \mathcal{T}_n^{(\phi)}[r(\theta)] \ \sin n\theta \sin 2\varphi \right.$$

$$\left. + \ \mathcal{M}_n^{(\phi)}[r(\theta)] \ \cos n\theta \sin^2\varphi \right\} \left\{ \begin{array}{c} \cos l\theta \\ \sin l\theta \end{array} \right\} d\theta \qquad \text{(C.6a)}$$

$$\left\{ \begin{array}{c} \left(\underline{\underline{f_{12}}}\right)_{ln} \\ \left(\underline{\underline{f_{22}}}\right)_{ln} \end{array} \right\} = \frac{i^n \varepsilon_n}{\pi \epsilon_l} \int_0^{2\pi} \left\{ \mathcal{R}_n^{(\phi)}[r(\theta)] \ \sin n\theta \cos^2\varphi + \mathcal{T}_n^{(\phi)}[r(\theta)] \ \cos n\theta \sin 2\varphi \right.$$

$$\left. + \ \mathcal{M}_n^{(\phi)}[r(\theta)] \ \sin n\mathcal{C} \sin^2\varphi \right\} \left\{ \begin{array}{c} \cos l\theta \\ \sin l\theta \end{array} \right\} d\theta \qquad \text{(C.6b)}$$

$$\left\{ \begin{array}{c} \left(\underline{\underline{g_{11}}}\right)_{ln} \\ \left(\underline{\underline{g_{21}}}\right)_{ln} \end{array} \right\} = \frac{i^n \varepsilon_n}{\pi \epsilon_l} \int_0^{2\pi} \left\{ \mathcal{R}_n^{(\xi)}[r(\theta)] \ \cos n\theta \cos^2\varphi - \mathcal{T}_n^{(\xi)}[r(\theta)] \ \sin n\theta \sin 2\varphi \right.$$

$$\left. + \ \mathcal{M}_n^{(\xi)}[r(\theta)] \ \cos n\theta \sin^2\varphi \right\} \left\{ \begin{array}{c} \cos l\theta \\ \sin l\theta \end{array} \right\} d\theta \qquad \text{(C.7a)}$$

$$\left\{ \begin{array}{c} \left(\underline{\underline{g_{12}}}\right)_{ln} \\ \left(\underline{\underline{g_{22}}}\right)_{ln} \end{array} \right\} = \frac{i^n \varepsilon_n}{\pi \epsilon_l} \int_0^{2\pi} \left\{ \mathcal{R}_n^{(\xi)}[r(\theta)] \ \sin n\theta \cos^2\varphi + \mathcal{T}_n^{(\xi)}[r(\theta)] \ \cos n\theta \sin 2\varphi \right.$$

$$\left. + \ \mathcal{M}_n^{(\xi)}[r(\theta)] \ \sin n\theta \sin^2\varphi \right\} \left\{ \begin{array}{c} \cos l\theta \\ \sin l\theta \end{array} \right\} d\theta \qquad \text{(C.7b)}$$

$$\left\{ \begin{array}{c} \left(\underline{\underline{h_{11}}}\right)_{ln} \\ \left(\underline{\underline{h_{21}}}\right)_{ln} \end{array} \right\} = \frac{i^n \varepsilon_n}{\pi \epsilon_l} \int_0^{2\pi} \left\{ \mathcal{R}_n^{(\psi)}[r(\theta)] \cos n\theta \cos^2 \varphi - \mathcal{T}_n^{(\psi)}[r(\theta)] \sin n\theta \sin 2\varphi \right.$$

$$\left. + \mathcal{M}_n^{(\psi)}[r(\theta)] \cos n\theta \sin^2 \varphi \right\} \left\{ \begin{array}{c} \cos l\theta \\ \sin l\theta \end{array} \right\} d\theta \qquad \text{(C.8a)}$$

$$\left\{ \begin{array}{c} \left(\underline{\underline{h_{12}}}\right)_{ln} \\ \left(\underline{\underline{h_{22}}}\right)_{ln} \end{array} \right\} = \frac{i^n \varepsilon_n}{\pi \epsilon_l} \int_0^{2\pi} \left\{ \mathcal{R}_n^{(\psi)}[r(\theta)] \sin n\theta \cos^2 \varphi + \mathcal{T}_n^{(\psi)}[r(\theta)] \cos n\theta \sin 2\varphi \right.$$

$$\left. + \mathcal{M}_n^{(\psi)}[r(\theta)] \sin n\theta \sin^2 \varphi \right\} \left\{ \begin{array}{c} \cos l\theta \\ \sin l\theta \end{array} \right\} d\theta \qquad \text{(C.8b)}$$

$$\left\{ \begin{array}{c} \left(\underline{\underline{o_{11}}}\right)_{ln} \\ \left(\underline{\underline{o_{21}}}\right)_{ln} \end{array} \right\} = \frac{i^n \varepsilon_n}{\pi \epsilon_l} \int_0^{2\pi} \left\{ \left[\mathcal{M}_n^{(\phi)}[r(\theta)] - \mathcal{R}_n^{(\phi)}[r(\theta)] \right] \cos n\theta \sin \varphi \cos \varphi \right.$$

$$\left. - \mathcal{T}_n^{(\phi)}[r(\theta)] \sin n\theta \, (\cos^2 \varphi - \sin^2 \varphi) \right\} \left\{ \begin{array}{c} \cos l\theta \\ \sin l\theta \end{array} \right\} d\theta \qquad \text{(C.9a)}$$

$$\left\{ \begin{array}{c} \left(\underline{\underline{o_{12}}}\right)_{ln} \\ \left(\underline{\underline{o_{22}}}\right)_{ln} \end{array} \right\} = \frac{i^n \varepsilon_n}{\pi \epsilon_l} \int_0^{2\pi} \left\{ \left[\mathcal{M}_n^{(\phi)}[r(\theta)] - \mathcal{R}_n^{(\phi)}[r(\theta)] \right] \sin n\theta \sin \varphi \cos \varphi \right.$$

$$\left. + \mathcal{T}_n^{(\phi)}[r(\theta)] \cos n\theta \, (\cos^2 \varphi - \sin^2 \varphi) \right\} \left\{ \begin{array}{c} \cos l\theta \\ \sin l\theta \end{array} \right\} d\theta \qquad \text{(C.9b)}$$

$$\left\{ \begin{array}{c} \left(\underline{\underline{p_{11}}}\right)_{ln} \\ \left(\underline{\underline{p_{21}}}\right)_{ln} \end{array} \right\} = \frac{i^n \varepsilon_n}{\pi \epsilon_l} \int_0^{2\pi} \left\{ \left[\mathcal{M}_n^{(\xi)}[r(\theta)] - \mathcal{R}_n^{(\xi)}[r(\theta)] \right] \cos n\theta \sin \varphi \cos \varphi \right.$$

$$\left. - \mathcal{T}_n^{(\xi)}[r(\theta)] \sin n\theta \, (\cos^2 \varphi - \sin^2 \varphi) \right\} \left\{ \begin{array}{c} \cos l\theta \\ \sin l\theta \end{array} \right\} d\theta \qquad \text{(C.10a)}$$

$$\left\{ \begin{array}{c} \left(\underline{\underline{p_{12}}}\right)_{ln} \\ \left(\underline{\underline{p_{22}}}\right)_{ln} \end{array} \right\} = \frac{i^n \varepsilon_n}{\pi \epsilon_l} \int_0^{2\pi} \left\{ \left[\mathcal{M}_n^{(\xi)}[r(\theta)] - \mathcal{R}_n^{(\xi)}[r(\theta)] \right] \sin n\theta \sin \varphi \cos \varphi \right.$$

$$\left. + \mathcal{T}_n^{(\xi)}[r(\theta)] \cos n\theta \, (\cos^2 \varphi - \sin^2 \varphi) \right\} \left\{ \begin{array}{c} \cos l\theta \\ \sin l\theta \end{array} \right\} d\theta \qquad \text{(C.10b)}$$

$$\left\{ \begin{array}{c} \left(\underline{\underline{q_{11}}}\right)_{ln} \\ \left(\underline{\underline{q_{21}}}\right)_{ln} \end{array} \right\} = \frac{i^n \varepsilon_n}{\pi \epsilon_l} \int_0^{2\pi} \left\{ \left[\mathcal{M}_n^{(\psi)}[r(\theta)] - \mathcal{R}_n^{(\psi)}[r(\theta)] \right] \cos n\theta \sin\varphi \cos\varphi \right.$$

$$\left. - \mathcal{T}_n^{(\psi)}[r(\theta)] \sin n\theta \, (\cos^2\varphi - \sin^2\varphi) \right\} \left\{ \begin{array}{c} \cos l\theta \\ \sin l\theta \end{array} \right\} d\theta \qquad \text{(C.11a)}$$

$$\left\{ \begin{array}{c} \left(\underline{\underline{q_{12}}}\right)_{ln} \\ \left(\underline{\underline{q_{22}}}\right)_{ln} \end{array} \right\} = \frac{i^n \varepsilon_n}{\pi \epsilon_l} \int_0^{2\pi} \left\{ \left[\mathcal{M}_n^{(\psi)}[r(\theta)] - \mathcal{R}_n^{(\psi)}[r(\theta)] \right] \sin n\theta \sin\varphi \cos\varphi \right.$$

$$\left. + \mathcal{T}_n^{(\psi)}[r(\theta)] \cos n\theta \, (\cos^2\varphi - \sin^2\varphi) \right\} \left\{ \begin{array}{c} \cos l\theta \\ \sin l\theta \end{array} \right\} d\theta \qquad \text{(C.11b)}$$

$$\left\{ \begin{array}{c} \left(\underline{\underline{r_{11}}}\right)_{ln} \\ \left(\underline{\underline{r_{21}}}\right)_{ln} \end{array} \right\} = \frac{i^n \varepsilon_n}{\pi \epsilon_l} \int_0^{2\pi} \left\{ \mathcal{Z}_n^{(\phi)}[r(\theta)] \cos n\theta \cos\varphi - \mathcal{N}_n^{(\phi)}[r(\theta)] \sin n\theta \sin\varphi \right\}$$

$$\left\{ \begin{array}{c} \cos l\theta \\ \sin l\theta \end{array} \right\} d\theta \qquad \text{(C.12a)}$$

$$\left\{ \begin{array}{c} \left(\underline{\underline{r_{12}}}\right)_{ln} \\ \left(\underline{\underline{r_{22}}}\right)_{ln} \end{array} \right\} = \frac{i^n \varepsilon_n}{\pi \epsilon_l} \int_0^{2\pi} \left\{ \mathcal{Z}_n^{(\phi)}[r(\theta)] \sin n\theta \cos\varphi + \mathcal{N}_n^{(\phi)}[r(\theta)] \cos n\theta \sin\varphi \right\}$$

$$\left\{ \begin{array}{c} \cos l\theta \\ \sin l\theta \end{array} \right\} d\theta \qquad \text{(C.12b)}$$

$$\left\{ \begin{array}{c} \left(\underline{\underline{s_{11}}}\right)_{ln} \\ \left(\underline{\underline{s_{21}}}\right)_{ln} \end{array} \right\} = \frac{i^n \varepsilon_n}{\pi \epsilon_l} \int_0^{2\pi} \left\{ \mathcal{Z}_n^{(\xi)}[r(\theta)] \cos n\theta \cos\varphi - \mathcal{N}_n^{(\xi)}[r(\theta)] \sin n\theta \sin\varphi \right\}$$

$$\left\{ \begin{array}{c} \cos l\theta \\ \sin l\theta \end{array} \right\} d\theta \qquad \text{(C.13a)}$$

$$\left\{ \begin{array}{c} \left(\underline{\underline{s_{12}}}\right)_{ln} \\ \left(\underline{\underline{s_{22}}}\right)_{ln} \end{array} \right\} = \frac{i^n \varepsilon_n}{\pi \epsilon_l} \int_0^{2\pi} \left\{ \mathcal{Z}_n^{(\xi)}[r(\theta)] \sin n\theta \cos\varphi + \mathcal{N}_n^{(\xi)}[r(\theta)] \cos n\theta \sin\varphi \right\}$$

$$\left\{ \begin{array}{c} \cos l\theta \\ \sin l\theta \end{array} \right\} d\theta \qquad \text{(C.13b)}$$

$$\left\{ \begin{array}{c} \left(\underline{\underline{t_{11}}}\right)_{ln} \\ \left(\underline{\underline{t_{21}}}\right)_{ln} \end{array} \right\} = \frac{i^n \epsilon_n}{\pi \epsilon_l} \int_0^{2\pi} \left\{ \mathcal{Z}_n^{(\psi)}[r(\theta)] \cos n\theta \cos\varphi - \mathcal{N}_n^{(\psi)}[r(\theta)] \ \sin n\theta \ \sin\varphi \right\} \left\{ \begin{array}{c} \cos l\theta \\ \sin l\theta \end{array} \right\} d\theta \tag{C.14a}$$

$$\left\{ \begin{array}{c} \left(\underline{\underline{t_{12}}}\right)_{ln} \\ \left(\underline{\underline{t_{22}}}\right)_{ln} \end{array} \right\} = \frac{i^n \epsilon_n}{\pi \epsilon_l} \int_0^{2\pi} \left\{ \mathcal{Z}_n^{(\psi)}[r(\theta)] \sin n\theta \cos\varphi + \mathcal{N}_n^{(\psi)}[r(\theta)] \ \cos n\theta \ \sin\varphi \right\} \left\{ \begin{array}{c} \cos l\theta \\ \sin l\theta \end{array} \right\} d\theta \tag{C.14b}$$

Appendix D

Discrete Least Squares Approximation by Trigonometric Polynomials

This appendix summerizes an algorithm developled by Reichel et al. (1991) for the discrete least squares approximation of a real-valued function by trigonometric polynomials. The function values are given at arbitrary distinct nodes in the interval $[0, 2\pi)$. This algorithm has been employed in section 4.1.3 to minimize the errors of satisfying the fluid-solid interface boundary conditions in a borehole of irregular shape.

This algorithm solves the following minimization problem

$$||f - t|| \equiv \left(\sum_{k=1}^{m} |f(\theta_k) - t(\theta_k)|^2 w_k^2 \right)^{1/2} = \text{minimum} , \tag{D.1}$$

given a set of samples $\{f(\theta_k)\}_{k=1}^m$ of $f(\theta)$ at distinct nodes $\{\theta_k\}_{k=1}^m$ in the interval $[0, 2\pi)$. $\{w_k^2\}_{k=1}^m$ is a set of positive weights and

$$t(\theta) = a_0 + \sum_{j=1}^{l} (a_j \cos j\theta + b_j \sin j\theta), \quad a_j, b_j \in \mathbf{R}, \tag{D.2}$$

is a trigonometric polynomial of order l. The problem is to find the coefficients $\{a_j, b_j\}_{j=0}^{l}$ such that the error in equation (D.1) is as small as possible[1].

Making the substitution $z = e^{i\theta}$ and noticing that equation (D.2) can be written as (Grenander and Szegö, 1984)

$$t(\theta) = z^{-l}\, p(z),$$

we can recast the minimization in equation (D.1) as

$$\left(\sum_{k=1}^{m} \overline{(g(z_k) - p(z_k))}\, (g(z_k) - p(z_k))\, w_k^2 \right)^{1/2} = \text{minimum}\ , \tag{D.3}$$

where $g(z) = z^l f(\theta)$ is the known data, and $p(z) = \sum_{j=0}^{n-1} c_j z^j$ is a polynomial of degree n with $n = 2l + 1$. The coefficients $\{c_j\}_{j=0}^{n-1}$ are related to the coefficients $\{a_j, b_j\}_{j=0}^{l}$ by

$$\begin{cases} a_0 = c_l, \\ a_j = c_{l+j} + c_{l-j}, \\ b_j = i(c_{l+j} - c_{l-j}). \end{cases}$$

Let $\mathrm{R} = [r_{jk}]$ be an upper triangular matrix whose nontrivial elements are determined by

$$z^{k-1} = \sum_{j=1}^{k} r_{jk}\, \psi_{j-1}(z), \quad 1 \le k \le n \tag{D.4}$$

and let $\mathrm{Q} = [q_{kj}]$ be a $m \times n$ matrix defined by

$$q_{kj} = \psi_j(z_k)\, w_k, \quad j = 0, ..., n-1;\ k = 1, ..., m \tag{D.5}$$

where $\{\psi_j\}_{j=0}^{m-1}$ is the family of *orthonormal* Szegö polynomials[2] with respect to the

[1] if $w_k \equiv 1$ and $\{\theta_k\}_{k=1}^{m}$ are equally sampled between $[0, 2\pi)$, the Reichel et al. algorithm reduces to FFT (the fast Fourier transform).

[2] The Szegö polynomial $\psi_j(z)$ and its complementary polynomial $\widetilde{\psi_j}(z)$ satisfy the following Szegö recurrence relations (Reichel et al., 1991):

$$\psi_0(z) = \widetilde{\psi_0}(z) = 1/\sigma_0, \tag{D.6a}$$

$$\sigma_{j+1}\, \psi_{j+1}(z) = z\psi_j(z) + \gamma_{j+1}\, \widetilde{\psi_j}(z), \tag{D.6b}$$

inner product defined by

$$< g, h > \equiv \sum_{k=1}^{m} \overline{g(z_k)}\ h(z_k)\ w_k^2.$$

The usefulness of the matrices R and Q becomes obvious if we write down the result

$$\mathrm{Q}\ \mathrm{R}\ \vec{c} = \mathrm{D}\ \vec{g} \tag{D.7}$$

obtained by Reichel et al. (1991). Where $\vec{c} = [c_0, c_1, ..., c_{n-1}]^T \in \mathbf{C}^n$ is the coefficient vector solving equation (D.3), and $\vec{g} = [g(z_1), g(z_2), ..., g(z_m)]^T \in \mathbf{C}^m$ is the data vector. $\mathrm{D} = diag[w_1, w_2, ..., w_m]$ is a diagonal matrix whose elements are the positive weights $\{w_k\}$. That matrix serves as a weighting factor or as the variance of the data.

This technique relies upon the speed and accuracy for computing Q^* and R^{-1}. The matrix Q, by definition, has orthonormal columns. That is, $\mathrm{Q}^*\mathrm{Q} = \mathrm{I}$, where the superscript star denotes the Hermitian transpose. Q is obtained by simply evaluating the Szegö polynomials at the set of samples $\{z_k\}_{k=1}^m$; R^{-1} is composed of the coefficients of the Szegö polynomials in the power basis $\{1, z, z^2, ..., z^n\}$, and is obtained directly from the coefficients of the Szegö polynomials. The Szegö polynomials and its expansions on the power basis can be efficiently computed by making use of the Szegö recurrence relations. The scheme requires only $O(mn)$ arithmetic operations as compared to $O(mn^2)$ operations needed for other algorithms, where m is number of nodes (samples), n is the number of unknown coefficients. A detailed account of this technique can be found in algorithm 3.1 and algorithm 4.1 of Reichel et al. (1991).

$$\sigma_{j+1}\ \widetilde{\psi}_{j+1}(z) = z\overline{\gamma}_{j+1}\ \psi_j(z) + \widetilde{\psi}_j(z),\ \ j = 0, 1, ..., n-2, \tag{D.6c}$$

where the recurrence coefficients $\gamma_{j+1} \in \mathbf{C}$ and $\sigma_{j+1} > 0$ are determined by

$$\sigma_0 = \alpha_0 = \left(\sum_{k=1}^{m} w_k^2 \right)^{1/2},$$

$$\gamma_{j+1} = - < 1,\ z\psi_j(z) > / \alpha_j,$$

$$\sigma_{j+1} = (1 - |\gamma_{j+1}|^2)^{1/2},$$

$$\alpha_{j+1} = \alpha_j \sigma_{j+1}.$$

The Szegö polynomials are dependent on the set of weights $\{w_k\}$ and the set of samples $\{z_k\}_{k=1}^{m}$ on the unit circle. The merit of the Reichel et al. algorithm is that the basis functions $\{\psi_j(z_k)\}_{j=1}^{n}$ are adaptive to the shape of the noncircular borehole. Figure D-1 shows a representative Szegö polynomial $\psi_5(z)$ on the unit circle, using the elliptical borehole in Figure 4-2 and the discretization as marked in the figure. Recall that 180 elements are used in discretizing the borehole and the order of truncation is L =10. The Szegö polynomial is similar to a sinusoidal function. However, its amplitude is modulated by the shape of the borehole: it is larger near the minor axis and smaller near the major axis of the borehole. Although it is periodic with a 2π periodicity, the real part is not at a maximum and the imaginary part is not zero at $\theta = 0$, π, and 2π.

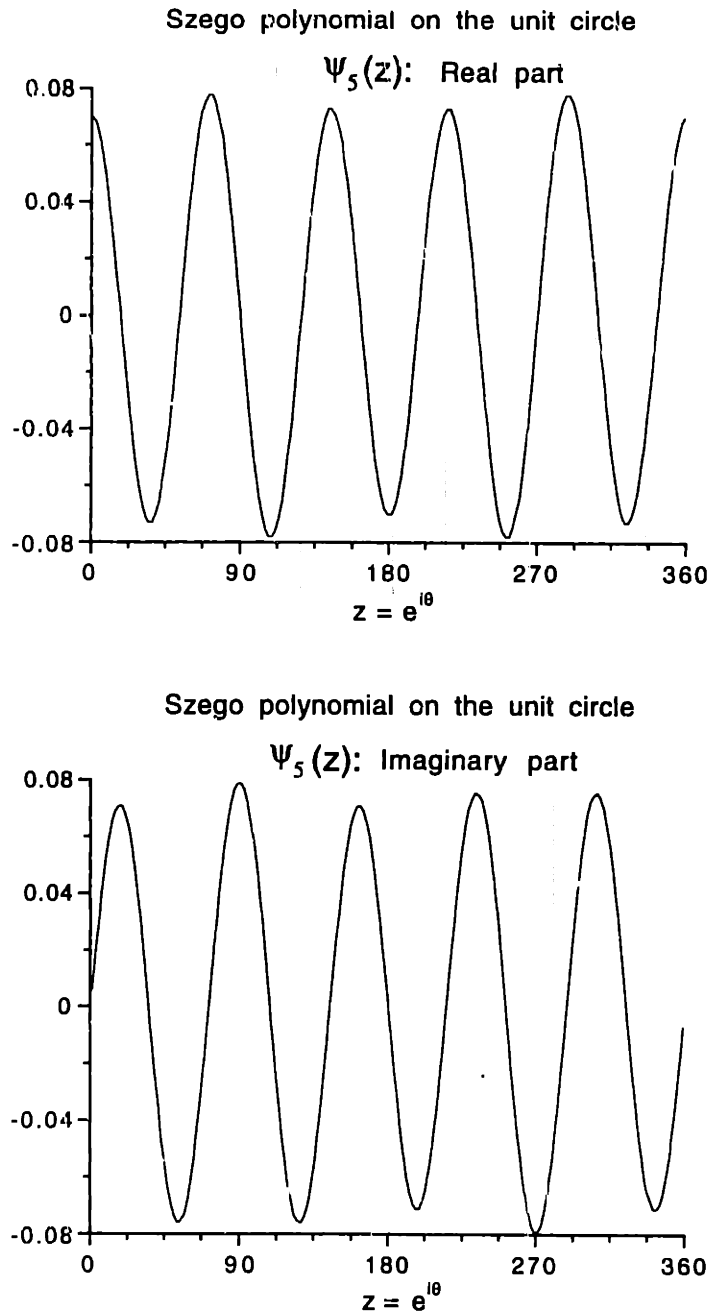

Figure D-1: The Szegö polynomial $\psi_5(z)$ on the unit circle: (top) real part and (bottom) imaginary part. It is computed for the elliptical borehole shown in Figure 4-2.

Appendix E

Determination of the Coefficients of an Optimal Absorbing Boundary Condition

In this appendix, we present a method to compute $\{a_{ij}\}$, the coefficients of an optimal absorbing boundary condition. Recall that they are determined by the following set of equations:

$$\frac{a_{00}z + a_{10} + a_{20}z^{-1} - z}{a_{02}z + a_{12} + a_{22}z^{-1}} = \cos(\vartheta_+ + \vartheta_-) + i\sin(\vartheta_+ + \vartheta_-), \tag{E.1}$$

$$\frac{a_{01}z + a_{11} + a_{21}z^{-1}}{a_{02}z + a_{12} + a_{22}z^{-1}} = -(\cos\vartheta_+ + \cos\vartheta_-) - i(\sin\vartheta_+ + \sin\vartheta_-), \tag{E.2}$$

$$\sum_{i=0,j=0} a_{ij} = 1, \tag{E.3}$$

$$\sum_{j=0}(a_{0j} - a_{2j}) = 1, \tag{E.4}$$

$$\sum_{i=0}(a_{i0} - a_{i2}) = 1, \tag{E.5}$$

and

$$\sum_{i=0,j=0} a_{ij}^2 = \text{minimum}, \tag{E.6}$$

where $z = e^{i\widetilde{\Delta}t}$.

The problem is a quadratic minimization subject to linear constraints. In our method, equation (E.6) is replaced by a linear equation

$$\sum_{i=0,j=0} (-1)^{i+j} a_{ij} = \lambda, \tag{E.7}$$

where λ is to be determined. Any linear function will serve the purpose as long as it is independent of the other 7 equations.

In terms of λ, $\{a_{ij}\}$ can be solved by

$$\mathcal{A} \begin{bmatrix} a_{01} \\ a_{02} \\ a_{10} \\ a_{11} \\ a_{12} \\ a_{20} \\ a_{21} \\ a_{22} \end{bmatrix} = \begin{bmatrix} 1 \\ 1 \\ 1 \\ \lambda \\ R_z \\ I_z \\ 0 \\ 0 \end{bmatrix}$$

where

$$\mathcal{A} = \begin{bmatrix} 1 & 1 & 1 & 1 & 1 & 1 & 1 & 1 \\ 1 & 1 & 0 & 0 & 0 & -1 & -1 & -1 \\ 0 & -1 & 1 & 0 & -1 & 1 & 0 & -1 \\ -1 & 1 & -1 & 1 & -1 & 1 & -1 & 1 \\ 0 & -(R_xR_z - I_xI_z) & 1 & 0 & -R_x & R_z & 0 & -(R_xR_z + I_xI_z) \\ 0 & -(R_xI_z + R_zI_x) & 0 & 0 & -I_x & -I_z & 0 & -(R_zI_x - R_xI_z) \\ R_z & -(R_yR_z - I_yI_z) & 0 & 1 & -R_y & 0 & R_z & -(R_yR_z + I_yI_z) \\ I_z & -(R_yI_z + R_zI_y) & 0 & 0 & -I_y & 0 & -I_z & -(R_zI_y - R_yI_z) \end{bmatrix}$$

and $R_z = \cos\widetilde{\Delta}t$, $I_z = \sin\widetilde{\Delta}t$, $R_x = \cos(\vartheta_+ + \vartheta_-)$, $I_x = \sin(\vartheta_+ + \vartheta_-)$, $R_y = -(\cos\vartheta_+ + \cos\vartheta_-)$, and $I_y = -(\sin\vartheta_+ + \sin\vartheta_-)$.

The solution of the above 8×8 matrix equation can be expressed as

$$a_{ij} = \gamma_{ij}^{(0)} + \gamma_{ij}^{(1)}\lambda,$$

where $\gamma_{ij}^{(0)}$ and $\gamma_{ij}^{(1)}$ are derived from the inverse of $\mathcal{A}$.

The choice of λ is to make (E.6) minimum, which yields

$$\lambda = -\frac{\sum_{i=0,j=0} \gamma_{ij}^{(0)}\gamma_{ij}^{(1)}}{\sum_{i=0,j=0} \gamma_{ij}^{(1)}\gamma_{ij}^{(1)}}.$$

Thus the optimal coefficients are computed by

$$a_{ij} = \gamma_{ij}^{(0)} - \frac{\sum_{k=0,l=0} \gamma_{kl}^{(0)}\gamma_{kl}^{(1)}}{\sum_{k=0,l=0} \gamma_{kl}^{(1)}\gamma_{kl}^{(1)}}\gamma_{ij}^{(1)}. \tag{E.8}$$